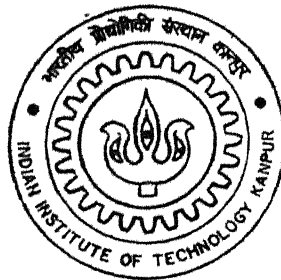


Roll no. - 7210603

Role of Cerium In The Electrochemical Behaviour of Carbon-Alloyed Iron Aluminides

By

Anand Kumar Nigam



**DEPARTMENT OF MATERIALS AND METALLURGICAL ENGINEERING
Indian Institute of Technology Kanpur**

MAY, 2004

TH
mmE/2004/m
N567

Role of Cerium In The Electrochemical Behaviour of Carbon-Alloyed Iron Aluminides

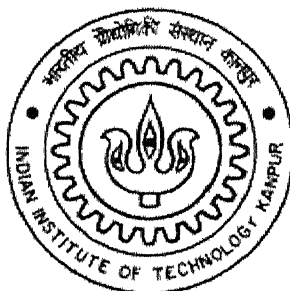
A Thesis submitted

In partial Fulfillment of the Requirements
For the degree of

MASTER OF TECHNOLOGY

by

Anand Kumar Nigam
(Y210603)



to the

DEPARTMENT OF MATERIALS AND METALLURGICAL ENGINEERING

INDIAN INSTITUTE OF TECHNOLOGY, KANPUR

INDIA 208016

May 2004

2004/MME

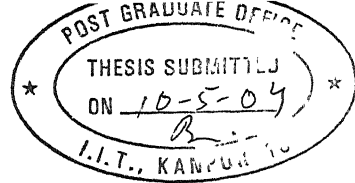
वृत्तपोतम ...
भारतीय ...
... 148412

Tir
MME/2004/M
N562



A148412

Dedicated to
my Parents



CERTIFICATE

This is to certify that the present thesis work entitled “**Role of Cerium in The Electrochemical Behaviour of Carbon-Alloyed Iron Aluminides**”, has been carried out by Anand Kumar Nigam (Y210603), under our supervision and to the best of our knowledge it has not been submitted elsewhere for the award of a degree.

Dr. R. Balasubramaniam

Professor

Dept. of Mat. and Met. Engg.

Indian Institute of Technology,

Kanpur 208016, INDIA.

Dr. Sanjeev Bhargava

Professor

Dept. of Mat. and Met. Engg.

Indian Institute of Technology,

Kanpur 208016, INDIA.

ACKNOWLEDGEMENTS

I wish to express my deep sense of gratitude and sincere thanks to Dr. R. Balasubramaniam and Dr. Sanjeev Bhargava for their able guidance, remarkable patience and constant encouragement throughout the course of the thesis.

I express my sincere appreciation to the assistance of Dr. M.N. Mungole, Senior Research Engineer, Department of MME, IIT Kanpur.

I am immensely thankful to Harish ji and Santosh, Lab assistants, for helping me in many ways during my experimental work.

I am also thankful to Anoop Shukla, Ashish Srivastava, Ajit Misra, T.S.R.Ch. Murthy, Gopi Kishore Mandal and all other friends who have helped me in various capacities throughout my thesis at IIT Kanpur. I will never forget the nice time I spent with my colleagues in the laboratory.

I could not have reached this stage in my life without the sacrifice, constant encouragement and unfailing emotional support from my loving parents.

I am indebted to IIT Kanpur for providing me the best environment to stay and do research in the most fruitful way.

Anand Kumar Nigam
IIT Kanpur
May 2004

CONTENTS

	Page number
Abstract	i
List of Figures	iv
List of Tables	xi
Chapter 1 Introduction	
1.1. Intermetallics	1
1.2. Iron aluminides	4
1.3. Carbon alloyed iron aluminides	5
1.4. Objectives of the present study	5
1.5. Plan of work	6
Chapter 2 Literature review	
2.1 Fe-Al phase diagram and crystal structure	7
2.1.1 Iron aluminides	7
2.1.2 Phase equilibria in Fe-Al-C system	10
2.2 Passivity of B2 iron aluminides in sulphuric acid solution.	14
2.3 Effect of alloying elements	17
2.4 Effect of Cerium	19
2.5 Effect of carbon	21
2.5.1 Earlier work on corrosion of carbon-alloyed iron aluminides.	25
2.6 Electrochemical corrosion	34
2.7 Polarization	38
2.7.1 Potentiodynamic polarisation	43
2.7.2 Criterion for selection of active passive metals	45
2.8 Electrochemical Impedance Spectroscopy	48
2.8.1 Introduction	48
2.8.2 AC Circuit Theory and Representation of Complex	48

	Impedance Values.	
2.8.3	Data Presentation	49
2.8.4	Physical Electrochemistry and Equivalent Circuit Elements	51
2.8.5	Equivalent circuits used for modeling in the AC-impedance study.	57
2.9	Electrochemical impedance spectroscopy study of the surface film of aluminium	64
2.10	Cyclic Voltammetry	73
2.11	Anodic dissolution of iron alloy in sulphuric acid	82
Chapter 3	Experimental procedure	
3.1	Raw materials	88
3.2	Material characterization	91
3.2.1	Optical microscopy	91
3.2.2	Scanning electron microscopy	95
3.3	Electrochemical studies	95
3.3.1	Apparatus for polarization studies, cyclic voltammetry and electrochemical impedance spectroscopy	95
3.3.2	Electrolytes	101
3.3.3	Test procedure for electrochemical studies	101
3.3.4	Potential stabilization	102
3.3.5	Potentiodynamic polarization	102
3.3.6	Electrochemical impedance spectroscopy	103
3.3.7	Cyclic voltammetry	103
Chapter 4	Results and discussion	
4.1	Free corrosion Potential	106
4.1.1	Borate buffer solution	106
4.1.2	Acidic solution	112
4.2	Polarization behaviour	120

4.3	Electrochemical Impedance Spectroscopy	127
4.3.1	Borate buffer solution	127
4.3.2	Acidic solution	139
4.4	Cyclic Voltammetry	160
4.5	Scanning electron microscopy	168

Chapter 5 Summary

5.1	Conclusions	174
5.2	Suggestions for future work	179

References

Appendix A

Appendix B

ABSTRACT

The electrochemical behaviour of three carbon-alloyed iron aluminides has been studied in borate buffered solution (of pH=7.6) using potentiodynamic polarization and electrochemical impedance spectroscopy (EIS), and in 0.25 mol/lit H_2SO_4 solution (of pH=0.74) by using electrochemical impedance spectroscopy and cyclic voltammetry techniques. The carbon-alloyed iron aluminides were obtained from Defence Metallurgical Research Laboratory, Hyderabad. They possessed the composition (in atom percent), Fe-20.0Al-2.0C (referred as ESR74), Fe-18.5Al-3.6C (referred as ESR127) and Fe-19.2Al-3.3C-0.07Ce (referred as ESR137). The composition of these alloys in weight percent, were Fe-11.0Al-0.5C (ESR137), Fe-10.5Al-0.9C (ESR127) and Fe-10.5Al-0.8C-0.2Ce (ESR137). These alloys were processed by arc induction melting and eletro-slag remelting at DMRL, Hyderabad. Electrochemical impedance spectroscopy (EIS) studies were conducted at free corrosion potential (FCP), as a function of immersion time, for long immersion times. The immersion time in borate buffered solution was 168 hours and in 0.25 mol/lit H_2SO_4 solution for 24 hours. For comparison purpose, the immersion studies were also conducted in both the solutions, using electrochemical impedance spectroscopy for 0.05%C mild steel, 316L SS, and Al6063 alloys. Long term immersion studies of 304 SS and 430 SS were performed in addition to the other alloys, in 0.25 mol/lit H_2SO_4 solution. Cyclic voltammetry of the carbon-alloyed iron aluminides was performed 0.25 mol/lit H_2SO_4 solution, without the stabilization of free corrosion potential at scan rates of 10, 50 and 100 mV/sec. Surfaces of Fe-18.5Al-3.6C and Fe-19.2Al-3.3C-0.07Ce after immersion for 24 hours in acidic solution was studied by scanning electron microscopy. All the EIS results were then analyzed in detail by fitting the experimental data with the appropriate equivalent circuit models. The following conclusions were drawn from the study.

The free corrosion potential (FCP) of all the alloys in borate buffered solution moved from active to noble direction, and after 168 hours of immersion the FCP moved in positive direction. This indicated the thickening of surface film with immersion time. The FCP of all the alloys in 0.25 mol/lit H_2SO_4 solution stabilized in more active potentials than in borate buffered solution. This was attributed to the aggressively corrosive nature of 0.25 mol/lit H_2SO_4 solution as compared to the mildly corrosive borate buffered solution.

In borate buffered solution, effect of Ce addition to carbon-alloyed iron aluminides could not be revealed by potentiodynamic polarization studies performed at open circuit potentials. The results obtained from the EIS studies in borate buffered solution showed that the Nyquist plots of all the alloys, i.e. carbon-alloyed iron aluminides, 0.05%C mild steel 316L SS and Al 6063, consisted only of a semicircular arc, both on first immersion and after 168 hours of immersion. The impedance measurements were interpreted using appropriate equivalent circuits. The analysis revealed that the passive film nature of *all* the alloys except Esr127, improved after seven days of immersion in borate buffered solution. This was attributed to improvement in the surface film properties with time. The polarization resistance of Fe-19.2Al-3.3C-0.07Ce improved while that of Fe-18.5Al-3.6C deteriorated slightly, after seven days of immersion in borate buffered solution. The improvement in the polarization resistance of Fe-19.2Al-3.3C-0.07Ce with time was attributed to the effect of cerium addition. Moreover, the higher polarization resistance of Fe-20.0Al-2.0C as against Fe-18.5Al-3.6C, both on first immersion and after seven days of immersion, indicated improved surface film properties in case of Fe-20.0Al-2.0C. This was related to the lower carbon content of Fe-20.0Al-2.0C.

EIS studies in 0.25 mol/lit H_2SO_4 solution showed that the Nyquist plots of carbon-alloyed intermetallics, mild steel and 430 SS after 2 hours, consisted of an inductive loop at very high frequencies, a large capacitive loop at high frequencies (HF), a capacitive loop at low frequency (in case of all the sections of Esr137) and a small inductive one at low frequencies (LF). In case of 316L SS and 304 SS the Nyquist plots consisted of only a semicircular arc. Nyquist plot of Al 6063 consisted of a large capacitive loop at high frequencies (HFs) and an inductive loop at intermediate frequencies (IF), followed by a second capacitive loop at LF values. The data was analyzed using appropriate equivalent circuit models. EIS studies in 0.25 mol/lit H_2SO_4 solution revealed that the nature of surface film of 304 SS, 316L SS and Al 6063 improved, while that of the carbon-alloyed iron aluminides, 0.05%C mild steel and 430 SS deteriorated after 1 day of immersion in 0.25 mol/lit H_2SO_4 solution. Therefore, it was concluded that in case of 316L SS, 304 SS and Al6063 the surface film that forms on the surface with time in the acidic solution is much more protective as compared to that on 430 SS and the carbon alloyed intermetallics. This was attributed to the presence of chromium and nickel in 304 SS and 316L SS. EIS studies in

0.25 mol/lit H_2SO_4 also revealed improved surface film properties, in the case of Ce-alloyed iron aluminide when compared to the non Ce-alloyed iron aluminides, both on first immersion and after 1 day of immersion. Therefore, it was concluded, that Ce-addition positively modified the surface film on carbon-alloyed iron aluminides.

Cyclic voltammetry studies, conducted on the carbon-alloyed iron aluminides in 0.25 mol/lit H_2SO_4 solution, showed that the dissolution of iron into Fe^{+3} was prominent reaction at potentials anodic to the zero current potential for non-Ce alloyed sample, whereas the formation of $\text{Fe}(\text{OH})_2^+$ and FeOH^{+2} ions were prominent for Ce-alloyed sample. It was proposed that the adsorption of $\text{Fe}(\text{OH})_2^+$ and FeOH^{+2} ions on the surface may result in the enhanced passivity noticed in case of Ce-alloyed iron aluminide.

REFERENCES

1. N. S. Stoloff, "Ordered alloys – physical metallurgy and structural applications," *International Metal Review*, 29, 1984, pp 123-135.
2. T. Yamamoto. "The development of Sendust and other ferromagnetic alloys, ". Chiba: *Committee of Academic achievements*, 1980, pp 1-6.
3. C. T. Liu, J.O. Stiegler and F.H. Froes, "Ordered Intermetallics," *Metals Handbook*, 10th ed., ASM, Metals Park, USA, 2, 1990, pp. 913-942.
4. G. Sauthoff, *Z. Metallkd*, 80, 1989, pp 337-344.
5. A. J. Bradley and A.H. Jay, *J of Iron and Steel Institute*, 125, 1932, p 339.
6. C Sykis and J. Bampfylde, *J of Iron and Steel Institute*, 130, 1934, p 389.
7. C. T. Liu and K.S. Kumar, "Ordered Intermetallic Alloys, Part 1, Nickel and Iron aluminides," *JOM*, 45, 1993, pp. 38-44.
8. C. T. Liu, C.G. McKamey and E. H. Lee, "An environmental effect as the major cause room temperature embrittlement in FeAl," *Scripta Metall.*, 23, 1996, pp. 875-880.
9. C. G. McKamey and C.T.Liu. "Chromium addition and environmental embrittlement Fe₃Al," *Scripta Metall. Mater.* 24, 1992, pp. 119-2122.
10. Zhonghua, S. Yangshan, L. Guijun, and G. Jun, "Ductility improvement of Fe₃Al based alloys with surface coating," *Scripta Mater.*, 34, 1996, pp 1071-1075.
11. R. Balasubramaniam, "On the role of chromium in minimizing room temperature hydrogen embrittlement in iron aluminides," *Scripta Mater.*, 34, 1996, pp.127-133.
12. R. Balasubramaniam, "Alloy development to minimize room temperature hydrogen embrittlement in iron aluminides," *J. Alloys and Comp.*, 1994, pp. 253-254.
13. R. G. Baligidad, U. Prakash, A. Radhakrishna and V. Ramakrishna Rao, "Effect of carbides on embrittlement of Fe₃Al based intermetallic alloys," *Scripta Mater*, 36, 1997, pp. 667-671.
14. R. G. Baligidad, U. Prakash, A. Radhakrishna and V. Ramakrishna Rao, "Effect of carbon contents on high temperature tensile properties of Fe₃Al based intermetallic alloy," *Scripta Mater.*, 36, 1997, pp.105-109.

LIST OF FIGURES

1.	The Fe-Al phase diagram.	8
2.	The DO3 and B2 ordered crystal structure of FeAl and Fe ₃ Al.	9
3.	The perovskite crystal structure of Fe ₃ AlC.	9
4.	Al-C-Fe liquidus in weight percent.	11
5.	Fe-Al-C isotherms at 25°C in weight percent.	11
6.	Fe-Al-C isotherms at 1000°C in weight percent.	12
7.	Schematic picture of the passive film formation on FeAl alloy in sulphuric acid: (A) surface of active FeAl after cathodic treatment covered with an Al-rich oxide layer; (B) formation of an outermost precipitated mixed aluminium-iron oxy-hydroxide layer; (C) passive FeAl with a fully developed aluminium-iron oxy-hydroxide layer superposing the inner passive Al-rich oxide layer.	16
8.	Typical transition for HSLA steel without inclusion shape control.	22
9.	Effect of cerium-sulphur ratio in the upper shelf impact energy for HSLA steel [41]	22
10.	Potentiodynamic polarization behaviour of Fe-20.0Al-2.0C, Fe-18.5Al-3.6C, Fe- 19.2Al-3.3C-0.07Ce and mild steel in freely aerated 0.25 mol/lit H ₂ SO ₄ using a scan rate of 1 mV/sec.	26
11.	Corrosion rate as a function of time for the carbon-alloyed iron aluminides and mild steel in freely aerated 0.25 mol/lit H ₂ SO ₄ solution: (a) total duration of 11 hours (b) total duration of 85 hours.	27
12.	Potentiodynamic polarization diagrams obtained in 0.05 mol/l H ₂ SO ₄ solution of pH = 1, at a scan rate of 1 mV/s. The intermetallics exhibited active-passive behaviour.	29
13.	Potentiodynamic polarization diagrams obtained in 0.15 N H ₃ BO ₄ + 0.15N Na ₂ B ₄ O ₇ .10H ₂ O solution of pH = 8.44, at a scan rate of 1 mV/s. The intermetallics exhibited stable passive behaviour.	29
14.	Corrosion rate as a function of time for the intermetallics in 0.05 mol/l H ₂ SO ₄	30

solution. Data were obtained after 24 h intervals. The data for Fe–28Al is from Babu *et al* (2000).

15.	SEM micrograph of Fe–28.1Al–2.1C: (a) basic microstructure, (b) after immersion for 2 h and (c) after immersion for 24 h in 0.05 mol/l H ₂ SO ₄ solution.	31
16.	Thermodynamic energy profile for metals and their compounds.	35
17.	Basic wet corrosion cell.	37
18.	Evans diagram for an active metal.	40
19.	Various types of polarization methods.	42
20.	Anodic polarization curve for metal exhibiting passivity.	44
21.	Schematic curve showing active passive polarization behaviour.	46
22.	Schematic anodic polarization curves for hypothetical alloy A, B, C and D in 1) reducing 2) moderately oxidizing 3) highly oxidizing environments.	46
23.	Sinusoidal Current Response in a Linear System.	50
24.	Nyquist Plot with Impedance Vector.	50
25.	Simple Equivalent Circuit with One Time Constant.	52
26.	Bode plot with one time constant.	52
27.	Equivalent circuits and the corresponding physical picture of the corroding surface.	58
28.	Typical impedance response by the equivalent circuit shown in Fig. 27a	60
29.	Typical impedance response by the equivalent circuits shown in Fig. 27b, c and d.	60
30.	Typical impedance response by the equivalent circuit shown in Fig 15e	63
31.	Sequential Nyquist diagrams for pure aluminium RDE in 0.75% citric acid solution at the OCP. (x) First, (○) second, (┘) third	66
32.	EIS spectra of pure aluminum in 1 M KOH at different potentials	66
33.	Circuit model of aluminum in 1 M KOH	68
34.	EIS response of the three Al samples in 0.50 N Na ₂ SO ₄ solution at the OCP and at 30 °C	68
35.	The equivalent circuit model used to fit the experimental data presented in Fig.	68

34.		
36.	Typical complex plane impedance plot measured for pure Al in 0.5 M $\text{Na}_2\text{SO}_4 + 0.2 \text{ N NaX}$ solution ($\text{pH} \approx 6.80$) at the OCP and at 30 °C	70
37.	The equivalent circuit model used to analyse the experimental data presented in Fig.36	70
38.	Effect of surfactant concentration on the impedance response of pure Al in deaerated 1.0 M HCl solution at OCP and at 30 °C. (1) 0.00 M NS; (2) 0.0002 M; (3) 0.0004 M; (4) 0.0006 M; (5) 0.002 M; (6) 0.004 M; (7) 0.006 M; (8) 0.01 M	70
39.	The equivalent circuit model used to fit the experimental data	72
40.	Bode plots for Al–0.40 wt.%Sn alloy in borate buffer solution ($T=25$ °C; pH 7.8) after (—) 0.5 h and (...) 8 h of stabilisation at the open circuit potential. An equivalent circuit is given in the figure.	72
41.	Variation of applied potential with time in linear sweep voltammetry, showing the initial potential, V_1 and the final potential V_2 . The sweep rate $ dV/dt = v$.	74
42.	Linear sweep voltammogram for a reversible reduction at a planar electrode.	74
43.	Linear sweep voltammogram for different sweep rates, for a reversible reduction at a planar electrode	76
44.	Series of linear sweep voltammograms recorded at a single voltage sweep rate for different values of the reduction rate constant (k_{red}).	78
45.	Variation of applied potential with time in cyclic voltammetry, showing the initial potential, V_1 and the final potential V_2 . The sweep rate $ dV/dt = v$.	78
46.	Cyclic voltammogram for a reversible reaction.	78
47.	Cyclic voltammograms at different scan rates for a reversible electron reaction.	81
48.	The effect of increasing irreversibility on the shape of cyclic voltammograms	81
49.	Experimental results of electrochemical impedance, Z (a)– (c), and dissolution efficiency of F(II), Φ_{diss} (d)–(f), on Fe-2.5 wt% Mo electrode in sulphuric acid solution ($\text{pH}=1$).	84
50.	Nyquist impedance spectra for the iron electrode in $0.5 \text{ mol/dm}^{-3} \text{ HClO}_4$ solution at different potentials: (a) Corrosion potential, -482 mV (vs. SCE);	85

	(b) -400 mV; (c) -350 mV; (d) -300 mV; (e) -250 mV; (f) -200 mV	
51.	Nyquist impedance spectra for the iron electrode in 0.5 mol/dm ⁻³ H ₂ SO ₄ solution at different potentials. (a) Corrosion potential, -530 mV (vs. SCE); (b) -450 mV; (c) -400 mV; (d) -350 mV.	86
52.	Optical microstructure of Fe-18.5Al-3.6C alloy in (a) rolling plane (b) long transverse transverse (c) short transverse direction.	92
53.	Optical microstructure of Fe-20.0Al-2.0C alloy in (a) rolling plane (b) long transverse transverse (c) short transverse direction.	93
54.	Optical microstructure of Fe-19.2Al-3.3C-0.07Ce alloy in (a) rolling plane (b) long transverse transverse (c) short transverse direction.	94
55.	Electrochemical polarisation round bottom cell used for conducting polarisation studies	96
56.	Schematic diagram showing the connections in the potentiostat	98
57.	Electrochemical cell used for conducting long term electrochemical impedance spectroscopy (EIS) experiments.	99
58.	Potential waveform applied in cyclic voltammetry, showing the initial potential and the final potential.	104
59.	Variation in free corrosion potential as a function of time for Fe-20.0Al-2.0C (ESR 74), Fe-18.5Al-3.6C (ESR 127), Fe-19.2Al-3.3C-0.07Ce (ESR 137) alloys and 0.05 %C mild steel in borate buffered solution (a) immediately after immersion (b) after 168 hours of immersion.	108
60.	Variation in free corrosion potential as a function of time for 316L SS and Al 6063 alloys in borate buffered solution (a) immediately after immersion (b) after 168 hours of immersion.	110
61.	Variation in free corrosion potential as a function of time for Fe-20.0Al-2.0C, Fe-18.5Al-3.6C and Fe-19.2Al-3.3C-0.07Ce alloys in freely-aerated 1 mol/lit H ₂ SO ₄ solution (a) immediately after immersion (b) after 24 hours of immersion.	113
62.	Variation in free corrosion potential as a function of time of Fe-19.2Al-3.3C-0.07Ce for the rolling plane (RD), long transverse plane (LT), and short	115

	transverse planes (ST) in freely aerated 0.25 mol/lit H_2SO_4 solution (a) immediately after immersion (b) after 24 hours of immersion.	
63.	Variation in free corrosion potential as a function of time for 0.05 % C mild steel, 304 SS, 430 SS, 316L SS and Al 6063 in freely-aerated 0.25 mol/lit H_2SO_4 solution (a) immediately after immersion (b) after 24 hours of immersion.	117
64.	Potentiodynamic polarization behavior of the rolling plane of as received Fe-18.5Al-3.6C, Fe-20.0Al-2.0C and Fe-19.2Al-3.3C-0.07Ce alloys in borate buffered solution. The polarization curve of mild steel has also been presented for comparison	121
65.	Potentiodynamic polarization behaviour of Fe-20.0Al-2.0C, Fe-18.5Al-3.6C, Fe- 19.2Al-3.3C-0.07Ce and mild steel in freely aerated 0.25 mol/lit H_2SO_4 using a scan rate of 1 mV/sec [19][12].	122
66.	Corrosion rate as a function of time for the carbon-alloyed iron aluminides and mild steel in freely aerated 0.25 mol/lit H_2SO_4 solution: (a) total duration of 11 hours (b) total duration of 85 hours	124
67.	Nyquist plots for the alloys in borate buffered solution, at free corrosion potential, after 2 hours and 168 hours of immersion: (a) Fe-19.2Al-3.3C-0.07Ce (b) Fe-18.5Al-3.6C (c) Fe-20.0Al-2.0C (d) Mild steel (e) 316L SS (f) Al6063 alloy.	128
68.	Bode phase plots for the alloys in borate buffered solution, after 2 hours and 168 hours of immersion: (a) Fe-19.2Al-3.3C-0.07Ce (b) Fe-18.5Al-3.6C (c) Fe-20.0Al-2.0C (d) Mild steel (e) 316L SS (f) Al6063 alloy.	129
69.	Bode magnitude plot for all the alloys in borate buffered solution after 2 hours and 168 hours of immersion: : (a) Fe-19.2Al-3.3C-0.07Ce (b) Fe-18.5Al-3.6C (c) Fe-20.0Al-2.0C (d) Mild steel (e) 316L SS (f) Al6063 alloy.	130
70.	Equivalent circuit used for fitting experimental EIS data obtained in borate buffered solution.	134
71.	Nyquist plots for the alloys in freely aerated 0.25 mol/lit H_2SO_4 after 2 hours and 24 hours (one day) of immersion time: (a) Fe-19.2Al-3.3C-0.07Ce (b) Fe-18.5Al-3.6C (c) Fe-20.0Al-2.0C (d) Fe-19.2Al-3.3C-0.07Ce (LT) (e) Fe-	140

	19.2Al-3.3C-0.07Ce (ST) (f) Mild steel (g) 316L SS (h) Al 6063 (i) 304 SS (j) 430 SS.	
72.	Bode phase plot for the alloys in freely aerated 0.25 mol/lit H ₂ SO ₄ after 2 hours and 24 hours (one day) of immersion time: (a) Fe-19.2Al-3.3C-0.07Ce (b) Fe-18.5Al-3.6C (c) Fe-20.0Al-2.0C (d) Fe-19.2Al-3.3C-0.07Ce (LT) (e) Fe-19.2Al-3.3C-0.07Ce (ST) (f) Mild steel (g) 316L SS (h) Al 6063 (i) 304 SS (j) 430 SS.	144
73.	Bode magnitude plots for the alloys in freely aerated 0.25 mol/lit H ₂ SO ₄ after 2 hours and 24 hours (one day) of immersion time (a) Fe-19.2Al-3.3C-0.07Ce (b) Fe-18.5Al-3.6C (c) Fe-20.0Al-2.0C (d) Fe-19.2Al-3.3C-0.07Ce (LT) (e) Fe-19.2Al-3.3C-0.07Ce (ST) (f) Mild steel (g) 316L SS (h) Al 6063 (i) 304 SS (j) 430 SS.	148
74.	The equivalent circuit to fit the complex plane plots composed of (a) a single capacitive loop (b) a high frequency inductive loop and capacitive loop (c) a high frequency inductive loop, a high frequency capacitive loop and a low frequency inductive loop (d) a high frequency inductive loop, two capacitive loops and a low frequency inductive loop (e) a high frequency capacitive loop, intermediate frequency inductive loop and low frequency capacitive loop.	151
75.	Cyclic voltammograms for Fe-19.2Al-3.3C-0.07Ce in 0.25 mol/lit H ₂ SO ₄ (a) 10 mV/sec (b) 50 mV/sec (c) 100 mV/sec.	161
76.	Cyclic voltammograms for Fe-18.5Al-3.6C in 0.25 mol/lit H ₂ SO ₄ (a) 10 mV/sec (b) 50 mV/sec (c) 100 mV/sec.	162
77.	Cyclic voltammograms for Fe-20.0Al-2.0C in 0.25 mol/lit H ₂ SO ₄ (a) 10 mV/sec (b) 50 mV/sec (c) 100 mV/sec.	163
78.	SEM Micrograph of Fe-19.2Al-3.3C-0.07Ce (ESR137) (a) after immersion in freely aerated 0.25 mol/lit H ₂ SO ₄ solution for 24 hour (b) without immersion in acidic solution.	169
79.	SEM Micrograph of Fe-19.2Al-3.3C-0.07Ce (ESR137) (a) after immersion in freely aerated 0.25 mol/lit H ₂ SO ₄ solution for 24 hour (b) without immersion in acidic solution.	170
80.	SEM Micrograph of Fe-19.2Al-3.3C-0.07Ce (ESR137) (a) after immersion in	171

freely aerated 0.25 mol/lit H_2SO_4 solution for 24 hour (b) without immersion in acidic solution.

- | | | |
|-----|--|-----|
| 81. | SEM Micrograph of Fe-19.2Al-3.3C-0.07Ce (ESR137) after immersion in freely aerated 0.25 mol/lit H_2SO_4 solution for 24 hours. | 172 |
| 82. | SEM Micrograph of Fe-18.5Al-3.6C (ESR127) after immersion in freely aerated 0.25 mol/lit H_2SO_4 solution for 24 hour. | 172 |
| 83. | SEM Micrograph of Fe-18.5Al-3.6C (ESR127) after immersion in freely aerated 0.25 mol/lit H_2SO_4 solution for 24 hour. | 173 |
| 84. | SEM Micrograph of Fe-18.5Al-3.6C (ESR127) after immersion in freely aerated 0.25 mol/lit H_2SO_4 solution for 24 hour. | 173 |

LIST OF TABLES

1.	Some past and present applications of intermetallics.	3
2.	Potential applications of Iron aluminides.	3
3.	Typical room temperature properties of Iron aluminides	8
4.	Passivation parameters obtained from the potentiodynamic polarisation of the Fe-18.5Al-3.6C, Fe-20.0Al-2.0C and, Fe-19.2Al-3.3C-0.07Ce alloys in freely aerated 0.25 mol/lit H ₂ SO ₄ solution.	33
5.	5 Parameters determined from the potentiodynamic polarization curves for the carbon-alloyed iron aluminides	33
6.	Standard reference electrode potentials	37
7.	a) Chemical compositions of 304 SS, 430 SS and 316L SS alloys. b) Chemical composition of Al 6063 alloy.	90
8.	Stabilized value of free corrosion potential (FCP) of the alloys in borate buffered solution after first immersion and after 168 hours of immersion.	119
9.	Stabilized value of free corrosion potential (FCP) of all the alloys in freely aerated 0.25 mol/lit H ₂ SO ₄ after first immersion and after 24 hours of immersion.	119
10.	Passivation parameters obtained from the potentiodynamic polarization curves of the Fe-18.5Al-3.6C, Fe-20.0Al-2.0C, Fe-19.2Al-3.3C-0.07Ce and 0.05 %C mild steel alloys in borate buffered solution.	125
11.	Passivation parameters obtained from the potentiodynamic polarisation of the Fe-18.5Al-3.6C, Fe-20.0Al-2.0C and, Fe-19.2Al-3.3C-0.07Ce alloys in freely aerated 0.25 mol/lit H ₂ SO ₄ solution	126
12.	Values of all the circuit parameters obtained after fitting the experimental EIS data obtained in borate buffered solution of pH=7.6 with the circuit shown in Fig. 70.	138
13.	Values of all the circuit parameter for different sections of Fe-19.2Al-3.3C-0.07Ce, Fe-18.5Al-3.6C and Fe-20.0Al-2.0C obtained after fitting the experimental data obtained in acidic solution with the circuit shown in	157

Figure 74

- | | | |
|-----|---|-----|
| 14. | Values of all the circuit parameter for Mild Steel, 304 SS and 430 SS obtained after fitting the experimental data in acidic solution with the circuit shown in Figure 74. The percentage error is shown within brackets. | 158 |
| 15. | Values of all the circuit parameters for Al 6063 obtained after fitting the experimental data in acidic solution with the circuit shown in Figure 74e. | 159 |
| 16. | List of anticipated redox reactions | 166 |
| 17. | Peak potential and peak current values at different scan rate for different peaks in the voltammogram of Fe-18.5Al-3.6C, Fe-20.0Al-2.0C and Fe-19.2Al-3.3C-0.07Ce | 167 |

INTRODUCTION

1.1 Intermetallics

Ordered intermetallics constitute a unique class of advanced materials that form long range ordered crystal structure below a critical temperature termed as critical ordering temperature (T_c) [1]. These intermetallics usually exist in narrow or fixed compositional ranges around simple stoichiometric ratios (similar to inorganic compounds). The research on ordered intermetallic alloys was motivated by the need to develop materials possessing high specific strength for structural applications at elevated temperatures.

Intermetallics is the short and summarizing designation for the intermetallic phases and compounds which result from the combination of various metals and which form a tremendously numerous and manifold class of materials.(Table 1). Intermetallics became a subject of scientific research during the 19th century with the development of physical metallurgy and the first validated instance of intermetallic compound formation was reported by Karsten (1839) in Germany. The early work on intermetallics during the first decades of the 20th century included studies of phase stabilities, phase equilibria and phase reactions in order to establish phase diagrams, as well as studies of various properties i.e chemical and electrochemical properties, mechanical properties and physical properties including magnetism and superconductivity. With respect to mechanical behaviour, it was realized that the outstanding hardness of intermetallics is accompanied by an unusual brittleness.

Intermetallics were used in 20th century primarily for applications as functional materials as is exemplified in Table 1. Indeed the first industrial application relied on the special magnetic behaviour of certain phases, and respective materials developments led to Sendust, which shows outstanding magnetic properties and wear resistance and is widely used for magnetic heads of tape recorders. [2]. In the second half of the 20th century another important application resulted from the development of new superconducting materials based on A15 compounds which are used as superconducting

magnets. A third group of functional materials, the shape memory alloys, makes use of a martensitic phase transformation and has again found manifold applications during the last three decades. An important group of functional materials is formed by the III-V compounds, e.g. InSb, InAs, GaAs, which have found applications in electronics and in thermoelectric power generation.

Intermetallics did not find application as structural materials in the past because of their brittleness. The only noteworthy exception is the continuing use of amalgams as dental restoratives. On the other hand various intermetallics were successfully used as strengthening second phases in conventional alloys for structural applications. Thus it was clear that intermetallics are promising materials for applications as structural materials at high temperatures because of their high hardness and stability.

Intermetallic aluminides exhibit many interesting features that project them as the candidate material for high temperature structural applications [3]. They contain enough aluminium that forms a stable thin film of aluminium oxide in the oxidizing environment. They are characterised by low densities, relatively high melting points and good mechanical properties at elevated temperatures. (Table 3). However there are two limitations in using these alloys: lack of appreciable ductility at ambient temperature and lack of adequate creep resistance at high temperatures. Efforts are being made by the scientific community to find solution to the above said demerits of these materials.

The aluminides that have attracted attention as potential candidates for high temperature applications include titanium, nickel and iron aluminides. Continuous research is in progress to develop these materials by effecting modifications on the existing systems (either by alloying or by the modifications in the processing methodology) in order to optimise their properties. Limited work has been reported by the scientific community on the effect of rare earth metals in the electrochemical behaviour of iron aluminides. In the present thesis the, effect of Ce addition on the electrochemical behaviour of iron aluminides has been addressed.

Table 1 Some past and present applications of intermetallics [4]

2500 B C Britain)	Cementation	Cu ₃ As	Coating of bronze tools. (Egypt,
100 B C	Yellow brass	CuZn	Coins, ornamental parts (Rome)
0	High tin bronze	Cu ₃₁ Sn ₈	Mirror (China)
600	Amalgam	Ag ₂ Hg ₃ , Sn ₆ Hg	Dental restoratives (China)
1500	Amalgam	Cu ₄ Hg ₃	Dental restorative (Germany)
1505	Amalgam	Sn ₈ Hg	Mirror surface (Venice)
1540	Type metal	SbSn	Printing
1910	Acutal	(Cu,Mn) ₃ Al	Fruit knife (Germany)
1921	Permalloy	Ni ₃ Fe	High permeability magnetic alloy
1926	Permendur	FeCo(-2V)	Soft magnetic alloy
1931	Alnico	NiAl-Fe-Co	Permanent magnet material
1935	Sendust	Fe ₃ (Si,Al)	Magnetic head material
1938	Cu-Zn-Al & Cu-Al-Ni	CuZn-Al (Cu,Ni) ₃ Al	Shape memory alloys
1950	Pack aluminide	NiAl,CoAl	Surface Coating Materials
1956	Kanthal Super,	MoSi ₂	Electric heating elements
1961	A 15 compound	Nb ₃ Sn	Superconductors
1962	Nitinol	NiTi	Shape memory alloy
1967	Co-Sm magnets	Co ₅ Sm	Permanent magnets

Table 2 Potential applications of Iron aluminides [5, 6]

Application	Component System
Wrapping wire	Insulation wrapping for investment casting moulds.
Heating elements	Toaster, stoves, ovens,cigarette lighters and dryers
Regenerator disks	Automotive gas-turbine engines.
Hot-gas filters	Coal-gasification systems.
Tooling	Dies for superplastic forming of titanium based alloys
Automotive	Exhaust manifolds, and catalytic converters
Molten metals	Sensor sheathing material for molten Al, Zr and Cd

1.2 Iron aluminides

Iron aluminides have been of interest since 1930's when their excellent oxidation resistance was first noted [5,6]. These aluminides have exhibited attractive properties for application at elevated temperatures and severe environments over conventional structural materials like stainless steel and nickel based super alloys. Specific advantages of iron aluminides over stainless steel are, excellent sulphidation resistance, very good oxidation resistance, lower density ($5400 - 6700 \text{ Kg/m}^3$) which is 30% of that of the commercially available high temperature materials, good wear resistance, good cavitation erosion resistance, potentially lower cost and reduced consumption of strategic element such as chromium [7]. One of the key factors in increasing the maximum use temperature is the enhanced oxidation resistance. Iron aluminides are therefore considered as candidate materials to replace stainless steels in structural parts for many industrial applications (Table 2).

The major obstacle to their widespread use is their lack of ductility, susceptibility to brittle fracture at ambient temperatures and a rapid drop of strength and poor creep resistance at high temperatures. This poor ambient temperature ductility has been identified to be caused by an extrinsic effect, namely environmental embrittlement due to hydrogen [8]. Hydrogen is produced as a result of the reaction that happens between the fresh surfaces of iron aluminide with moisture and diffuses into the material to cause embrittlement, and therefore the poor room temperature ductility has been attributed to moisture induced embrittlement. Most of the methods proposed to tackle hydrogen embrittlement (HE) rely on restricting the entry of hydrogen into the lattice. This is achieved either by thermo mechanical treatments [9] or by surface modifications (directly by coatings [10] or indirectly by alloying with passivity inducing elements [11,12]. In addition, alloying could also be effective in enhancing other mechanical properties of these intermetallics. It has been proposed that alloying with passivity inducing elements in appropriate proportion (less than solubility limit) to iron aluminides would reduce the hydrogen liberation rates on the surface and passive layer would further hinder the diffusion of hydrogen into the intermetallic, thereby minimising hydrogen embrittlement. [11].

1.3 Carbon alloyed iron aluminides

Since carbon is known to embrittle iron aluminides and cause significant reduction in ductility, most of the earlier studies have been conducted on iron aluminide compositions with very low (0.01wt%) carbon contents. For the first time, Baligidad et al reported that addition of carbon in the range of 0.14 to 0.50 wt % significantly increases the room temperature strength of Fe-16 wt% (28 at%) Al alloys [13]. These alloys also exhibited some room temperature ductility probably due to the entrapment of hydrogen by Fe_3AlC particles, which were supposed to lower hydrogen diffusivity in these alloys and reduce the susceptibility to environmental embrittlement [13]. The increase in room temperature yield strength was attributed to the solid solution strengthening by the interstitial carbon, as well as precipitation hardening due to the presence of Fe_3AlC precipitates [14]. These carbon alloyed iron aluminides have been produced in Defence Metallurgical Research Laboratory, Hyderabad, by a combination of air induction melting and electroslag remelting (ESR). The melting practice has been described in detail in chapter 2

1.4 Objectives of the present study

The present study is specifically concerned with the evaluating and understanding of ambient temperature electrochemical behaviour of Ce containing carbon alloyed iron aluminide. An earlier study by Yangshan *et al* has reported that small additions of Ce to Fe_3Al based alloys results in enhancement of ductility and strength of iron aluminides at ambient temperature.. Moreover, they also observed improvements in tensile properties and creep resistance at high temperature of 600°C. Improvements were observed at the combined addition of Ce with molybdenum, zirconium and niobium. [15]. Addition of Ce in small amounts modifies surface passive layers and therefore is expected to affect the corrosion behaviour. Sriram [12] conducted a study on the same carbon-alloyed iron aluminides which were used in the present study, to understand the effect of Ce addition on the electrochemical behaviour of these carbon-alloyed iron aluminides. He conducted the potentiodynamic polarization and long term immersion testing of the carbon-alloyed

iron aluminides in 0.25mol/lit H_2SO_4 solution. Through, these studies it was observed that the corrosion rate of the Ce-alloyed iron aluminide was significantly lower than that of the non-Ce alloyed iron aluminides. The present study was, therefore motivated by the need to understand the electrochemical and corrosion behaviour of Ce containing intermetallics in relatively mild borate buffered solution as well as in an aggressively corrosive sulphuric acid environment, at ambient temperatures.

1.5 Plan of work

The following plan of work has been adopted for the thesis.

1. Selection of materials for study.
2. Electrochemical polarization behaviour of the samples in borate buffered solution.
3. Time dependent electrochemical impedance spectroscopy study of the samples in borate buffered solution of pH= 7.6 and in 0.25 mol/lit H_2SO_4 solution of pH= 0.74.
4. Cyclic voltammetry study of the samples in 0.25 mol/lit H_2SO_4 solution
5. Microstructural characterization of the samples after exposing the samples to 1mol/lit H_2SO_4 solution, by scanning electron microscopy.
6. Analysis of data.

LITERATURE REVIEW

The phase diagram and structure of iron aluminides would be briefly reviewed in the beginning of the chapter. The room temperature mechanical properties of iron aluminides would be addressed and the hydrogen embrittlement mechanism shall be highlighted. An overview of the effect of alloying elements on the mechanical properties and corrosion behaviour of the Fe_3Al based alloys, with a special focus on the effect of Ce as an alloying element in the carbon-alloyed iron aluminides has been provided. Finally, the chapter ends with a brief survey of room temperature aqueous corrosion behavior of iron aluminides.

2.1 Fe-Al phase diagram and crystal structure

2.1.1 Iron aluminides

Ordered iron aluminides exist in relatively narrow compositional ranges around simple stoichiometric ratios. The phase diagram of Fe-Al system is shown in Fig. 1. Iron aluminides based on Fe_3Al and FeAl can exist in two crystal allotropic modifications. These structures (DO_3 and B2) are both ordered BCC structures and these are presented in Fig 2. Fe_3Al can exist both in B2 and DO_3 ordered structure (depending upon the temperature) while FeAl can exist only in the B2 ordered form. The crystal structure of Fe_3AlC is perovskite and is shown in the Fig. 3. Table 3 presents some typical room temperature properties and critical ordering temperatures for different allotropic modifications of Fe_3Al [7]. The room temperature strength and room temperature ductility of iron aluminides are low.

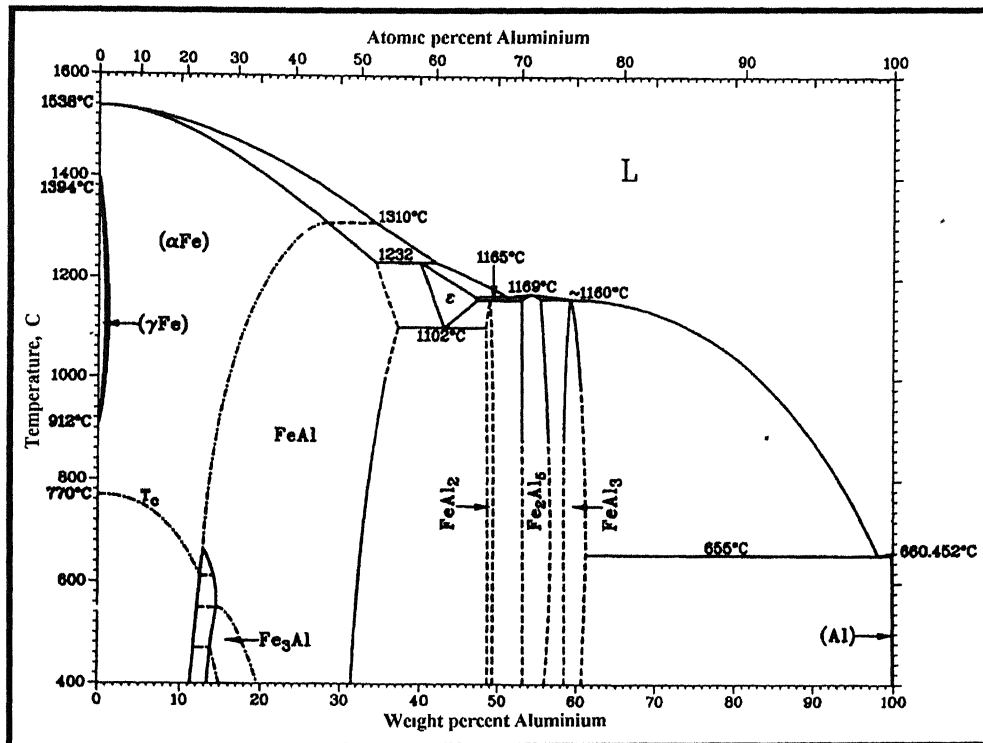


Fig. 1 The Fe-Al phase diagram.

Table 3 Typical room temperature properties of Iron aluminides [7].

Alloy	Crystal structure	Ordering temp °C	Melting point °C	Density (gm/cc)	Y.S. (Mpa)	Elongation (%)
Fe ₃ Al	DO ₃	540	1540	6.72	300	3.7
Fe ₃ Al	B2	760	1540	6.72	380	4.1
FeAl	B2	1250	1250	5.56	360	2.2

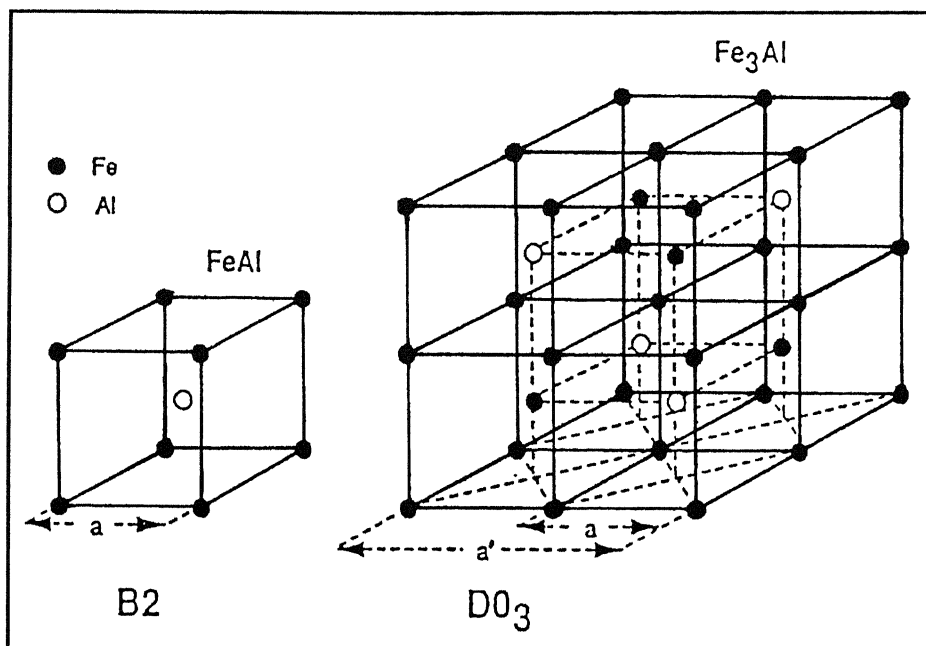


Fig. 2 The DO₃ and B2 ordered crystal structure of FeAl and Fe₃Al.

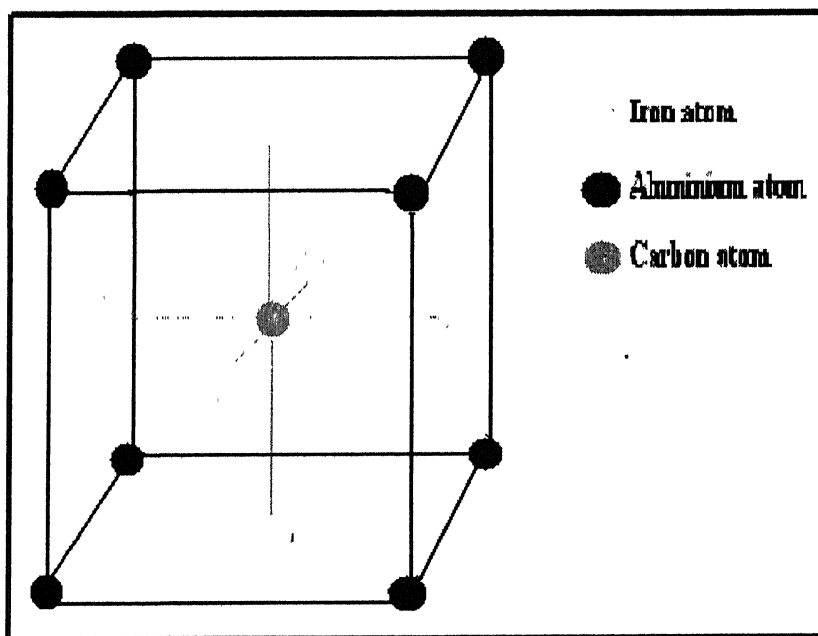


Fig. 3 The perovskite crystal structure of Fe₃AlC.

2.1.2 Phase equilibria in the Fe-Al-C system

The phase equilibria of Fe-Al-C system were determined from electron microprobe analysis (EPMA) of quenched samples. There are four phases of primary crystallization viz. κ , α , γ and graphite [3, 16]. The extent of the field of primary crystallization of κ shown is tentative in Fig. 4. Fig. 5 and 6 show the Fe-Al-C isotherms at 25°C and 1000 °C, respectively. Al increases the temperature of the graphitic eutectic reaction, as Al is a graphitic stabilizer [17]. At low carbon contents, the BCC (α) phase exists in the disordered state A2 as well as in the long range ordered states of type B2 and DO₃. At higher carbon contents, the FCC (γ) solid solution is stable and a ternary intermetallic phase, denoted by κ -phase, exists which is based on the perovskite structure [3,16,17].

The κ phase

κ phase can be considered as an ordered FCC arrangement of type L1₂, with carbon atom in the octahedral interstices rather than regarding it as carbide. A perfect atomic arrangement of this type would correspond to the formula Fe₃AlC.(refer to Fig 3) In fact, this particular stoichiometry has never been observed. Recently, the formula Fe_{4-y}Al_yC_x was suggested for the κ phase by Palm *et.al.*, where x may vary between 0.8 to 1.2 and y between 0.42 and 0.71 [16]. While, Baligidad *et.al* [18] suggested the formula of the carbide as Fe₃AlC_{0.5}. The phase diagram and, in particular, the existence domain of this phase are not well known. It is difficult to determine the exact composition of κ phase. The solubility of carbon in iron aluminide melts decreases with increasing temperature leading to the precipitation of primary graphite. At the ideal composition of the κ -phase Fe₃AlC, the precipitation of graphite starts already at 2150°C, while the κ -phase might form at 1400°C. Even by rapid quenching, it is not possible to avoid graphite precipitation. Therefore, single-phase material of the κ phase can not be obtained directly from the melt. The homogeneity range of κ phase is markedly shifted to higher carbon concentration with decreasing temperature. Upon quenching the alloy may thus hit and penetrate into two-phase field α + κ . Therefore, at compositions where single-

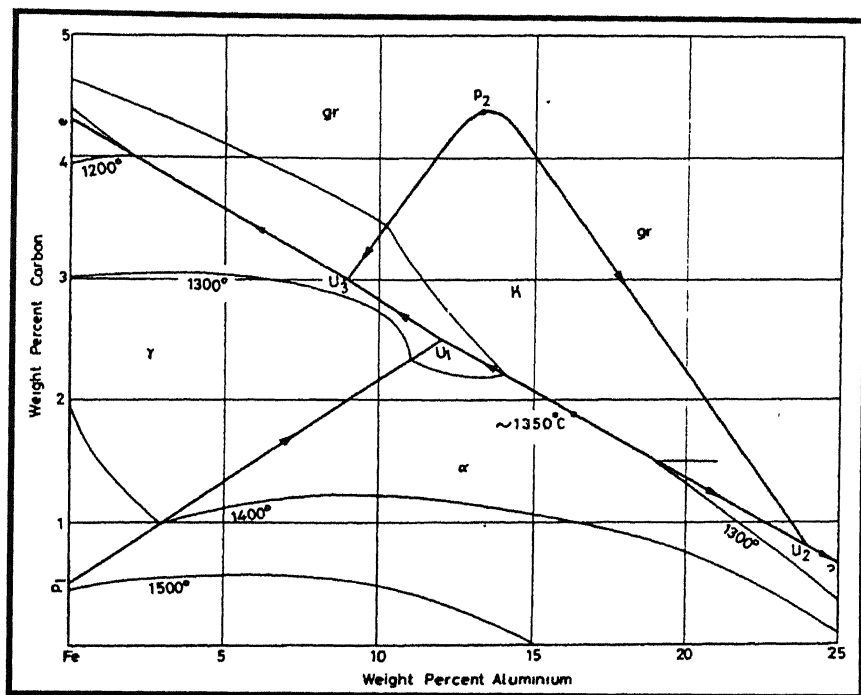


Fig. 4 Al-C-Fe liquidus in weight percent.

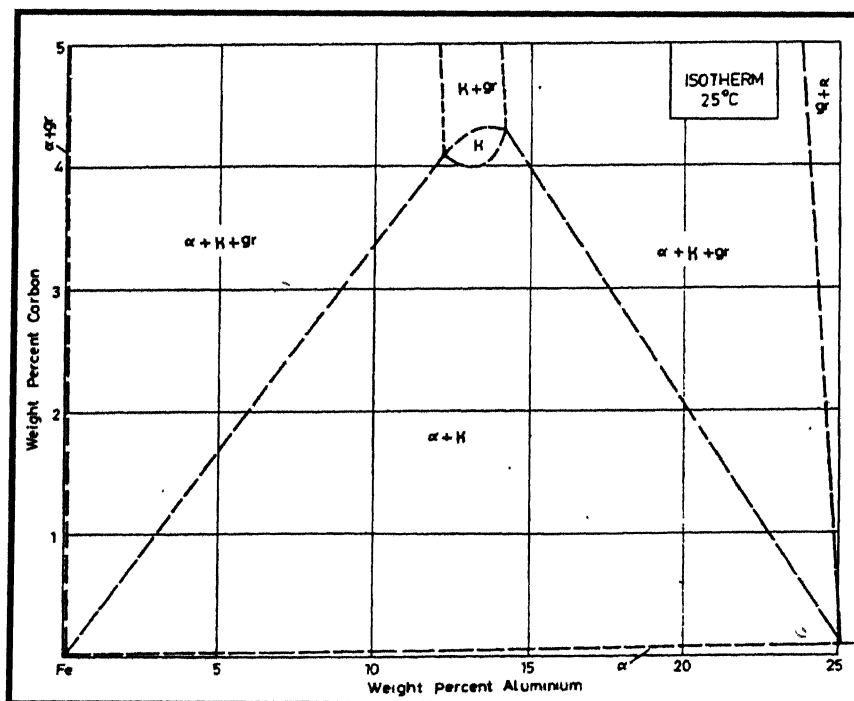


Fig. 5 Fe-Al-C isotherms at 25°C in weight percent.

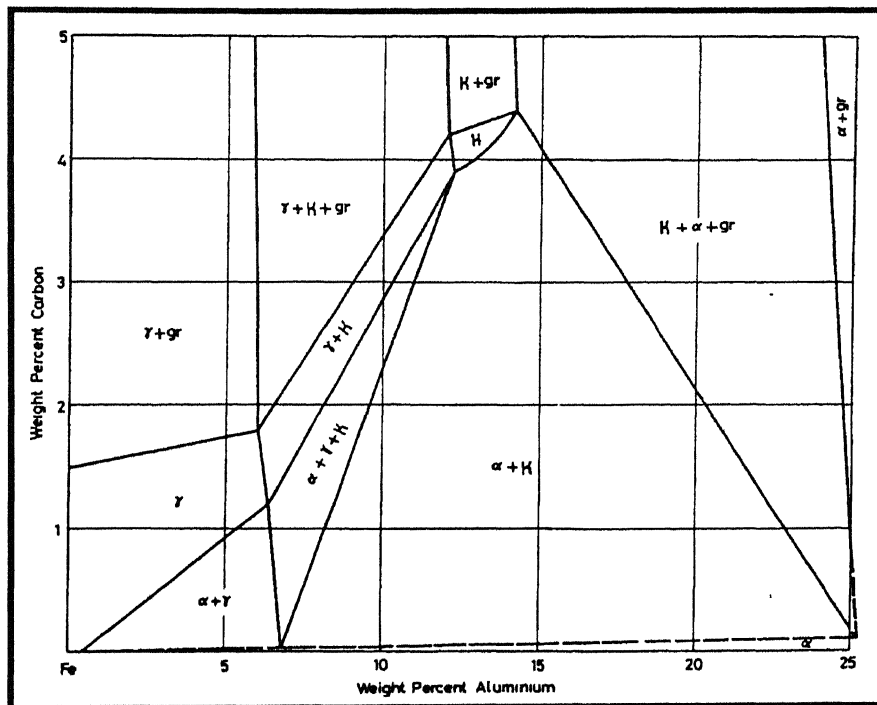


Fig. 6 Fe-Al-C isotherms at 1000°C in weight percent.

phase material of the κ phase would be expected, in fact three phases may be observed, the κ phase plus primary graphite and ferrite [16,17].

The α solid solution

There is a noticeable solubility for carbon in the BCC (α) solid solution of up to 1.5 at wt % carbon. With increasing Al content the transition temperature of A2/B2 transformation increases with respect to the carbon-free crystals from about 40°C at 25 at % Al, to up to 100°C at 35 at % Al. This means that by the introduction of carbon the ordered B2 structure is stabilized with respect to the disordered A2 structure. This has been suggested to be because the B2 structure offers favorable surroundings of six iron atoms for carbon [16,17].

The γ solid solution

The extension of the stability range of the γ phase varies considerably as a function of temperature. With increasing temperature, the aluminium content increases from 7.5 at % at 800°C to 24 at % at 1315°C while the solubility for carbon is about constant. During cooling to room temperature, the γ phase undergoes a martensitic transformation. The temperature for this transformation is yet to be determined. The hardness of the martensite is considerably higher than that of the κ -phase .

Little is known about the Al-C system. The solubility of C in both liquid and solid Al is very limited (0.32 wt.% at 1227°C, decreasing to 0.10 wt.% at 830°C and extrapolating to 0.07 wt.% at 660°C. The only known compound of the system is Al_4C_3 [17].

2.2 Passivity of B2 iron aluminides in sulphuric acid solution.

It has been reported in the literature that, in FeAl intermetallics containing 40 at% Al, the presence of Al is beneficial both in improving the ability to passivate iron in sulphuric acid and in increasing the stability of the passive film [19, 20]. It has been shown that the presence of Al causes a delay in the self-activation process in sulphuric acid [19] and results in an increased resistance to chloride breakdown.[20]. It is now well known that alloying elements have a dramatic influence on the passive properties of iron-based alloys. Film formers, such as Cr, Ti, Si, etc. are very effective for the development of passivating films forming passive films more stable than iron oxides

Aluminium has a beneficial effect in weakly acid, neutral and slight alkaline solutions in accordance with its amphoteric nature. Defrancq *et al* [21] in their studies on the corrosion properties of a cast iron with high Al-content (25 wt%) have noted the formation of a good protecting passive film on the electrode surface whose stability in sulphuric acid was better than that obtained on a cast iron containing 3% aluminium. Cho and coworkers [22] have found that Al can replace almost the 90% of the Cr in amorphous Fe-Cr-P-C alloys without causing any appreciable reduction in the corrosion resistance of the alloy.

Frangini *et al* [23] conducted a study to characterize the chemical composition of the passive film on $\beta 2$ FeAl intermetallic providing further insight into the role of aluminium in improving the passive properties of iron in a strong non-oxidizing acidic medium where a stable passivating. Al oxide is not expected. To achieve this, they conducted X-ray photo-electron spectroscopy (XPS) studies to get quantitative information about the composition and thickness of surface films formed in 1 N H₂SO₄. Their study has shown a clear improvement of the protective properties of the passive films formed on FeAl compared with iron. XPS analysis of the surface films showed that passivation of FeAl is accomplished by a strong enrichment of aluminium within the film. The structure of the passive film was considered to be bilayered with the outer part composed of precipitated mixed aluminium-iron oxy-hydroxide and the inner part composed mostly of an aluminium-rich oxide phase which is responsible for the onset of passivity (Fig. 7). The stabilizing effect of aluminium on the passive properties of iron

has been ascribed mainly to the formation of a passivating film whose characteristics are greatly modified by the presence of aluminium ions in the lattice. This is suggested to favour the development of a more amorphous film with enhanced protective characteristics, through improved structural flexibility of the metal-oxygen bond.

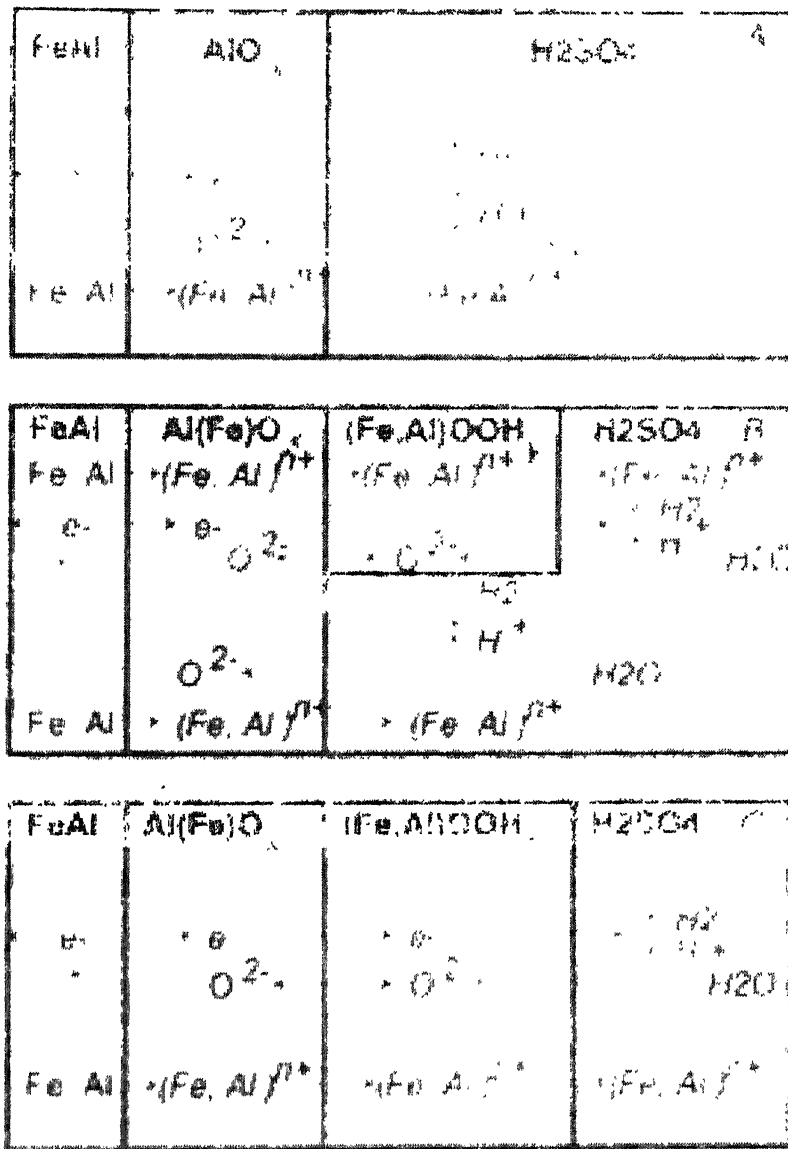


Fig. 7 Schematic picture of the passive film formation on FeAl alloy in sulphuric acid: (A) surface of active FeAl after cathodic treatment covered with an Al-rich oxide layer; (B) formation of an outermost precipitated mixed aluminium--iron oxy-hydroxide layer; (C) passive FeAl with a fully developed aluminium-iron oxy-hydroxide layer superposing the inner passive Al-rich oxide layer [23].

2.3 Effect of alloying elements

Alloying addition has been one of the schemes to improve the ductility of iron aluminides. Alloying control surface condition, reduction in hydrogen solubility and diffusion, refinement of grain structure, enhancement of grain boundary cohesion, grain shape and recrystallisation condition [7].

Several passivity inducing elements (Ti, Zr, V, Nb, Ta, Cr, Mo, W, Si, and Ni) have been alloyed to the base Fe_3Al intermetallic (to produce Fe_3Al -5M intermetallics) in order to test the ductility enhancement philosophy [24]. Ni could not be alloyed due to a violent reaction with the intermetallic on mixing, which is possibly due to the large exothermic heat of mixing between Ni and Al [25]. Electrochemical polarization studies of the alloyed intermetallics in acidic 0.05mol/l H_2SO_4 solution indicated that all the intermetallics except the V-alloyed one; induced passivity to the base iron aluminide, which exhibited active corrosion in this medium. Therefore, passivity enhancement by the addition of these elements has been verified. In view of the beneficial effect of the surface passive films in lowering the HE on iron aluminides [26], an alloy development philosophy was proposed wherein it was stated that elements that induce passivity in iron when added to Fe_3Al would inhibit hydrogen reduction and its entry by maintaining a passive layer [12, 27].

Among the metals alloyed with iron aluminide, the most effective alloying addition that results in ductility enhancements is Cr. Even Cr additions as low as 2% has been reported to be effective in providing ductilities [28]. The mechanism for the increase in ductility by Cr addition has been elucidated by the mixed potential theory by Balasubramaniam [12]. The potentiodynamic polarization curves of the base Fe_3Al and Cr-alloyed Fe_3Al have been theoretically deciphered and it was now clear that on alloying with Cr the mixed potential of the intermetallic is established in the passive region at a potential noble to the reversible hydrogen potential [29] suggesting that Cr induces passivity which results in reduction in the rate of hydrogen liberation rates on the surface of Cr alloyed iron aluminides. Moreover the passive layer would also hinder hydrogen entry into the lattice to cause embrittlement. This mechanism, hence, suggests that the entry of hydrogen into the lattice can be checked and HE minimized by alloying passivity inducing elements into iron aluminides. McKamey and Liu have earlier

suggested that the beneficial effect of Cr comes from surface oxide modification, rather than modification of bulk properties [9]. They suggested a change in oxide chemistry and properties or a change in kinetics of oxide formation, thereby reducing the water vapour reaction.

Lin *et al* have studied the effect of Ti addition to Fe₃Al on the mechanical behaviour of at high temperatures [31]. They have demonstrated superplastic behaviour in the Fe₃Al-2Ti alloy at high temperature. Interestingly, this alloy showed superplastic behaviour even at a grain size of 100 microns. This has been ascribed to the process of dynamic recovery and recrystallisation occurring in Fe₃Al-2Ti intermetallic at high temperature.

The base Fe₃Al [32] and the abovesaid alloyed intermetallics [24] were thermomechanically processed at 1000°C by multipass rolling after a homogenization treatment (in order to make the composition of the buttons uniform). It was observed that only the Fe₃Al, Fe₃Al-5Cr and Fe₃Al-Ti intermetallics could be rolled successfully to 80% deformation in multipasses at 1000°C. The Cr and Ti alloyed intermetallic cracked after 50% deformation and the Fe₃Al-5Nb intermetallic cracked after 40% deformation. The Fe₃Al-5Mo, Fe₃Al-5Si and Fe₃Al-5V could not be rolled as they cracked in the first rolling pass itself. Thermomechanical processing of the intermetallic is also an important aspect of alloy development as the material should be amenable to deformation processing from a commercial angle. Though the passivation inducing alloy additions induce passivity in the base intermetallic, the thermomechanical response of the intermetallics alloyed with Ta, Nb, Mo, Si and V was poor due to the formation of brittle phases. A detailed fractographic and microstructural study of other intermetallics revealed the precipitation of brittle phases on the alloying Ta, Mo, V, Nb and Si to Fe₃Al [33]. It is therefore important that the addition of passivity inducing elements should not lead to brittle intermetallic precipitation. If this aspect can be taken care of by various compositional and structural modifications, then higher room temperature ductilities can be achieved with minimum hydrogen embrittlement. Moreover these alloying elements would also provide additional solid solution strengthening to these intermetallics.

Zirconium, has been alloyed to Fe₃Al to strengthen grain boundaries and to prevent recrystallisation [30]. McKamey and Pierce have confirmed that, a partially

recrystallised microstructure reduces hydrogen embrittlement [30]. Therefore, zirconium additions can help in minimizing hydrogen embrittlement.

Boron addition (in ppm range) has been found to be very effective in increasing the grain boundary cohesiveness in ordered intermetallic alloys [34]. Boron has also been effective for Fe-Al class of aluminides. Boron segregates at grain boundaries and reduces intrinsic brittleness of B2 iron aluminides [35].

2.4 Effect of Cerium

Yangshan *et al* [15] have shown that Ce addition in a very small amount increases significantly the ductility of base Fe-28Al and Cr alloyed iron aluminides. They proposed that Ce additions accelerated the formation of aluminium and chromium oxides which passivated the specimen surface, thus preventing hydrogen from diffusing into the specimen. Their observation was that small amounts of Ce additions caused primarily ductile failure instead of brittle failure as in the case of iron aluminides without Ce addition. Addition of Ce also produced a fine grain structure after complete recrystallisation in contrast to the large grain size observed without Ce additions. Therefore, strength was not significantly reduced upon complete recrystallisation in the Ce-alloyed iron aluminides. They also observed precipitates rich in Fe, Al and Ce to form in the grain boundary regions of Ce-alloyed intermetallics. It is reasonable to assume that the Ce containing phases acts as irreversible traps for hydrogen and therefore lowers the amount of hydrogen present in the material, thereby, delaying embrittlement. Therefore, the presence of strong hydrogen trapping compounds, homogeneously distributed throughout the iron aluminide matrix, could also be beneficial in delaying embrittlement. Interestingly, the addition of Ce had also changed the composition of the surface passive film. The composition of the surface film was determined by XPS. With the addition of Ce, the surface layer contained a larger amount of Al_2O_3 and Cr_2O_3 and a lower amount of Fe_2O_3 than that of the Fe-28Al-2Cr alloy without Ce addition.

In view of this, studies were performed by Banerjee by addition of Mm (Indian mischmetal, a mixture of rare earth elements). Mm was added in small amounts to the Cr- and Ti alloyed iron aluminides [36, 37]. The Indian Mm added possessed had the

composition, in weight percent, 43Ce, 23La, 18Nd, 5Pr, 3Sm and 8Fe. The main aim of adding the Mm was to observe if enhanced room temperature ductilities would be obtained. However, the Mm added intermetallics were fairly brittle. Microstructural analysis indicated that several grain boundaries had cracked after the thermomechanical processing operation. The major elements that constituted Mm (namely Ce, La, and Nd) were enriched at the grain boundaries. In fact, La was analysed to be present only at grain boundaries. The poor ductilities obtained in the alloyed aluminides has been attributed to the presence of these elements (either in their elemental form or in the form of precipitates) along the grain boundaries which resulted in grain boundary weakening and to initiation of surface cracks during milling operation. Therefore, careful control of Mm (or Ce) addition may be required to render the iron aluminides ductile [35].

The improvement of oxidation behaviour of Fe₃Al based alloys with Ce addition at 1000°C was reported by Yu *et al.* [38]. They observed that the oxidation resistance of Fe₃Al based alloy was significantly improved by Ce addition at temperatures above 1000°C. Compared with Ce-free alloys, the oxidation rate of Ce-containing alloy was much lower and no cracks or signs of spallation existed on the surface of oxide scale. The oxide scales on the alloy with Ce addition were smooth and flat in the whole duration of 120 hour oxidation at 1200°C. Ce addition results in significant refinement of oxide grains and reduction of iron or chromium oxides in alumina scale, both of which are beneficial to the improvement of strength for an alumina scale, and prevent the crack formation on the scale. The fine grains and almost pure alumina will also improve the compactness and continuity of oxide scales for alloy containing Ce, thereby effectively hindering further reaction between substrate and air after forming a continuous scale in the initial stage, This resulted in significant decrease of the oxidation rate.[38]. The beneficial aspects of alloying Mm on the oxidation rate of iron aluminides has also been explored by Babu *et al* [39]. They observed that the addition of Ti and Mm changed the nature, colour and morphology of the scale leading to improved adherence.

Cerium may be added to steel to change the shape of the manganese sulphide inclusions form being needlelike or ribbonlike to being globular. Globular inclusions reduce the likelihood of cracking if the sheet is formed without restraining the edges [40]. In microalloyed HSLA steels, the changes in mechanical properties resulting from the use

of niobium and vanadium, together with controlled rolling, result in improved yield strength, weldability and toughness. The ferrite grain size is reduced, with an attendant increase in the yield strength. Because of this increase any reduction in toughness due to precipitation strengthening can easily be tolerated. The remaining properties are however, typical only of samples tested in the direction of rolling.

In the transverse direction, the toughness of the HSLA steels is reduced considerably and formability is inadequate because of the characteristic shape of nonmetallic inclusions (primarily sulphides) which during rolling become elongated in the rolling direction. The effect of elongated inclusions on the notch toughness is shown Fig. 8. For the data presented the impact energy for 100% shear fracture (upper shelf energy) exceeds 55 J in the longitudinal direction but is only 20 J in the transverse direction. For aluminum killed steels, the low shelf energy in the transverse section is caused primarily by elongated sulphide inclusions. Reduction in sulfur content to 0.010% is not sufficient to eliminate directionality. To prevent sulfides from becoming excessively elongated, it necessary to alter there composition. This can be done by adding elements such as cerium, lanthanum, and praseodymium which form sulfides with high melting points. Sulfides with high melting points are less plastic at hot rolling temperatures and cannot be deformed readily. As indicated in Fig. 9, rare earth metal additions can effectively enhance transverse toughness so that when cerium-sulphur ratio is between 1.5 and 2.0, the transverse upper shelf energy approaches that of the longitudinal direction [41].

2.5 Effect of carbon

Most of the reported literature is on iron aluminides containing very low (<0.01 wt %) carbon content, produced using very high purity raw material because carbon was believed to embrittle these alloys [7]. It was recently reported that addition of carbon to the Fe-16 wt % Al alloy results in improved strength, machinability, resistance to environmental embrittlement and creep resistance [42, 43]. Carbon additions of 0.03 wt % or more result in precipitation of $\text{Fe}_{4-y}\text{Al}_y\text{C}_x$ phase (where x may vary between

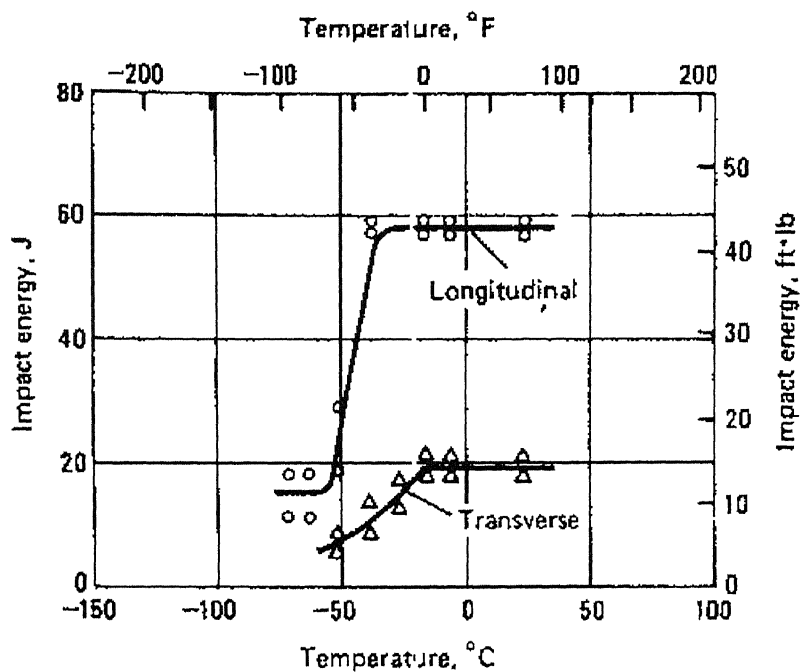


Fig. 8 Typical transition for HSLA steel without inclusion shape control [41].

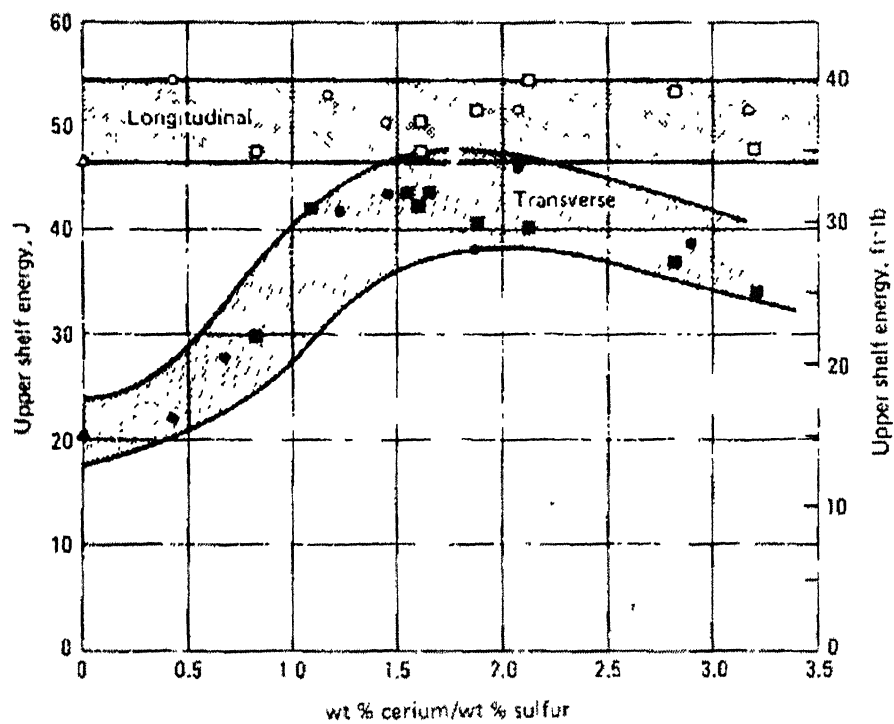


Fig. 9 Effect of cerium-sulphur ratio in the upper shelf impact energy for HSLA steel [41].

0.8 to 1.2 and y between 0.42 and 0.71 [16] in these alloys, which imparts significant dispersion strengthening and leads to improved creep resistance. Though $\text{Fe}_{4-y}\text{Al}_y\text{C}_x$ is a hard and brittle phase, its presence in the alloys matrix did not lead to reduction in ductility. This is because $\text{Fe}_{4-y}\text{Al}_y\text{C}_x$ precipitates were supposed to act as hydrogen traps, reducing the susceptibility of the alloy to hydrogen embrittlement [44]. This susceptibility to embrittlement in moist environments is a major cause for poor room temperature ductility and machinability. Addition of carbon has been reported for alloys with low (16 wt.%) Al-contents. In these alloys the addition of 1 wt % carbon was found to lead to the best combination of mechanical properties [45]. The addition of carbon (in the range of 0.5 to 1.1 wt %) to the Fe-Al alloy (the range of Al content is 16 to 20 wt %) also allowed the use of low cost processing techniques such as air induction melting (AIM) followed by electro slag remelting (ESR) [42, 44]. Cheap raw material such as steel scrap (which may contain significant amount of carbon) and commercial aluminium were used for melting of these alloys. The AIM and ESR ingots exhibited significant amount of precipitate $\text{Fe}_{4-y}\text{Al}_y\text{C}_x$ (where x may vary between 0.8 to 1.2 and y between 0.42 and 0.71 [16]). These precipitates form a continuous network resulting in a duplex $\text{Fe}_3\text{Al} - \text{Fe}_{4-y}\text{Al}_y\text{C}_x$ structure [42]. Tensile testing was carried out for Fe-8.5Al-C alloys (where the range of carbon varied from .04 to 1.1 wt %) by Baligidad *et al* [47]. According to them, the alloys showed cleavage mode fracture at room temperature. The fracture changed to mixed (cleavage + dimple) mode at 400°C and finally to dimple mode fracture at 600°C.

The reduced susceptibility to cracking of high carbon alloys was attributed [44, 45] to (i) likely decrease in hydrogen solubility with increasing carbon content of the alloy and (ii) hydrogen entrapment by the precipitates. The surface cracking has been attributed to hydrogen liberated by the reaction between aluminium in the alloy and water used as the coolant [44]. Addition of carbon leads to the formation of FeAlC phase, which may improve machinability by (i) reducing susceptibility to environmental embrittlement [44] and (ii) by allowing formation $\text{Fe}_{4-y}\text{Al}_y\text{C}_x$ of small even size chips during machining [45] in Fe-16Al (in wt %) alloys.

The addition of carbon resulted in a significant increase in yield strength [43]. This was attributed to the presence of a large volume fraction of hard. $\text{Fe}_{4-y}\text{Al}_y\text{C}_x$

precipitates and the formation of a $\text{Fe}_3\text{Al}-\text{Fe}_{4-y}\text{Al}_y\text{C}_x$ duplex structure. Similar results were obtained for Fe_3Al -based alloys with lower aluminium content [43]. The drop in strength observed above 600°C has also been reported for the low carbon alloys with similar Al contents [46]. The increase in ductility above 600°C may be related to the changes in failure mode from cleavage to the more ductile mixed mode failure and a likely change from DO_3 to B2 order in the material. Since the yield strength sharply fall for these intermetallics above 600°C irrespective of their carbon contents, it appears that the addition of carbon does not significantly affect the DO_3 to B2 structural transformation [42].

The addition of carbon to Fe-Al alloys resulted in significant strength improvements. At very low Al-contents (e.g. 8.5 wt % Al), the alloy was not susceptible to environmental embrittlement and the increase in strength is accompanied by a drop in ductility due to the presence of $\text{Fe}_{4-y}\text{Al}_y\text{C}_x$ precipitates. At higher Al contents (16-20 wt %), where the alloys are susceptible to environmental embrittlement, the benefits include improvement in machinability and strengthening without loss of ductility. However, the strength drops on increasing the Al-content from 16 to 20 wt %. Similar results have been reported for low carbon alloys where the loss in strength with increasing Al content has been attributed to weaker DO_3 order and increased dislocation mobility. On increasing the Al-content to still higher levels, the strength starts increasing after 23 to 24 wt % (38-40 at %) Al when the alloys have a B2 structure. However, any carbon added to alloys containing more than 22 wt % (36.5 at %) Al, is likely to precipitate out as graphite, which is a very soft phase. It is, therefore, unlikely that the addition of carbon to B2 Fe-Al alloys will lead to significant strengthening. Cast Fe-Al alloys with low carbon contents exhibit poor ductility (1-3%) and optimum ductility is obtained only after extensive thermomechanical processing. In contrast high carbon electro slag remelted (ESR) alloys exhibit good (4-5%) ductility even in the cast condition. It is also observed that further increase in carbon content from 0.14 to 0.5wt% does not improve the creep and stress rupture properties [22, 41].

The addition of Carbon enhanced corrosion which was attributed to the presence of cathodic carbides distributed in the matrix. A higher carbon content results in higher corrosion rate. These results are in conformity with the earlier studies [46, 43].

2.5.1 Earlier work on corrosion of carbon-alloyed iron aluminides.

The effect of Ce addition on the electrochemical addition on the electrochemical behaviour of the same carbon-alloyed iron aluminides was earlier studied by Sriram [48]. The potentiodynamic polarization behavior of alloys Fe-20.0Al-2.0C, Fe-18.5Al-3.6C and Fe-19.2Al-3.3C-0.07Ce alloy was studied in freely-aerated 0.25 mol/lit H_2SO_4 (pH of 0.74). Fig. 10 shows that potentiodynamic polarization curves for the carbon-alloyed iron aluminides and low carbon mild steel in 0.25 mol/lit H_2SO_4 , of pH= 0.74 solution and the passivation parameters obtained from these curves are tabulated in Table 4 [48]. From Fig. 10, it can be noted that all the alloys exhibited active-passive behaviour in the acidic solution. The passivation parameters were found to be generally comparable between the two alloys Fe-20.0Al-2.0C and Fe-18.5Al-3.6C. This was attributed to the similar carbon content and carbide distribution in these alloys. The lower carbon content alloy Fe-20.0Al-2.0C, exhibited a comparatively lower critical current density. The Ce-alloyed iron aluminide Fe-19.2Al-3.3C-0.07Ce exhibited a lower passive range when compared to the other carbon alloyed iron aluminides.

Sriram [48] also studied the corrosion kinetics by weight loss method. Corrosion rate as a function of time plotted for Fe-18.5Al-3.6C, Fe-20.0Al-2.0C and Fe-19.2Al-3.3C-0.07Ce in 0.25 mol/lit H_2SO_4 solution, for long term and short term immersion testing is shown in Fig. 11a and b. It was observed, that in the long term experiment of 85 hours, the rates of corrosion were high for the first 12 hours for Fe-18.5Al-3.6C and Fe-20.0Al-2.0C. Thereafter, the corrosion rate decreased and it was almost constant in the last few days of the experiment. In contrast, the Ce alloyed aluminide (Fe-19.2Al-3.3C-0.07Ce) exhibited a lower corrosion rate that was almost constant throughout the experiment period. In the short term experiment of 11 hours, the corrosion rates for the alloys Fe-18.5Al-3.6C and Fe-20.0Al-2.0C increased initially and after attaining a peak of about 2 hours decreased. The corrosion rate attained a steady state in an oscillatory mode. It was noticed that the addition of Ce resulted in a finer distribution of the carbides (i.e. smaller sizes) through the alteration of the microstructure. As the corrosion rate for Ce- alloyed material was lower, therefore it was proposed that the Ce addition

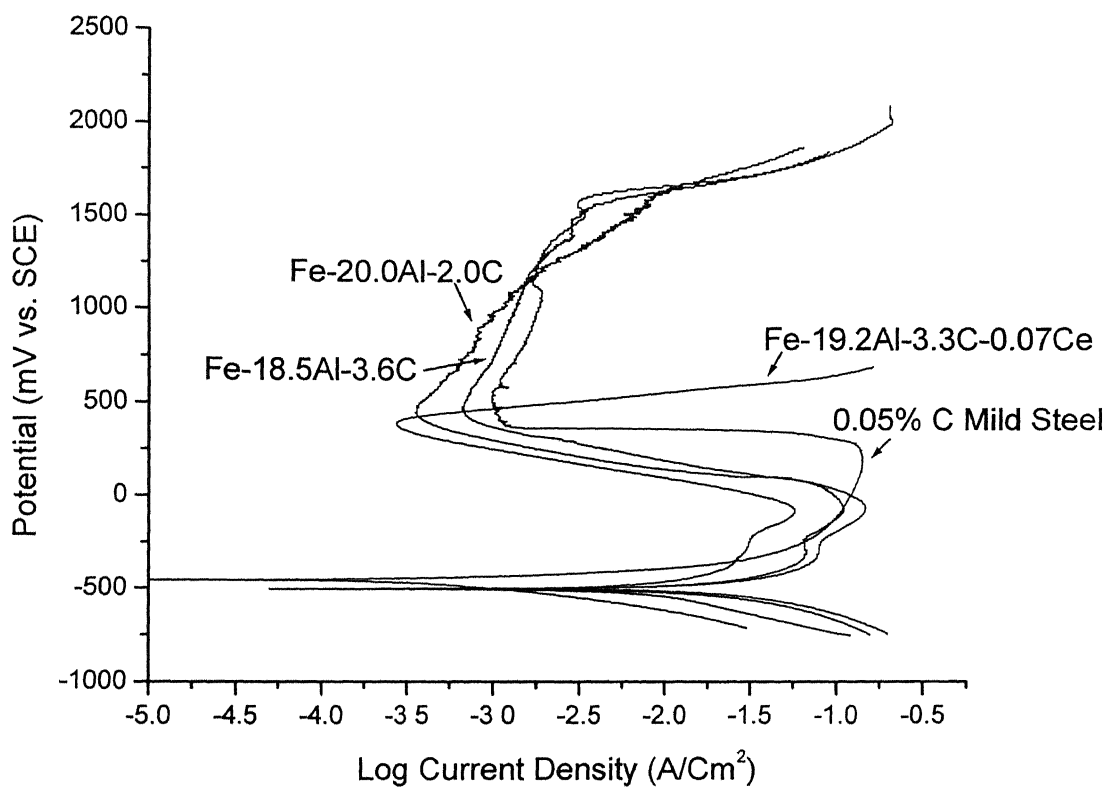
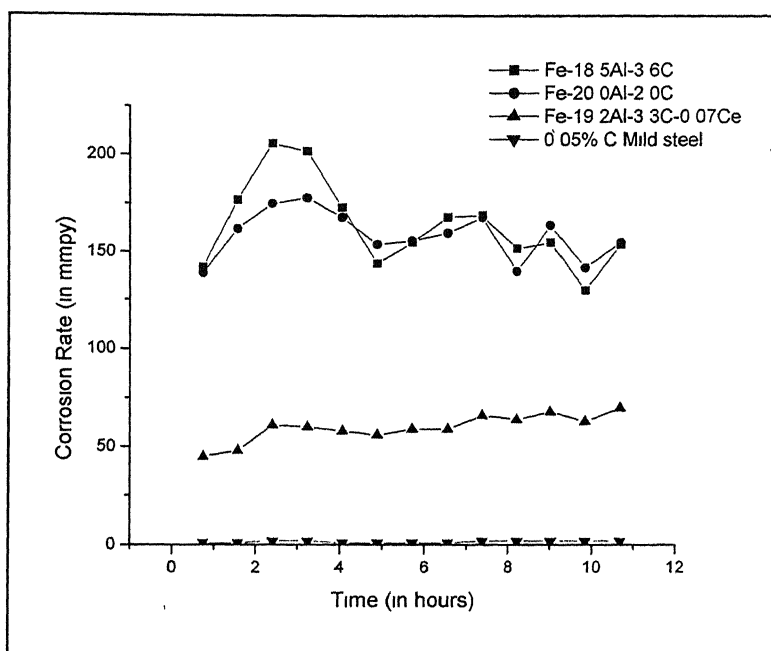


Fig. 10 Potentiodynamic polarization behaviour of Fe-20.0Al-2.0C, Fe-18.5Al-3.6C, Fe-19.2Al-3.3C-0.07Ce and mild steel in freely aerated 0.25 mol/lit H_2SO_4 using a scan rate of 1 mV/sec [48].

(a)



(b)

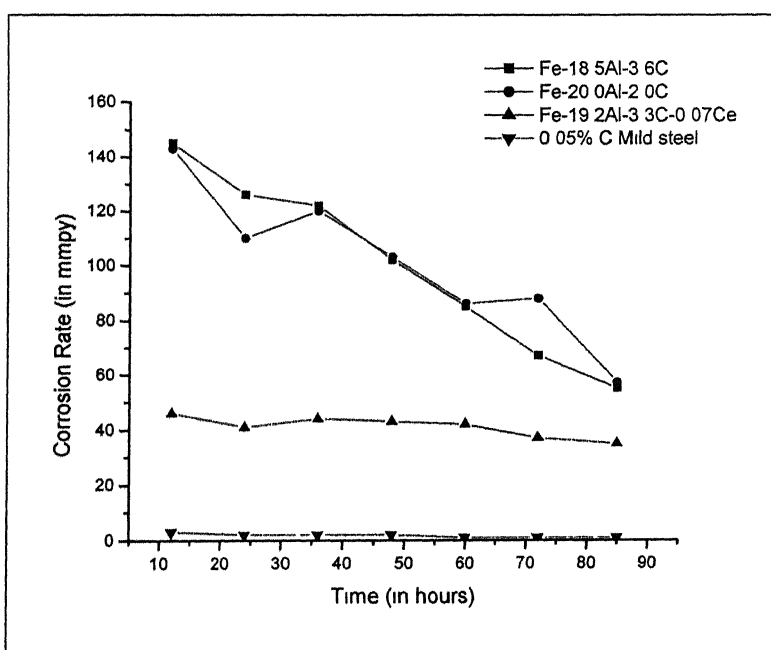


Fig. 11 Corrosion rate as a function of time for the carbon-alloyed iron aluminides and mild steel in freely aerated 0.25 mol/lit H_2SO_4 solution: (a) total duration of 11 hours (b) total duration of 85 hours [48].

modified the surface film. The effect of Ce on the corrosion of carbon alloyed intermetallics was summarised as follows: The initial fast rate of corrosion of matrix leads to Ce enrichment on the surface. Ce enrichment induces a more protective film formation on the surface. Therefore, the corrosion rate was lowered. The effect became more apparent with increasing immersion time.

Sen et. al. [45] studied the corrosion behaviour of two carbon-alloyed intermetallics of composition (in at %) Fe-28.1Al-2.1C and Fe-27.5Al-3.7C and compared with that of binary Fe-28Al intermetallic, using potentiodynamic polarization technique. Potentiodynamic polarization studies indicated that the intermetallics exhibited active-passive behaviour in an acidic solution (0.05 mol/l H_2SO_4) of pH = 1 (Fig. 12). [45]. In borate buffer solution (0.15 N boric acid + 0.15 N $\text{Na}_2\text{B}_4\text{O}_7 \cdot 10\text{H}_2\text{O}$) of pH = 8.4 both the intermetallics exhibited stable passivity in a (Fig. 13). The passivity parameters from these plots are tabulated in Table 5. The passive current densities (i_{pass}) for both the intermetallics were found to be lower in the buffer solution, when compared to those in the acidic solution. In the acidic solution, the critical current density for passivation (i_{crit}) was lower for Fe-28.1Al-2.1C when compared to Fe-27.5Al-3.7C. Moreover, the i_{crit} for the binary Fe-28Al was lower than those of both these intermetallics, thereby indicating that the i_{crit} increased with increasing carbon addition.

Corrosion rates were also obtained by immersion testing, wherein it was observed that both the intermetallics exhibited similar behaviour. The corrosion rate as a function of time is presented in Fig. 14 for both the intermetallics. It was observed that the corrosion rates increased in the initial stage and acquired a maximum, after which they decreased. In the final stages, the corrosion rate remained almost constant.

In order to gain further insights into the Microstructural aspects of the corroding surfaces, independent immersion experiments were conducted and the corroded surfaces were observed in a scanning electron microscope. SEM micrographs of the both the carbon-alloyed intermetallics used in there study are shown in Fig. 15. Both the carbon-alloyed intermetallics exhibited similar microstructural features—a uniform distribution of relatively large Fe_3AlC carbide precipitates. Scanning electron microscopy of the corroded surfaces indicated that the carbon-alloyed intermetallics were susceptible to

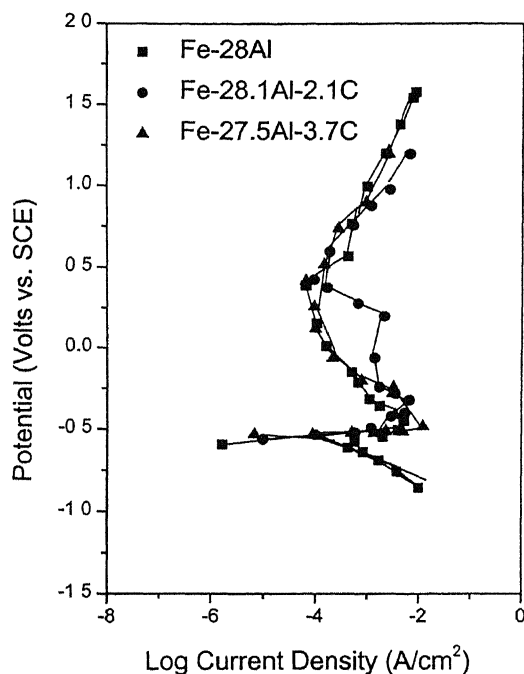


Fig. 12 Potentiodynamic polarization diagrams obtained in 0.05 mol/l H_2SO_4 solution of pH = 1, at a scan rate of 1 mV/s. The intermetallics exhibited active-passive behaviour [45].

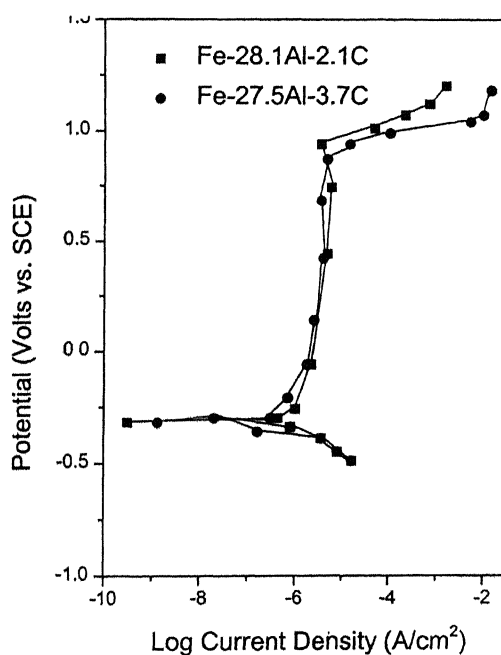


Fig. 13 Potentiodynamic polarization diagrams obtained in 0.15 N H_3BO_4 + 0.15N $Na_2B_4O_7 \cdot 10H_2O$ solution of pH = 8.44, at a scan rate of 1 mV/s. The intermetallics exhibited stable passive behaviour [45].

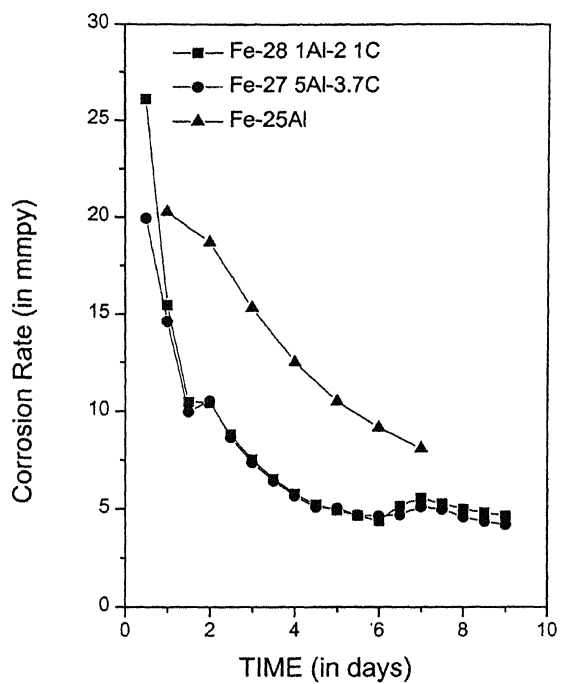


Fig. 14 Corrosion rate as a function of time for the intermetallics in 0.05 mol/l H_2SO_4 solution. Data were obtained after 24 h intervals. The data for Fe-28Al is from Babu *et al* (2000) [45].

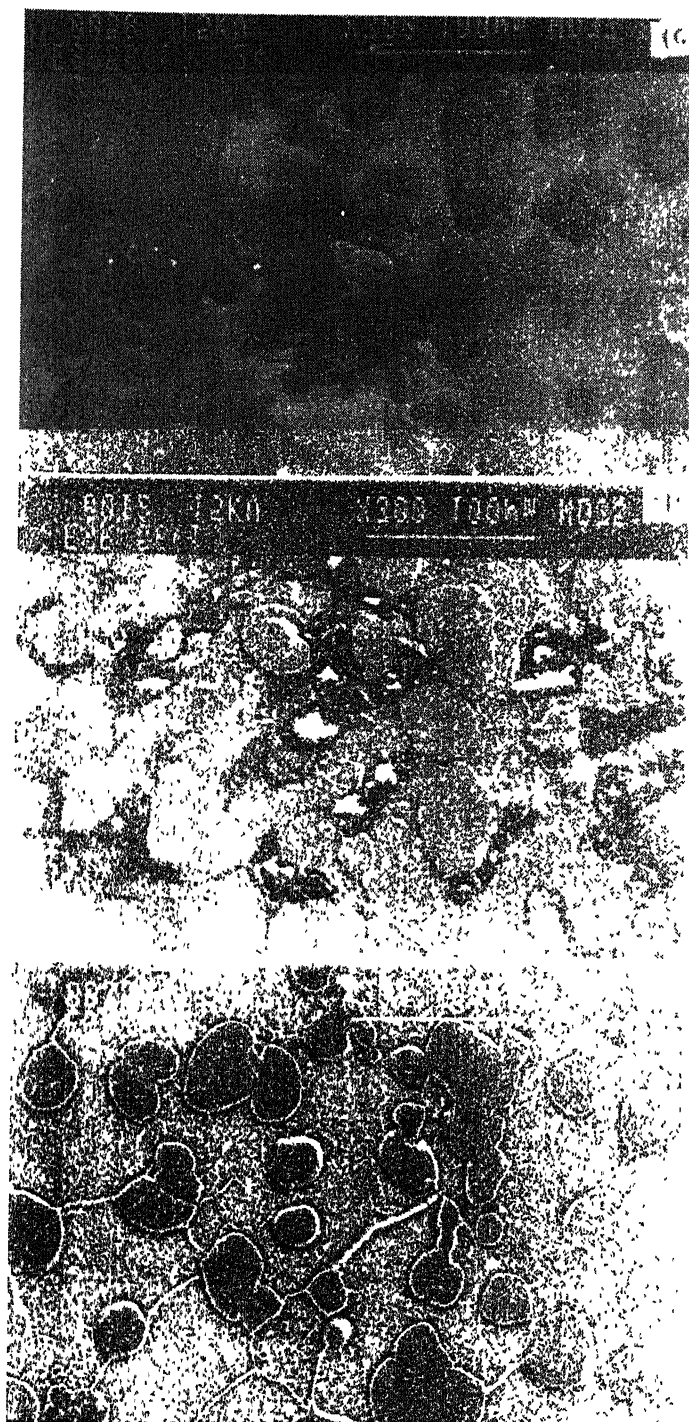


Fig. 15 SEM micrograph of Fe-28×1Al-2×1C: (a) basic microstructure, (b) after immersion for 2 h and (c) after immersion for 24 h in 0.05 mol/l H₂SO₄ solution [45].

galvanic corrosion due to the presence of the carbides in the intermetallic matrix. Baligdad et. al. [49] have reported that addition of carbon in the range of 0.14 to 0.50 wt% significantly increased the room temperature strength of Fe-16wt% (28 at%) Al alloys.

Table 4 Passivation parameters obtained from the potentiodynamic polarisation of the Fe-18.5Al-3.6C, Fe-20.0Al-2.0C and, Fe-19.2Al-3.3C-0.07Ce alloys in freely aerated 0.25 mol/lit H₂SO₄ solution [48].

Alloy	Plane	Composition	ZCP (mV vs. SCE)	Epp (mV vs. SCE)	Ecp (mV vs.SCE)	E _b (mV vs. SCE)	E _b Ecp (mV)	I _{crit} (mA / Cm ²)	i _{pass} (μA/cm ²)
ESR 74	RD	Fe-20.0Al-2.0C	-515	-45	418	1530	1112	105	350
ESR 127	RD	Fe-18.5Al-3.6C	-501	-65	432	1570	1138	149	670
ESR 137	RD	Fe-19.2Al-3.3C-0.07Ce	-511	-61	364	394	30	53	270
ESR 137	LT	Fe-19.2Al-3.3C-0.07Ce	-548	-85	419	526	107	66	170
ESR 137	ST	Fe-19.2Al-3.3C-0.07Ce	-524	-96	306	331	25	102	1620

Table 5 Parameters determined from the potentiodynamic polarization curves for the carbon-alloyed iron aluminides [45]

Sample	β_a (V/dec)	β_c (V/dec)	E_{corr} (V)	i_c (A/cm ²)	i_{corr} (A/cm ²)	F_{corr} (V)	i_{pass} (A/cm ²)	E_p (V)	Remarks
Fe-28.1Al-2.1C (pH = 8.4)	0.04	0.08	-0.304	2.00×10^{-7}	—	—	1.3×10^{-6}	0.933	Stable
Fe-28.1Al-2.1C (pH = 1.0)	0.20	0.26	-0.537	1.54×10^{-6}	6.69×10^{-6}	0.36	8.3×10^{-6}	0.369	passivity Active- passive
Fe-27.5Al-3.7C (pH = 8.4)	0.04	0.12	-0.279	3.14×10^{-7}	—	—	2.8×10^{-7}	0.885	Stable
Fe-27.5Al-3.7C (pH = 1.0)	0.24	0.27	-0.573	2.44×10^{-6}	9.86×10^{-6}	0.41	7.2×10^{-6}	0.408	passivity Active- passive

2.6 Electrochemical corrosion

Corrosion can be defined as the degradation of a metal by an electrochemical reaction with its environment [50]. All metals are found in their low energy state ores, in the form of their oxides, sulfides, carbonates or more complex compounds. Large amount of energy is required in order to extract a pure metal from its ore. This pure metal is a high-energy state of the metal and hence they tend to come back to the low energy state by recombining with the environment. This process is called corrosion. Fig. 16 shows the thermodynamic energy profile for metals and their compounds. The thermodynamic aspects of corrosion will be briefly discussed. All the interactions between elements and compounds are governed by the free energy changes (ΔG). Any reaction is said to be spontaneous when ΔG for the reaction is negative. At room temperature most of the chemical compounds of metals have lower free energy than the pure metals and hence most of the metals have an inherent tendency to corrode.

In all kinds of aqueous corrosion, there are two reactions occurring at the metal/liquid interface; an electron producing reaction (anodic or oxidation reaction) and an electron consuming reaction (cathodic or reduction reaction). The corrosion reaction for the creation of a wet electrochemical cell requires four basic requirements, the cathode on which the reduction reaction occurs, an anode on which oxidation occurs, an electrolyte to act as the conducting medium for ions and a electrical connection for electron to flow between the anode and cathode. The anodic reaction is invariably corrosion of the metal as shown in Eqn. 1. Several cathodic reactions can occur during corrosion [51]. The simplest of them is reduction of hydrogen ions as in Eqn.2. In the absence of any of these reactions water reduction will occur as in Eqn. 3. Another is reduction of an oxidized ion in solution (redox reaction) as in Eqn. 4. And yet another reaction is reduction of dissolved oxygen as in Equations 5 and 6.

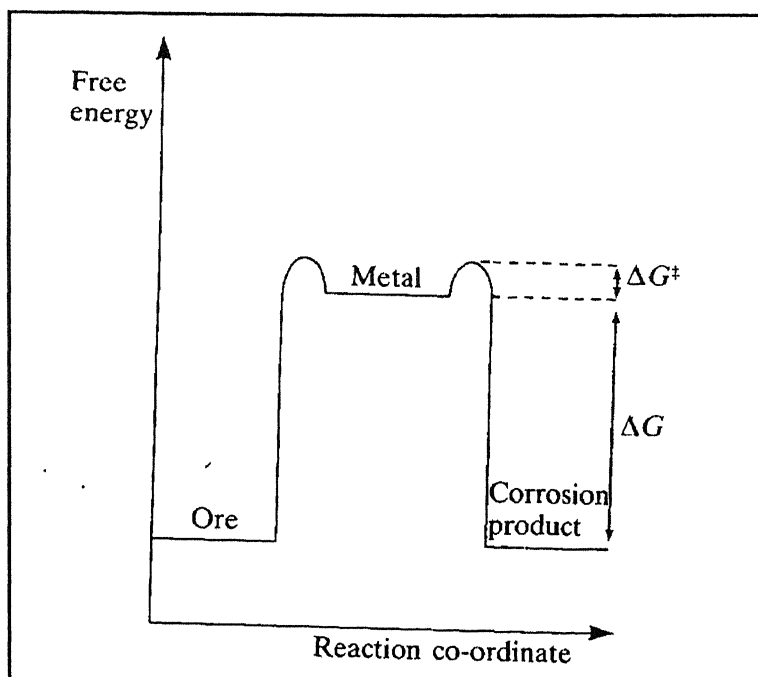


Fig. 16 Thermodynamic energy profile for metals and their compounds [50].

$M \Rightarrow M^{n+} + ne^{-}$	(Anodic Reaction)	Eqn. 1
$2H^{+} + 2e^{-} \Rightarrow H_2$	(Hydrogen Reduction Reaction) $pH \leq 7$	Eqn. 2
$2H_2O + 2e^{-} \Rightarrow H_2 + 2OH^{-}$	(Water Reduction Reaction) $pH > 7$	Eqn. 3
$Fe^{3+} + e^{-} \Rightarrow Fe^{2+}$	(Redox Reaction)	Eqn. 4
$O_2 + 4H^{+} + 4e^{-} \Rightarrow 2H_2O$	(Oxygen Reduction Reaction) $pH \leq 7$	Eqn. 5
$O_2 + 2H_2O + 4e^{-} \Rightarrow 4OH^{-}$	(Oxygen Reduction Reaction) $pH > 7$	Eqn. 6

A basic wet corrosion cell is shown in the Fig 17. The potential difference between the anode and the cathode could be measured by using a high impedance voltmeter in the circuit. This provides only the potential difference between the electrodes and in order to measure the absolute potential we need a third electrode. This third electrode is called as the standard electrode against which all the measurements can be made. Reference electrodes like standard hydrogen electrode (SHE), saturated calomel electrode (SCE), etc. are usually used as the standard electrodes. Table 6 lists some commonly used standard electrodes and their potentials.

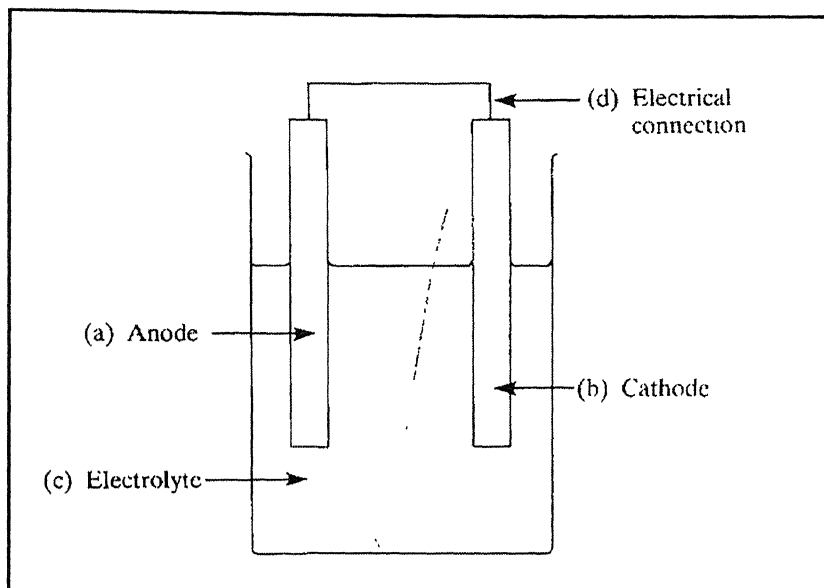


Fig. 17 Basic wet corrosion cell [52].

Table 6 Standard reference electrode potentials [52].

Electrode	Electrolyte	Potential (V)
Calomel (SCE)	Saturated KCl	+0.2420
Calomel (NCE)	1.0 M KCl	+0.2810
Calomel	0.1 M KCl	+0.3335
Silver/Silver Chloride (SSC)	1.0M KCl	+0.2224
SSC	Sea water	+0.25 (approx)
Copper/Copper sulfate (CSE)	Sea water	+0.30 (approx)
Zinc	Sea water	-0.79

2.7 Polarization

When a metal is not in equilibrium with the solution of ions, the electrode potential differs from the standard electrode potential by an amount known as the polarization [50]. It can also be said as over-potential or over-voltage. Polarization is a very important corrosion parameter as it is useful in calculating the rates of the corrosion process. The deviation of the equilibrium potential is a combination of an anodic polarization of metal and a cathodic polarization of the environment. If the electrons are made available the potentials at the surface becomes more negative, suggesting that excess electrons with their negative charges accumulate at the metal/solution interface waiting for the reaction. This negative potential charge is called as cathodic polarization. Similarly, if electrons are removed from the metal surface interface a positive potential change will occur called anodic polarization [51]. In an aqueous electrolyte solution, the surface will reach a steady potential, E_{corr} , which depends on the ability and rate at which electrons can be exchanged by the anodic and cathodic reactions. When the surface potential increases above the E_{corr} value, to a value E , then the anodic polarization is given by the difference between E and E_{corr} . At equilibrium, the forward anodic reaction, i_a is equal to the reverse cathodic reaction, i_c . Hence the rate of the reaction can be given by,

$$i_a = i_c = i_o = A_o \exp[-\Delta G/RT] \quad \text{Eqn. 7}$$

There are two methods available for measurement of corrosion rate using polarization methods, namely Tafel extrapolation and polarization resistance. The polarization methods to measure corrosion rates have their inherent advantages. The polarisation resistance R_p is derived from the slope of the linear polarisation curve and is used in calculating the corrosion rates of the alloys using equation

$$R_p = \beta_a \beta_c / 2.3 i_{\text{corr}} (\beta_a + \beta_c) \quad \text{Eqn 8}$$

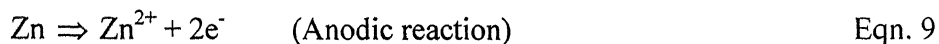
where β_a and β_c are the tafel constants and i_{corr} is the corrosion current density. The main advantage of these methods is that the time taken for conducting experiments is relatively short, whereas the conventional weight loss methods require several days. The polarization methods are highly sensitive, and accelerating factors such as elevated temperature, to increase rates, is generally not necessary. Moreover, these methods are

non-destructive and several repetition experiments can be carried out using the same sample.

The mixed potential theory forms a basic for explaining the polarization techniques. The mixed potential theory consists of two simple hypotheses:

1. Any electrochemical reaction can be divided into two or more partial oxidation and reduction reactions.
2. There cannot be net accumulation of electrical charge during an chemical reaction i.e., corrosion reaction the sum of the anodic oxidation currents should be equal to the sum of the cathodic reduction currents. In other words the total rate of oxidation should be equal to total rate of reduction [52].

Consider the reactions for zinc getting corroded in an acid solution. Then the anodic and cathodic reactions are given by,



These reactions are called as the half-cell reactions and the potential corresponding to them are called cell potential. The potentials cannot coexist separately on an electrically conducting surface. The potentials will polarize to an intermediate value called as the corrosion potential or mixed potential (E_{corr}). When there is no external current flowing into the system, then the equilibrium potential attained is called free corrosion potential (E_{corr}).

As the reactions polarize on the same surface the change in potentials is given by,

$$\eta_a = \beta_a \log (i_a/i_o) \quad \text{Eqn. 11}$$

$$\eta_c = \beta_c \log (i_c/i_o) \quad \text{Eqn. 12}$$

where η_a and η_c are anodic and cathodic polarization, β_a and β_c are the Tafel constants, i_a and i_c are the anodic and cathodic currents respectively. At E_{corr} , the rates of anodic and cathodic reactions are equal and are equal to the current density, i_{corr} . The half-cell reactions for dissolution of Zn in acid are shown in the Fig. 18. This figure is called as Evans diagram or polarization diagram and represents the corrosion of an active material.

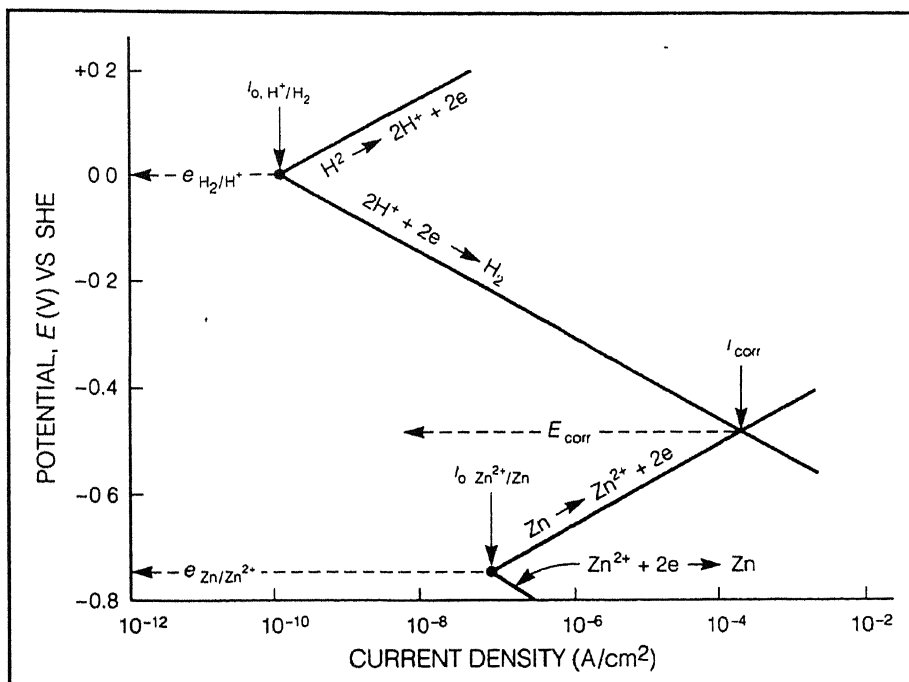


Fig. 18 Evans diagram for an active metal (Zn) [52].

The various polarization techniques that are commonly used are linear polarization, Tafel extrapolation, potentiodynamic polarization and cyclic polarization. These polarization techniques are summarized in the Figure 19.

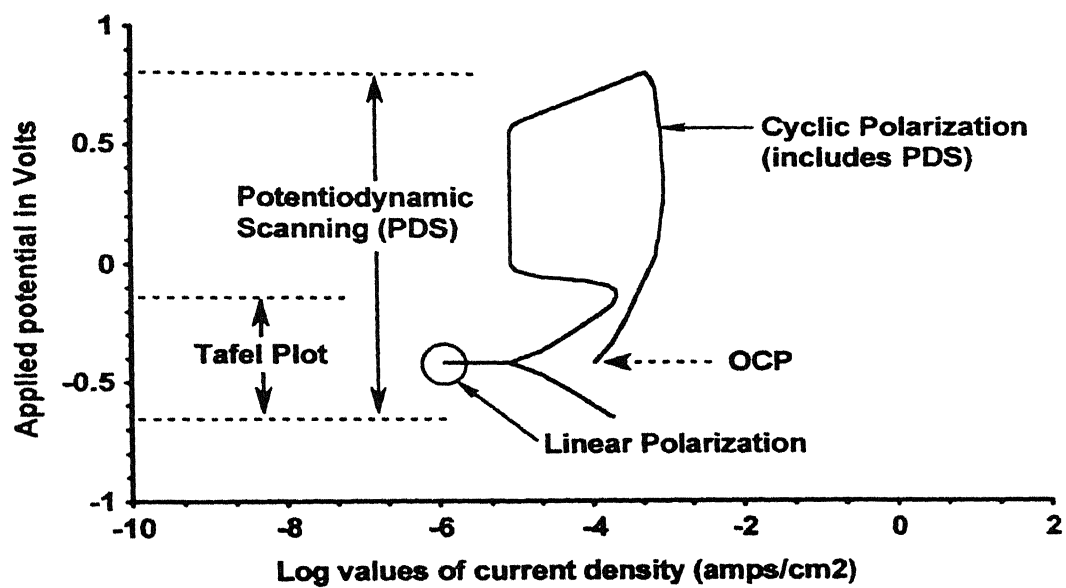


Fig. 19 Various types of polarization methods [51].

2.7.1 Potentiodynamic Polarization

The potentiodynamic polarization is carried out in a wider range of potential spectrum and gives much more details about the samples response to the environment. The potentiodynamic polarization provides data about the metal behavior i.e., whether the metal is active or passive or active passive in the given environment. The plot elucidates the properties of the passive film and the effect of inhibitors on the corrosion behavior of the metal. Depending upon the nature of potentiodynamic polarization curve, alloys can be divided into active alloys and active-passive alloys. For an active metal the corrosion rate increases linearly with increase in the anodic polarization potential. This is due to the non-protective oxide layer, which forms on the metal surface. For an active passive metal the corrosion rate increases with polarization potential up to a critical current density, (i_{crit}) after which it falls down rapidly due to the formation of a protective passive film.

Fig. 20 shows a typical potentiostatic/dynamic anodic polarization curve of a metal exhibiting passivity. The important points in this curve are described below.

- A- Corresponds to the equilibrium potential of the metal under a given environment condition.
- AB- Anodic polarization behavior of a normal corroding metal.
- B- Corresponds to equilibrium potential for initiation of passive growth E_{ip} .
- C- At potential of primary passivation E_{pp} acceleration of metal dissolution occurs. At potential E_{pp} , the rate of protective film growth already exceeds the rate of its chemical dissolution and the process of protective film formation begins.
- D- At potential E_{cp} where formation of continuous protective film is completed and complete passivation is obtained.
- DE- Metal dissolution occurs at a constant rate through the passivating oxide film.
- E End of passivity range.

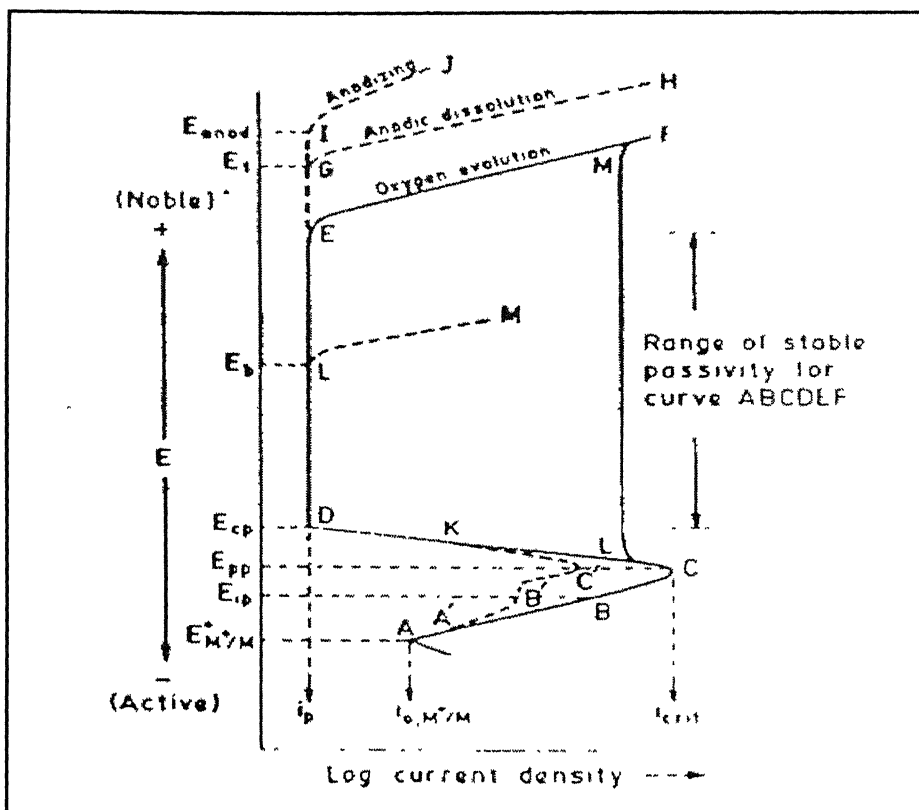


Fig. 20 Anodic polarization curve for metal exhibiting passivity.

The anodic region in the Figure 20 can be subdivided into three main regions namely, the active region, the passive region and the trans-passive region. The active region and the cathodic curve can be extrapolated to extract the values of E_{corr} and i_{corr} . The active region ends at the primary passivation potential (E_{pp}) at which the passive film becomes stable and the corrosion rate falls rapidly. The current corresponding to this value is called as critical current density (i_{crit}). As the potential is increased beyond this value, the current density decreases until it reaches a steady current called as the passive current density (i_{pass}). The range over which the steady current is maintained is known as the passive range and it relates to the stability of the passive film. As the potential is increased further the passive layer breaks down and the anodic rate increases in the transpassive region. This breakdown in passivity can be attributed to the oxygen evolution or due to localized mechanisms such as pitting. In certain kind of alloys like stainless steel, there will be an additional region showing secondary passivity. This results due to the formation of some secondary oxide layer, which ultimately breaks leading to increase in the corrosion rate. The potential at which the passive film breaks is known as pitting potential (E_{pitt}) and the potential at which the surface oxide film is destabilised is often called the breakdown potential (E_b).

2.7.2 Criterion for selection of active passive metals

Potentiostatic/potentiodynamic anodic polarization is widely used method to compare the corrosion resistance of different metals and alloys in a specific environment [51]. A schematic representation of various comparing parameters is given in Fig. 21 and a schematic comparison of the hypothetical alloys is given in Fig. 22. For reducing conditions, as in number 1, either the non-passivating alloy A or the partially passivating alloy B is superior to the other two because A and B have lower corrosion rates (or current densities, $i_{\text{corr, 1A}}$ and $i_{\text{corr, 1B}}$) in the active condition without oxidizers. The alloying elements, for example chromium, needed to produce strong passivity passivity make C and D far more expensive and thus unjustified for service in condition 1.

For moderately oxidizing conditions, number 2, the recommended alloy would be C because the reduction curve exceeds the critical current density for passivation and it is

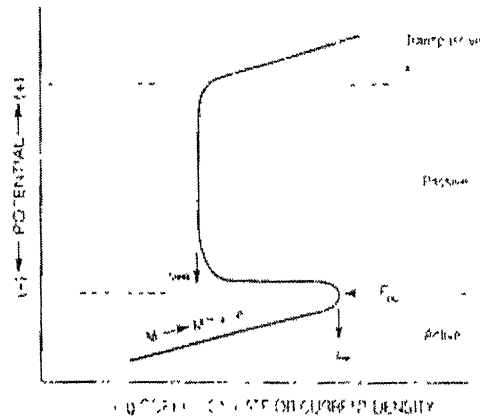


Fig. 21 Schematic curve showing active passive polarisation behaviour [51].

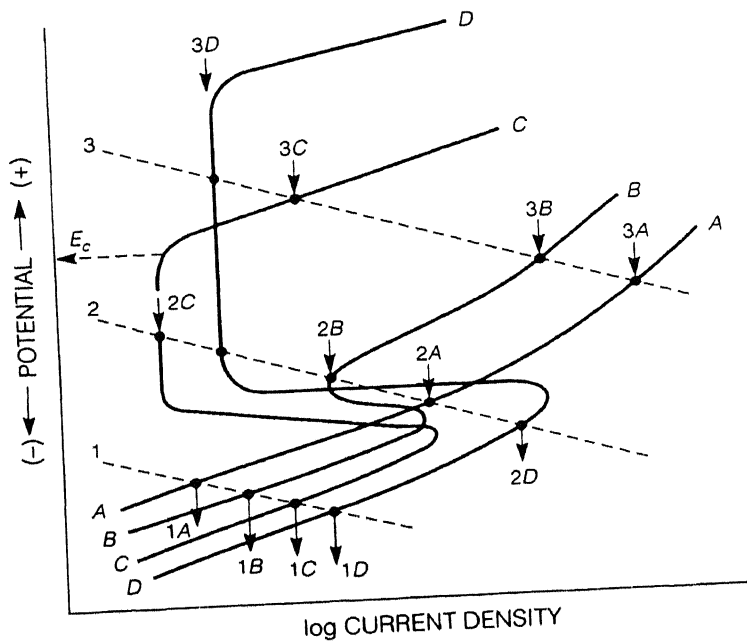


Fig. 22 Schematic anodic polarization curves for hypothetical alloy A,B,C and D in 1) reducing 2) moderately oxidizing 3) highly oxidizing environments [51].

the only alloy in the stable passive condition. Although the reduction curve also exceeds the critical passivation current density for alloy B, the passivation current at 2B is not enough and the passive region is not broad enough to ensure good resistance in the passive state. Alloy D is in a state of borderline passivity with both active, 2D, and passive state possible. The active state is generally chosen as the most likely in cases of borderline passivity. The corrosion rate of the non-passive alloy, A, is predictably high at 2A in oxidizing conditions of any degree.

The recommended alloy in highly oxidizing condition (number 3) is D, since now the reduction curve exceeds the critical current density for passivation, and the corrosion rate is low at 3D. passivity breaks down for alloy C at E_C , and corrosion rate is increased at 3C, which is above the passive current density at 2C. alloys A and B are not resistance to highly oxidizing conditions.

The breakdown of the alloy C, at E_C , may occur due to initiation of localized corrosion in pits or crevices. With no breakdown either of the alloys C or D may be chosen because corrosion rates 2C and 3D in the passive state are both very low.

It can therefore be predicted about the choice of the alloy according to the parameters derived from potentiostatic anodic polarization.

1. i_{corr} should be as low as possible.
2. I_{crit} should be as low as possible.
3. E_{cp} should be as low as possible.
4. E_{pp} should be as low as possible.
5. E_{pit} should be as high as possible.
6. Range of passivity should be as high as possible.

2.8 Electrochemical Impedance Spectroscopy

2.8.1 Introduction

Electrochemical systems can be studied with the methods based on impedance measurements. These methods involve the application of a small voltage perturbation, whereas in the methods based on linear sweep or potential step the system is perturbed far from equilibrium. EIS voltages cycle from peak anodic to cathodic magnitudes (and vice versa) using a spectrum of alternating current (AC) voltage frequencies, instead of a range of single magnitude and polarity direct current (DC) voltages. Resistance and capacitance values are obtained from each frequency, and these quantities can provide information on corrosion behavior and rates, diffusion and coating properties. The passive films formed and the electrical double layer is supposed to offer resistance and capacitance to the circuit, whose values are determined from the EIS data. The comparison of these values for similar systems gives us some idea about the systems [53, 109]. The corrosion rate of a metal in an electrolyte can be determined by AC techniques. These techniques are more or less explicitly based on the hypothesis that the impedance of the metal-electrolyte interface is equivalent to the polarization resistance, R_p , i.e. the slope of the steady-state current potential curve ($R_p = dV/di$) $E = E_{\text{corr}}$. R_p is inversely proportional to corrosion current density, i_{corr} , i.e. the current density which is proportional to the corrosion rate. For determination of R_p , a sinusoidal current or potential perturbation of very small amplitude (to ensure that the measurement is performed in the linear region of the system) is applied as a function of frequency.

2.8.2 AC Circuit Theory and Representation of Complex Impedance Values

Like resistance, impedance is a measure of the ability of a circuit to resist the flow of electrical current. Electrochemical impedance is usually measured by applying an AC potential to an electrochemical cell and measuring the current through the cell. The response to a sinusoidal potential excitation potential is an AC current signal, containing

the excitation frequency and its harmonics. Electrochemical impedance is normally measured using a small excitation signal [57]. This is done so that the cell's response is pseudo-linear. In a linear (or pseudo-linear) system, the current response to a sinusoidal potential is a sinusoid at the same frequency but shifted in phase (see Fig. 23). The excitation signal, expressed as a function of time, has the form:

$$E(t) = E_0 \cos(\omega t) \quad \text{Eqn. 13}$$

$E(t)$ is the potential at time t , E_0 is the amplitude of the signal, and ω is the radial frequency [54]. The relationship between radial frequency ω (expressed in radians/second) and frequency f (expressed in hertz) is:

$$\omega = 2 \pi f \quad \text{Eqn. 14}$$

In a linear system, the response signal, I_t , is shifted in phase and has a different amplitude, I_0 :

$$I(t) = I_0 \cos(\omega t - \phi) \quad \text{Eqn. 15}$$

An expression analogous to Ohm's Law allows us to calculate the impedance of the system as:

$$Z = \frac{E(t)}{I(t)} = \frac{E_0 \cos(\omega t)}{I_0 \cos(\omega t - \phi)} = Z_0 \frac{\cos(\omega t)}{\cos(\omega t - \phi)} \quad \text{Eqn. 16}$$

The impedance is therefore expressed in terms of a magnitude, Z_0 , and a phase shift, ϕ .

2.8.3 Data Presentation

The expression for impedance (Z) is composed of a real and an imaginary part. If the real part is plotted on the Y-axis and the imaginary part on the X-axis of a chart, we get a "Nyquist plot" (see Fig. 24). It can be noted, that in this plot the y-axis is negative and that each point on the Nyquist plot is the impedance at one frequency. Fig. 24 is annotated to show that low frequency data are on the right side of the plot and higher frequencies are on the left [55]. This is true for EIS data where impedance usually falls as frequency rises (this is not true of all circuits). On the Nyquist plot, the impedance can be

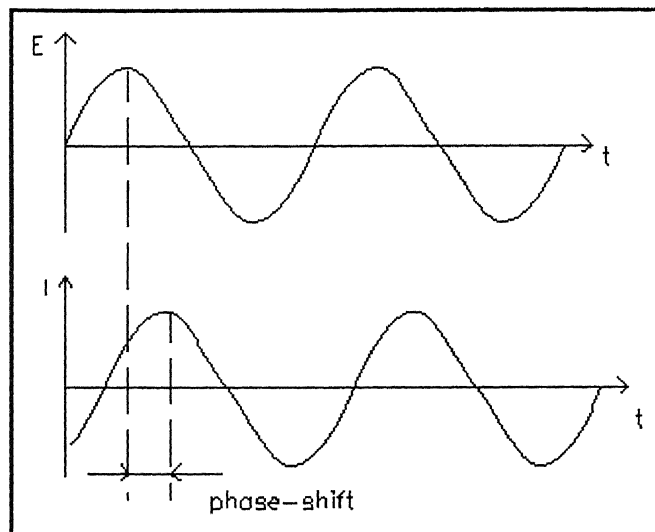


Fig. 23 Sinusoidal Current Response in a Linear System.

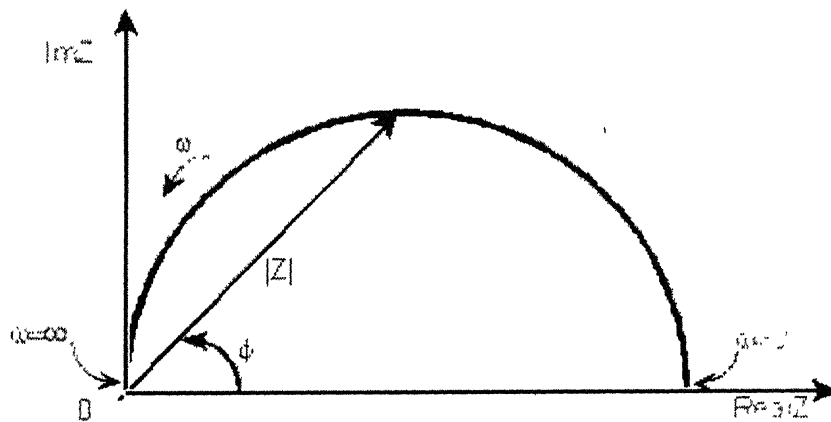


Fig. 24 Nyquist Plot with Impedance Vector.

represented as a vector of length $|Z|$. The angle between this vector and the x-axis is phase shift. However, Nyquist plots have one major shortcoming. It does not give the information about the frequency at which a data point is obtained. The Nyquist plot in Fig. 24, results from the electrical circuit of Fig. 25. The semicircle is characteristic of a single "time constant". Electrochemical Impedance plots often contain several time constants. Often only a portion of one or more of their semicircles is seen. Another popular presentation method is the Bode plot (Fig. 26). The X-axis of a Bode magnitude plot contains log values of frequencies (base 10) and the Y-axis contains log values of the total impedance for each frequency. Locations for R_1 , R_2 and capacitance reactance are also noted on the magnitude plot. Plot slope is zero when polarization is through resistances, and slope is less than zero when capacitive reactance becomes part of the circuit response to a polarization. Slope magnitude is determined by the ratio of R_2 to R_1 , and approaches -1 as the ratio increases. Bode phase plot contains log of frequency on the X-axis and the absolute value of the impedance ($|Z| = Z_0$) on the Y-axis [55, 56].

2.8.4 Physical Electrochemistry and Equivalent Circuit Elements

Electrolyte Resistance

Solution resistance is often a significant factor in the impedance of an electrochemical cell. A modern 3 electrode potentiostat compensates for the solution resistance between the counter and reference electrodes. However, any solution resistance between the reference electrode and the working electrode must be considered when the cell is modelled. The resistance of an ionic solution depends on the ionic concentration, type of ions, temperature and the geometry of the area in which current is carried. In a bounded area with area A and length l carrying a uniform current the resistance is defined as:

$$R = \rho \frac{l}{A}$$

प्रमुखतम कापीकरण केन्द्र गुप्तका
भारतीय प्रौद्योगिकी सं.
वाराणसी 221 005

Eqn. 17

where, ρ is the solution resistivity [58]. The conductivity of the solution (k) is more commonly used in solution resistance calculations. Its relationship with solution resistance is:

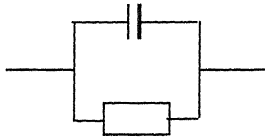


Fig. 25 Simple Equivalent Circuit with One Time Constant.

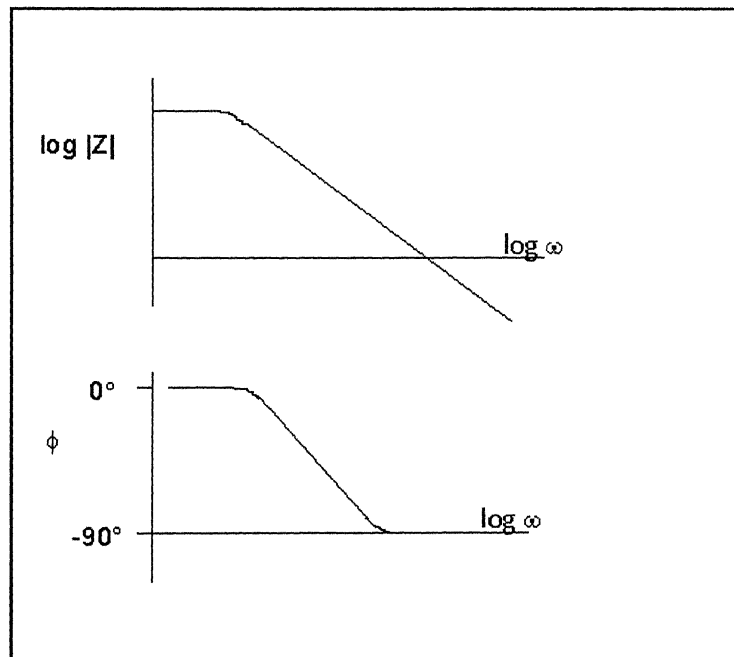


Fig. 26 Bode plot with one time constant.

$$R = \frac{1}{\kappa} \frac{l}{A} \Rightarrow \kappa = \frac{l}{RA} \quad \text{Eqn. 18}$$

Unfortunately, most electrochemical cells do not have uniform current distribution through a definite electrolyte area. The major problem in calculating solution resistance therefore concerns determination of the current flow path and the geometry of the electrolyte that carries the current fortunately; solution resistance is not usually calculated from ionic conductance [58]. Instead, it is found when you fit a model is fit to experimental EIS data.

Double Layer Capacitance

An electrical double layer exists at the interface between an electrode and its surrounding electrolyte. This double layer is formed as ions from the solution "stick on" the electrode surface. Charges in the electrode are separated from the charges of these ions. The separation is very small, on the order of angstroms [59]. Charges separated by an insulator form a capacitor. The value of the double layer capacitance depends on many variables including electrode potential, temperature, ionic concentrations, types of ions, oxide layers, electrode roughness, impurity adsorption, etc.

Polarization Resistance

Whenever the potential of an electrode is forced away from its value at open circuit, that is referred to as polarizing the electrode. When an electrode is polarized, it can cause current to flow via electrochemical reactions that occur at the electrode surface. The amount of current is controlled by the kinetics of the reactions and the diffusion of reactants both towards and away from the electrode. In cells where an electrode undergoes uniform corrosion at open circuit, the open circuit potential is controlled by the equilibrium between two different electrochemical reactions. One of the reactions generates cathodic current and the other anodic current. The open circuit potential ends up at the potential where the cathodic and anodic currents are equal. It is referred to as a

mixed potential. The value of the current for either of the reactions is known as the corrosion current.

When there are two simple, kinetically controlled reactions occurring, the potential of the cell is related to the current by the following (known as the Butler-Volmer equation).

$$I = I_{corr} \left\{ 10^{\frac{2.303(E-E_{oc})}{\beta_a}} - 10^{\frac{-2.303(E-E_{oc})}{\beta_c}} \right\} \quad \text{Eqn. 19}$$

where,

I is the measured cell current in amps,

I_{corr} is the corrosion current in amps,

E_{oc} is the open circuit potential in volts,

β_a is the anodic Beta coefficient in volts/decade,

β_c is the cathodic Beta coefficient in volts/decade.

If a small signal approximation ($E-E_{oc}$ is small) is applied to then following expression for I_{corr} , which is indicative of corrosion rate, is obtained:

$$I_{corr} = \frac{\beta_a \beta_c}{2.303 (\beta_a + \beta_c)} \left(\frac{1}{R_p} \right) \quad \text{Eqn. 20}$$

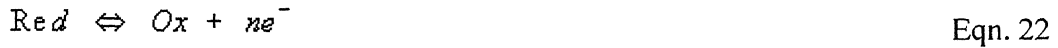
This introduces a new parameter, R_p , the polarization resistance. The polarization resistance behaves like a resistor. From the above equation it is visible that I_{corr} is inversely proportional to R_p .

Charge Transfer Resistance

A similar resistance is formed by a single kinetically controlled electrochemical reaction. In this case we do not have a mixed potential, but rather a single reaction at equilibrium. Consider a metal substrate in contact with an electrolyte. The metal molecules can electrolytically dissolve into the electrolyte, according to:



or more generally:



In the forward reaction in the first equation, electrons enter the metal and metal ions diffuse into the electrolyte. Charge is being transferred. This charge transfer reaction has a certain speed. The speed depends on the kind of reaction, the temperature, the concentration of the reaction products and the potential. The general relation between the potential and the current is:

$$i = i_0 \left[\frac{C_O}{C_O^*} e^{\left(\frac{\alpha n F \eta}{RT}\right)} - \frac{C_R}{C_R^*} e^{\frac{-(1-\alpha)n F \eta}{RT}} \right] \quad \text{Eqn. 23}$$

with,

i_0 = exchange current density

C_O = concentration of oxidant at the electrode surface

C_O^* = concentration of oxidant in the bulk (*delete the spaces*)

C_R = concentration of reductant at the electrode surface

F = Faradays constant

T = temperature

R = gas constant

α = reaction order

n = number of electrons involved

η = over potential ($E - E_0$)

The over potential, η , measures the degree of polarization. It is the electrode potential minus the equilibrium potential for the reaction. When the concentration in the bulk is the same as at the electrode surface, $C_O = C_O^*$ and $C_R = C_R^*$. This simplifies the above equation into:

$$i = i_0 \left[e^{\alpha \frac{nF}{RT} \eta} - e^{-(1-\alpha) \frac{nF}{RT} \eta} \right] \quad \text{Eqn. 24}$$

This equation is called the Butler-Volmer equation. It is applicable when the polarization depends only on the charge transfer kinetics. Stirring will minimize diffusion effects and keep the assumptions of $C_O = C_O^*$ and $C_R = C_R^*$ valid. When the over potential, η , is very

small and the electrochemical system is at equilibrium, the expression for the charge transfer resistance changes into:

$$R_{ct} = \frac{RT}{n F i_0} \quad \text{Eqn. 25}$$

From this equation the exchange current density can be calculated when R_{ct} is known.

Diffusion

Diffusion can create impedance known as the Warburg impedance. This impedance depends on the frequency of the potential perturbation. At high frequencies the Warburg impedance is small since diffusing reactants don't have to move very far. At low frequencies the reactants have to diffuse farther, thereby increasing the Warburg impedance. This form of the Warburg impedance is only valid if the diffusion layer has an infinite thickness. Quite often this is not the case. If the diffusion layer is bounded, the impedance at lower frequencies no longer obeys the equation above

Coating Capacitance

A capacitor is formed when two conducting plates are separated by a non-conducting media, called the dielectric. The value of the capacitance depends on the size of the plates, the distance between the plates and the properties of the dielectric [60]. The relationship is:

$$C = \frac{\epsilon_0 \epsilon_r A}{d} \quad \text{Eqn. 26}$$

With,

ϵ_0 = electrical permittivity

ϵ_r = relative electrical permittivity

A = surface of one plate

d = distances between two plates

Virtual Inductor

The impedance of an electrochemical cell can also appear to be inductive. Some authors have ascribed inductive behavior to adsorbed reactants [54, 78]. Both the adsorption process and the electrochemical reaction are potential dependent. The net result of these dependencies can be an inductive phase shift in the cell current. Inductive behavior can also result from nonhomogeneous current distribution, cell lead inductance and potentiostat non-idealities. In these cases, it represents an error in the EIS measurement.

2.8.5 Equivalent circuits used for modeling in the AC-impedance study.

In order to obtain information about physical parameters such as polarization resistance, double layer capacitance etc, AC equivalent circuits are fitted to the experimental data. The goodness of the fit is indicated by the value of the Chi-Square. Theoretically, the Chi-Square value can vary from 0 to 1, depending upon the quality of the fit. But for, good fitting of the experimental data, the value of the Chi-Square should be as close to zero as possible.

Circuits and there typical impedance response, used in the chapter 4 to fit the experimental data of various alloys used in the AC-impedance study, will be discussed in this section. If the impedance response consists, only of a capacitive loop, then the equivalent circuit shown in Fig. 27a is used for modeling. Typical impedance response due to this circuit is shown in Fig. 28b.

Fig. 29 shows the typical impedance response due to the equivalent circuits shown in Fig. 27b, c and d. The Nyquist diagram shown in the Fig. 29 consists of four parts, namely, very high frequency (VHF) inductance loop, high frequency (HF) capacitive loop, a low frequency (LF) capacitive loop (present only in the impedance response of Esr137) and a very low frequency (VLF) inductive loop. All the positions of these respective loops have been marked schematically in Fig. 29. However, it must be

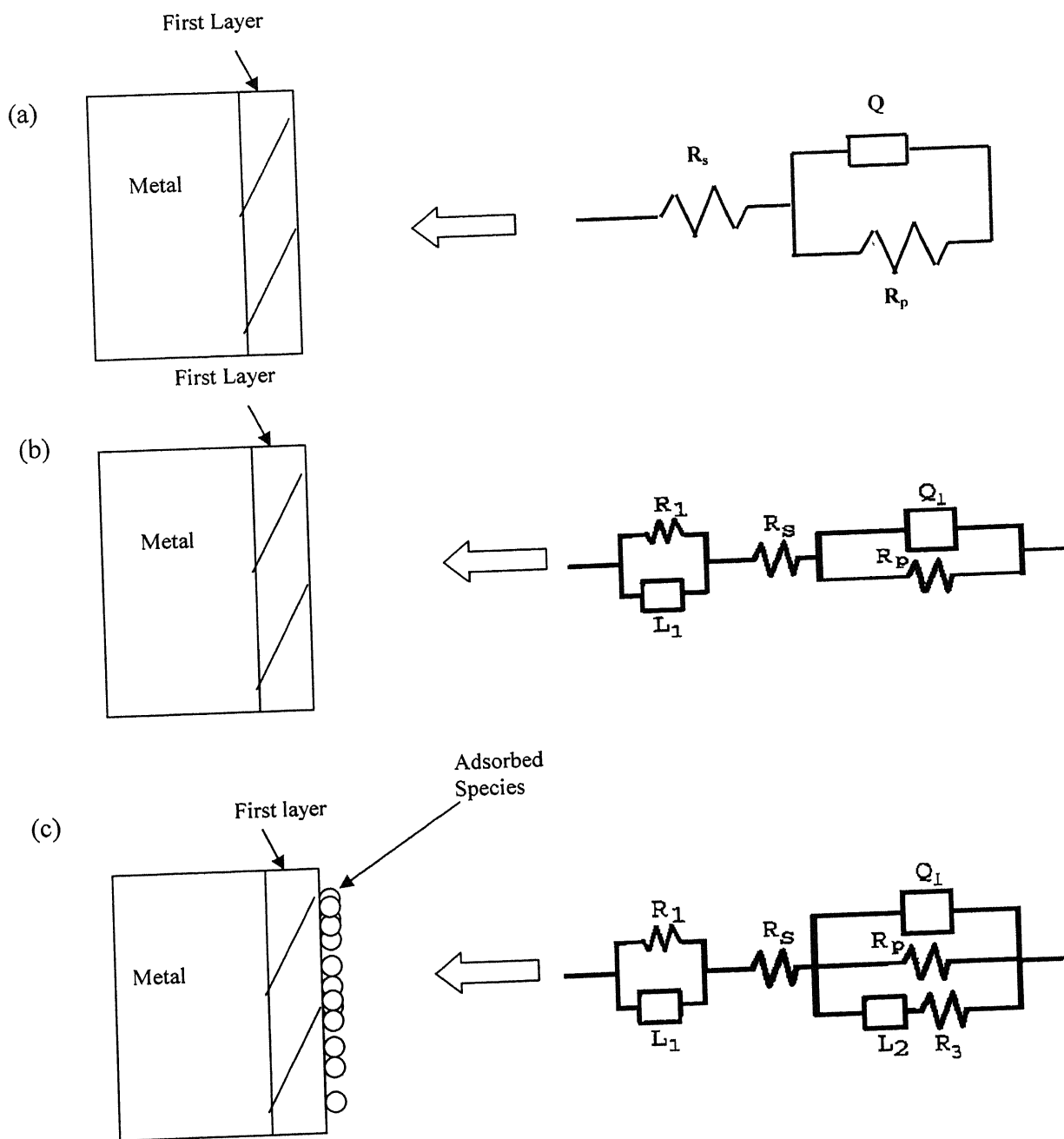
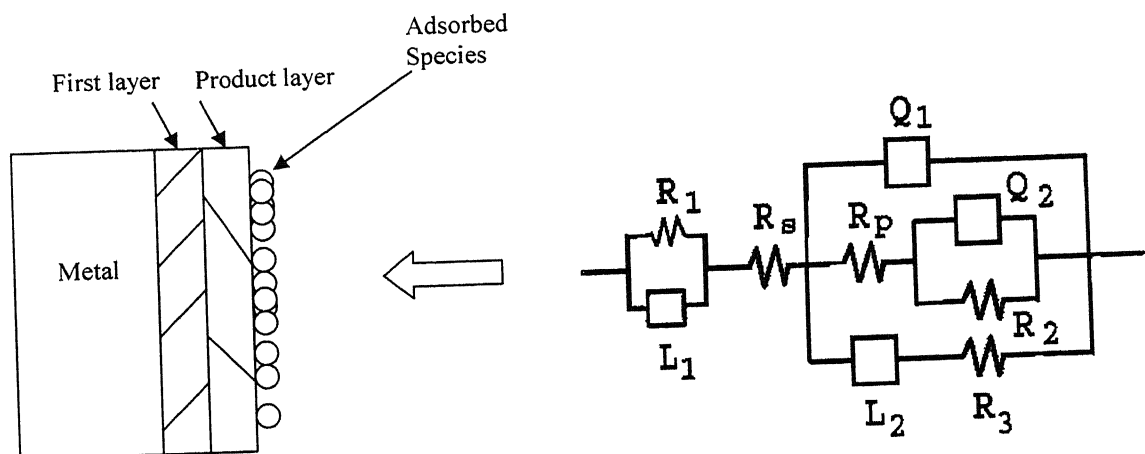


Fig. 27 Equivalent circuits and the corresponding physical picture of the corroding surface.

(d)



(e)

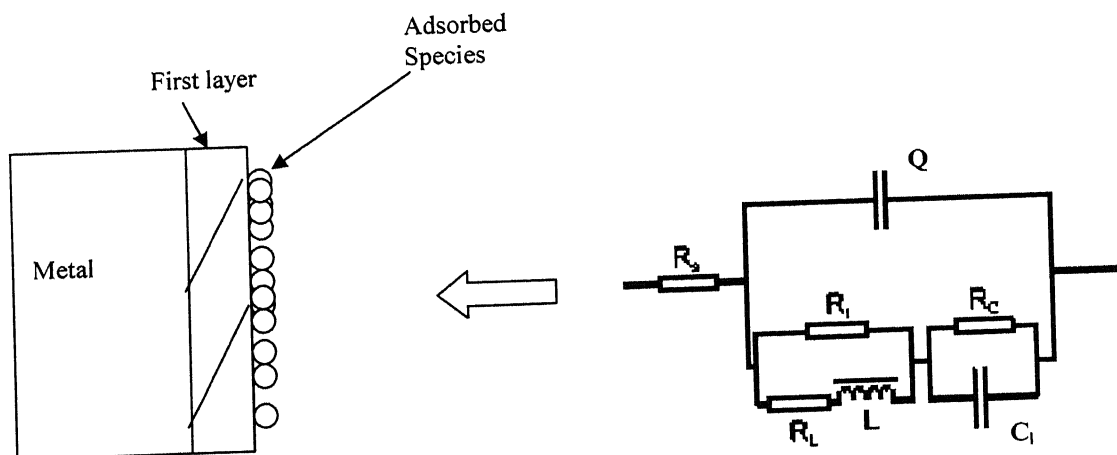


Fig. 27 (continued) Equivalent circuits and the corresponding physical picture of the corroding surface.

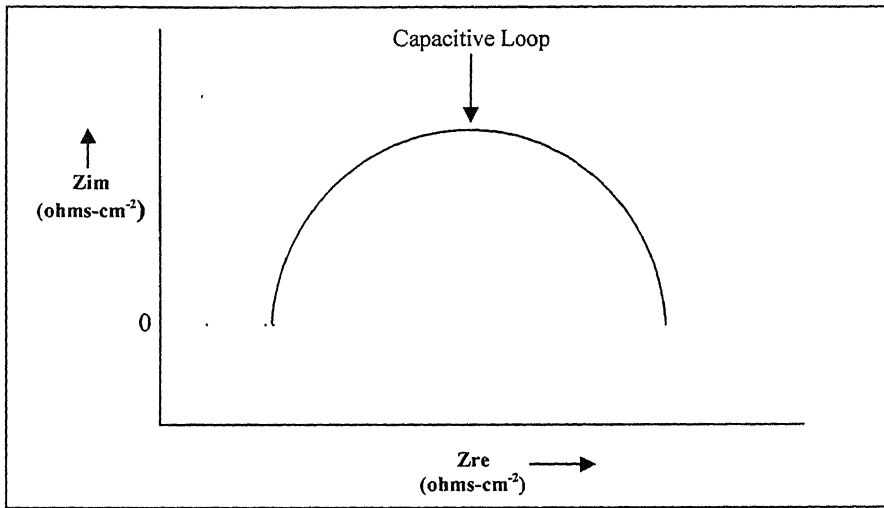


Fig. 28 Typical impedance response by the equivalent circuit shown in Fig. 27a

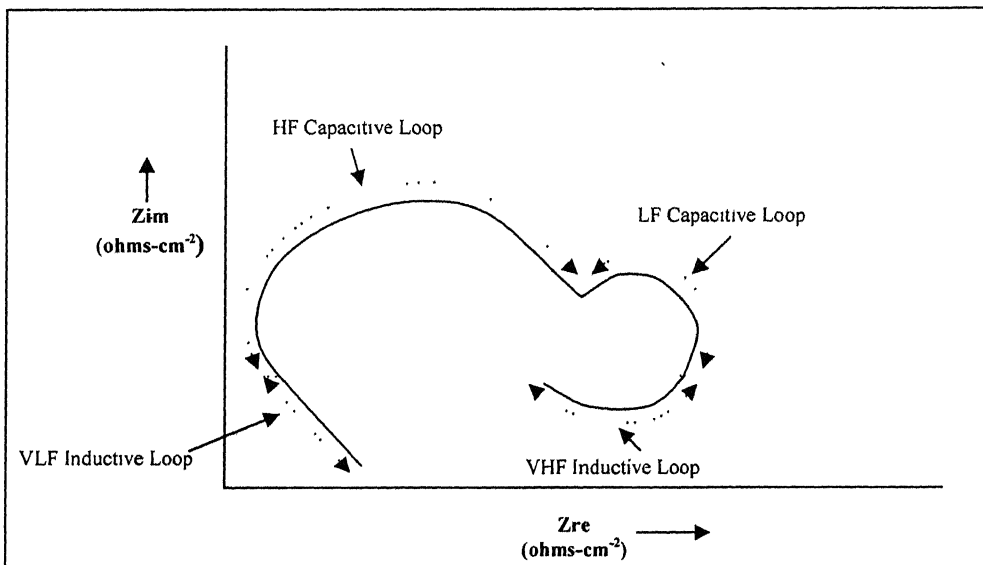


Fig. 29 Typical impedance response by the equivalent circuits shown in Fig. 27b, c and d

noted that, each of the four parts shown in Fig. 29 is not present in the typical impedance response of all the three equivalent circuits.

For the circuits shown in Fig. 27a through Fig. 27d, the meaning of various symbols is as follows:

L_1	High frequency inductance
R_1	Resistance due to high frequency inductance
R_s	Solution Resistance
Q_1	CPE due to surface film
R_p	Polarization Resistance (Resistance due to surface film)
Q_2	CPE due to porous product layer
R_2	Resistance due to porous product layer
L_2	Low frequency inductance
R_3	Resistance due to low frequency inductance

L_1 and R_1 which are the part of all the three equivalent circuits (Fig. 27b, c and d) account for the very low frequency VLF inductive loop. Similarly, R_s , Q_1 , and R_p are also present in all the three circuits. The combination of these three circuit elements accounts for the HF capacitive loop. L_2 and R_3 which are present only in the equivalent circuits shown in Fig. 27 c and d, account for the VLF inductive loop. Q_2 and R_2 are present only in the equivalent circuit shown in Fig. 27d. The combination of these two circuit elements accounts for the LF capacitive loop.

In summary, the equivalent circuit shown in Fig. 27d is used for modeling the experimental data, when all the four parts shown in Fig. 29 are present in the impedance response.

The equivalent circuit shown in Fig. 27c is used, when the impedance response consists of VHF inductive loop, HF capacitive loop and VLF inductive loop. Whereas, the equivalent circuit shown in Fig. 27b is used for modeling, when, only a VHF inductive loop and a HF capacitive loop are present in the impedance response.

The typical impedance response due to the circuit shown in Fig 27e is shown in Fig. 30. This type of impedance response was obtained in the case of Al 6063 in 0.25

mol/lit H_2SO_4 solution. The meaning of various symbols used in the circuit shown in Fig. 27e:

R_s	Solution Resistance
Q	CPE due to surface film
R_t	Polarization Resistance (Resistance due to passive oxide film)
C_l	Capacitance due to porous product layer
R_c	Resistance due to porous product layer
L	Low frequency inductance
R_l	Resistance due to low frequency inductance

All the positions of these respective loops have been marked schematically in Fig. 30. It consists of a high frequency (HF) capacitive loop, an intermediate frequency (IF) inductive loop and a low frequency (LF) capacitive loop. The combination of R C and R accounts for HF capacitive loop. R and L together, account for the IF inductive loop. The parallel combination of R and C , accounts for the LF capacitive loop.

The physical picture of the surface when different equivalent circuits are used for modeling are presented in Fig. 27. Equivalent circuit shown in Fig. 27 are used for modeling when only a single surface film is present on the surface as shown in Fig. 27a. Equivalent circuit shown in Fig. 27 are used for modeling when a product layer is also present in addition to the first layer on the corroding surface. Surface film is present on the surface as shown in Fig. 27a.

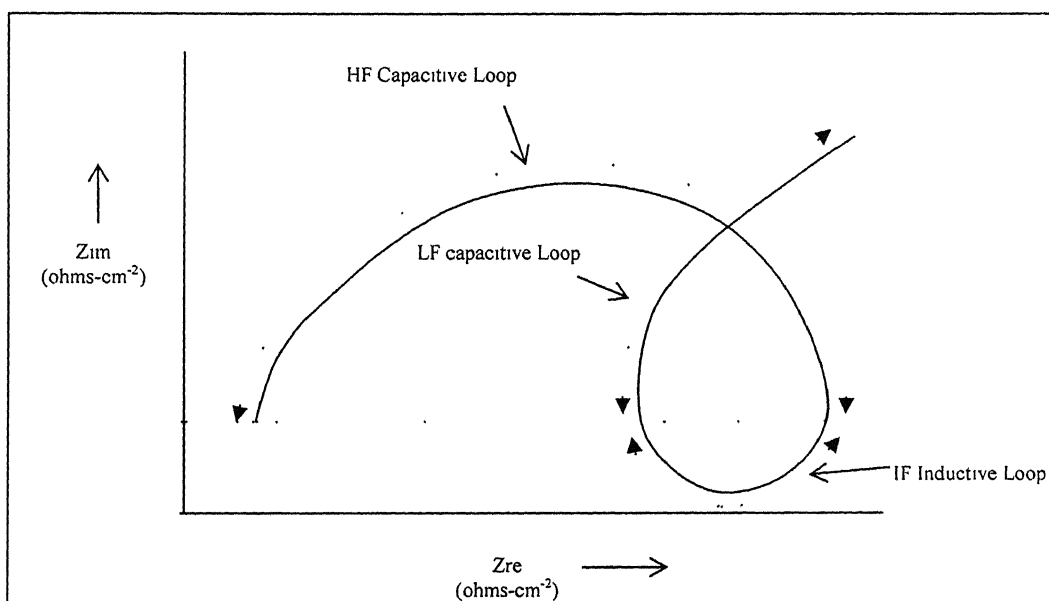


Fig. 30 Typical impedance response by the equivalent circuit shown in Fig 15e

2.9 Electrochemical impedance spectroscopy study of the surface film of aluminium.

Aluminium and its alloys are used widely in industry. Due to this fact in recent decades a great effort has been devoted to the understanding of the electrochemical behaviour of this metal in a variety of electrolytes. Ac impedance has played an important role in helping to build mechanisms [61, 62, 63, 64, 65, 66, 67, 68, 69, 70 and 71].

In the major part of impedance work performed with aluminium electrodes, Nyquist diagrams are composed of one HF capacitive loop, followed by a LF inductive loop [67, 68, 70 and 71], but in some cases, where VLF regions could be explored, a second capacitive loop was evidenced [61-65, 67 and 69]. While there is almost a consensus in the literature regarding the phenomena at the origin of the inductive loop, which is mainly attributed to the relaxation of adsorbed intermediates, following the formalism proposed by Epelboin and Keddam [72], there are diverging explanations about the origin of the two capacitive loops. As to the phenomena at the origin of the HF capacitive loop, some authors attribute its existence to transport process through the aluminium oxide layer [62, 67 and 70], while others either consider that it is only due to charge transfer with double layer charging in parallel, or to a combination of two highly superimposed capacitive loops [69 and 73].

In the literature the VLF capacitive loop has been assigned to different phenomena. De Wit et al. [74] associated this loop to the modulation of the oxide layer thickness. Frers et al. [62], studying the behaviour of aluminium in NaCl solution, ascribed this loop to the presence of chloride ions in the solution, while Bessone et al. [65], in neutral solutions, attributed this loop to a diffusion controlled process within the oxide layer. Brett [64] explained this loop as a result of the passive current through the oxide layer, while de Wit and Lenderink [69] suggested that it might be due to adsorbed anions, mainly oxygen anions. Recently, Peter et al. [75] and Bai and Conway [76] had investigated the dissolution mechanism of aluminium in organic media by ac impedance. The inductive loops present in the diagrams were attributed to the adsorption of organic anions playing a role in metal dissolution.

Aoki et. al. [77] studied the electrochemical behaviour of pure aluminium in citric acid solution with a rotating disk electrode (RDE) at the open circuit potential (OCP), in the presence and in the absence of chloride, using electrochemical impedance spectroscopy and Raman spectroscopy. Nyquist plots for pure aluminium RDE in 0.75% citric acid solution at open circuit potential is shown in Fig. 31. The impedance diagrams were composed of four frequency domains: at very high frequency (VHF), a Warburg-like behaviour was attributed to the porosity effect of the external part of the oxide layer. A slightly depressed capacitive loop at high frequency (HF) was explained as the combination of two capacitive loops, one corresponding to the same phenomenon as in the VHF domain but insensitive to the porosity (barrier layer resistance in parallel to the oxide film capacity), the other one to the charge transfer resistance in parallel to the double layer capacity. An inductive loop at low frequencies (LF) appeared as due to the relaxation of oxygen species adsorbed at the film – solution interface, while the very low frequencies (VLF) capacitive loop was ascribed to the coverage relaxation of adsorbed citrate species. Possible modulation of the passive layer thickness was also envisaged as a phenomenon at the origin of this latter loop. The diagrams shape was also insensitive to the addition of 104 ppm chloride ions to the solution, even though a diameter decrease of the HF capacitive loop was observed together with an increase of the frequency response. Raman Spectroscopy showed that citrate ions adsorb strongly to the electrode surface and that the time scale of this process was consistent with the frequency domain observed for the VLF capacitive loop. The interaction of citrate with the oxide layer was found to be hindered by the addition of chloride ions to the electrolytic solution.

Shao et al. [78] conducted the analysis on the electrochemical dissolution of aluminium in an alkaline solution using electrochemical impedance spectroscopy (EIS). A model based on its reaction mechanism was proposed. The kinetic parameters including rate constants of each step and covering densities of intermediates were obtained. The EIS was well analyzed by this model. EIS experiments of pure aluminum in 1 M KOH were performed over the range of -1.5 to -0.75 V. Some of their results are shown in Fig. 32. The EIS response indicated that the mechanism of aluminum dissolution does not change as the potential varies in this range. These EIS include a high-frequency capacitive loop, a middle-frequency inductive loop and a low-frequency

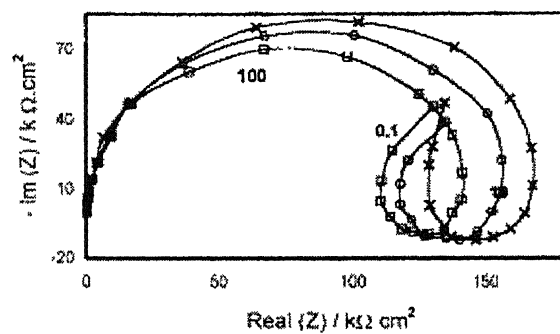


Fig. 31 Sequential Nyquist diagrams for pure aluminium RDE in 0.75% citric acid solution at the OCP. (x) First, (o) second, (□) third [77].

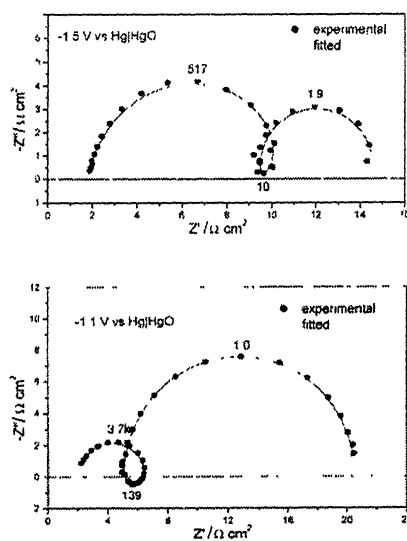


Fig. 32 EIS spectra of pure aluminum in 1 M KOH at different potentials [78].

capacitive loop. The high-frequency capacitive loop was attributed to charge transfer resistance (R_t) in parallel with a double-layer capacitance (C_{dl}). These EIS could be fitted well, using the circuit model described in Fig. 33.

Rehim et. al [79] used EIS technique to study corrosion behaviour of pure Al and (Al+6%Cu) and (Al+6%Si) alloys in quiescent deaerated Na_2SO_4 solutions containing various concentrations of NaCl, NaBr and NaI under the influence of different experimental variables at open circuit potential. and presence of NaCl, NaBr and NaI under the influence of various experimental variables at the open circuit potential (OCP). They found that that in the absence of halide ions the rates of corrosion of the three Al samples are enhanced with increasing concentration, acidity, and alkalinity of the Na_2SO_4 solution and in the presence of halide ions. EIS measurements were carried out using AC signals of amplitude 5 mV peak to peak at the OCP in the frequency range of 100 kHz–10 Hz. Fig. 34 shows typical complex plan impedance plots for pure Al and its two alloys in 0.50 M Na_2SO_4 solution at OCP and at 30 °C. The data revealed that each impedance diagram consisted of a large capacitive loop at high frequency (HF) and a small inductive one at low frequency (LF) values. The HF capacitive loop was assigned to the relaxation process in the natural oxide film covering the surface of the three Al samples and its dielectric properties [80 and 81].

The inductive loop was attributed to the relaxation process obtained by adsorption and penetration of SO_4^{2-} ions on and into the oxide film [82]. The equivalent circuit model used to fit the experimental data is shown in Fig. 35, as previously reported [83 and 84]. In this circuit, C_{dl} is the double layer capacitance, R_t the interfacial charge-transfer resistance, L the inductance, and R_L the inductive resistance. When an inductive loop is present, the polarization resistance R_p can be calculated from the following equation [85 and 86]:

$$R_p = R_L R_t / (R_L + R_t) \quad \text{Eqn. 27}$$

The effect of SO_4^{2-} concentration on the complex plane impedance diagram of pure Al and its two alloys at the OCP and at 30 °C was investigated. In all cases studied, it was observed that the values of C_{dl} increased, while those of R_p decreased with an increase in SO_4^{2-} concentration. The effect of solution pH (from 1.80 up to 11.80) on the impedance

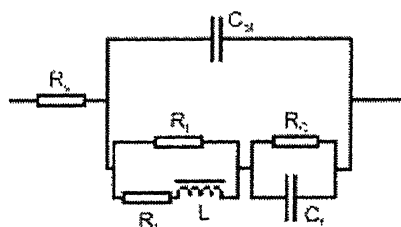


Fig. 33. Circuit model of aluminum in 1 M KOH [78].

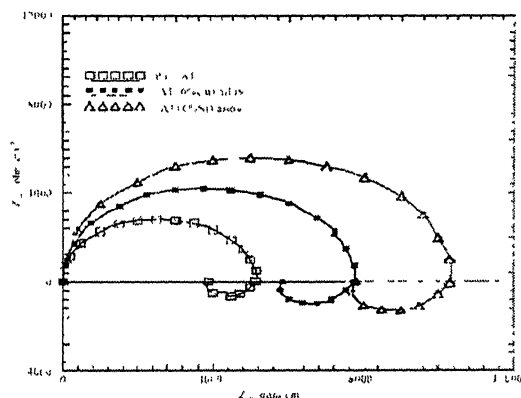


Fig. 34 EIS response of the three Al samples in 0.50 N Na_2SO_4 solution at the OCP and at 30 °C [79]

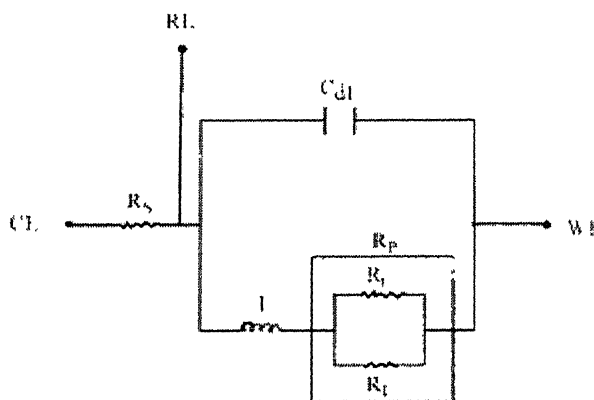


Fig. 35 The equivalent circuit model used to fit the experimental data presented in Fig. 34 [79].

characteristics of the three Al samples in 0.50 M Na₂SO₄ solution at OCP and at 30 °C was investigated. The data reveal that the values of C_{dl} increase, while those of R_p decrease with increasing acidity and alkalinity of the solution. The data showed that the corrosion rate of Al and its two alloys is lowest in the pH range from ca. 4.8 to 8.8. In this pH range, Al and its alloys are usually covered with a protective oxide film, and therefore show the least corrosion rates. However, in acidic media, Al dissolves as a simple salt in conjunction with hydrogen depolarization reaction [87]. In alkaline media, the acceptable mechanism of the Al corrosion is based on the dissolution of Al atoms from the active sites or flawed regions of the oxide film and the gradual removal of these atoms through the formation of hydroxide with increased coordination number from 1 to 3 to form independent molecular species of Al(OH)₃, which react in a pure chemical manner to form a soluble aluminate ion, AlO_2^- that goes in solution leaving a bare surface site ready for another dissolution process [88]. Fig. 36 shows a typical Nyquist plots for pure Al in Na₂SO₄ solution containing 0.20 M NaX (where X=Cl⁻, Br⁻ or I⁻) at the OCP and at 30 °C. The points in the figures represent the experimental data, while the solid lines represent the best fits. The impedance spectra consists of a large capacitive loop at HF and an inductive loop at intermediate frequencies (IF), followed by a second capacitive loop at LF values. The HF capacitive loop is attributed to the presence of a protective oxide film covering the surface of Al and its two alloys. The (IF) inductive loop may be related to the relaxation process obtained by adsorption and incorporation of both X⁻ and SO₄²⁻ ions on and into the oxide film. The second capacitive loop observed at LF values could be assigned to the metal dissolution. The equivalent circuit used to fit the experimental data of Fig. 36 is shown in Fig. 37. Where, polarization resistance (R_p) is calculated as:

$$R_p = [R_L R_i / (R_L + R_i)] + R_2 \quad \text{Eqn. 28}$$

Rehim et. al. [89] also used electrochemical impedance spectroscopy (EIS) in order to study the corrosion inhibition process of pure Al, (Al + 6%Cu) and (Al + 6%Si) alloys in 1.0 M HCl solution at the open circuit potential (OCP) in the temperature range 10–60 °C. Some of their results are shown in Fig. 38. The Nyquist diagrams consisted of a capacitive semicircle at high frequencies followed by a well defined inductive loop at

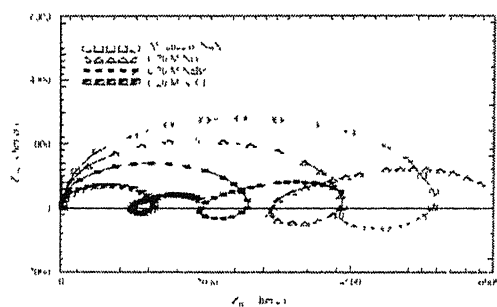


Fig. 36 Typical complex plane impedance plot measured for pure Al in 0.5 M $\text{Na}_2\text{SO}_4 + 0.2 \text{ N NaX}$ solution ($\text{pH} \cong 6.80$) at the OCP and at 30 °C [79]

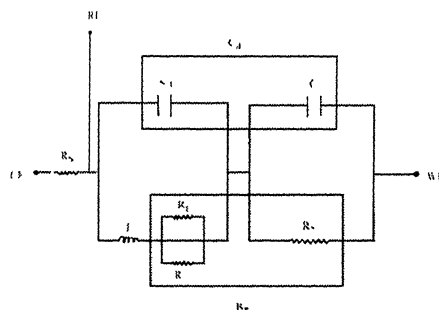


Fig. 37 The equivalent circuit model used to analyse the experimental data presented in Fig.36 [79].

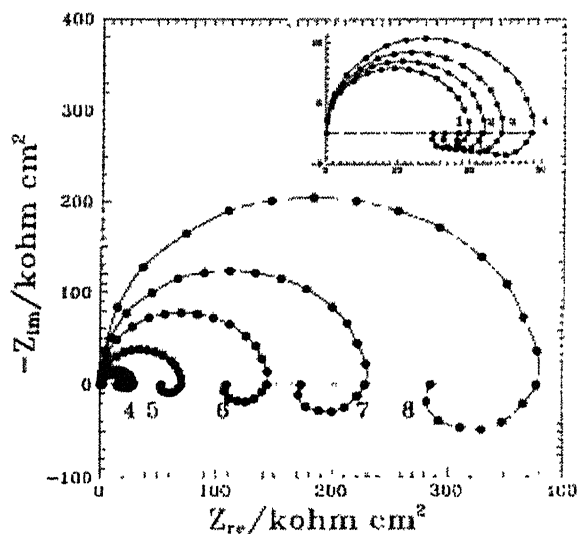


Fig. 38 Effect of surfactant concentration on the impedance response of pure Al in deareated 1.0 M HCl solution at OCP and at 30 °C. (1) 0.00 M NS; (2) 0.0002 M; (3) 0.0004 M; (4) 0.0006 M; (5) 0.002 M; (6) 0.004 M; (7) 0.006 M; (8) 0.01 M [89].

low frequency values. The HF capacitive loop could be assigned to the relaxation process in the natural oxide presents on the surface of the three Al samples and its dielectric properties [90 and 91]. The inductive loop may be attributed to the relaxation process in oxide presents on the electrode surface obtained by adsorption species as Cl_{ads}^- and H_{ads}^+ . The impedance measurements were interpreted according to a suitable equivalent circuit shown in Fig. 39. The results obtained showed that the addition of the surfactant inhibits the hydrochloric acid corrosion of the three Al samples. The inhibition occurs through adsorption of the surfactant on the metal surface without modifying the mechanism of corrosion process.

Gudic et. al [92] conducted a study to understand the passivation of Al and Al-Sn alloys in borate buffer solutions using electrochemical impedance spectroscopy. Equivalent circuits have been proposed that completely illustrate the Al (Al-Sn alloy)/oxide film/electrolyte systems examined, and properties of oxide films were determined. The stability (thickness and resistance) of oxide films has been found to increase with increased Sn content in the alloy, with increased passivation potential, and with longer time of anodising. The increase in temperature of anodising significantly reduces impedance in systems observed. The equivalent circuit, shown in Fig. 40 was used to fit the experimental data. R_{el} represents the resistance of the electrolyte ($\approx 20 \text{ } \Omega \text{ cm}^2$). R_1 is the resistance and Q is the capacitance of the oxide film. Nature of some of the Bode phase plots obtained by them in the case of Al and Al-Sn alloys in borate buffered solution at open circuit potential is shown in Fig. 40.

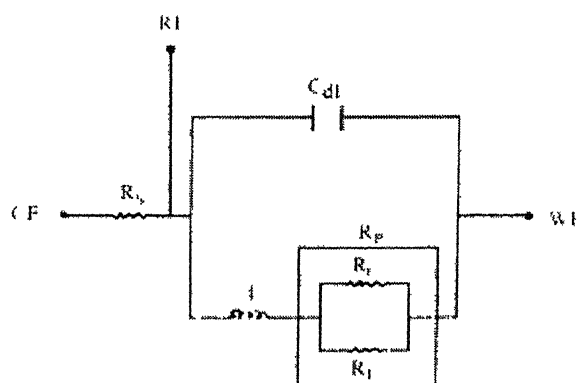


Fig. 39 The equivalent circuit model used to fit the experimental data [89].

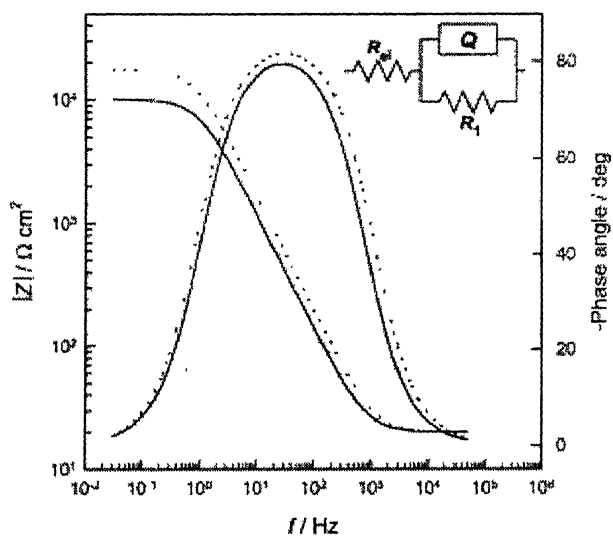


Fig. 40 Bode plots for Al-0.40 wt.%Sn alloy in borate buffer solution ($T=25\text{ }^{\circ}\text{C}$; pH 7.8) after (—) 0.5 h and (...) 8 h of stabilisation at the open circuit potential. An equivalent circuit is given in the figure [92].

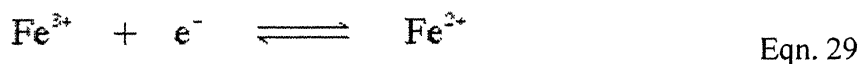
2.10 Cyclic voltammetry

Of all the methods available for studying electrode process, potential sweep methods are probable the most widely used. It consists in the application of a continuously time varying potential to the working electrode. This results in the occurrence of the oxidation or reduction reactions of electroactive species in the solution (faradic reactions), possibly adsorption of the species according to the potential and a capacitive current due to double layer charging [93]. The observed current is therefore different from that in the steady state. The potential technique is normally used in the stationary electrodes but can also be used at hydrodynamic electrodes. Its principle use has been to diagnose the mechanism of electrochemical reactions, for the identification of the species present in the solution and for semi-quantitative analysis of the reaction rates. Two closely related forms of voltammetry are there [93, 94].

1) Linear sweep voltammetry

2) Cyclic voltammetry

In linear sweep voltammetry (LSV) a fixed potential range is employed much like potential step measurements. However in LSV the voltage is scanned from a lower limit to an upper limit as shown in Fig. 41. In LSV measurements the current response is plotted as a function of voltage rather than time, unlike potential step measurements. For example in the case of the $\text{Fe}^{3+}/\text{Fe}^{2+}$ system,



voltammogram shown in Fig. 42 would be seen for a single voltage scan using an electrolyte solution containing only Fe^{3+} resulting from a voltage sweep. The scan begins from the left hand side of the current/voltage plot where no current flows. As the voltage is swept further to the right (to more reductive values) a current begins to flow and eventually reaches a peak before dropping. To rationalise this behaviour we need to consider the influence of voltage on the equilibrium established at the electrode surface. If the electrochemical reduction of Fe^{3+} to Fe^{2+} is considered, the rate of electron transfer is fast in comparison to the voltage sweep rate [93]. Therefore at the electrode surface an equilibrium is established identical to that predicted by thermodynamics. From equilibrium electrochemistry the Nernst equation can be written as:

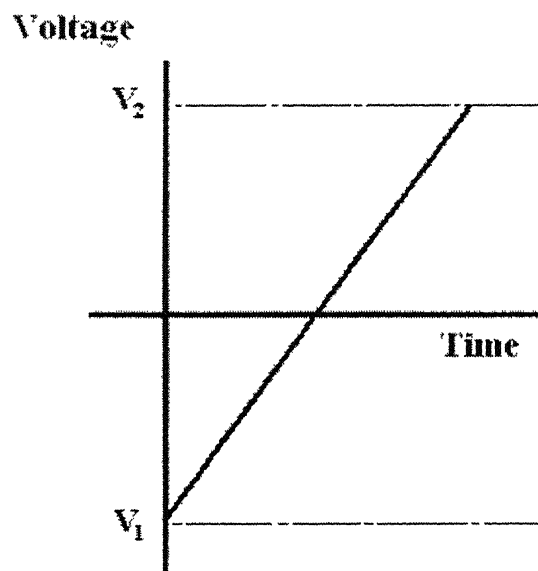


Fig. 41 Variation of applied potential with time in linear sweep voltammetry, showing the initial potential, V_1 and the final potential V_2 . The sweep rate $|dV/dt| = v$.

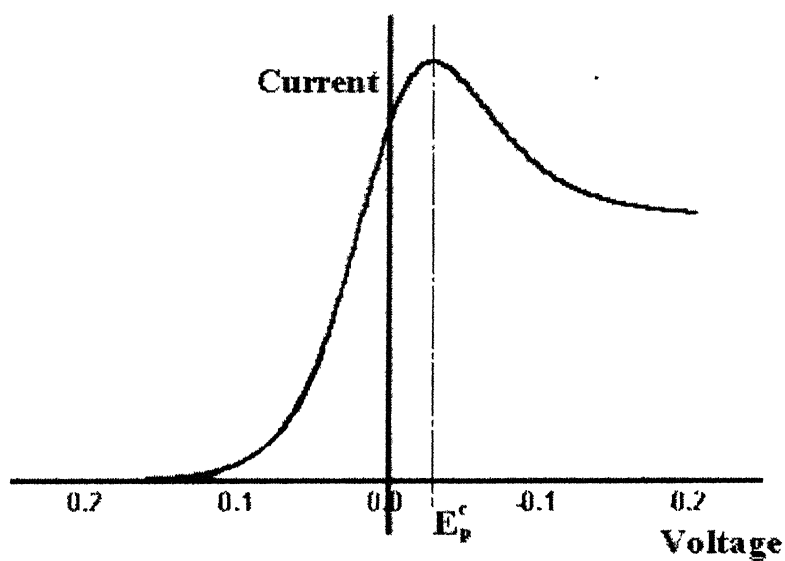
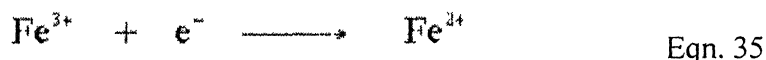
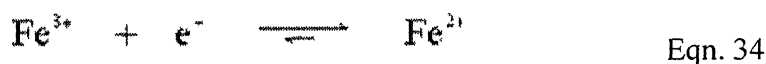
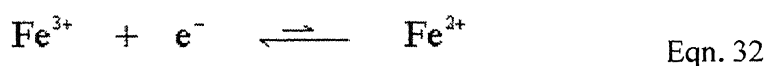


Fig. 42 Linear sweep voltammogram for a reversible reduction at a planar electrode.[book]

$$E = E^{\ominus} + \frac{RT}{nF} \ln \frac{[Fe^{3+}]}{[Fe^{2+}]} \quad \text{Eqn. 30}$$

It predicts the relationship between concentration and voltage (potential difference), where E is the applied potential difference and E^{\ominus} is the standard electrode potential. So as the voltage is swept from V_1 to V_2 the equilibrium position shifts from no conversion at V_1 to full conversion at V_2 of the reactant at the electrode surface [94]. The exact form of the voltammogram can be rationalised by considering the voltage and mass transport effects. As the voltage is initially swept from V^1 the equilibrium at the surface begins to alter and the current begins to flow:



The current rises as the voltage is swept further from its initial value as the equilibrium position is shifted further to the right hand side, thus converting more reactant. The peak occurs, since at some point the diffusion layer has grown sufficiently above the electrode so that the flux of reactant to the electrode is not fast enough to satisfy that required by the Nernst equation. In this situation the current begins to drop just as it did in the potential step measurements. In fact the drop in current follows the same behaviour as that predicted by the Cottrell equation.

If the scan rate is altered the current response also changes. Fig. 43 shows a series of linear sweep voltammograms recorded at different scan rates for an electrolyte solution containing only Fe^{3+} . Each curve has the same form but it is apparent that the total current increases with increasing scan rate. This again can be rationalised by considering the size of the diffusion layer and the time taken to record the scan. Clearly the linear sweep voltammogram will take longer to record as the scan rate is decreased. Therefore the size of the diffusion layer above the electrode surface will be different depending

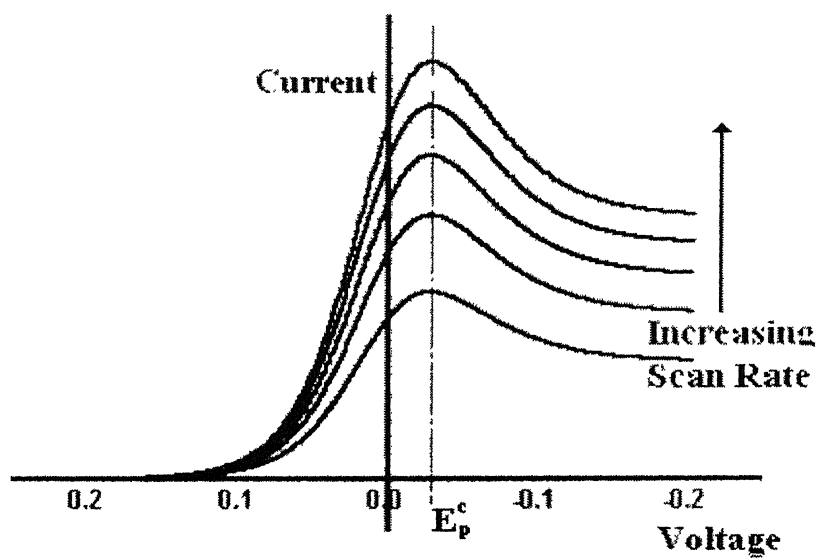


Fig. 43 Linear sweep voltammogram for different sweep rates, for a reversible reduction at a planar electrode [94]

upon the voltage scan rate used. In a slow voltage scan the diffusion layer will grow much further from the electrode in comparison to a fast scan. Consequently the flux to the electrode surface is considerably smaller at slow scan rates than it is at faster rates. As the current is proportional to the flux towards the electrode the magnitude of the current will be lower at slow scan rates and higher at high rates. This highlights an important point when examining LSV (and cyclic voltammograms), although there is no time axis on the graph the voltage scan rate (and therefore the time taken to record the voltammogram) strongly effects the behaviour seen. A final point to note from the figure is the position of the current maximum, it is clear that the peak occurs at the same voltage and this is a characteristic of electrode reactions which have rapid electron transfer kinetics. These rapid processes are often referred to as reversible electron transfer reactions. It may also be the case that the electron transfer processes are 'slow' (relative to the voltage scan rate) [93]. For these cases the reactions are referred to as quasi-reversible or irreversible electron transfer reactions. Fig. 44 shows a series of voltammograms recorded at a single voltage sweep rate for different values of the reduction rate constant (k_{red}).

In this situation the voltage applied does not results in the generation of the concentrations at the electrode surface predicted by the Nernst equation. This happens because the kinetics of the reaction are 'slow' and thus the equilibria are not established rapidly (in comparison to the voltage scan rate). In this situation the overall form of the voltammogram recorded is similar to that above, but unlike the reversible reaction now the position of the current maximum shifts depending upon the reduction rate constant (and also the voltage scan rate). This occurs because the current takes more time to respond to the applied voltage than the reversible case.

Cyclic voltammetry (CV) is very similar to LSV. In this case the voltage is swept between two values V_1 and V_2 (Fig. 45) at a fixed rate, however in the case of CV, when the voltage reaches V_2 the scan is reversed and the voltage is swept back to V_1 . A typical cyclic voltammogram recorded for a reversible single electron transfer reaction is shown in Fig. 46. Here, the solution contained only a single electrochemical reactant. The forward sweep produces an identical response to that seen for the LSV experiment. On reversing the scan, the voltage simply sweeps back through the equilibrium positions gradually converting electrolysis product (Fe^{2+} back to reactant (Fe^{3+}). The current flow

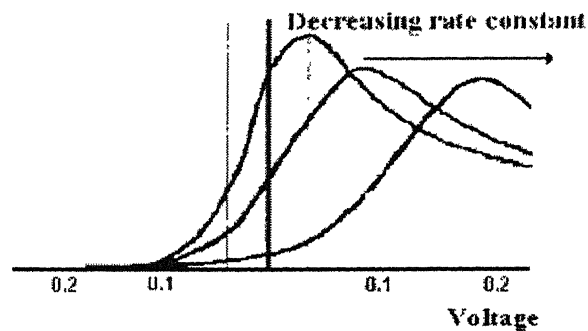


Fig. 44 Series of linear sweep voltammograms recorded at a single voltage sweep rate for different values of the reduction rate constant (k_{red}).

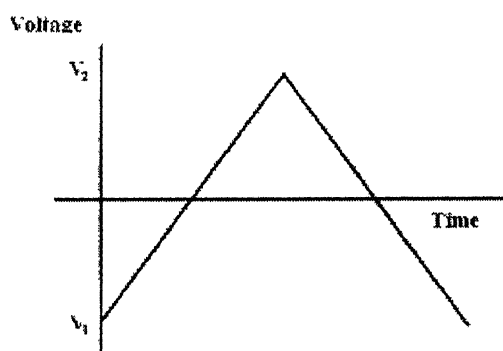


Fig. 45 Variation of applied potential with time in cyclic voltammetry, showing the initial potential, V_1 and the final potential V_2 . The sweep rate $|dV/dt| = v$.

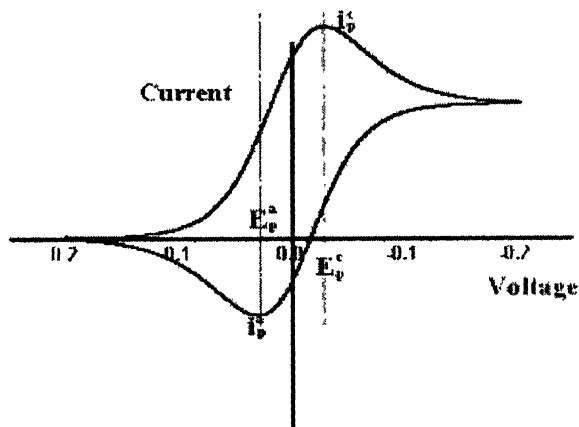


Fig. 46 Cyclic voltammogram for a reversible reaction.

is now from the solution species back to the electrode and so occurs in the opposite sense to the forward sweep but otherwise the behaviour can be explained in an identical manner.

The influence of the voltage scan rate on the current for a reversible electron transfer can be seen in Fig. 47 [94]. As with LSV the influence of scan rate is explained for a reversible electron transfer reaction in terms of the diffusion layer thickness. The cyclic voltammogram in the cases, where the electron transfer is not reversible shows considerably different behaviour from their reversible counterparts. Fig. 48 shows the voltammogram for a quasi-reversible reaction for different values of the reduction and oxidation rate constants. The first curve shows the case where both the oxidation and reduction rate constants are still fast, however, as the rate constants are lowered the curves shift to more reductive potentials. Again this may be rationalised in terms of the equilibrium at the surface is no longer establishing so rapidly. In these cases the peak separation is no longer fixed but varies as a function of the scan rate. Similarly the peak current no longer varies as a function of the square root of the scan rate. By analysing the variation of peak position as a function of scan rates it is possible to gain an estimate for the electron transfer rate constants.

Overall it can be summarized that for a reversible electrochemical reaction the linear sweep and cyclic voltammograms recorded have following well defined characteristics:

- 1) The peak currents are proportional to the square root of the scan rate [93, 94].

$$i_p^a \text{ and } i_p^c \propto \sqrt{v} \quad \text{Eqn. 36}$$

- 2) The positions of peak voltage do not alter as a function of voltage scan rate [93].

- 3) The voltage separation between the current peaks is [93]-

$$\Delta E = E_p^a - E_p^c = \frac{59}{n} \text{mV} \quad \text{Eqn. 37}$$

- 4) The ratio of the peak currents is equal to one

$$\left| \frac{\mathbf{i}_p^2}{\mathbf{i}_p^2} \right| = 1$$

Eqn. 38

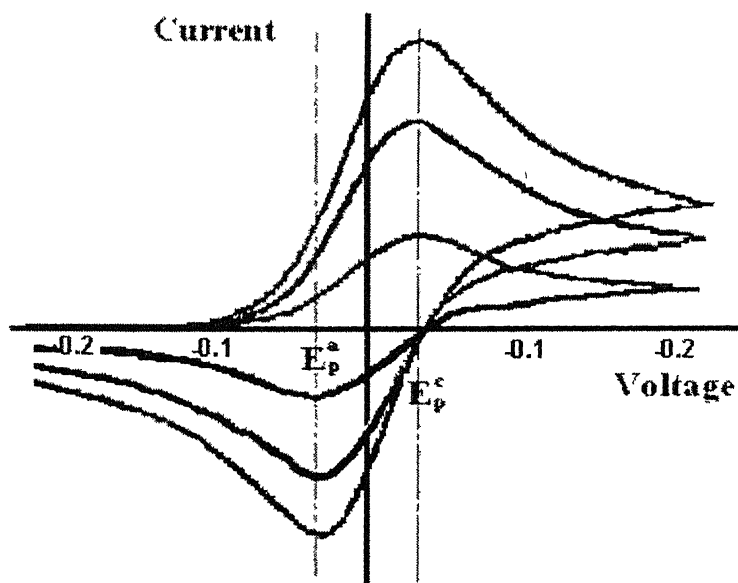


Fig. 47 Cyclic voltammograms at different scan rates for a reversible electron reaction.

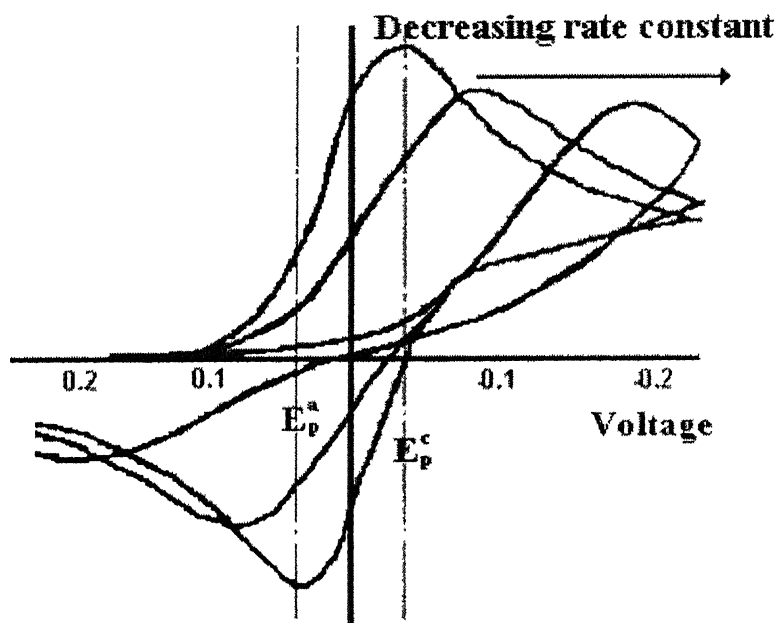


Fig. 48 The effect of increasing irreversibility on the shape of cyclic voltammograms

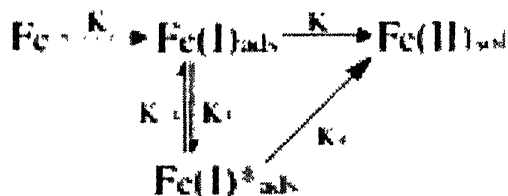
2.11 Anodic dissolution of iron alloy in sulphuric acid

Earlier mechanisms, including the well known consecutive dissolution mechanism and catalyzed mechanism, have been proposed to explain the steady-state polarization results. It is likely that different mechanisms operate under different conditions. For example, anodic dissolution of iron in the presence of chloride follows the other mechanisms as chloride ions involve in the iron dissolution. Now it is generally accepted that elucidating a complicated reaction mechanism by means of steady-state techniques alone, especially for a multi-electron transfer process, is very difficult because the steadystate approach only provides rather little information on the process to be investigated [95, 96, 97]. In contrast, electrochemical impedance spectroscopy (EIS) method applies to the investigation of mechanisms about complicated electrode processes, and impedance behavior can be diagnostically informative as it contains various information, in particular, on behavior of reaction intermediates on the surface of the dissolving metal [9,11,15]. In the earlier eighties, Keddam et al. found that impedance diagrams in the iron– sulfate systems revealed at least three time constants in addition to the well-known high frequency capacitive loop, and the similar result was also observed by schweikert et al. [97], which indicates existence of three adsorbed intermediates at least during the iron dissolution. Consequently, a complex reaction model comprising three dissolution paths was established, in which the dissolution of iron proceeds through different paths at different potentials. In most mechanisms, hydroxide ion (OH^-) is usually considered to be involved in the dissolution of iron in acidic solution [97]. Some authors' studies have also shown that anions in electrolyte solutions usually affect the iron dissolution to some extent [97]. In this sense, it is necessary to choose a kind of acid whose anion does not participate in the iron dissolution as a ligand or an oxidant so that we can ignore the effect of anions and determine more clearly the mechanism of iron dissolution in acidic solution.

Itagaki et. al [99] conducted the study of the anodic dissolution of Fe-Mo alloys using electrochemical impedance spectroscopy (EIS) with channel flow double electrode (CFDE). Nyquist plots of the electrochemical impedance showed capacitive and inductive loops, which are typical features of iron dissolution in the acidic media. By the

application of CFDE to EIS, dissolution efficiency Φ_{diss} , which corresponds to the ratio of the current from the $\text{Fe(II)}_{\text{sol}}$. Dissolved component to the total current in the frequency domain of Fe-Mo electrode. Φ_{diss} not only gives the information concerning $\text{Fe(II)}_{\text{sol}}$ dissolution but also gives information about the adsorbed intermediates. Φ_{diss} measured during iron dissolution showed a semicircle on the complex plane and was interpreted by the adsorbed intermediate $\text{Fe(I)}_{\text{sol}}$. Upon the addition of molybdenum into the alloy Φ_{diss} showed two semicircles. These two semicircles were explained by two adsorbed species. Nyquist plots if some of the cases are shown in Fig. 49.

Houyi Ma et al. [100] studied that the anodic iron dissolution in 0.5 mol/dm^{-3} perchloric acid (HClO_4) by the electrochemical impedance spectroscopy, the potentiodynamic sweep and the scanning electron microscopy measurements. The anodic polarization behavior of iron in HClO_4 solution showed that the strong current oscillations occurred in a narrow potential region, particularly the pitting corrosion was observed in the active dissolution region. These characteristics were quite different from those of iron in the sulfuric acid (H_2SO_4). Nyquist impedance spectra for the iron electrode in 0.5 mol/dm^{-3} perchloric acid solution and in 0.5 mol/dm^{-3} sulphuric acid, at different potentials are shown in Fig. 50 and 51 respectively. Some the At the potentials 82 and 132 mV more positive than the corrosion potential (-482 mV vs. SCE), the impedance spectra for the iron in HClO_4 displayed two inductive arcs; however, by gradually increasing potential the lower frequency inductive arc disappeared at -300 mV at first, and then the higher frequency inductive arc changed into a capacitive arc at -250 mV. Based on the impedance display of iron at various potentials, a reaction model involving two adsorbed intermediate species was proposed, in terms of which the impedance behavior at different potentials were described.



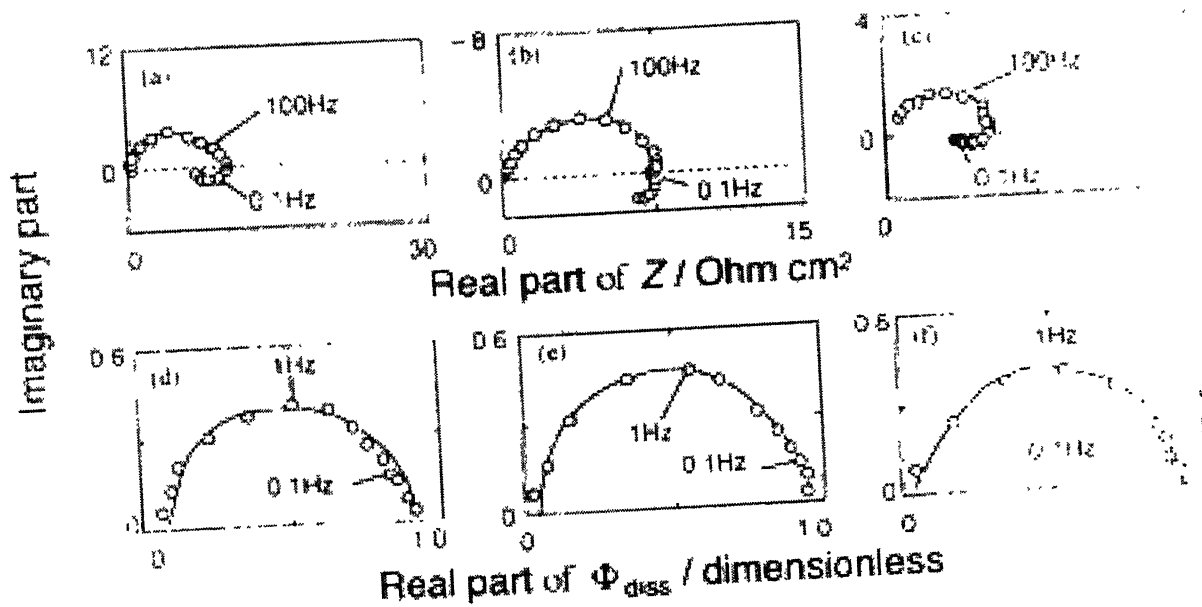


Fig. 49 Experimental results of electrochemical impedance, Z (a)-(c), and dissolution efficiency of F(II) , Φ_{diss} (d)-(f), on Fe-2.5 wt% Mo electrode in sulphuric acid solution (pH=1) [99].

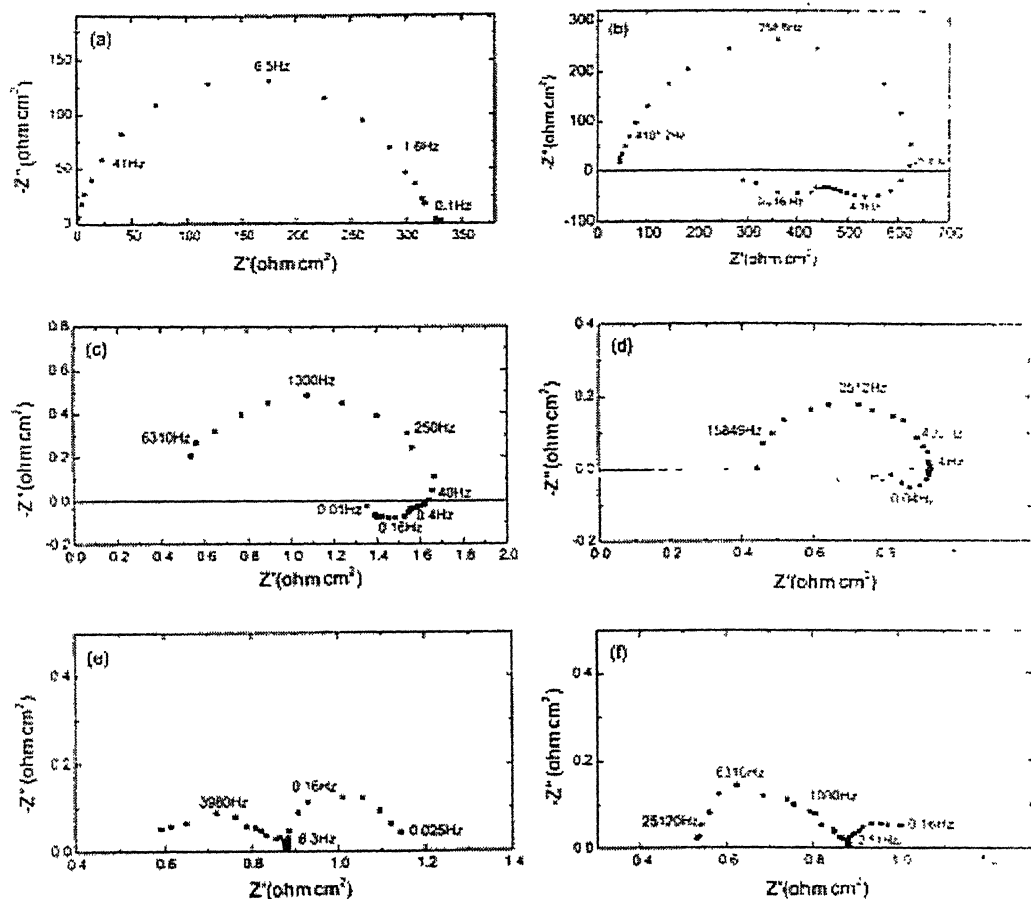


Fig. 50 Nyquist impedance spectra for the iron electrode in 0.5 mol/dm⁻³ HClO₄ solution at different potentials: (a) Corrosion potential, -482 mV (vs. SCE); (b) -400 mV; (c) -350 mV; (d) -300 mV; (e) -250 mV; (f) -200 mV [100].

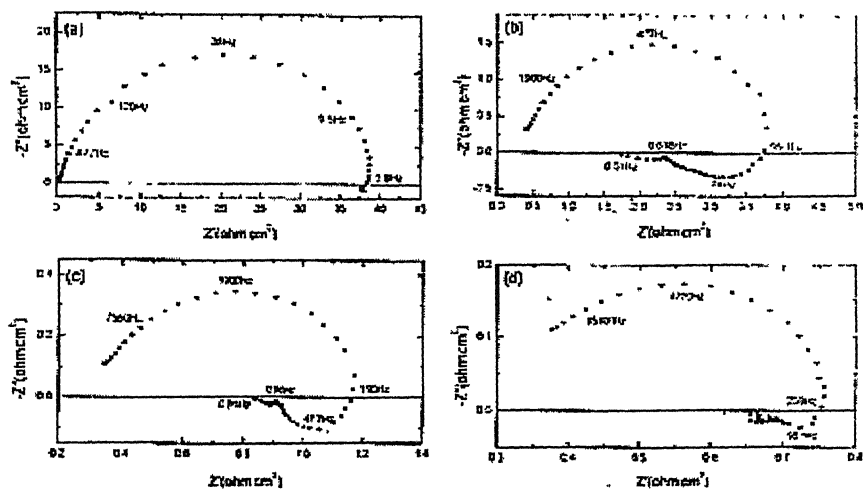


Fig. 51 Nyquist impedance spectra for the iron electrode in 0.5 mol/dm⁻³ H₂SO₄ solution at different potentials. (a) Corrosion potential, -530 mV (vs. SCE); (b) -450 mV; (c) -400 mV; (d) -350 mV [100].

The anodic behavior of iron in the perchloric acid was found to be quite different from that in the sulfuric acid of the same concentration. At lower anodic potential, iron dissolved through two paths that $\text{Fe(I)}_{\text{ads}} \rightarrow \text{Fe(II)}_{\text{sol}}$ and $\text{Fe(I)}^*_{\text{ads}} \rightarrow \text{Fe(II)}_{\text{sol}}$ and the relation among rate constants, K_1 , K_2 and K_4 follows: (i) $b_1 > b_2$, $K_2 > K_1$, $K_4 > K_1$ or (ii) $b_1 < b_2$, $K_2 < K_1$, $K_4 < K_1$. In this case, the impedance diagrams for iron dissolution displayed two inductive loops. Whereas at higher potential, the dissolution path via $K_4\theta_1$ is blocked and iron mainly dissolved via $K_4\theta_2$, which makes the lower frequency inductive arc disappear at first, and then the left higher frequency inductive arc change into a capacitive arc at the much higher potentials. The pitting corrosion occurring at the surface of iron electrode in active region was attributed to the non-uniform dissolution of iron.

CHAPTER 3

EXPERIMENTAL PROCEDURE

The aim of the present work is to understand the effect of Ce addition on the electrochemical behaviour of carbon-alloyed iron aluminide.

3.1. Raw materials

The carbon-alloyed iron aluminides were obtained from the Defense Metallurgical Research Laboratory (DMRL), Hyderabad. Their composition (in at %) were Fe-18.5Al-3.6C (ESR127) and Fe-20.0Al-2.0C (ESR74) and Fe-19.2Al-3.3C-0.07Ce (ESR137). In terms of wt %, the compositions were Fe-10.5Al-0.9C (ESR127) and Fe-11.0Al-0.5C (ESR74) and Fe-10.5Al-0.8C-0.2Ce (ESR137). Here, ESR stands for electro slag remelted specimens and these marked materials were obtained from DMRL, Hyderabad, in the form of rolled strips. The thickness of the iron aluminide samples was nearly 10 mm.

The alloys were originally processed via ingot metallurgy route. The processing technique utilized to obtain these strips is described as follows [101]. Commercial purity aluminium and mild steel scrap were used as raw materials for preparing the base iron aluminide ingots. Grinding was done to clean the surface of the iron charge. After melting the raw materials through the air induction melting process (AIM), the slag product was skimmed off. Aluminium pieces were then added to the molten iron bath. The melt was held at 1620°C for a very short time (2 minutes) to prevent aluminium losses and then normalized to room temperature and was then cast into cast iron moulds. The ingots were then tested for their soundness by radiography. These AIM ingots (55 mm diameter, 360 mm long) were machined to 50 mm diameter. They were then refined by electro slag remelting (ESR) process in an ESR furnace of 350 kVA capacity. A commercial prefused flux based on CaF_2 was used. The flux was preheated and held at 850°C for 2 hours before use in order to remove moisture. The iron aluminide electrode was remelted under this flux cover and cast into 76 mm ingot in a water cooled steel mould. At the end of the process, the power supply was gradually reduced to impose a

condition of hot topping. To check their soundness, the ESR ingots were also radiographed. The ingots were then forged to a reduction ratio of 70% and after forging they exhibited recrystallized grains [101].

Iron aluminide of composition Fe-19.2Al-3.3C-0.07Ce was prepared under an inert (argon) atmosphere using the base iron aluminide ingots with Ce (of purity 99.99%) as the alloying element. This alloy button and the base Fe₃Al were homogenized at 1000°C for 4 hours before processing to further minimize segregation. The alloy buttons and the base iron aluminide thin strips were rolled in multi passes to 80% deformation at 1000°C (in disordered α phase field). Prior to rolling, the materials were soaked in a furnace for 1 hour. All the strips had a brown layer of oxide after rolling.

Low carbon mild steel, Al 6063, 316L SS, 304 SS and 430 SS were the other alloys used in the study for comparison purpose. 316L SS, 304 SS and 430 SS alloys were acquired from Salem Steel Plant, Tamil Nadu. The Al 6063 alloy was obtained from General Motors, USA. The chemical compositions of these alloys are provided in Table 7a and b.

Table 7a Chemical compositions of 304 SS, 430 SS and 316L SS alloys.

Coil no	Grade	% C	% Si	% Mn	% P	% S	% Cr	% Ni	% N	% Mo	% Co	% Cu	% Ti	% Al
81072	304	0.039	0.46	1.34	0.025	0.006	18.17	8.55	0.022	-	-	-	-	-
54921	430	0.047	0.19	0.29	0.026	0.003	16.15	0.22	0.047	-	-	-	-	-
76806B	316L	0.020	0.23	1.68	0.025	0.002	17.64	11.13	-	2.58	-	-	-	-
-	Mild Steel	0.062	0.005	0.185	0.006	0.012	0.042	0.02	-	0.005	0.004	0.024	0.0007	0.032

Table 7b Chemical composition of Al 6063 alloy.

Element	Wt %
Mg	0.45 - 0.9
Si	0.20 - 0.6
Fe	<= 0.35
Ti	<= 0.10
Zn	<= 0.10
Cr	<= 0.10
Mn	<= 0.10
Cu	<= 0.10
Other Elem	<= 0.05
Total Other	<= 0.15

3.2 Material characterization.

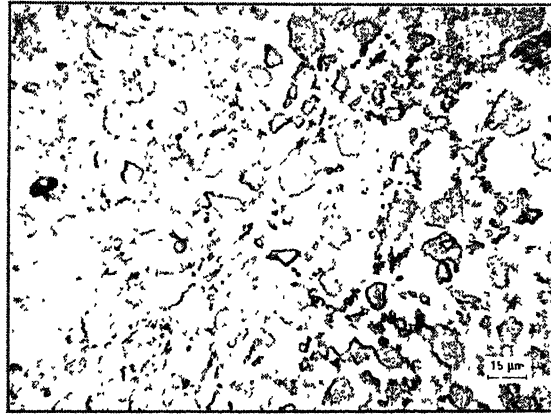
3.2.1 Optical microscopy.

Standard metallographic techniques were used for preparation of the samples: sectioning, mounting, grinding and polishing. Rectangular specimens were cut from the as received alloy samples by using a abrasive cutter (Buehler, Germany).

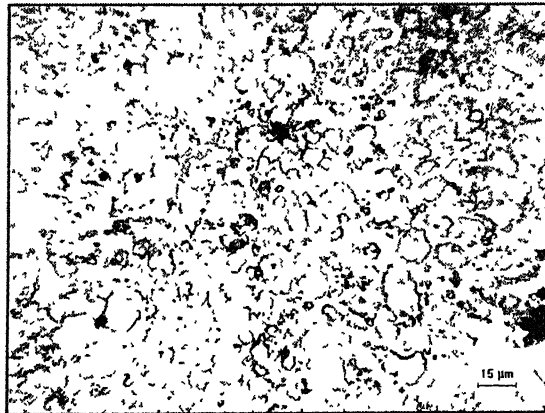
All the surfaces of the specimens, were mechanically polished in fine cloth using 0.5 μ alumina powder and then degreased using acetone before being used for each electrochemical experiment. In order to understand the microstructure the specimens were hot mounted. Care was taken while mounting to maintain the flatness of the sample and the mount. Grinding of the sample was performed in a series of emery papers starting from coarse grit to fine grit. The sample was ground carefully to avoid higher relief of the softer matrix than the hard carbides. Polishing was performed by using 0.5 μ m alumina powder. For revealing the microstructures, an etchant of composition (volumetric) 33% acetic acid (CH_3COOH), 33% nitric acid (HNO_3), 33%water (H_2O) and 1% hydrofluoric acid (HF) was used. Optimum etching time was determined as 5 seconds after several trials.

The microstructures were recorded using an optical microscope (Axiolab A, Zeiss, Germany), attached with a digital camera (CE, Japan). They were later analyzed by the image-analysis program (Image-Pro Plus, version 4.1, Media Cybernetics, USA). The microstructures of the all the three carbon-alloyed iron aluminides are shown in Fig. 52, 53 and 54.

(a)



(b)



(c)

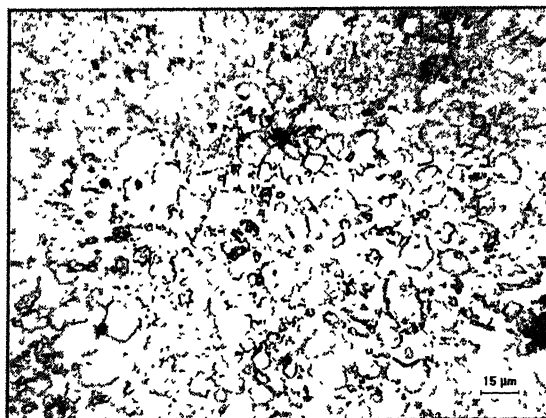
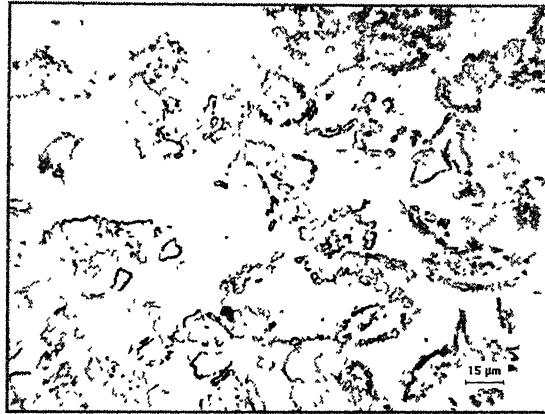
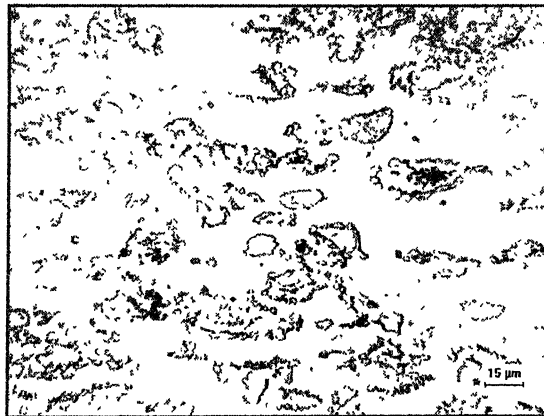


Fig. 52 Optical microstructure of Fe-18.5Al-3.6C alloy in (a) rolling plane (b) long transverse (c) short transverse direction.

(a)



(b)



(c)

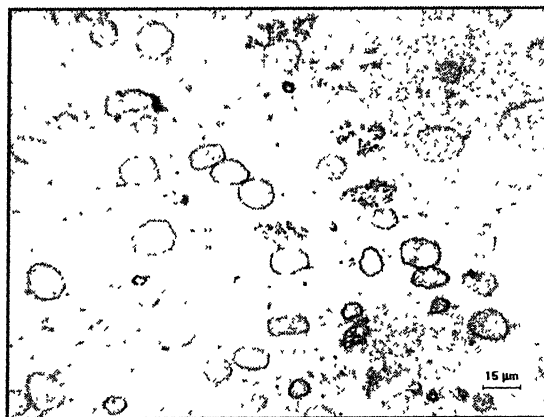
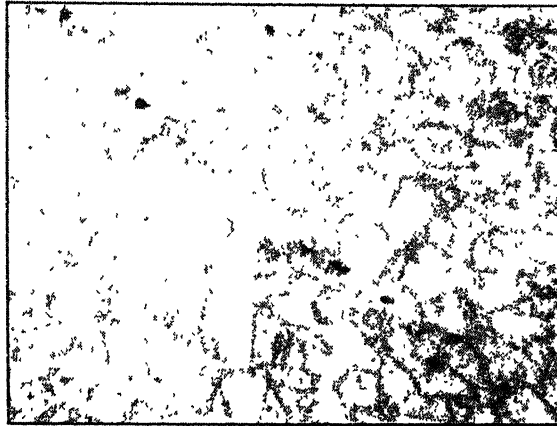
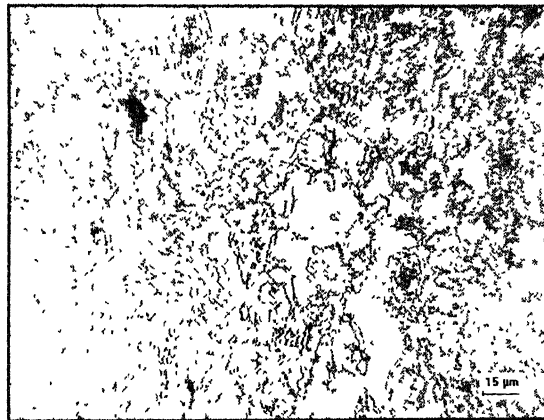


Fig. 53 Optical microstructure of Fe-20.0Al-2.0C alloy in (a) rolling plane (b) long transverse (c) short transverse direction.

(a)



(b)



(c)

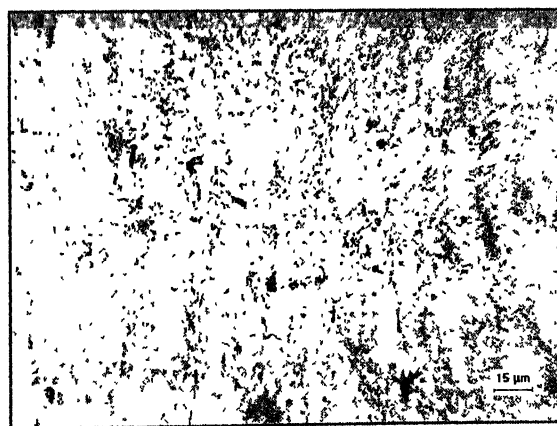


Fig. 54 Optical microstructure of Fe-19.2Al-3.3C-0.07Ce alloy in (a) rolling plane (b) long transverse (c) short transverse direction.

3.2.2 Scanning electron microscopy.

Scanning electron micrographs were obtained for all the samples (rolling direction) in a scanning electron microscope (SEM) (JEOL JSM 840A). In order to take the SEM micrographs the specimens were hot mounted. Care was taken while mounting to maintain the flatness of the sample and the mount. Grinding of the sample was performed in a series of emery papers starting from coarse grit to fine grit. The sample was ground carefully to avoid higher relief of the softer matrix than the hard carbides. The samples were finely polished up to 0.5-micrometer finish using Al_2O_3 powder and then were etched prior to the SEM observations. The composition of the etchant used, was (volumetric) 33% acetic acid (CH_3COOH), 33% nitric acid (HNO_3), 33% water (H_2O) and 1% hydrofluoric acid (HF) was used. The samples were over etched slightly in order to obtain better contrast for SEM observations. SEM micrographs of Esr137 and Es127 were also taken, after immersing these samples of these carbon-alloyed iron aluminides in 0.25 mol/lit H_2SO_4 solution for a period of 24 hours. The surface of the samples was cleaned by ultrasonic cleaning for a period of 15 minutes and then the surface was cleaned with acetone.

3.3 Electrochemical studies

3.3.1 Apparatus for polarization studies, cyclic voltammetry and electrochemical impedance spectroscopy.

The main apparatus used for the electrochemical experiments were a polarization cell and a potentiostat interfaced to a personal computer. Two potentiostats were used in the present study and their models were Perkin Elmer potentiostat, Model 263A and Parstat 2263. The potentiostats used in the study were capable of performing electrochemical impedance spectroscopy and a wide variety of potentiodynamic and galvanostatic functions required for basic and applied studies in the field of corrosion. The schematic of a potentiostat connected with the electrochemical cell is shown in Fig. 55. The potentiostat consists of an ammeter, an electrometer and a power supply. Three probes

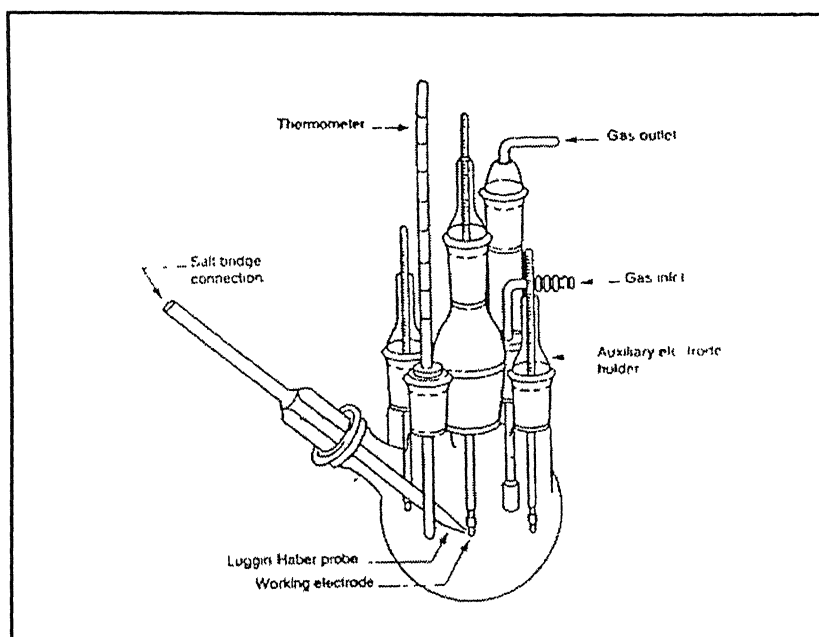


Fig. 55 Electrochemical polarisation round bottom cell used for conducting polarisation studies

from the potentiostat were connected to the working electrode, reference electrode and counter electrode. The fourth probe was grounded.

Electrochemical polarization studies were conducted using a Perkin Elmer potentiostat (Model 263A). Its ± 20 V compliance and ± 200 mA (± 2 A with 94 Option) output capabilities allowed rapid and accurate potential or current control in the electrochemical cell. The polarization experiments for all the samples were conducted in a round-bottom polarization cell. All the experiments were conducted at a scan rate of 1 mV/sec. The schematic representations of the round bottom cell are shown in Fig. 56. A round bottom cell is a flask with a round bottom and has provisions in the form of various necks on the top to permit the introduction of electrodes, gas inlet and outlet tubes, and a thermometer. Standard calomel electrode (SCE) in saturated KCl was used as the reference electrode and the counter electrode was a high purity graphite rod. The potential of the reference electrode was + 0.242 V with respect to standard hydrogen electrode (SHE).

Electrochemical impedance spectroscopy (EIS) and cyclic voltammetry experiments were conducted using a potentiostat (Model Parstat 2263), supplied by EG&G Instruments Inc, Princeton Applied research USA. The EIS experiments were controlled using a computer and the data were collected using PowerSuite- 2.35.2 Software and analysed by ZsimpWin Version 3.00 Software. EIS experiments were carried out in a specifically designed electrochemical cell. This cell was used Standard calomel electrode (SCE) in saturated KCl was used as the reference electrode and the counter electrode was a high purity graphite rod. The potential of the reference electrode was +242 mV with respect to standard hydrogen electrode (SHE). This cell consists of a cylindrical flask with a cover on top, which had provisions in the form of circular openings of different sizes to permit the introduction of various electrodes. The distance between the openings was maintained in such a way that a very small gap was obtained on putting the different electrodes through these openings. The schematic representations of the cell are shown in Fig 57. Cyclic voltammetry experiments were conducted in a round bottom polarization cell (Fig.56).

The samples used as working electrode in the cell were cold mounted. Cold mounting was done using a resin powder and an organic solvent. An electrical wire was

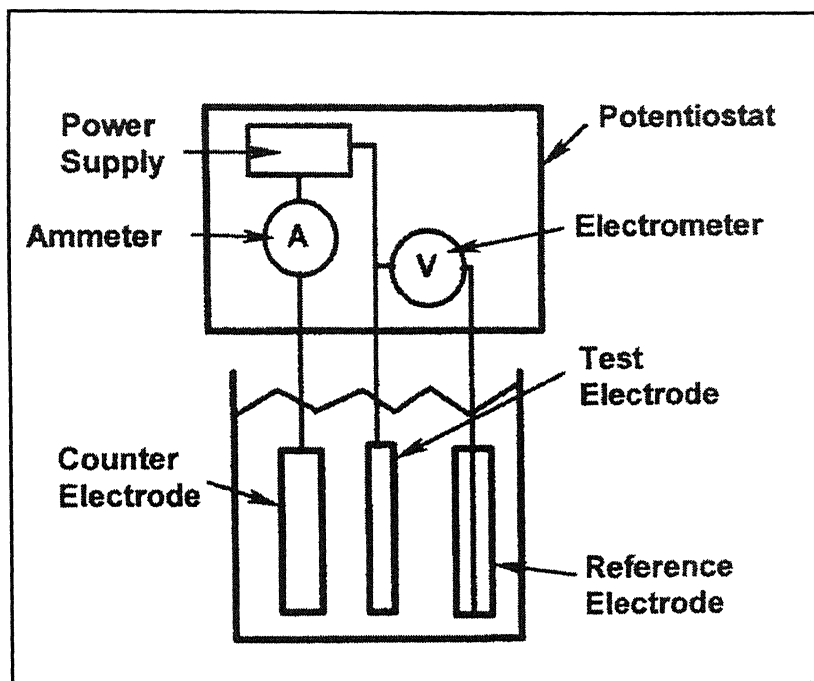


Fig. 56 Schematic diagram showing the connections in the potentiostat

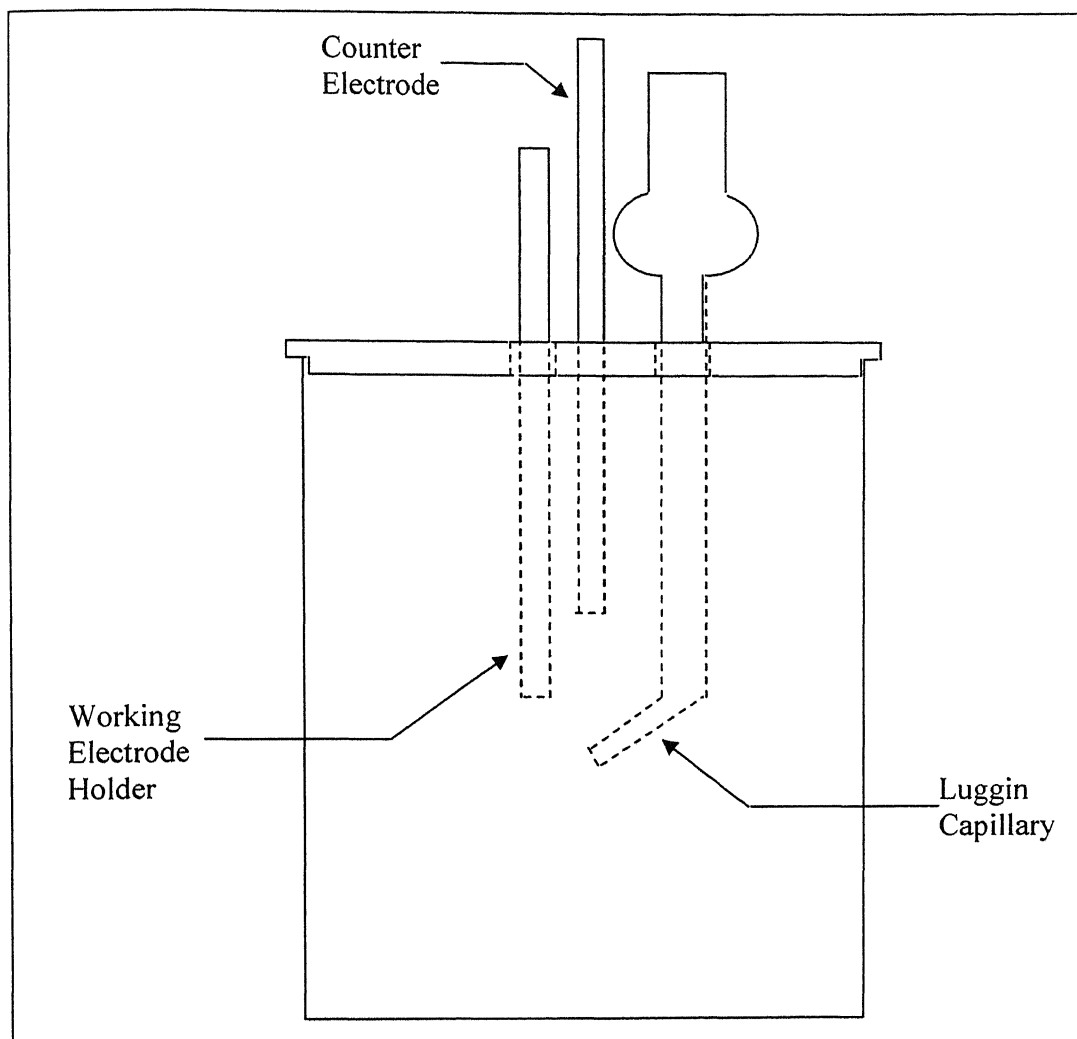


Fig. 57 Electrochemical cell used for conducting long term electrochemical impedance spectroscopy (EIS) experiments.

soldered before the mounting to the sample in order to provide electrical contact with the sample. The sample with the attached wire was cold mounted to expose only the material surface. An exposed area of 1 cm² was maintained for all the samples. Rolling direction (RD section) of the samples was addressed in all the electrochemical studies. In the case of Fe-19.2Al-3.3C-0.07Ce (ESR137), short transverse (ST) and long transverse (LT) sections were also addressed. The Luggin probe connected with KCl salt bridge separated the bulk solution from the saturated calomel reference electrode (SCE). The probe tip could be easily adjusted to bring in close proximity with the working electrode (both in the round bottom cell and the special cell used for EIS experiments).

The three electrodes used are the working electrode (mounted specimen connected with a wire), the counter electrode (high purity graphite rod) and the reference electrode. (A saturated calomel electrode with $E^0 = + 0.242$ V vs. standard hydrogen electrode), as per the ASTM recommendations [102]. The potential of the calomel electrode was checked at periodic intervals to ensure the accuracy of the potential of the electrode.

3.3.2 Electrolytes

The following electrolytes were used in the present study to evaluate the corrosion behavior of carbon-alloyed iron aluminides and the other alloys.

- (a) 0.25 mol/lit H_2SO_4 of pH 0.74
- (b) Borate buffered solution ($1.5\text{N } \text{H}_3\text{BO}_3 + 0.1\text{N } \text{Na}_2\text{B}_4\text{O}_7 \cdot 10\text{H}_2\text{O} + 0.01\text{N } \text{KNO}_3$) of pH 7.6

0.25 mol/lit H_2SO_4 solution of pH 0.74, was prepared by adding 13.3 ml of 99% pure concentrated sulphuric acid (with density of 1.835 g/ml) in 986.7 ml of distilled water. Borate buffered solution was prepared by adding 19.069g borax ($\text{Na}_2\text{B}_4\text{O}_7 \cdot 10\text{H}_2\text{O}$), 30.915g boric acid (H_3BO_3) and 1.01g potassium nitrate (KNO_3) into 1000 ml of distilled water. The solutions were thoroughly stirred before using in the experiment pH of the solution was monitored using a pH meter (EcoScan pH 5/6). Although ASTM recommends 40 ml of test solution to every 1 cm^2 area of the test surface [102], it is also recommended to keep the ratio of the solution volume to specimen surface area high in order to avoid any appreciable change in the corrosivity of the solution during the test, especially since the solution would not be recirculated [102]. Only test solutions that were freshly prepared were used for each experiment in order to minimize contamination of the electrolyte. Additional care was taken to stir the solution thoroughly before starting each test. The temperature of the electrolytes was not controlled. Moreover, the variation in temperature ($20^\circ - 25^\circ \text{C}$) was minimum during the period in which the experiments were carried out. All the experiments were conducted in freely (naturally) aerated solution.

3.3.3 Test procedure for electrochemical studies

Before each experiment, the working electrode was ground with 4/0 emery paper. After this surface finishing operation, the samples were degreased in methanol. The electrolyte solution (500 ml) was transferred to the electrochemical cell. The electrodes were immersed in the electrolyte and secured in a place using a retort stand. Precaution

suitable for the reliable measurement of equilibrium electrochemical characteristics for these alloys. Generally, the total duration of each test was around 45 minutes. The data was processed by the computer and stored digitally. The specimen area for all the samples was taken into account during the processing of data.

3.3.6 Electrochemical impedance spectroscopy

Electrochemical impedance spectroscopy (EIS) measurements were performed by applying a sinusoidal potential perturbation of 10 mV at the open circuit potentials. The impedance spectra were measured with frequency sweep from 100 kHz to 10 mHz in logarithmic increment. A total number of 36 points was recorded for each experiment. Generally, the total duration of the experiment was around 10 minutes. EIS experiments were started after stabilization of free corrosion potential for all the specimens. After completing the EIS experiment on first immersion, the electrochemical cell was disconnected from the potentiostat and the counter and the reference electrodes were removed. However, the specimen was allowed to remain immersed in the solution. Reference electrode was kept in saturated KCl solution. The EIS experiment was repeated after 24 hours in case of EIS study in acidic solution and after 168 hours in case of EIS study in borate buffered solution. The reference and the counter electrodes were put back into the solution through the respective openings provided for these electrodes in the cell. Each time the free corrosion potential was also measured prior to EIS experiment.

3.3.7 Cyclic voltammetry experiments

Cyclic voltammetry (CV) experiments were performed in freely aerated 0.25 mol/lit H_2SO_4 solution, by applying a potential waveform shown in the Fig. 58. CV experiments were carried out at the scan rates of 10, 50 and 100 mV/sec. The range of potential for cyclic voltammetry experiments was -0.75 V to +0.5 V vs. SCE. Initial sweep direction was from negative to positive potential. Moreover, CV experiments were

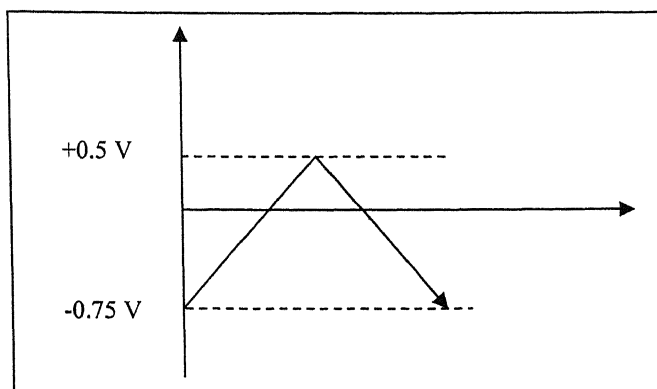


Fig. 58 Potential waveform applied in cyclic voltammetry, showing the initial potential and the final potential.

carried out immediately after immersing the samples into the solution without the stabilization of free corrosion potential. This prevented the formation of a surface film before the experiment was started.

CHAPTER 4

RESULTS AND DISCUSSION

The results of electrochemical polarization studies, electrochemical impedance spectroscopy and cyclic voltammetry conducted on carbon-alloyed iron aluminides with and without Ce addition will be presented in this chapter. The results for Al 6063, 304 SS, 316L SS and 430 SS alloys will also be presented for comparison purpose. The aim of the study was to understand the effect of Ce on the electrochemical behavior of the carbon-alloyed iron aluminides.

4.1 Free corrosion potential

The nature of stabilization of the free corrosion potential (FCP) provides information about the nature of the film that forms on the surface of materials under free corrosion conditions [103]. If the FCP moves from an active to noble potential during stabilization (i.e. in the positive direction), it suggests thickening of surface film under free corrosion conditions and equilibrium FCP is attained when the dissolution rate equals the growth rate of the film. In case the FCP moves from noble to active potential during stabilization (i.e. in the negative direction), it suggests thinning of surface film under free corrosion conditions and the equilibrium potential is attained when the growth rate equals the film dissolution rate. The film formed on the material when the FCP stabilized at noble potential indicates that the film may be more protective. Further, in case the FCP stabilizes immediately upon immersion, it implies that the equilibrium conditions are attained relatively fast. The stabilization of FCP in the borate buffered solution and 0.25 M H_2SO_4 solution will be addressed below.

4.1.1 Borate buffered solution

The variations of the free corrosion potentials with time in the borate buffered solution, of pH= 7.6, of carbon-alloyed intermetallics Fe-20.0Al-2.0C, Fe-19.2Al-3.3C-0.07Ce and Fe-18.5Al-3.6C immediately on immersion in the electrolyte are presented in

Fig. 59a. The FCP of the intermetallics stabilized in the range of -210 mV to -253 mV vs. SCE on immersion. The stable FCP values have been tabulated in Table 8. It can be observed from the data presented in Table 8 that the stabilized value of the FCP decreased in the order: Fe-18.5Al-3.6C > Fe-20.0Al-2.0C > Fe-19.2Al-3.3C-0.07Ce. The nature of the stabilization curves was similar for all the cases. The potentials moved from active to noble direction on stabilization, indicating the growth of some surface film. The time for stabilization was around 6000 seconds for Fe-18.5Al-3.6C, 8000 seconds for Fe-19.2Al-3.3C-0.07Ce and 10000 seconds for Fe-20.0Al-2.0C. After stabilization of FCP, the samples were allowed to remain immersed in the solution to analyse the effect of time on the corrosion behaviour of intermetallics. The FCP was again measured after a total immersion time of 168 hours.

Fig. 59b shows the time variation of the free corrosion potentials for the three carbon-alloyed intermetallics after 168 hours of immersion in borate buffered solution. After 168 hours of immersion, the FCP of the intermetallics stabilized in the range of -84 mV to -45 mV vs. SCE. The stable FCP values have been also tabulated in Table 8. Data presented in Table 8 shows that the stabilized values of the free corrosion potential after 168 hours of immersion decreased in the order: Fe-20.0Al-2.0C > Fe-19.2Al-3.3C-0.07Ce > Fe-18.5Al-3.6C. This is different from that observed immediately on immersion. However, the order of alloys as regards the stabilization potential may not be important because all of them stabilized within a relatively narrow range of potential. It must, however, be noted that FCP shifted towards the noble direction for *all* the three intermetallics after long term immersion. The shifts in FCP with time have been indicated in the last column of Table 8. The magnitude of shift in FCP was maximum for Fe-19.2Al-3.3C-0.07Ce amongst the three intermetallics and minimum for Fe-18.5Al-3.6C (Table 8). The shifts are of the same order of magnitude and not drastically different for the three alloys. The shift of FCP in the noble direction may be attributed to the thickening of the surface film. Moreover, the higher magnitude of shift in FCP in the case of Ce-alloyed iron aluminide may be indicative of a thicker surface film on it. Since the composition of Fe-19.2Al-3.3C-0.07Ce is not much different from that of Fe-18.5Al-3.6C, it can be concluded that Ce may aid thickening of the surface film.

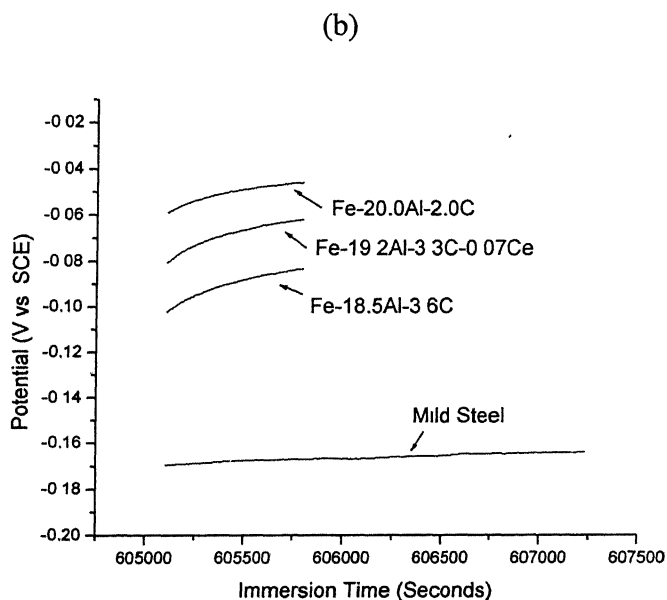
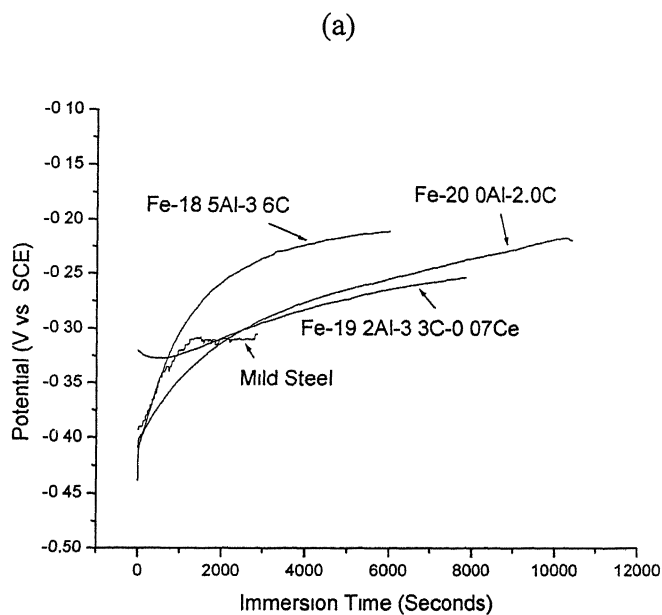


Fig. 59 Variation in free corrosion potential as a function of time for Fe-20.0Al-2.0C (ESR 74), Fe-18.5Al-3.6C (ESR 127), Fe-19.2Al-3.3C-0.07Ce (ESR 137) alloys and 0.05 %C mild steel in borate buffered solution (a) immediately after immersion (b) after 168 hours of immersion.

In order to make a comparative study, the data for free corrosion potential stabilization of 0.05%C mild steel are presented in Fig.59a and b, while that for Al 6063 alloy and 316L stainless steel are provided in Fig. 60a and b. The data have been obtained in the same borate buffered solution and the stable FCP values have been presented in Table 8. Time variation of FCP immediately after immersion for 0.05% C mild steel (Fig. 59a) indicates that the FCP for mild steel also moves from active to noble direction with time. The time for stabilization immediately on immersion was around 3000 seconds. Time variation of FCP after 168 hours of immersion for mild steel is shown in Fig. 59b. It can be noted that after immersion for 168 hours the FCP shifted towards noble direction by nearly 146 mV. Moreover, it can also be noted from Fig. 59a and b that the FCP of mild steel was lower than that of the carbon-alloyed intermetallics, both immediately on immersion and after 168 hours of immersion. In fact, the difference between mild steel and the carbon-alloyed iron aluminides was enhanced after 168 hours (Table 8). This could imply a thicker and more stable surface film on the carbon-alloyed iron aluminide as compared to that on low carbon mild steel. Cristofaro et. al. [104], studied the passivity and passivity breakdown of a β -FeAl-based iron aluminide containing 24 wt% Al in borate buffer solution (pH 8.4) containing sulphates, chlorides and mixtures of both using potentiodynamic techniques complemented with SEM analysis. They found that, while iron suffers from pitting in sulphate-borate solutions, this phenomenon was not observed on FeAl aluminides. Hence, it was concluded that the addition of aluminium to iron enabled the formation of a passivating layer. It was also noted that the voltammetric response of iron aluminide in the borate solution showed the peak characteristic of iron oxidation/reduction processes. Sulphate addition to the buffer solution modified the voltammetric profile and made the passive film more stable. It was proposed that a mixed iron (II)-(III) oxide film was responsible for passivation of FeAl aluminide in sulphate-borate solution in contrast to a rich iron (III) oxide film forming in absence of sulphate. Therefore, it is reasonable to attribute the improved surface properties of carbon-alloyed iron aluminides to the presence of aluminium in them.

Fig. 60a shows the variation of FCP with time immediately on immersion for Al 6063 and 316L SS alloys. Evidently, FCP moved from active to noble direction with time for both the alloys. The time for stabilization was 6000 seconds for Al 6063 and 9000

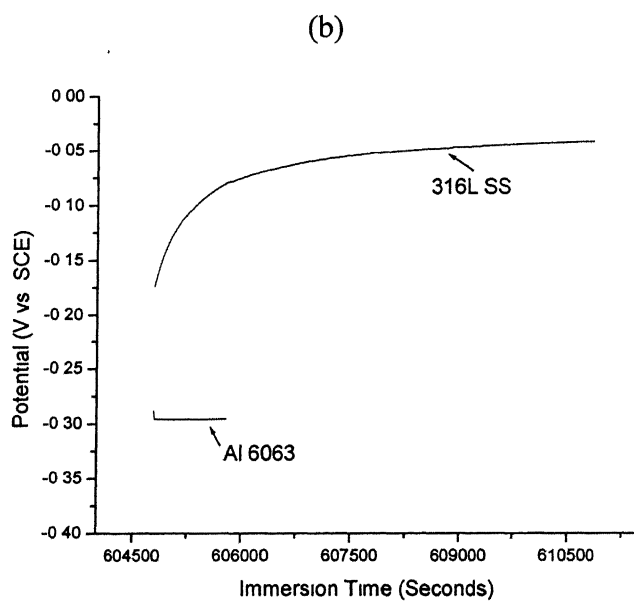
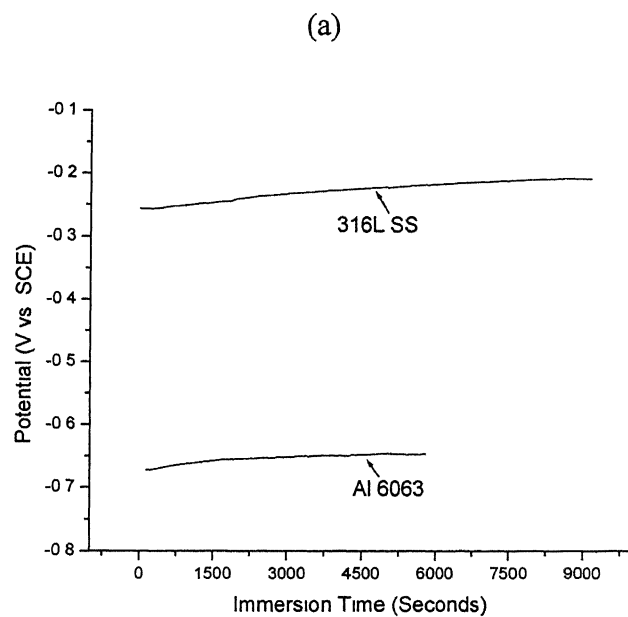


Fig. 60 Variation in free corrosion potential as a function of time for 316L SS and Al 6063 alloys in borate buffered solution (a) immediately after immersion (b) after 168 hours of immersion.

seconds for 316L SS. The time variation of FCP after 168 hours of immersion is shown in Fig. 60b. It can be noted that for these two alloys, as well, the FCP shifted toward the noble direction after 168 hours of immersion. The magnitude of shift in the noble direction was higher for Al 6063 alloy as compared to that of 316L SS. (Table 8). In fact, the shift in FCP was much more drastic in the case of the Al alloy compared to the other iron based alloys. It has been reported earlier by Rehim et. al. [79] that the corrosion rate of Al is lowest in the pH range of 4.8 to 8.8. In this pH range Al and its alloys are covered with protective oxide film. This conclusion can also be easily drawn from the pourbaix diagram for Al-H₂O system [107]. Therefore, the drastic shift in the FCP in the noble direction, in the case of Al alloy, can be attributed to the thickening of the protective oxide film formed on the surface [92].

It can also be observed from Table 8 that, as compared to the low carbon mild steel, the FCP of 316L SS stabilized at higher (i.e. positive) potentials both on first immersion and after 168 hours of immersion. Moreover, the shift in potential after 168 hours of immersion in case of 316L SS was higher than that of the mild steel. This is suggestive of superior surface film properties in the case of 316L SS, than that of low carbon mild steel. A higher shift in potential towards positive direction for 316L SS also suggests the increase thickness of the surface film [92]. It has earlier been reported by Oblonsky et. al. [105] that in borate buffered solution, the passive film on 308 stainless steel (composition 20% Cr, 12% Ni, 0.06% C, 0.5% Mn, >5 % Si, 0.03% S+P, balance Fe) which contains Ni and Cr as major alloying elements, is composed of amorphous Fe(OH)₂ and Fe₃O₄, Ni(OH)₂, NiO, Cr(OH)₃ and the Cr(OH)₂ -like species. Montemor et. al. [106] used auger analysis, capacitance measurements and photoelectrochemical measurements techniques in order to study the oxide films formed on 316L stainless steel (Cr: 17.5%, Ni: 12.3%, Mn: 1.84%, Si: 0.44%, P: 0.021%, S: 0.001%, Mo: 2.47%, Fe: Bal) borate buffer solution. It was revealed from their study that iron-nickel oxide and chromium oxide were present in the outer and the inner parts of the film in the case of 316L stainless steel. Therefore, the improved surface film properties of 316L SS as against low carbon mild steel can be attributed to the presence of Ni and Cr in 316L SS.

From Table 8, it can also be noted that the FCP of 316L SS is only slightly higher than that of the carbon-alloyed iron aluminides. As discussed earlier, relatively good

surface film properties of carbon-alloyed iron aluminides can be attributed to the presence of Al in carbon-alloyed iron aluminides.

4.1.2 Acidic solution

Fig. 61a shows the variation of the free corrosion potentials (FCP) as a function of time in the acidic solution of 0.25 mol/lit H_2SO_4 for carbon-alloyed intermetallics Fe-20.0Al-2.0C, Fe-19.2Al-3.3C-0.07Ce and Fe-18.5Al-3.6C immediately on immersion. The FCP of the intermetallics stabilized in the range of -527 mV to -505 mV vs. SCE on immersion. The stabilized FCP data have been tabulated in Table 9. The time for FCP stabilization was around 4000 seconds for Fe-19.2Al-3.3C-0.07Ce and Fe-18.5Al-3.6C. For Fe-20.0Al-2.0C, FCP stabilized after 5000 seconds. The nature of the stabilization curves was similar for Fe-18.5Al-3.6C and Fe-20.0Al-2.0C. The potentials moved from active to noble direction on stabilization. However, the nature of the stabilization curve for the Ce-alloyed intermetallic Fe-19.2Al-3.3C-0.07Ce was slightly different.

An interesting trend was noticed in the case of Ce-alloyed intermetallic (Fe-19.2Al-3.3C-0.07Ce) when compared to the non Ce-alloyed intermetallics. Although the FCP stabilisation curve appears flat in Fig. 61a, on magnifying the scale of the potential axis, a consistent trend in the FCP variation was observed for the Ce-alloyed iron aluminide. This is shown in Fig. 62a (to be discussed later). The general trend seen was that the potential initially moved from noble to active potential, then eventually shifted to a noble potential. Interestingly this behaviour was noticed in all the sections i.e. RD, LT and ST (Fig. 62a). Similar behaviour of stabilization of free corrosion potential for Ce-alloyed (all sections) and non Ce-alloyed iron aluminides was earlier observed by Sriram [48]. It can be noted from Table 8 and 2 that the stabilized values of FCP in 0.25 mol/lit H_2SO_4 solution are much lower than that in borate buffered solution. This indicates that the alloys are more active in acidic solution than in borate buffered solution.

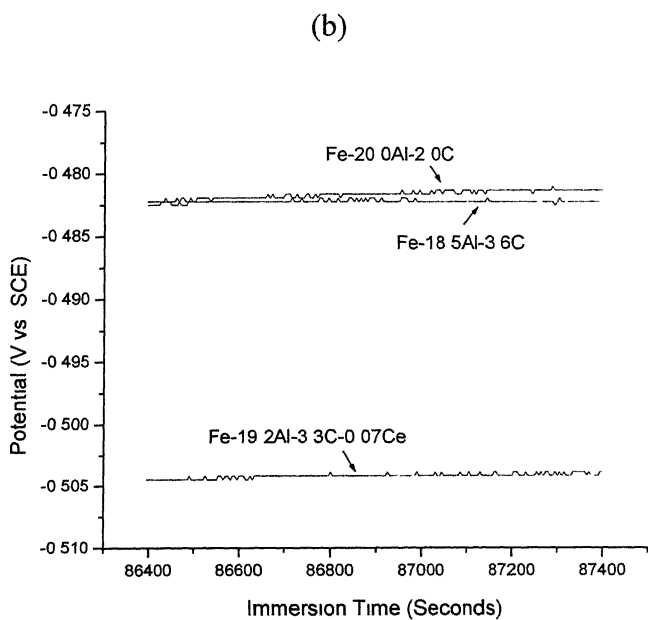
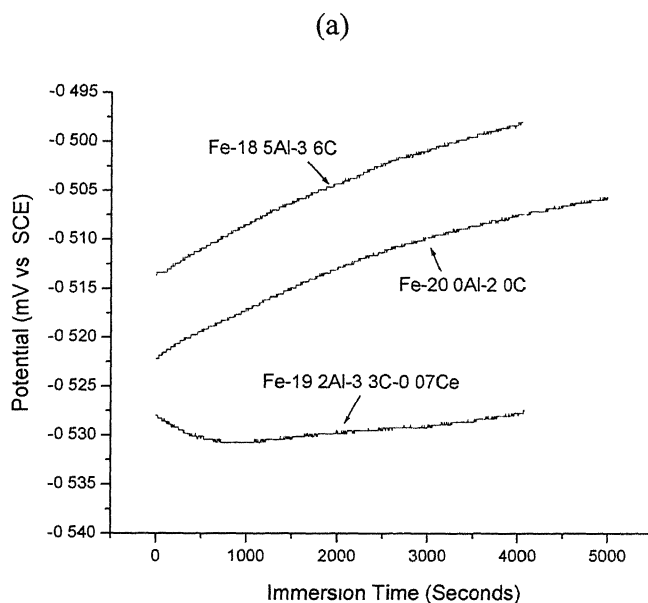


Fig. 61 Variation in free corrosion potential as a function of time for Fe-20.0Al-2.0C, Fe-18.5Al-3.6C and Fe-19.2Al-3.3C-0.07Ce alloys in freely-aerated 0.25 mol/lit H_2SO_4 solution (a) immediately after immersion (b) after 24 hours of immersion.

Fig. 61b shows the variation of the free corrosion potentials with time for the three carbon-alloyed intermetallics after 24 hours of immersion time in 0.25 mol/lit H_2SO_4 . Longer immersion times were avoided because it was observed that the alloys corroded more rapidly in the sulphuric acid solution compared to the borate buffered solution [48]. After 24 hours of immersion, the FCP of the intermetallics stabilized in relatively narrow range of -481 mV to -504 mV vs. SCE. It can be noted that, both immediately after immersion and after 168 hours of immersion, the stabilized value of FCP was lowest in the case of Fe-19.2Al-3.3C-0.07Ce. Table 9 indicates that FCP shifted only marginally towards noble direction for all the three intermetallics. Moreover, the magnitude of shift was nearly same for Fe-19.2Al-3.3C-0.07Ce and Fe-20.0Al-2.0C. For Fe-18.5Al-3.6C, the magnitude of the shift was slightly lower than the other two intermetallics.

Fig. 62 shows the variation of FCP with time for the rolling direction (RD), long transverse (LT) and short transverse (ST) sections of Fe-19.2Al-3.3C-0.07Ce. Immediately after immersion, the FCP for these sections showed a similar trend in that the FCP moved from noble to active direction. Then, after some time, it shifted towards the noble direction. Immediately after immersion, the FCP stabilized at -537 mV vs. SCE for ST section and at -523 mV vs. SCE for LT section (Table 9). After immersion for 24 hours, the FCP for both LT and ST sections shifted slightly towards noble direction. The magnitude of shift was almost similar for all the sections.

It can be noted that the stabilized value of FCP, in the acidic solution are lower than in borate buffered solution for all the three carbon-alloyed iron aluminides and low carbon mild steel (refer Table 8 and 2). This can be attributed to the aggressive corrosive nature of 0.25 mol/lit H_2SO_4 solution. Similarly, for Al 6063, the FCP stabilized towards more active potentials in 0.25 mol/lit H_2SO_4 solution than in borate buffered solution. It has been reported earlier by Rehim et. al. [79] that the corrosion rate of Al is lowest in the pH range of 4.8 to 8.8. In this pH range Al and its alloys are covered with protective oxide film. However, in acidic media of low pH, Al dissolves as a simple salt in conjunction with hydrogen depolarization reaction [87]. Therefore, the lower FCP values of Al 6063 alloy in 0.25 mol/lit H_2SO_4 solution compared to that in borate buffered solution can be attributed to its active dissolution in acidic solution as against

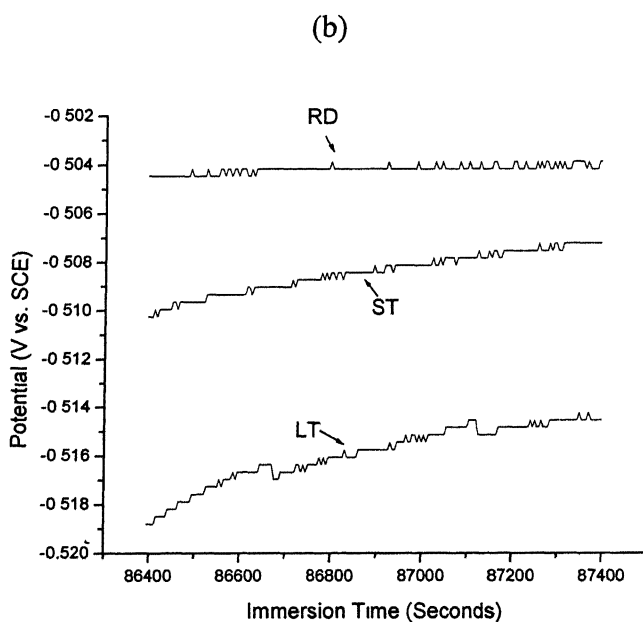
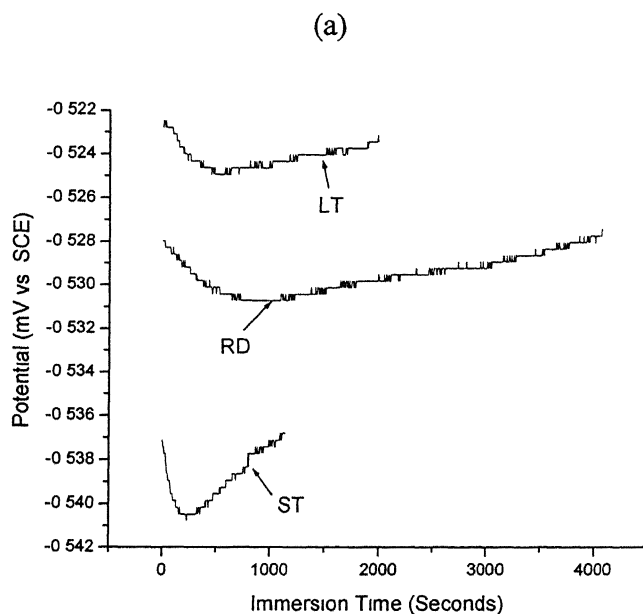


Fig. 62 Variation in free corrosion potential as a function of time of Fe-19.2Al-3.3C-0.07Ce for the rolling plane (RD), long transverse plane (LT), and short transverse planes (ST) in freely aerated 0.25 mol/lit H_2SO_4 solution (a) immediately after immersion (b) after 24 hours of immersion.

the formation of protective oxide film in borate buffered solution, of pH= 7.6. The stabilized value of FCP in case of 316L SS, on first immersion, was higher in 0.25 mol/lit H_2SO_4 solution than that in borate buffered solution.

For comparison purpose, the FCP data for 0.05 % C mild steel, 316L SS, 304 SS and 430 SS alloys have also been obtained in the acidic solution. Fig. 63a shows the variation of free corrosion potential with time for the above alloys immediately after immersion in 0.25 mol/lit H_2SO_4 solution. The FCP of carbon-alloyed iron aluminides, low carbon mild steel, and 430 SS stabilized in a narrow range of -545 mV to -495 mV vs. SCE, while, the FCP of 316L SS and 304 SS stabilized in the range of -170 mV to -39 mV vs. SCE. However, the stabilized value of FCP in the case of Al 6063 was -744 mV vs. SCE, which is much lower than that of the other alloys (Table 9). Moreover, it can be observed from the data of Table 9 that the stabilized value of the free corrosion potential decreased in the order: 304 SS > 316L SS > 0.05% C mild steel > 430 SS > Al 6063 immediately on immersion. This clearly indicates that the stabilized FCP value of iron based alloys is higher than that of Al 6063. The nature of the stabilization curves was different for all the alloys. In case of 316L SS, the FCP initially moved from active to noble direction and then eventually shifted towards active direction. In the case of 304 SS and 430 SS the potential moved smoothly from active to noble direction, while, in the case of Al 6063 alloy, the potential moved from noble to active direction. The time for stabilization of FCP for mild steel and 430 SS was 1000 seconds and for 316L SS it was around 4000 seconds. In the case of 304 SS, FCP stabilized after nearly 3000 seconds. FCP of Al 6063 alloy stabilized after 6000 seconds.

Fig. 63b shows the time variation of the free corrosion potentials for the above mentioned alloys after 24 hours of immersion in 0.25 mol/lit H_2SO_4 solution. It can be noted that, after 24 hours of immersion, the FCP of these alloys stabilize in the range of -662 mV to -100 mV vs. SCE. From Table 9, it can be observed that the stabilized values of the free corrosion potential decrease in the order: 316L SS > 304 SS > 430 SS > 0.05% C mild steel > Al 6063. The nature of the stabilization curves was similar for 304 SS, mild steel and 430 SS. For all these alloys, the potential stabilized uniformly without any oscillations. It can be noted from the data presented in Table 9 that after immersion for 24 hours, the potential shifted towards positive direction in the case of 430 SS, Al 6063 and

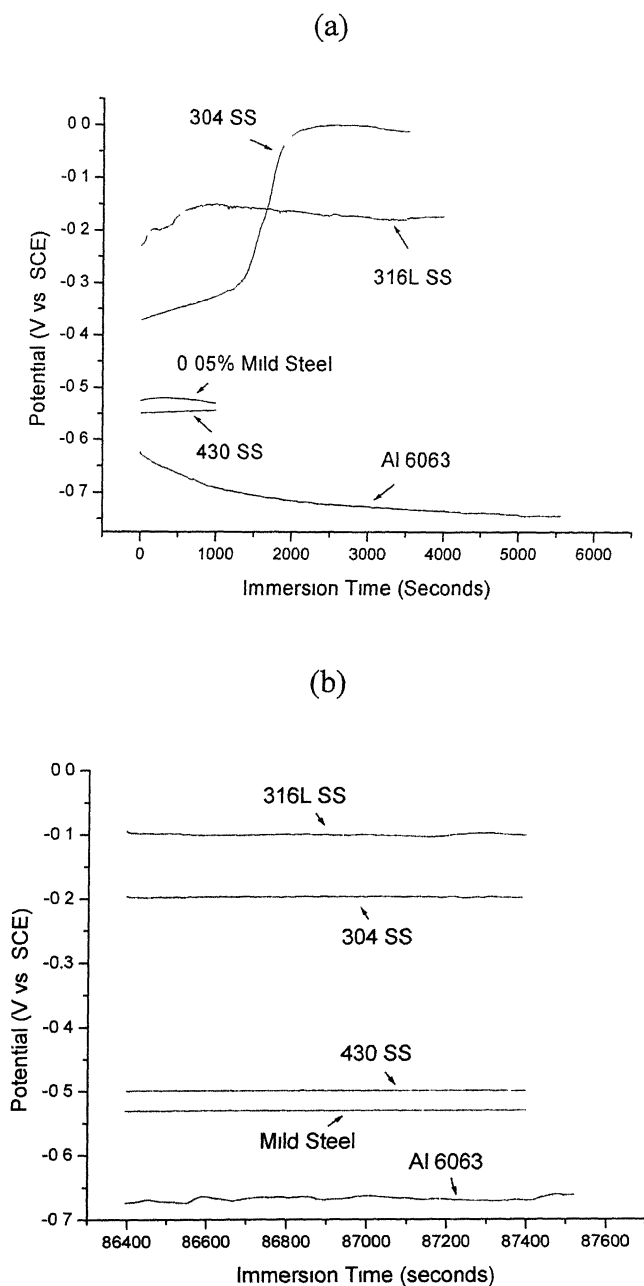


Fig. 63 Variation in free corrosion potential as a function of time for 0.05 % C mild steel, 304 SS, 430 SS, 316L SS and Al 6063 in freely-aerated 0.25 mol/lit H_2SO_4 solution (a) immediately after immersion (b) after 24 hours of immersion.

316L SS, whereas for 304 SS, the shift in potential after 24 hours, was in the negative direction. The magnitude of shift in potential for mild steel was negligible compared to that for the other alloys.

Overall, the FCP of all the iron based alloys (i.e. carbon-alloyed iron aluminides, low carbon mild steel, 430 SS, 316L SS and 304 SS) moved from active to noble direction, whereas in case of aluminium based Al 6063 alloy, the FCP moved in the reverse direction (i.e. from noble towards active direction) (Table 9). Such behaviour was observed both on first immersion and after 24 hours of immersion in 0.25 mol/lit H_2SO_4 solution. This can be attributed to the active dissolution of aluminium in acidic solutions of low pH, as indicated by the Pourbaix diagram [79 and 107]. As mentioned earlier, the FCP of carbon-alloyed iron aluminides, low carbon mild steel, and 430 SS stabilized in a narrow range of -545 mV to -495 mV vs. SCE. This indicates that the nature of surface film on these alloys is generally comparable. Compared to the carbon-alloyed iron aluminides, low carbon mild steel and 430 SS, the stabilized values of FCP for 304 SS and 316L SS were more towards noble direction, both on first immersion and after 168 hours of immersion in 0.25 mol/lit H_2SO_4 solution. This is indicative of better surface film properties in the case of 304 SS and 316L SS than the other alloys mentioned above. Better surface film properties of 316L SS and 304 SS can be attributed to the presence of Ni and Cr in these alloys.

After 24 hours of immersion in 0.25 mol/lit H_2SO_4 solution, it is noted that the stabilized values of the free corrosion potential decreased in the order: 316L SS > 304 SS > 430 SS > 0.05% C mild steel > Al 6063. This order is exactly in accordance with the order in which these alloys appear in the galvanic series in sea water [108].

Table 8 Stabilized value of free corrosion potential (FCP) of the alloys in borate buffered solution after first immersion and after 168 hours of immersion.

Nomenclature	Alloys	Section	E _{corr} (mV vs. SCE) (after first immersion)	E _{corr} (mV vs. SCE) (after 168 hrs)	ΔE _{corr} (mV)
ESR74	Fe-20.0Al-2.0C	RD	-216	-45	171
ESR127	Fe-18.5Al-3.6C	RD	-210	-84	126
ESR137	Fe-19.2Al-3.3C-0.07Ce	RD	-253	-62	191
Mild Steel	-	RD	-310	-164	146
Al 6063	-	RD	-647	-296	351
316L SS	-	RD	-208	-40	168

Table 9 Stabilized value of free corrosion potential (FCP) of all the alloys in freely aerated 0.25 mol/lit H₂SO₄ after first immersion and after 24 hours of immersion.

Nomenclature	Intermetallics	Section	E _{corr} (mV vs. SCE) (after first immersion)	E _{corr} (mV vs. SCE) (after 24 hrs)	ΔE _{corr} (mV)
ESR74	Fe-20.0Al-2.0C	RD	-505	-481	24
ESR127	Fe-18.5Al-3.6C	RD	-497	-482	15
ESR137	Fe-19.2Al-3.3C-0.07Ce	RD	-527	-504	23
ESR137	Fe-19.2Al-3.3C-0.07Ce	LT	-523	-514	09
ESR137	Fe-19.2Al-3.3C-0.07Ce	ST	-537	-507	30
Mild Steel	-	RD	-527	-531	-04
316L SS	-	RD	-170	-100	70
Al 6063	-	RD	-744	-662	82
430 SS	-	RD	-545	-499	46
304 SS	-	RD	-08	-198	-190

4.2 Polarization behavior

The electrochemical polarisation behavior of the as-received Fe-20.0Al-2.0C, Fe-18.5Al-3.6C and Fe-19.2Al-3.3C-0.07Ce alloys was also studied in the borate buffered solution of pH= 7.6. The mild steel sample was used for comparison. Borate buffered solutions are normally employed to understand the passivation phenomena in iron based alloys and hence this solution was chosen. The experiments were conducted after stabilization of free corrosion potential (FCP). The potentiodynamic polarization curves for the alloys have been presented in Fig. 64 and the passivation parameters obtained from these curves are tabulated in Table 10.

The passivation parameters are zero current potential (ZCP), breakdown potential (E_b), passive range (given by difference between E_b and ZCP) and passive current density (i_{pass}). The data for mild steel has also been presented for comparison purposes. All the materials exhibited stable passive behavior in the borate buffered solution. The polarization curves indicated that all the three alloys were passivated readily on immersion. The passive current densities of the alloys were similar for all the alloys. The breakdown potential for all the alloys was around 1000 mV. All the aluminides exhibited a similar behavior and the effect of Ce could not be revealed using this solution.

The potentiodynamic polarization behaviour of the same carbon-alloyed intermetallics in 0.25 mol/lit H_2SO_4 solution has been earlier evaluated by Sriram [48]. Fig. 65 shows that potentiodynamic polarization curves for the carbon-alloyed iron aluminides and low carbon mild steel in 0.25 mol/lit H_2SO_4 solution, of pH= 0.74, and the passivation parameters obtained from these curves are tabulated in Table 11 [48]. The passivation parameters evaluated are ZCP, potential for primary passivation, passivation potential (E_{pp}), Critical potential (E_{cp}), breakdown potential (E_b), passive range (given by difference between E_b and ZCP), critical current density (i_{crit}) and passive current density (i_{pass}). From Fig. 65, it can be noted that all the alloys exhibited active-passive behaviour in the acidic solution compared to stable passive behaviour in borate buffered solution (Fig. 64). Moreover, it can also be noted from Table 11 that the passivation parameters were generally comparable in acidic solution between Fe-20.0Al-2.0C and Fe-18.5Al-3.6C. This result was attributed to the

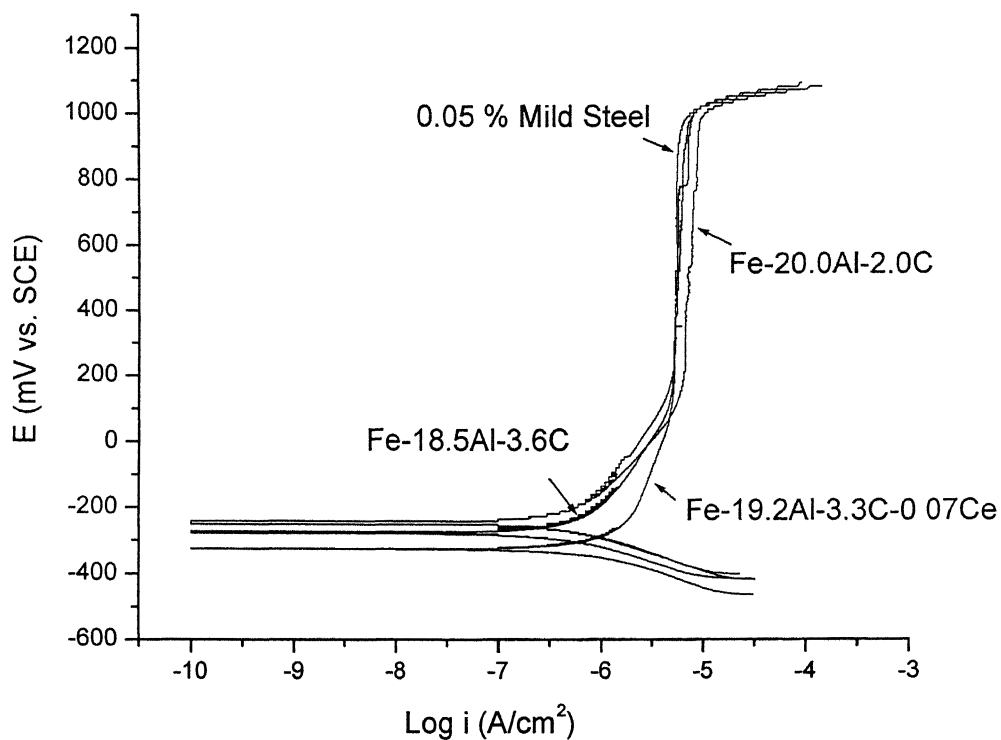


Fig. 64 Potentiodynamic polarization behavior of the rolling plane of as received Fe-18.5Al-3.6C, Fe-20.0Al-2.0C and Fe-19.2Al-3.3C-0.07Ce alloys in borate buffered solution. The polarization curve of mild steel has also been presented for comparison

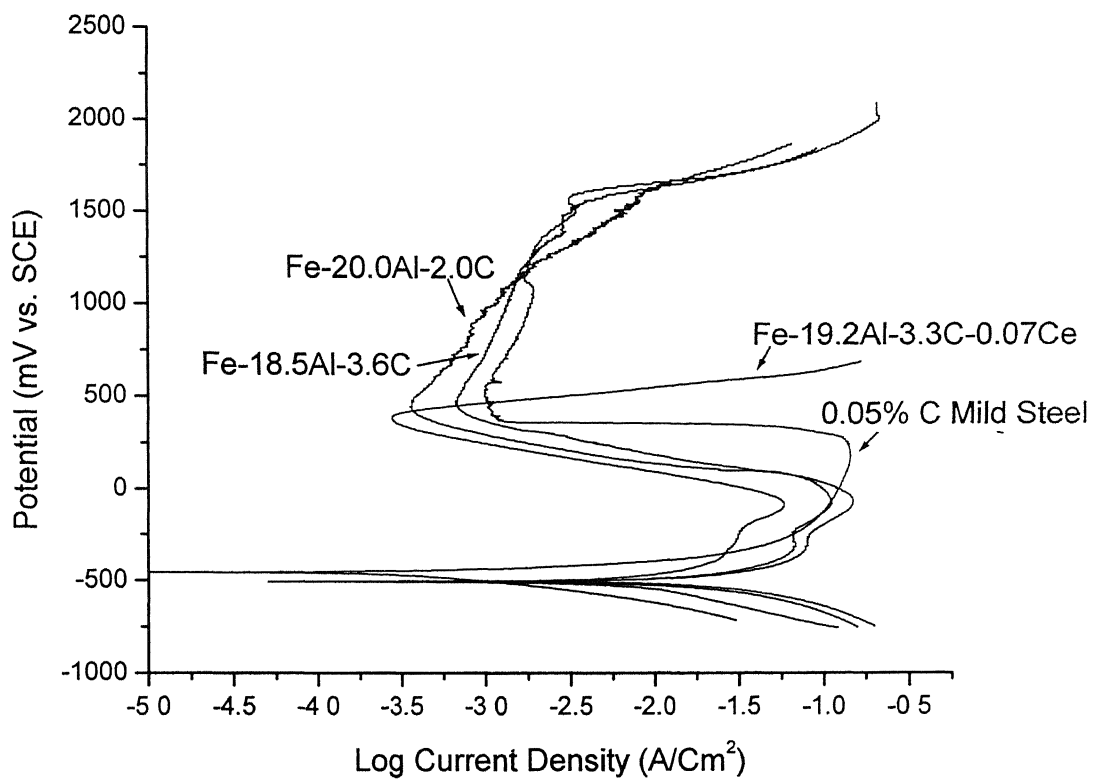


Fig. 65 Potentiodynamic polarization behaviour of Fe-20.0Al-2.0C, Fe-18.5Al-3.6C, Fe-19.2Al-3.3C-0.07Ce and mild steel in freely aerated 0.25 mol/lit H_2SO_4 using a scan rate of 1 mV/sec [48].

insignificant difference in the carbon contents between Fe-20.0Al-2.0C and Fe-18.5Al-3.6C and similar carbide distribution in these two alloys. It can be noted from Table 11 that the passive range of Ce-alloyed intermetallic (Fe-19.2Al-3.3C-0.07Ce) was lower when compared to the other carbon alloyed iron aluminides (Fig. 65) [48]. It was also noted that the passive current density of the RD and ST sections of Ce-alloyed iron aluminide, were lower than that of the other two carbon-alloyed iron aluminides [48]. From this it was concluded that Ce-addition modified the surface film, which results in passivation [48]. Sriram [48] also conducted the long term (85 hours) and short term (11 hours) immersion testing of the carbon-alloyed iron aluminides in 0.25 mol/lit H_2SO_4 solution. The corrosion rate was obtained as a function of time for Fe-18.5Al-3.6C, Fe-20.0Al-2.0C and Fe-19.2Al-3.3C-0.07Ce in 0.25 mol/lit H_2SO_4 solution, for long term and short term immersion testing is shown in Fig. 66a and b [48]. The results of both long term and short term immersion testing of the carbon-alloyed iron aluminides revealed that the corrosion rates in case of Fe-18.5Al-3.6C and Fe-20.0Al-2.0C were comparable. The Ce-alloyed iron aluminide exhibited significantly lower corrosion rate as compared to the other two carbon-alloyed iron aluminides. From these results, it was concluded that Ce plays a role in lowering corrosion rate of Fe-19.2Al-3.3C-0.07Ce by probably altering the nature of the passive film [48].

Comparison of the polarization behaviour of carbon-alloyed intermetallics in acidic solution studied by Sriram [48] with that in borate buffered solution in the present study revealed that the passive current densities of the carbon-alloyed iron aluminides were lower in borate buffered than in acidic solution (refer Table 10 and 11). It can be seen from Table 10 and 11, that the passive current densities in acidic solution were two orders of magnitude higher than that in borate buffered solution. This behaviour is expected because the borate buffered solution is only mildly corrosive as compared to the highly corrosive acidic solution.

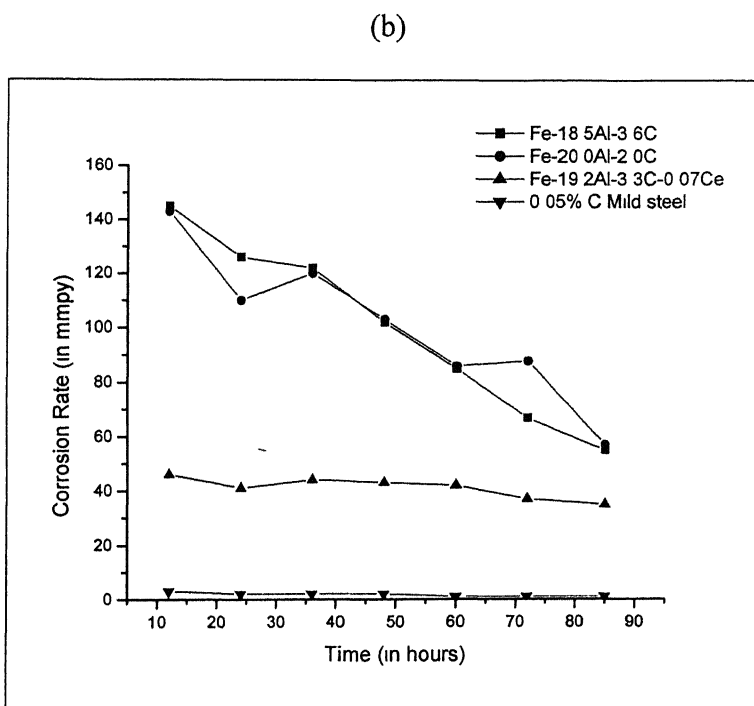
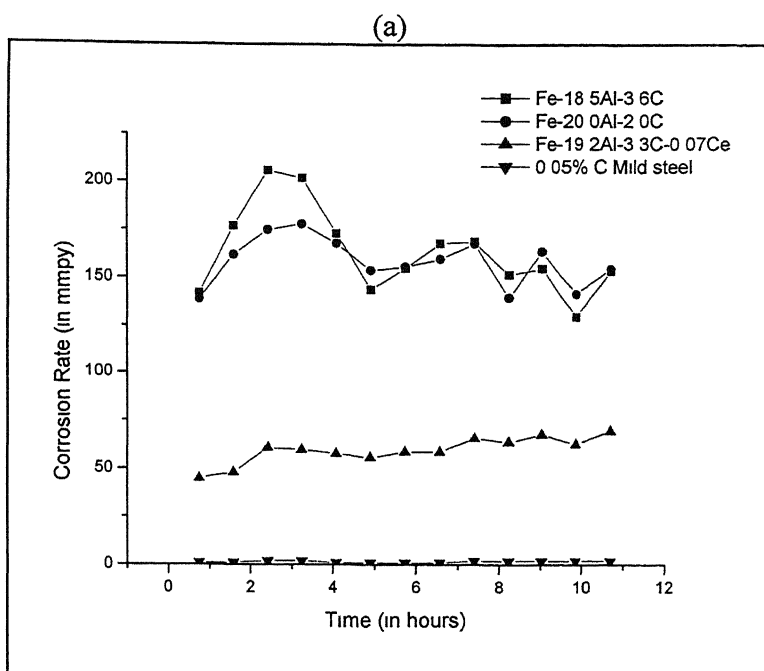


Fig. 66 Corrosion rate as a function of time for the carbon-alloyed iron aluminides and mild steel in freely aerated 0.25 mol/lit H_2SO_4 solution: (a) total duration of 11 hours (b) total duration of 85 hours [48].

Table 10 Passivation parameters obtained from the potentiodynamic polarization curves of the Fe-18.5Al-3.6C, Fe-20.0Al-2.0C, Fe-19.2Al-3.3C-0.07Ce and 0.05 %C mild steel alloys in borate buffered solution.

Alloy	Plane	ZCP (mV vs. SCE)	E _b (mV vs. SCE)	E _b -E _{zcp} (mV vs. SCE)	i _{pass} ($\mu\text{A}/\text{cm}^2$)
ESR74	RD	-243	1019	1407	7.53
ESR127	RD	-280	1024	1432	6.00
ESR137	RD	-325	1032	1257	6.15
Mild steel	RD	-250	1012	1252	5.77

Table 11 Passivation parameters obtained from the potentiodynamic polarisation of the Fe-18.5Al-3.6C, Fe-20.0Al-2.0C and, Fe-19.2Al-3.3C-0.07Ce alloys in freely aerated 0.25 mol/lit H₂SO₄ solution [48].

Alloy	Plane	Composition	ZCP (mV vs. SCE)	Epp (mV vs. SCE)	Ecp (mV vs.SCE)	E _b (mV vs. SCE)	E _b -Ecp (mV)	I _{cnt} (mA / Cm ²)	i _{pass} (μA/cm ²)
ESR 74	RD	Fe-20.0Al-2.0C	-515	-45	418	1530	1112	105	350
ESR 127	RD	Fe-18.5Al-3.6C	-501	-65	432	1570	1138	149	670
ESR 137	RD	Fe-19.2Al-3.3C-0.07Ce	-511	-61	364	394	30	53	270
ESR 137	LT	Fe-19.2Al-3.3C-0.07Ce	-548	-85	419	526	107	66	170
ESR 137	ST	Fe-19.2Al-3.3C-0.07Ce	-524	-96	306	331	25	102	1620

4.3 Electrochemical Impedance Spectroscopy

Electrochemical impedance spectroscopy (EIS) measurements are particularly useful in understanding the nature of surface films. They can also be conducted as a function of immersion time because they do not perturb the system dramatically. It is possible to follow the evolution of the nature of surface film over time. EIS measurements were performed in borate buffered solution of pH=7.6 and in 0.25 mol/lit H_2SO_4 solution of pH=0.74. Corrosion processes often involve a slow aqueous diffusion process, which generally have relatively large time constants (on the order of 0.1 to 10s). Therefore, most impedance studies of corroding systems use frequencies of between a few millihertz and 100 kHz [109]. All the EIS experiments were performed in the frequency range of 100 kHz to 10 mHz.

4.3.1 Borate buffered solution

Properties of passive films grown on Fe-20.0Al-2.0C, Fe-18.5Al-3.6C and Fe-19.2Al-3.3C-0.07Ce alloys in borate buffered solution of pH=7.6 were investigated as a function of immersion time by means of electrochemical impedance spectroscopy. All the impedance experiments were performed after stabilization of free corrosion potential. Impedance spectra of 316L stainless steel, mild steel and Al 6063 alloy are also presented for comparison.

The EIS data for all the alloys in borate buffered solution of pH=7.6, obtained at open circuit potential (after 2 hours and 168 hours of immersion), are presented in Figures 67 (Nyquist plots), 68 (Bode phase plots) and 69 (Bode magnitude plots).

From Fig. 67 it can be observed that the nature of the Nyquist plots (imaginary part of impedance vs. real part of impedance at different frequencies) was similar for all the alloys, consisting of an arc that can be extrapolated to a semicircle, which is associated with the corrosion process. The diameter of the semicircle corresponds to the polarization resistance (R_p). It can be observed from the Fig. 67 that after 168 hours of immersion, the diameter of the semicircle increased for all the alloys except for Fe-18.5Al-3.6C. In case of Fe-18.5Al-3.6C, there was a slight decrease in the diameter of the

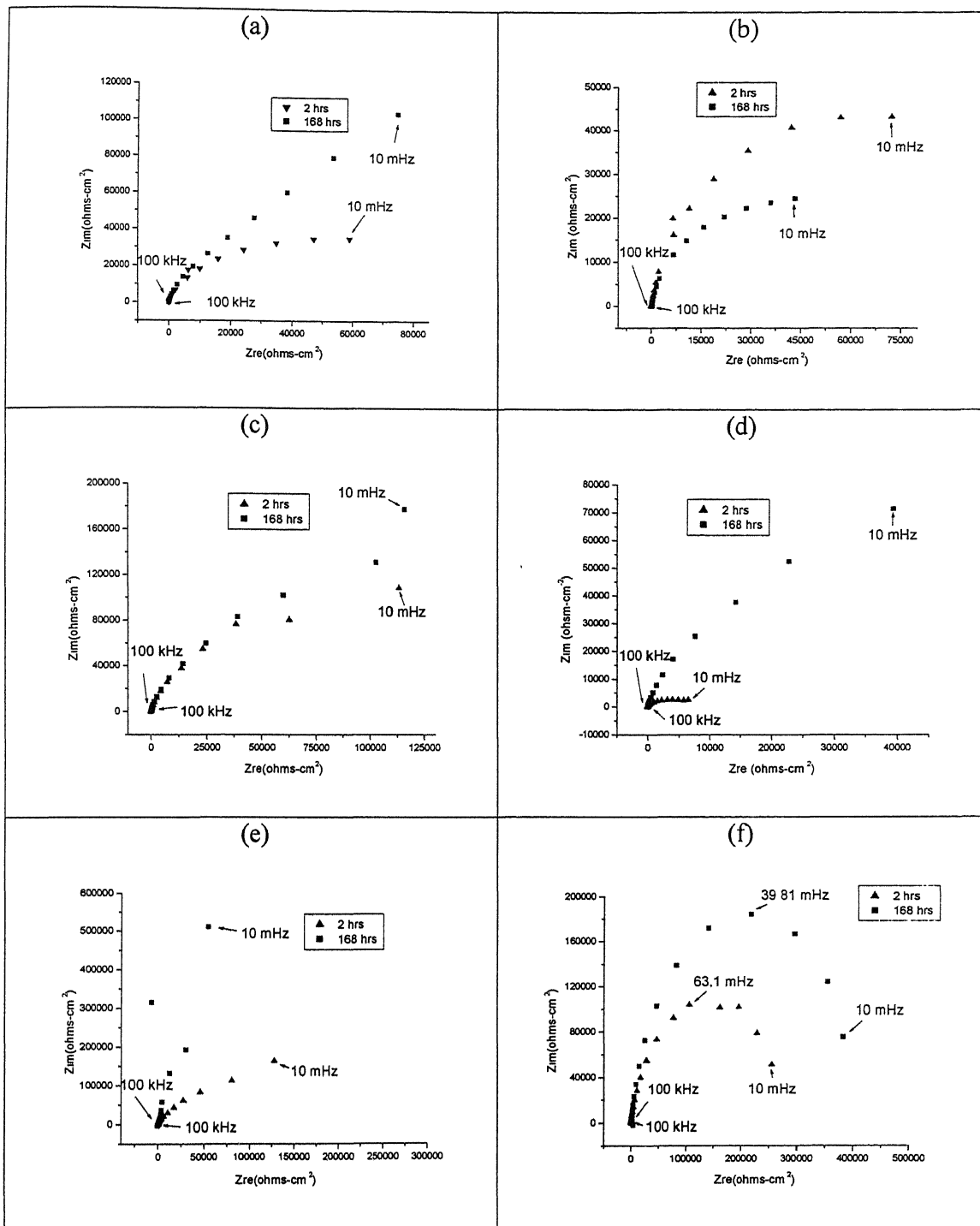


Fig. 67 Nyquist plots for the alloys in borate buffered solution, at free corrosion potential, after 2 hours and 168 hours of immersion: (a) Fe-19.2Al-3.3C-0.07Ce (b) Fe-18.5Al-3.6C (c) Fe-20.0Al-2.0C (d) Mild steel (e) 316L SS (f) Al6063 alloy.

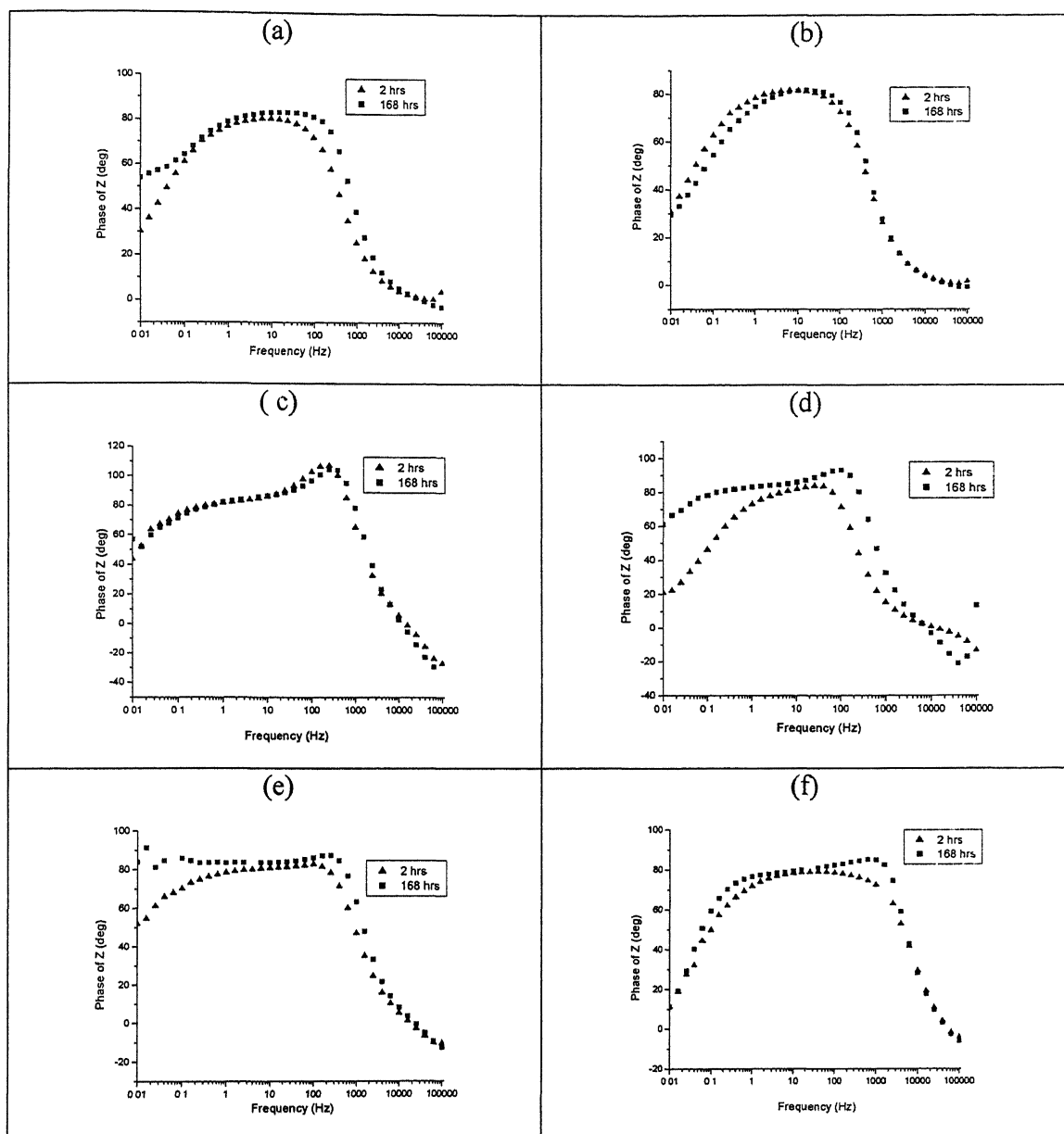


Fig. 68 Bode phase plots for the alloys in borate buffered solution, after 2 hours and 168 hours of immersion: (a) Fe-19.2Al-3.3C-0.07Ce (b) Fe-18.5Al-3.6C (c) Fe-20.0Al-2.0C (d) Mild steel (e) 316L SS (f) Al6063 alloy.

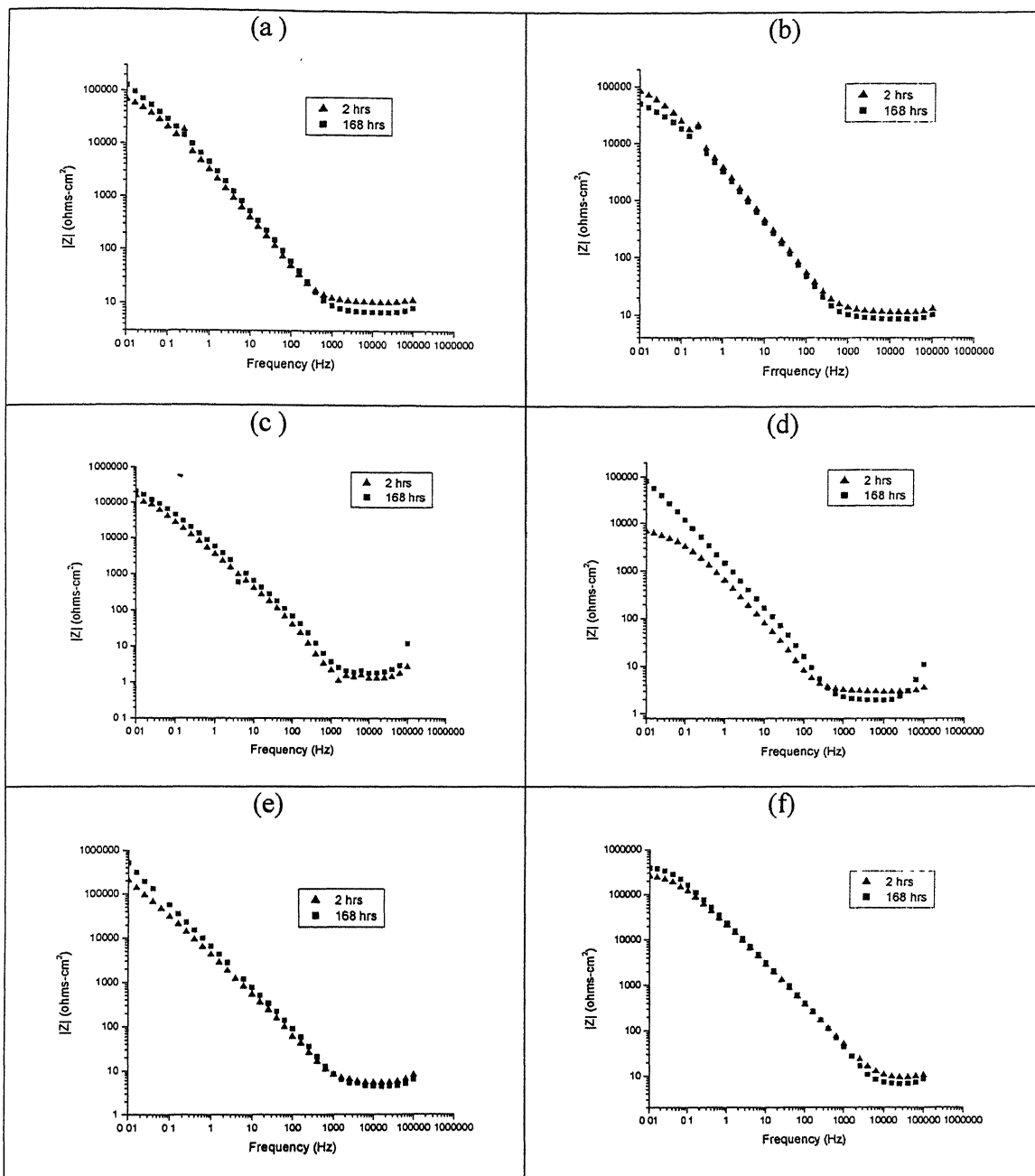


Fig. 69 Bode magnitude plot for all the alloys in borate buffered solution after 2 hours and 168 hours of immersion: (a) Fe-19.2Al-3.3C-0.07Ce (b) Fe-18.5Al-3.6C (c) Fe-20.0Al-2.0C (d) Mild steel (e) 316L SS (f) Al6063 alloy.

capacitive loop. This indicates that the corrosion resistance of all the alloys, except Fe-18.5Al-3.6C, improved after seven days of immersion.

From the Bode phase plots (logarithm of phase angle vs. logarithm of frequency), of all the alloys shown in Fig. 68, it can be noted that, both after first immersion and after 168 hours of immersion, the phase angle drops towards zero degree at very high frequencies. Similar results were obtained by Gudic et. al. who conducted the study of passivation of Al and its alloys in borate buffered solution using EIS. They observed that in the Bode phase plots of Al and its alloys in borate buffered solution, the phase angle dropped towards zero degree at high frequencies [92]. From this they concluded that impedance data was dominated by solution resistance. Gonzalez et. al. [110] in their study of the corrosion behaviour of Ti and some of its alloys in Ringer's solution observed that the Bode phase plots of Ti and its alloys were characterized by phase angle close to zero in the high frequency region. They also attributed this to the response of the solution resistance (resistive region). Therefore, it is reasonable to conclude that the drop in phase angle towards zero degree at high frequency indicates that the impedance is dominated by solution resistance in this frequency range.

Looking at the Bode phase plots after first immersion, it can be seen that the phase angle approached the value of nearly 30° in the case of Fe-19.2Al-3.3C-0.07Ce and Fe-18.5Al-3.6C, and nearly 45° in the case of Fe-20.0Al-2.0C, in the low frequency region (Fig. 68a, b and c). Moreover, the Bode phase plot of mild steel and Al 6063, obtained after first immersion, shows that the phase angle dropped to nearly 20° in case of mild steel and nearly 10° in the case of Al 6063, towards low frequencies (Fig. 68d and f). In case of 316L SS after first immersion, the phase angle dropped to nearly 50° at low frequencies (Fig. 68e). As high phase angle ($\sim 90^\circ$) indicates purely capacitive behaviour (compact surface film), it is reasonable to conclude that the drop in phase angle to lower angles in the low frequency region is indicative of the reduction in the capacitive behaviour. Moreover, the reduction in capacitive behaviour may be due to the contribution of the surface film resistance in the impedance [92]. After 168 hours of immersion, the phase angle at low frequencies, in the case of Fe-19.2Al-3.3C-0.07Ce increased from nearly 30° to nearly 55° , whereas no significant change in the phase angle at low frequency was observed in the case of Fe-20.0Al-2.0C and Fe-18.5Al-3.6C. Phase angles

in the low frequency region, also increased in the case low carbon mild steel and 316L SS to nearly 60° and 80° , respectively, after 168 hours of immersion in borate buffered solution. Moreover, no significant change was observed in the case of Al 6063. Increase in phase angle in low frequency region, after 168 hours of immersion in case of Fe-19.2Al-3.3C-0.07Ce, low carbon mild steel and 316L, indicates that the surface film became more capacitive (and hence more compact and stable) in nature after seven days of immersion for these alloys.

At medium frequencies, the capacitive behavior, determined by the dielectric properties of the naturally formed surface film of the system, is evident by the increase in phase angle (Fig. 68) [92]. Generally, the phase remains close to -90° over a wide range of frequency for all the alloys. This behavior is indicative of a typical thin surface film [110]. Similar behaviour was observed by Gudic et. al. [92] in their study of the corrosion behaviour of Ti alloys. They attributed this behaviour to be typical of a thin passive oxide film, i.e. a near capacitive response. However, it can be noted that in Bode plot after first immersion for low carbon mild steel (Fig. 68d), the frequency range over which the phase angle remains high was much narrower than that of the other alloys. This indicates that surface film formed on first immersion in the case of mild steel was less capacitive (and hence less compact) in nature than that of the other alloys.

The nature of the Bode phase plots was similar for all the alloys after 168 hours of immersion. Moreover, it can be observed from Fig. 68 that the frequency range over which the phase angle is close to -90° increases after 168 hours of immersion for all the alloys, indicating that generally the stability of the surface film improved with time for all the alloys [110]. However, it can be noted from Fig. 68d that the increase in the range over which the phase angle is close to -90° is maximum in the case of low carbon mild steel, indicating that the maximum improvement in the surface film properties occurred in the case of low carbon mild steel.

Bode magnitude plots (logarithm of impedance vs. logarithm of frequency) presented in Fig. 69 showed that the slope of $\text{Log } |Z|$ vs. $\text{Log } f$ is close to zero in the very high frequency region indicating that the dominance of solution resistance in this region. However, the slope changes from zero to ≈ -1 in the remaining frequency range, indicating a near capacitive response. The nature of the Bode magnitude plots were

similar after 168 hours of immersion. However, it can be noted that in case of low carbon mild steel the value of the impedance at lowest frequency, which is equal to the sum of solution resistance and polarization resistance, increased significantly after 168 hours of immersion in borate buffered solution. As can be seen from the Fig. 69d, the solution resistance, which is indicated by the value of impedance at highest frequencies, does not change by much with immersion time. Therefore, it can be concluded that there was a significant increase in the film resistance of low carbon mild, after 168 hours of immersion in borate buffered solution.

The equivalent circuit shown in Fig. 70 was used to fit the above experimental data. In the equivalent circuit, R_s is solution resistance, R_p is polarization resistance and Q is constant phase element (CPE). The fitting procedure revealed that better agreement between theoretical and experimental data was obtained if a frequency dependent constant-phase element (CPE) was used instead of pure capacitance and Warburg impedance. The impedance of a constant phase element is defined in as [92 and 109]:

$$Z_{CPE} = [Q(j\omega)^n]^{-1}$$

where Q and n are frequency independent parameters, which usually depend on temperature and $-1 \leq n \leq 1$ [109]. CPE describes an ideal capacitor for $n = 1$, an ideal inductor for $n = -1$ and an ideal resistor for $n = 0$. Generally the appearance of a CPE is due to the presence of inhomogeneities in the electrode-material system and it can be described in terms of a (nonnormalizable) distribution of relaxation times, or it may arise from non-uniform diffusion whose electrical analog is an inhomogeneously distributed RC transmission line [109]. The theoretically estimated impedance spectra based on fitting the experimental data with the circuits shown in Fig. 70 have all been presented in Appendix A.

The values of the circuit parameters, obtained on fitting the experimental data with the circuit shown in Fig. 70 are tabulated in Table 12. It can be noted from Table 12 that the solution resistance (R_s) was in the range of 1.0 to 12 ohms-cm⁻² both on first immersion and after 24 hours of immersion for all the alloys. Moreover, it can be noted there was no appreciable change in the value of solution resistance during 168 hours of

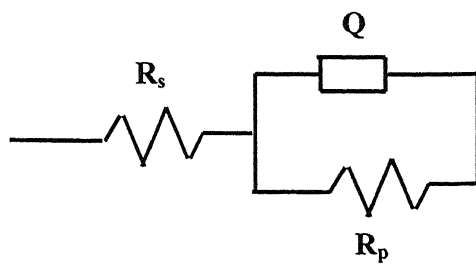


Fig. 70 Equivalent circuit used for fitting experimental EIS data obtained in borate buffered solution.

immersion. From this table, it can also be seen that the values of 'n' were very close to one, and therefore Z_{CPE} can be approximated to be equal to surface film capacitance [92]. Table 12 also shows the chi-squared values obtained on fitting the experimental data. The fit of the data to the theoretical model was good because relatively low chi-squared values were obtained.

From Table 12 it can be observed that after 2 hours, the polarization resistance (R_p) values of the three iron aluminide samples were nearly of the same order of magnitude as that of Al 6063 and 316L SS alloys. However, the polarization resistance of mild steel was one order of magnitude lower than that of carbon-alloyed intermetallics. Remarkable aluminium enrichment within the passive film on iron alloy containing 3 wt% Al has been reported by Kirchheim et. al. [111] It has also been reported by Frangini et. al. [23] that the passive film formed on FeAl alloy (containing 24.4 wt% Al) in sulphuric acid contained significant amounts of a aluminium oxide phase mixed with small quantities of iron oxy-hydroxide mostly located on the top surface of the films. Therefore, it is reasonable to conclude that the higher polarization resistance of iron aluminides compared to the low carbon mild steel may be due to the presence of Al in carbon alloyed intermetallics.

It can be noted from Table 12 that generally the polarization resistance of all the alloys except Fe-18.5Al-3.6C, improved after seven days of immersion. The polarization resistance of Fe-18.5Al-3.6C decreased slightly. Interestingly, the improvement in polarization resistance was of two orders of magnitude in the case of 316L SS and one order of magnitude in the case of mild steel. In the case of Fe-19.2Al-3.3C-0.07Ce, Fe-20.0Al-2.0C and Al 6063, the value of polarization resistance nearly doubled after seven days of immersion time. Moreover, the very high R_p values of all the alloys in borate buffered solution as compared to that in acidic solution (Refer Tables 13 and 14 to be presented later) indicate the formation of a relatively protective surface film with high corrosion resistance in borate buffered solution.

As discussed earlier, after seven days of immersion the polarization resistance of Fe-19.2Al-3.3C-0.07Ce increased, whereas that of Fe-18.5Al-3.6C, decreased slightly in the borate buffered solution. The composition of both Fe-19.2Al-3.3C-0.07Ce and Fe-18.5Al-3.6C are very similar, except that Fe-19.2Al-3.3C-0.07Ce is also alloyed with

cerium Therefore, the improvement in the polarization resistance of Fe-19.2Al-3.3C-0.07Ce with time may be attributed to the effect of cerium addition. The higher polarization resistance for Fe-20.0Al-2.0C as against Fe-18.5Al-3.6C can be attributed to the lower carbon content of Fe-20.0Al-2.0C. Carbide matrix interfaces are ideal locations for initiation of localized corrosion process. [45]. Moreover, carbides act as cathodic members in the galvanic couple between the matrix and the carbide. Therefore, a decrease in carbon content apparently results in improved corrosion resistance of carbon-alloyed aluminides.

The improvement in the passive film properties with time was also evident in the values of the capacitance of the passive film (Z_{CPE}) for these alloys. The surface film is considered to be a parallel circuit of a resistor due to the ionic conduction in the surface film, and a capacitor due to its dielectric properties [112]. Moreover, the value of capacitance is related to the surface film thickness according to the following relation [110]:

$$C_p = (\epsilon \epsilon_0 A) / d$$

where ϵ is the dielectric constant of surface film, ϵ_0 the permittivity of the free space ($8.9E-19 \text{ F cm}^{-1}$), A is the area of the surface and C_p is the capacitance of the surface film. Thus, the increase in the value of the capacitance with time corresponds to the growth of the surface film, indicating the long term stability of the surface film [110].

Therefore it can be inferred that both the decrease in capacitance and the increase in polarization resistance are indicative of improved surface film properties. It can be noted from the Table 12 that in case of Fe-19.2Al-3.3C-0.07Ce and Fe-20.0Al-2.0C, the value of capacitance decreased whereas that of Fe-18.5Al-3.6C increased after seven days of immersion, indicating that the stability of the film increased with time for Fe-19.2Al-3.3C-0.07Ce and Fe-20.0Al-2.0C, while that of Fe-20.0Al-2.0C decreased. This confirms the earlier conclusions based on polarization resistance values, that the corrosion resistance (and hence the surface film properties) of Fe-19.2Al-3.3C-0.07Ce and Fe-20.0Al-2.0C improved with time whereas that of Fe-18.5Al-3.6C deteriorated with time.

Moreover, it can be seen from the Table 12 that the values of capacitances for the three carbon-alloyed iron aluminides are generally comparable. Therefore, it can be concluded that the surface film thickness is of the same order of magnitude in all the three carbon-alloyed iron aluminides. Table 12 also shows that the capacitance values of Al 6063 and 316L SS also decreased after 168 hours immersion. This again indicates the growth and increase in the stability of surface film on these alloys with time.

Table 12 Values of all the circuit parameters obtained after fitting the experimental EIS data obtained in borate buffered solution of pH 7.6 with the circuit shown in Fig. 70. Numbers in the brackets indicate the percentage error.

	Fe-19.2Al-3.3C- 0.07Ce (Esr137)		Fe-18.5Al-3.6C (Esr127)		Fe-20.0Al-2.0C (Esr74)		0.05 %C Mild Steel		316L SS		Al 6063	
	2 Hours	168 hours	2 hours	168 hours	2 hours	168 Hours	2 hours	168 hours	2 hours	168 hours	2 hours	168 hours
R_s (ohms-cm ²)	10.65 (4.508)	6.912 (5.119)	11.61 (4.19)	8.788 (5.836)	1.785 (12.46)	12.01 (20.78)	2.985 (4.167)	1.966 (6.8)	5.858 (4.911)	4.783 (9.59)	8.915 (5.681)	7.153 (25.67)
Q_1 (S-sec ⁿ /cm ²)	5.548E-5 (4.908)	4.637E-5 (4.613)	4.819E-5 (4.506)	5.24E-5 (6.782)	4.679E-5 (10.38)	3.278e-5 (19)	2.964E-4 (5.526)	1.218E-4 (4.95)	4.513E-5 (4.122)	2.646E-5 (7.118)	91.71E-5 (4.613)	57.38E-5 (18.79)
n	0.9162 (1.167)	0.9108 (1.049)	0.9227 (1.066)	0.9323 (1.524)	0.9881 (2)	0.9259 (4.448)	0.9232 (1.327)	0.9672 (1.096)	0.9163 (0.9284)	0.9515 (1.491)	0.8842 (0.8629)	0.906 (3.269)
R_p (ohms-cm ²)	7.41E4 (9.066)	18.33Ee4 (13.24)	9.196E4 (8.603)	4.952E4 (9.885)	18.66E4 (26.91)	33.38E4 (63)	0.6423E4 (6.954)	15.36E4 (22.61)	31.19E4 (16.81)	4.468E7 (1.872)	26.00E4 (6.96)	40.45E4 (27.96)
Chi-Square	2.264E-2	2.518E-2	1.960E-2	3.736E-2	1.35E-1	4.53E-1	1.042E-2	3.01E-2	2.24E-02	7.94E-2	1.80E-2	3.094E-1

4.3.2 Acidic Solution

In order to obtain more information about the solution resistance (R_s), polarization resistance (R_p), surface film capacitance (C_p) and charge-transfer kinetics of the three iron aluminide samples in acidic solution, impedance measurements have been carried out in freely aerated 0.25 mol/lit H_2SO_4 with $pH=0.74$. Impedance spectra of low carbon mild steel, 304 stainless steel and 430 stainless steel were used to compare the behavior of iron aluminide samples with these alloys. All the impedance experiments were performed after the stabilization of free corrosion potentials. Impedance data was collected after FCP stabilization for two time intervals, on first immersion and after 1 day of immersion. Long immersion times leads to severe corrosion of the surface because the corrosion rates of the carbon-alloyed iron aluminide in acidic solution are relatively high [48].

Fig. 71 shows the Nyquist plots (imaginary part of impedance vs. real part of impedance, at different frequencies) of all the alloys obtained after 2 and 24 hours of stabilization. It can be seen from Fig 71 that Nyquist plots of the carbon-alloyed intermetallics, mild steel and 430 SS after 2 hours, consist of an inductive loop at very high frequencies, a large capacitive loop at high frequencies, a capacitive loop at low frequency (in case of Fe-19.2Al-3.3C-0.07Ce as shown in Fig. 71a) and a small inductive one at low frequencies. These loops have been explained earlier in the literature survey section (Chapter 2). The nature of Nyquist plots after first immersion, for long transverse and short transverse sections of the Ce-alloyed intermetallics (Fig. 71d and e) was similar to that of rolling direction. However, it can be noted that the low frequency capacitive loop was much more pronounced in case of RD section than the other two sections. In the case of LT and ST sections, the low frequency capacitive loop was almost merging into the high frequency capacitive loop, and it could not be distinguished. The inductance in the high frequency region can be attributed to the actual physical inductance of the wires and, possibly, of the electrode itself. The HF capacitive loop could be assigned to the relaxation process in the surface film present on the surface of the alloys and its dielectric properties. Capacitive loop at low frequency may be due to the formation of product layer

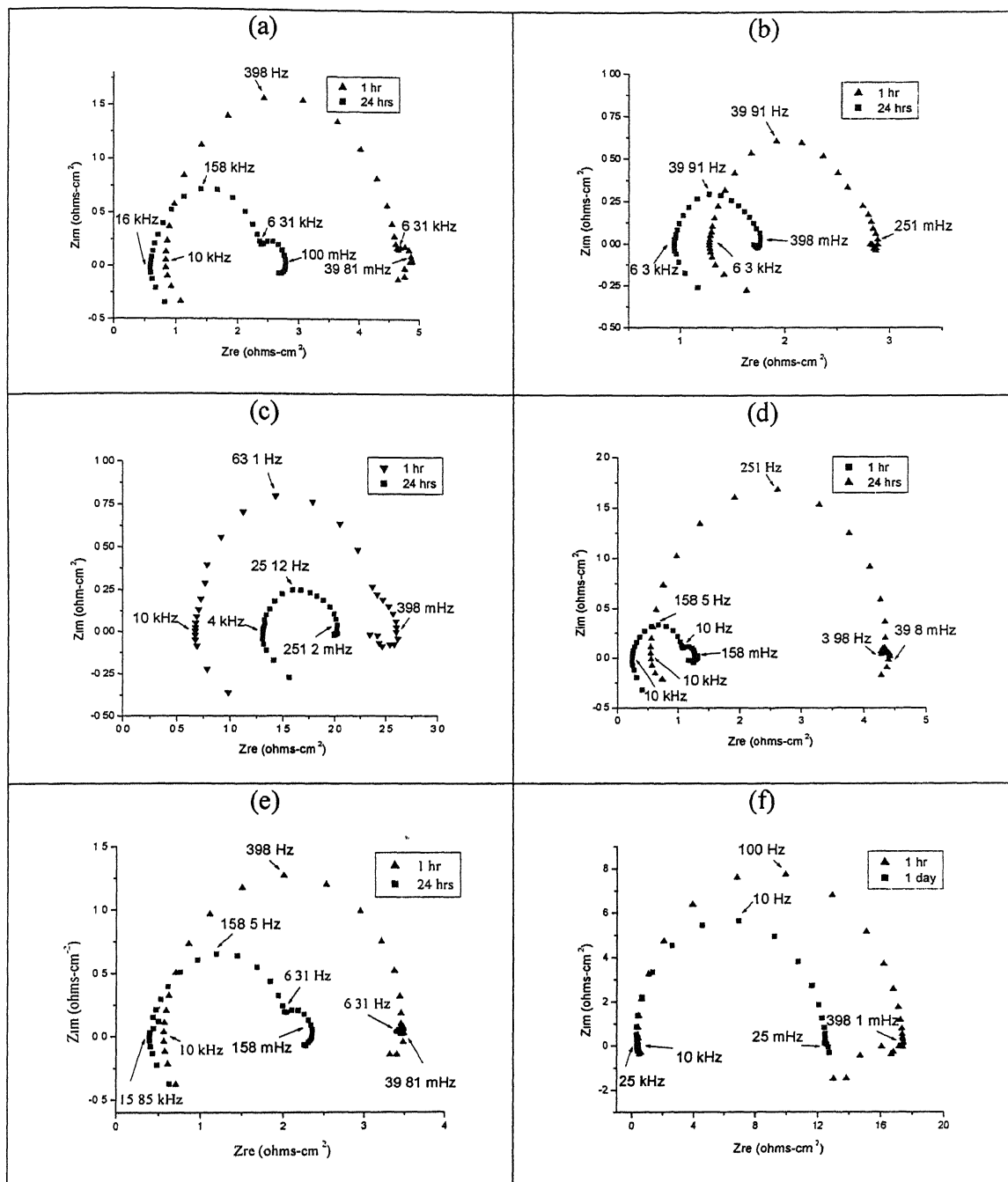


Fig.71 Nyquist plots for the alloys in freely aerated 0.25 mol/lit H_2SO_4 after 2 hours and 24 hours (one day) of immersion time: (a) Fe-19.2Al-3.3C-0.07Ce (b) Fe-18.5Al-3.6C (c) Fe-20.0Al-2.0C (d) Fe-19.2Al-3.3C-0.07Ce (LT) (e) Fe-19.2Al-3.3C-0.07Ce (ST) (f) Mild steel (g) 316L SS (h) Al 6063 (i) 304 SS (j) 430 SS.

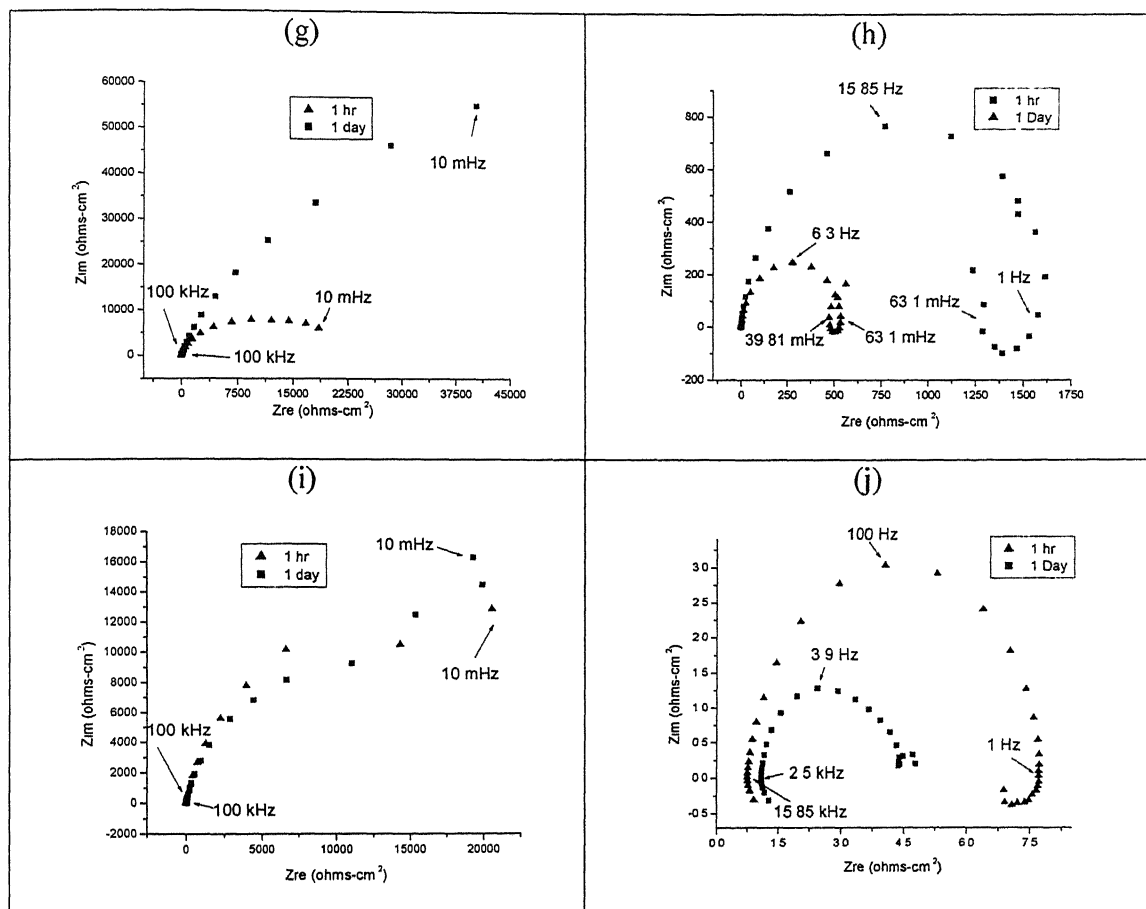


Fig. 71 (continued) Nyquist plots for the alloys in freely aerated 0.25 mol/lit H_2SO_4 after 2 hours and 24 hours (one day) of immersion time: (a) Fe-19.2Al-3.3C-0.07Ce (b) Fe-18.5Al-3.6C (c) Fe-20.0Al-2.0C (d) Fe-19.2Al-3.3C-0.07Ce (LT) (e) Fe-19.2Al-3.3C-0.07Ce (ST) (f) Mild steel (g) 316L SS (h) Al 6063 (i) 304 SS (j) 430 SS.

while the inductive loop at low frequency is a result of adsorption-desorption equilibria [89 and 113].

It can also be noted that after 24 hours of immersion in 0.25 mol/lit H_2SO_4 solution, the nature of the Nyquist plots for, carbon-alloyed iron aluminides and, remained same as it was after first immersion, i.e. consisting of an inductive loop at very high frequencies, a large capacitive loop at high frequencies, a capacitive loop at low frequency (in case of Fe-19.2Al-3.3C-0.07Ce as shown in Fig. 71a) and a small inductive one at low frequencies (Fig.71d). However, in case of low carbon mild steel 430 SS alloys, the low frequency inductive loop disappeared after 1 day of immersion in acidic solution. Moreover, it can be noted that the diameter of the HF capacitive loop, which is equal to the polarization resistance, decreased for all the three carbon-alloyed intermetallics as well as for mild steel and 430 SS. This indicates that, in general, the corrosion resistance of all these alloys deteriorated during 1 day of immersion in 0.25 mol/lit H_2SO_4 solution.

In case of 316L SS and 304 SS, the Nyquist plot consists of only an arc that can be extrapolated to a semicircle (Fig. 71g and i), which is associated with the corrosion process. The diameter of the semicircle corresponds to the polarization resistance (R_p). It can be noted that after 24 hours of immersion, the diameter of the semicircle increased indicating that the corrosion resistance of these alloys improved after 24 hours of immersion in acidic solution. Moreover it can be noted that improvement in polarization resistance is much more prominent in the case of 316L SS as compared to that of 304 SS.

The Nyquist plot of Al 6063 consists of a large capacitive loop at high frequencies (HFs) and an inductive loop at intermediate frequencies (IF), followed by a second capacitive loop at LF values [78 and 79]. The (IF) inductive loop may be related to the relaxation process obtained by adsorption and incorporation of SO_4^{2-} ions on and into the oxide film [79]. The second capacitive loop observed at LF values could be assigned to the metal dissolution. Rehim et. al [79] conducted the study of corrosion of Al and some of its alloys in sulphate solutions containing halide ions using EIS. They observed that the typical Nyquist plots for pure Al in Na_2SO_4 solution containing 0.20 M NaX (where $X = \text{Cl}^-$, Br^- or I^-) at the OCP consists of a large capacitive loop at HFs and an inductive loop at intermediate frequencies (IF), followed by a second capacitive loop at LF values.

The HF capacitive loop was attributed to the presence of a protective oxide film covering the surface of Al and its two alloys. The (IF) inductive loop was related to the relaxation process obtained by adsorption and incorporation of both X^- and SO_4^{-2} ions on and into the oxide film, while, the second capacitive loop observed at LF values was assigned to the metal dissolution. Similar findings were observed by Lenderink et al. [114] during the corrosion behaviour of pure Al in acidic and neutral solutions. Shoa et. al. [78] during the corrosion of pure aluminum in 1M KOH solution also observed that the EIS response of Al consisted of a high-frequency capacitive loop, a middle-frequency inductive loop and a low-frequency capacitive loop. It can also be noted that in case of Al 6063, the diameter of the high frequency capacitive loop increased after 24 hours of immersion, indicating the improvement in corrosion resistance.

Moreover, it can be noted that the impedance spectra did not display the Warburg impedance in any of the cases, showing that mass transport was unimportant compared with charge transfer processes.

Bode phase plots (logarithm of phase angle vs. logarithm of frequency) for all the alloys obtained after first immersion and after 24 hours immersion are presented in Fig. 72. It can be noted that at high frequencies the impedance was dominated by electrolyte resistance while at very low frequencies the impedance was dominated by the surface film resistance (polarization resistance). The phase angle dropped towards 0° at both high and low frequencies, except in the case of 304 SS and 316L SS. In case of 304 SS and 316L SS, the phase angle at low frequencies was higher than zero. At medium frequencies, the capacitive behaviour determined by the dielectric properties of the naturally formed surface film of the system, was evident by the increase in phase angle [92].

The maximum phase angle obtained after first immersion in the case of Fe-20.0Al-2.0C and Fe-18.5Al-3.6C was nearly 35° and 20° , respectively (Fig. 72b and c). Higher phase angle in the case of Fe-20.0Al-2.0C is indicative of more capacitive nature (and hence more compact nature) of the surface film than that of Fe-18.5Al-3.6C. Moreover, after 24 hours of immersion the maximum phase angle approached in the middle frequency range, decreased to nearly 10° for both Fe-18.5Al-3.6C and Fe-20.0Al-2.0C. The lowering of the phase angle for both these alloys indicated the deterioration in

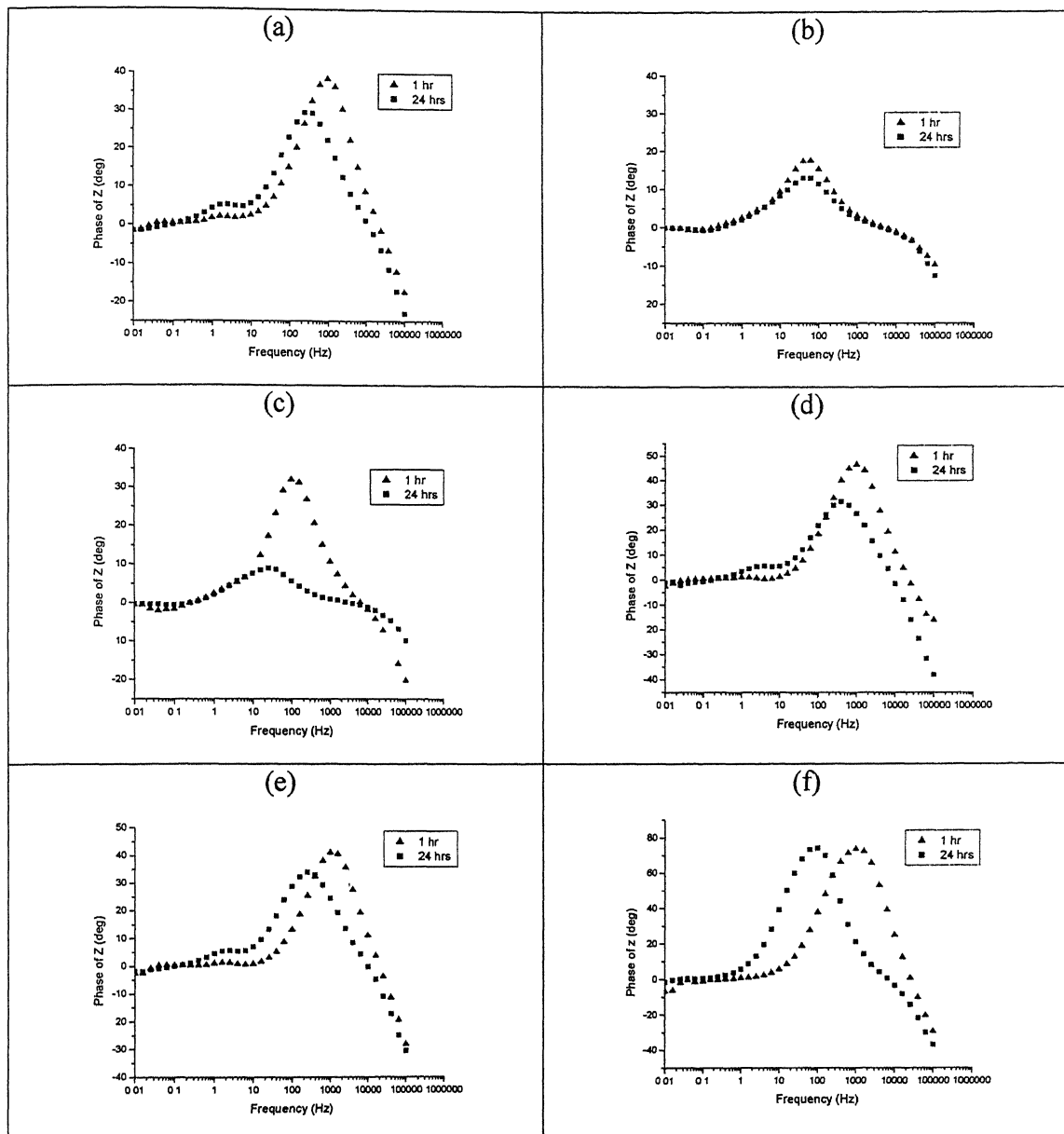


Fig. 72 Bode phase plot for the alloys in freely aerated 0.25 mol/lit H_2SO_4 after 2 hours and 24 hours (one day) of immersion time: (a) Fe-19.2Al-3.3C-0.07Ce (b) Fe-18.5Al-3.6C (c) Fe-20.0Al-2.0C (d) Fe-19.2Al-3.3C-0.07Ce (LT) (e) Fe-19.2Al-3.3C-0.07Ce (ST) (f) Mild steel (g) 316L SS (h) Al 6063 (i) 304 SS (j) 430 SS.

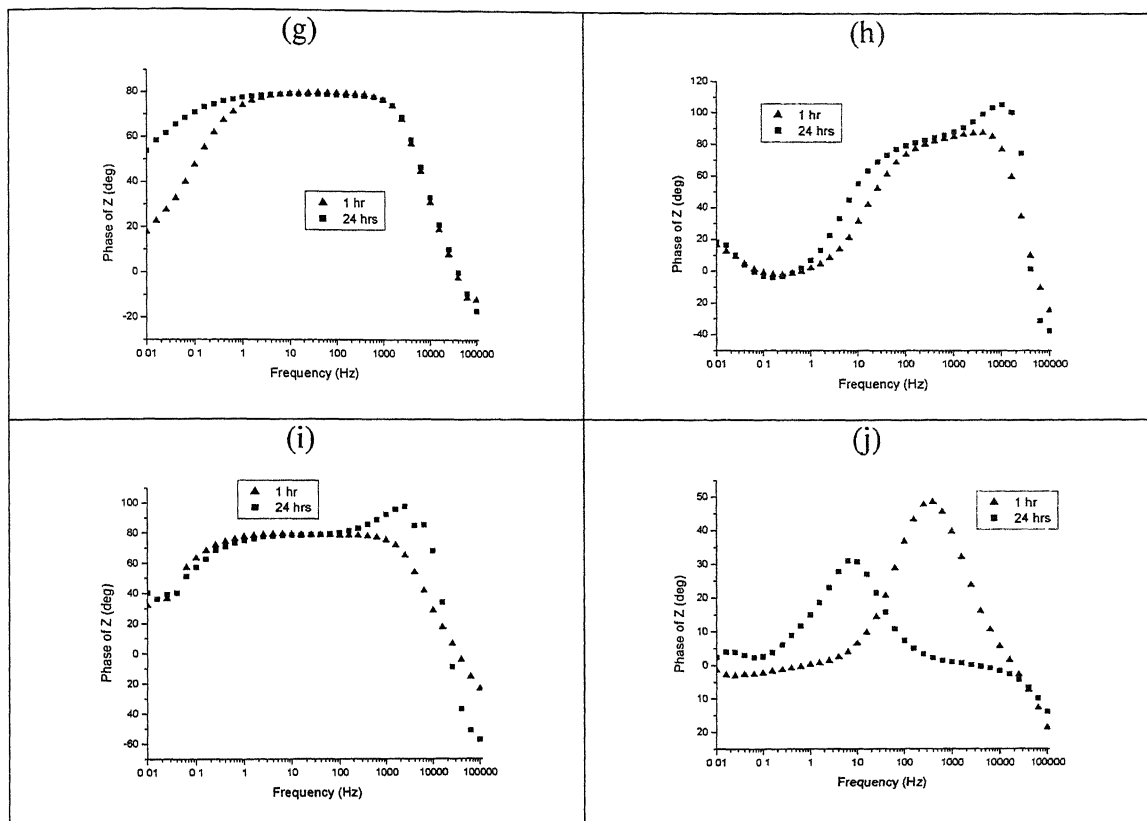


Fig.72 (continued) Bode phase plot for the alloys in freely aerated 0.25 mol/lit H_2SO_4 after 2 hours and 24 hours (one day) of immersion time (a) Fe-19.2Al-3.3C-0.07Ce (b) Fe-18.5Al-3.6C (c) Fe-20.0Al-2.0C (d) Fe-19.2Al-3.3C-0.07Ce (LT) (e) Fe-19.2Al-3.3C-0.07Ce (ST) (f) Mild steel (g) 316L SS (h) Al 6063 (i) 304 SS (j) 430 SS.

the surface film properties. Moreover, the very low phase angle of 10° for both these non-Ce alloyed iron aluminides indicated that the surface film becomes very less capacitive (and hence compact) in nature after 24 hours of immersion in acidic solution.

It can also be noted from Fig. 72a, d and e, that the behaviour of the RD, LT and ST sections of Fe-19.2Al-3.3C-0.07Ce was generally comparable. Phase angle after first immersion, for these three sections (RD, LT and ST) was in the range of 40 to 45 degrees (Fig. 72a, d and e). Similarly, after 24 hours of immersion in acidic solution, the maximum phase angle approached was nearly 30° for all the three sections (RD, LT and ST) of Fe-19.2Al-3.3C-0.07Ce. Nearly similar values of the maximum phase angle for all the three sections of Fe-19.2Al-3.3C-0.07Ce, was indicative of similar nature of the surface film on these sections. Moreover, the decrease in the maximum phase angle after 24 hours of immersion was indicative of the deterioration of the surface film properties with immersion time. Interestingly, the phase angle of the Ce-alloyed iron aluminide was higher than that of the other two iron aluminides, both after first immersion and after 24 hours of immersion. This is indicative of better surface film properties in the case of the Ce-alloyed iron aluminide.

In case of 430 SS, the phase angle in the medium frequency range decreased from nearly 50° on first immersion to nearly 30° after immersion period of 24 hours, indicating the deterioration of the surface film properties with time. Similar nature of the Bode phase plot was observed in the case of Ce-alloyed iron aluminide as well, hence it can be concluded that the nature of the surface film formed on 430 SS and the Ce-alloyed iron aluminide is comparable. For mild steel, the phase angle remained nearly same even after 24 hours of immersion. Moreover, the maximum phase angle in the case of low carbon mild steel (nearly 80°) was higher than that of the carbon-alloyed iron aluminides and 430 SS. This suggests that the surface film on low carbon mild steel is more capacitive in nature than that of the carbon-alloyed iron aluminides and 430 SS.

It can be noted that the Bode phase plot of Al 6063 (Fig. 72h) also exhibited a similar behavior as that of other alloys. Moreover, the difference in the case of Al 6063 was that after 24 hours of immersion the phase angle increased. The range over which the phase angle was close to -90° also increased, indicating that the stability of the oxide film improved with time [110]. Another difference that can be noted in case of Al 6063 is that,

towards low frequency (LF) the phase tends to increase, indicating capacitive behaviour. This can be attributed to the metal dissolution [79].

Bode phase plots in the case of 316L SS and 304 SS, exhibited only a near capacitive response illustrated by a phase angle close to -90° over a wide range of frequency. This behavior is indicative of typical thin passive surface film [110]. Moreover, it can be observed from Fig. 72 that the frequency range over which the phase angle is close to -90° increased after 168 hours of immersion, indicating that the stability of the oxide film improved with time [110]. It can be noted that the maximum phase angle and the range of the frequency over which the phase angle remains high in the case of Al 6063, 316L SS and 304 SS was higher than that of all the other alloys (i.e. carbon-alloyed iron aluminides, 430 SS and low carbon mild steel). Therefore it can be concluded that the nature of the surface film on Al 6063, 316L SS and 304 SS was much better than that of *all* the other alloys. Moreover, the range of the frequency over which the phase angle remains high, in the case of Al 6063 was lower than that of 304LSS and 304 SS. This is indicative of superior surface film properties in the case 304 SS and 304 SS than that of Al 6063. This can be attributed to the active dissolution of aluminium in acidic solutions with low pH [79].

Bode magnitude plots (logarithm of impedance vs. logarithm of frequency) for all the alloys obtained after 2 and 24 hours of stabilisation are presented in Fig. 73. It can be noted that at high frequencies the impedance is dominated by electrolyte resistance while at very low frequencies the impedance is dominated by the surface film resistance (polarization resistance). It can be noted that the slope of the $\text{Log } |Z|$ vs. $\text{Log } f$ becomes zero at both high and low frequencies. At medium frequencies the capacitive behaviour is evident by the increase in the value of slope, for all the alloys. It is known that, for ideal capacitive behaviour the slope of $\text{Log } |Z|$ vs. $\text{Log } f$ should be -1 [110]. It can be noted from the Fig.73 that generally for all the alloys the slope of $\text{Log } |Z|$ vs. $\text{Log } f$ deviated from the value of -1 . To account for these deviations from the ideal capacitive behaviour, the constant phase element (CPE) was used while fitting the experimental data instead of a capacitor. As mentioned earlier, the values of $n < 1$ denote non-ideal behaviour. From Tables 13, 14 and 15, it can be seen that the values of 'n' were much less than one in case of all the alloys except for low carbon mild steel and Al 6063, indicating the deviation

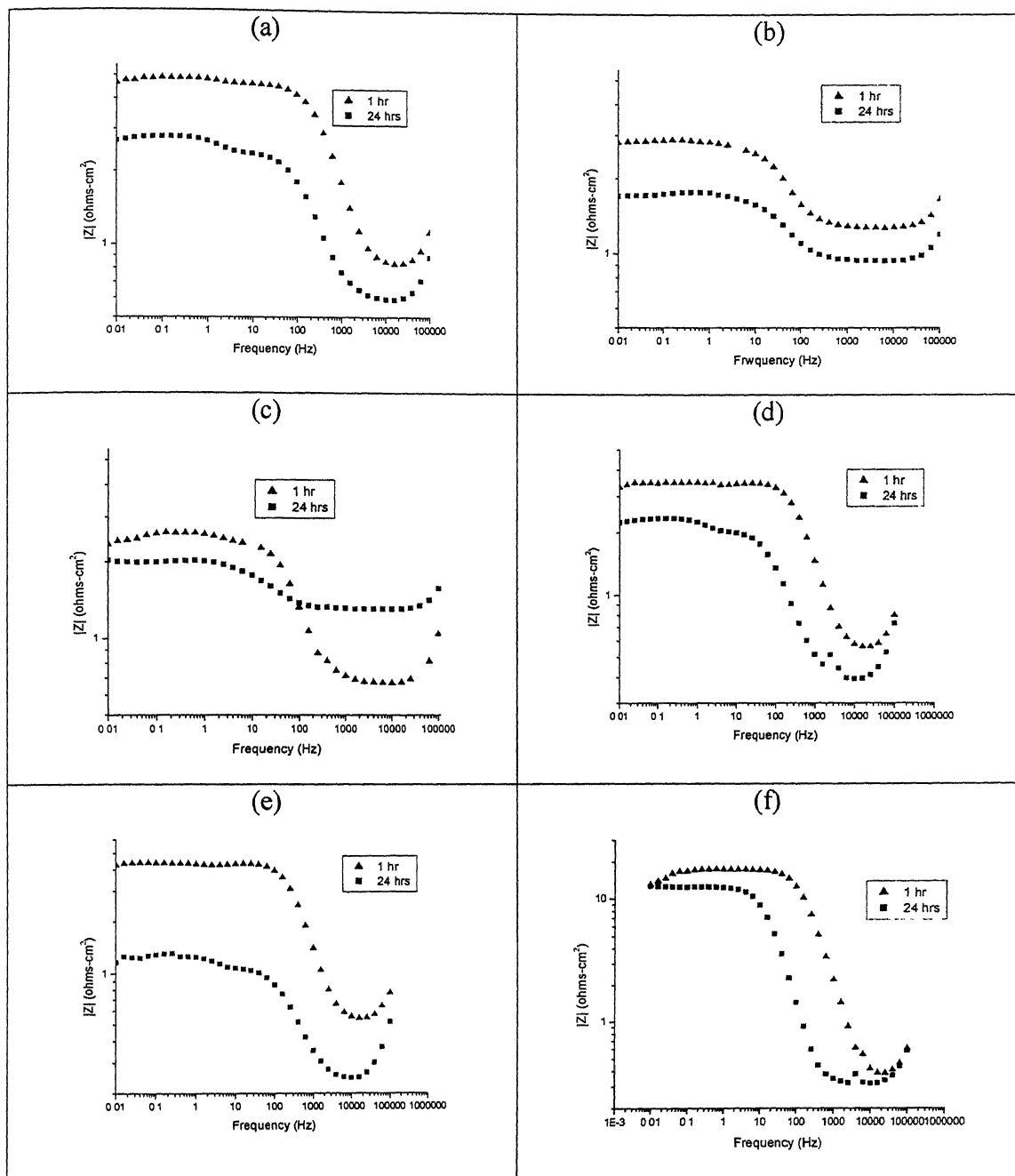


Fig. 73 Bode magnitude plots for the alloys in freely aerated 0.25 mol/lit H_2SO_4 after 2 hours and 24 hours (one day) of immersion time (a) Fe-19.2Al-3.3C-0.07Ce (b) Fe-18.5Al-3.6C (c) Fe-20.0Al-2.0C (d) Fe-19.2Al-3.3C-0.07Ce (LT) (e) Fe-19.2Al-3.3C-0.07Ce (ST) (f) Mild steel (g) 316L SS (h) Al 6063 (i) 304 SS (j) 430 SS.

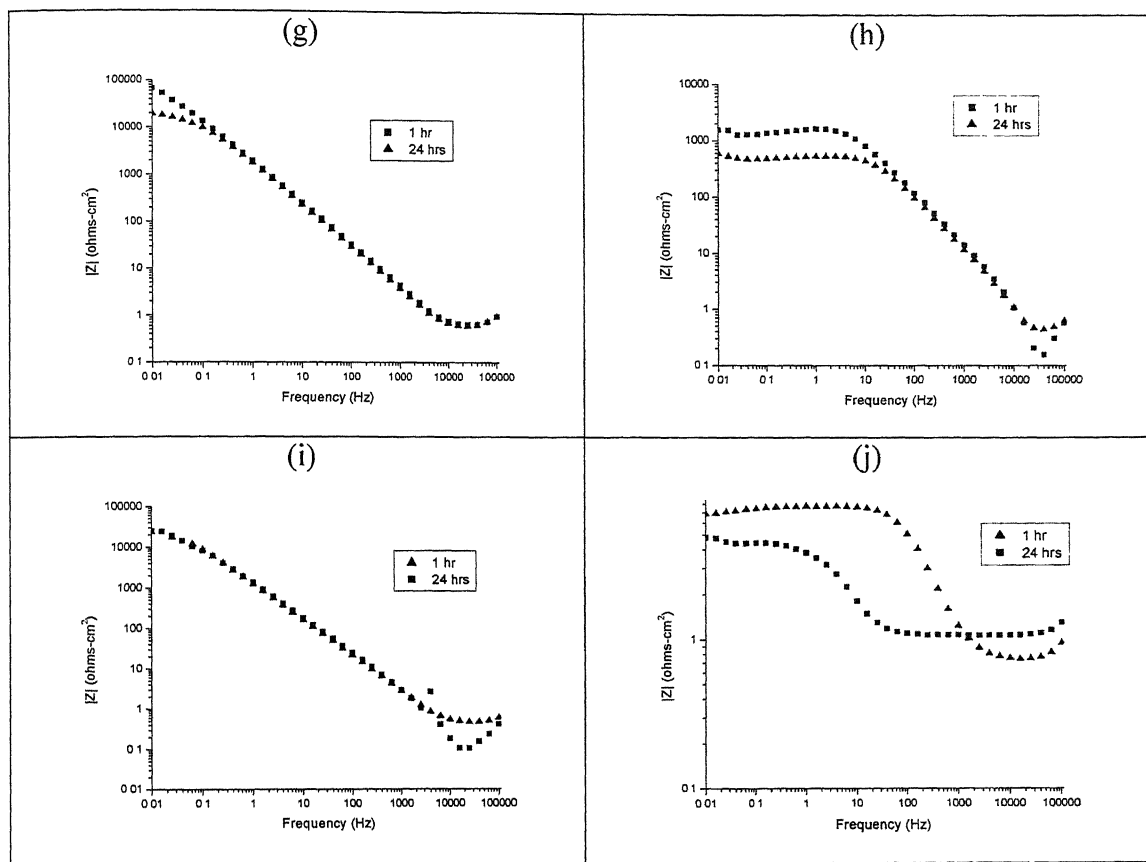


Fig. 73 (continued) Bode magnitude plots for the alloys in freely aerated 0.25 mol/lit H_2SO_4 after 2 hours and 24 hours (one day) of immersion time: (a) Fe-19.2Al-3.3C-0.07Ce (b) Fe-18.5Al-3.6C (c) Fe-20.0Al-2.0C (d) Fe-19.2Al-3.3C-0.07Ce (LT) (e) Fe-19.2Al-3.3C-0.07Ce (ST) (f) Mild steel (g) 316L SS (h) Al 6063 (i) 304 SS (j) 430 SS.

from ideal capacitive behaviour for all the alloys. The slopes of $\text{Log } |Z|$ vs. $\text{Log } f$, in the case of low carbon mild steel and Al 6063 were very close to 1. The nature of the Bode magnitude plot remained same for all the alloys after 24 hours of immersion. However, it can be noted that in case of 304 SS and 316L SS, the slope remained high even in the high frequency region.

The equivalent circuits used to fit the experimental data obtained in acidic solution are shown in the Fig. 74. The circuit shown in Fig. 74a was used to fit the experimental data when the impedance spectra contained only a single capacitive loop [115 and 116]. It can be noted that single capacitive loop is present in the case of 316L SS and 304 SS (refer Fig. 71g and i). The circuit shown in Fig. 74b was used to fit the experimental data when the impedance spectra contained a very high frequency inductive loop in addition to a high frequency capacitive loop. Such kind of an impedance spectra was obtained in the case of low carbon mild steel and 430 SS after 24 hours of immersion in 0.25 mol/lit H_2SO_4 (Fig. 71f and j). The circuit shown in Fig. 74c was used to fit the experimental data when the impedance spectra contained a low frequency inductive loop in addition to a high frequency capacitive loop and a very high frequency inductive loop [116]. Such an impedance response was obtained on first immersion, in the case of Fe-18.5Al-3.6C, Fe-20.0Al-2.0C, Fe-19.2Al-3.3C-0.07Ce (LT and ST sections), low carbon mild steel and 430 SS. (refer Fig. 71a through f and Fig. 71j). For Fe-18.5Al-3.6C and Fe-20.0Al-2.0C, the impedance spectra obtained after 24 hours of immersion exhibited all the components which were present on first immersion. The circuit shown in Fig. 74d was used to fit the experimental data when the impedance spectra contained a low frequency inductive loop and a low frequency capacitive loop in addition to a high frequency capacitive loop and a very high frequency inductive loop [116]. Such impedance spectra were obtained in case of Fe-19.2Al-3.3C-0.07Ce both on first immersion and after 24 hours of immersion. In the case of Al 6063, the circuit shown in Fig. 74e was used to fit the experimental data. A similar circuit was used by Shao et. al. [78] in the case of corrosion of pure aluminum in 1M KOH solution.

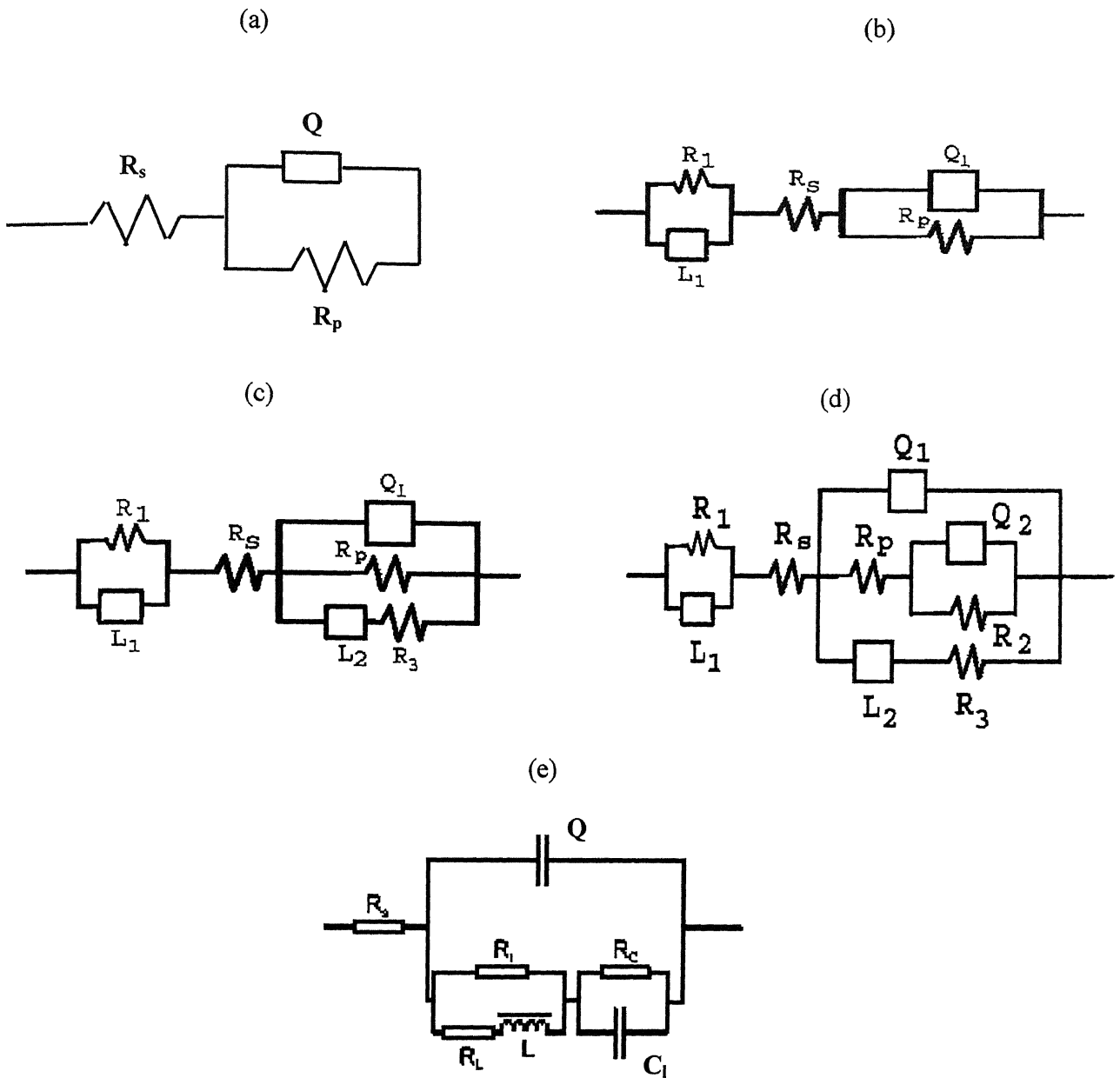


Fig. 74 The equivalent circuit to fit the complex plane plots composed of (a) a single capacitive loop (b) a high frequency inductive loop and capacitive loop (c) a high frequency inductive loop, a high frequency capacitive loop and a low frequency inductive loop (d) a high frequency inductive loop, two capacitive loops and a low frequency inductive loop (e) a high frequency capacitive loop, intermediate frequency inductive loop and low frequency capacitive loop.

For the circuits shown in Fig. 74a through Fig. 74d, the meaning of various symbols is as follows:

L_1	High frequency inductance
R_1	Resistance due to high frequency inductance
R_s	Solution Resistance
Q_1	CPE due to surface film
R_p	Polarization Resistance (Resistance due to surface film)
Q_2	CPE due to porous product layer
R_2	Resistance due to porous product layer
L_2	Low frequency inductance
R_3	Resistance due to low frequency inductance

And for the circuit shown in Fig. 74e, the meaning of various symbols is as follows:

R_s	Solution Resistance
Q	CPE due to surface film
R_t	Polarization Resistance (Resistance due to passive oxide film)
C_1	Capacitance due to porous product layer
R_c	Resistance due to porous product layer
L	Low frequency inductance
R_l	Resistance due to low frequency inductance

The theoretically estimated impedance spectra based on fitting the experimental data with the circuits shown in Fig. 74 have all been collected and presented in Appendix B. The circuit parameters obtained after fitting of the experimental data are presented in the Tables 13, 14 and 15 where very low chi-squared values obtained on fitting the experimental data indicate good fitting. It can be noted from Tables 13 and 14 that the solution resistance was in the range of 0.2 to 1.2 ohms-cm², both on first immersion and after 24 hours of immersion for all the alloys. Moreover it can be noted there was no appreciable change in the value of solution resistance during 24 hours of immersion.

The impedance spectra for Fe-18.5Al-3.6C and Fe-20.0Al-2.0C in the freely aerated 0.25 mol/lit H_2SO_4 solution are presented in Figures 71, 72 and 73. Both the alloys exhibited a very high frequency inductance, a high frequency capacitive loop and a low frequency inductive loop (Fig. 71b and c). The circuit parameters obtained after fitting the experimental data for these alloys with the circuit shown in Fig. 74c are tabulated in Table 13. On comparison of the polarization resistance (R_p values in Table 13) of the above two alloys, we can see that after 24 hours of immersion R_p values for both Fe-18.5Al-3.6C and Fe-20.0Al-2.0C decreased and were close to each other. Overall, it can be concluded that the surface film nature (and may be the corrosion resistance) of the two alloys Fe-18.5Al-3.6C and Fe-20.0Al-2.0C were generally comparable in 0.25 mol/lit H_2SO_4 solution. This is reasonable because the carbon contents are not significantly different and moreover the carbide distribution in these alloys was similar [48]. It can be noted here that in borate buffered solution, the effect of carbon content could be seen (Table 12). In 0.25 mol/lit H_2SO_4 solution, the effect of carbon addition (i.e. presence of carbide particles) could also not be observed. This can be attributed to the aggressively corrosive nature of 0.25 mol/lit H_2SO_4 as against mildly corrosive nature of borate buffered solution.

The impedance spectra of long transverse (LT) and short transverse (ST) sections of Fe-19.2Al-3.3C-0.07Ce in the freely aerated 0.25 mol/lit H_2SO_4 solution are presented in Fig. 71d & e, Fig. 72d & e and Fig. 73d & e. The circuit parameters obtained after fitting the experimental data for LT and ST sections of Fe-19.2Al-3.3C-0.07Ce with the circuits shown in Fig. 74c and d, are tabulated in Table 13. From Table 13 it can be observed that the values of the polarization resistance are not much different for the different sections of Fe-19.2Al-3.3C-0.07Ce. Moreover, it can also be noted that the decrease in polarization resistance of LT section after 24 hours of immersion is much more than that of other two sections.

The effect of the cerium addition to the intermetallics becomes clearer when the impedance spectra of alloys Fe-18.5Al-3.6C and Fe-19.2Al-3.3C-0.07Ce are compared, as these two alloys have almost equal aluminum and carbon contents. The most important difference from the other carbon-alloyed iron aluminides is the presence of a low frequency capacitive loop in the Nyquist plot of Fe-19.2Al-3.3C-0.07Ce (Fig 71a) which

becomes more prominent after 24 hours of immersion time. This indicates that some changes in the surface coverage occurred due to the addition of cerium. Moreover, on comparing the values of the polarization resistance of Fe-19.2Al-3.3C-0.07Ce and Fe-18.5Al-3.6C (Table 13) it can be observed that the polarization resistance of Fe-19.2Al-3.3C-0.07Ce was significantly higher than that of Fe-18.5Al-3.6C. Although the values of polarization resistance of both the alloys diminished after 24 hours of immersion, the polarization resistance of Fe-19.2Al-3.3C-0.07Ce was higher compared to that of Fe-18.5Al-3.6C. This is also evident in the Nyquist plots (Fig 71a and b) for these alloys which clearly revealed that the diameter of the high frequency capacitive loop was higher for Fe-19.2Al-3.3C-0.07Ce as compared to that of Fe-18.5Al-3.6C, both after 1 hr and 24 hours of immersion. Moreover, the Bode phase plots for the two alloys (Figures 72a and b) reveal that the phase angle for Fe-19.2Al-3.3C-0.07Ce was higher than that of Fe-18.5Al-3.6C both after one hr and 24 hours of immersion, indicating the formation of more compact capacitive layer in the case of Fe-19.2Al-3.3C-0.07Ce. As the corrosion rate for Ce-alloyed material was lower, it is reasonable to conclude based on EIS studies that Ce addition modified the surface film.

On comparing the polarization resistance values of the three carbon-alloyed iron aluminide samples with low-carbon mild steel (Tables 13 and 14), it can be observed that the polarization resistance of mild steel is much higher than that of the carbon-alloyed iron aluminide samples both, after one hr and after one day of immersion. It may be expected that the carbon-alloyed iron aluminide samples should exhibit enhanced polarization resistance compared to the mild steel sample because of the presence of aluminium in them. However, the Al contents at this level present in the alloys (19.2 wt% in Fe-19.2Al-3.3C-0.07Ce, 18.5 wt% in Fe-18.5Al-3.6C and 20.0 wt% in Fe-20.0Al-2.0C) did not affect surface sensitive properties. This indicates that the higher polarization resistance for mild steel may be due the low carbon content of mild steel as compared to the carbon-alloyed iron aluminide samples. As stated earlier, the higher dissolution rate of carbon-alloyed iron aluminide samples could be due to the preferential attack of matrix near carbide particles [45].

It can also be noted from Tables 13, 14 and 15 that the polarization resistance (R_p) values for 304 SS, 316L SS and Al 6063 in 0.25 mol/lit H_2SO_4 were much higher than

that of the carbon-alloyed iron aluminide samples while the polarization resistance of 430 SS was comparable. Therefore, it can be concluded that in case of 316L SS, 304 SS and Al6063 the surface film that forms on the surface in the acidic solution was much more protective as compared to that on 430 SS and the carbon alloyed intermetallics. This can be attributed to the presence of chromium and nickel in 304 SS and 316L SS. It can also be noted from Table 14, that the polarization resistance of 304 SS and 316L SS were comparable both on first immersion and after 24 hours of immersion in acidic solution. Moreover, it can also be noted from Table 14 and 15 that the polarization resistance of 316L SS and 304 SS was higher than that of Al 6063 alloy. Looking at the polarization resistance values 316L and 304 SS alloys from Table 14, it can be observed that the increase in the polarization resistance for 316L SS, after one day of immersion in 0.25 mol/lit H_2SO_4 solution, was much more than that of 304 SS. This indicates that the improvement in the surface film properties with time, for 316L SS was much more than that of 304 SS.

In summary, the values of polarization resistance for all the three iron aluminide alloys diminished after one day of immersion time. This may be due to the aggressively corrosive nature of 0.25 mol/lit H_2SO_4 solution. However, the polarization resistance of the Ce-alloyed iron aluminide was higher than the other iron aluminides at all times indicating that the Ce addition results in the improvement of the surface film properties of carbon-alloyed iron aluminides.

It can be noted that in case of Al 6063, the value of 'n' was very close to one both on first immersion and after 24 hours of immersion in 0.25 mol/lit H_2SO_4 solution (Table 15). Therefore, the magnitude of the CPE can be approximated to be equal to capacitance of the surface film [92]. The capacitance of the surface film is inversely proportional to the thickness of the surface film [92]. From Table 15, it can also be noted that the value of the CPE (approximated to be equal to capacitance of surface film) decreased, while the value of the polarization resistance increased after 24 hours of immersion in 0.25 mol/lit H_2SO_4 solution. The increase in the capacitance value can be attributed to the growth of the surface film with time, indicating long-term stability of the surface film [110]. Equivalent circuit used to fit the experimental data of Al 6063 is shown in Fig. 74e. A similar circuit was used by Shao et. al. [78] for fitting the impedance response of pure

aluminum in 1M KOH solution. However, they found that this circuit model could not explain the reason why the inductive loop and the low-frequency capacitive loop exist. The values of the equivalent elements, 'L' and 'C₁' were extraordinarily high ($\sim 10^{-2}$ H cm⁻² and 10^{-2} Fcm⁻²). A high value of a capacitor means a large electrode area and/or a small thickness of the dielectric, therefore they suggested that element 'C₁' does not represent a 'real' capacitor. They also denied the existence of a 'real' inductance exists. So they concluded that elements 'L' and 'C₁' reflect only the response characteristics caused by the electrochemical process, and their meaning could not be explained by the circuit model. In the present study also, the values of L and C₁ were extraordinarily high ($\sim 10^3$ H cm⁻² and 10^{-2} Fcm⁻²) (refer Table 15). Therefore, it is reasonable to conclude that elements 'L' and 'C₁' reflect only the response characteristics caused by the electrochemical process.

Table 13 Values of all the circuit parameter for different sections of Fe-19.2Al-3.3C-0.07Ce, Fe-18.5Al-3.6C and Fe-20.0Al-2.0C obtained after fitting the experimental data obtained in acidic solution with the circuit shown in Figure 74. The percentage error is shown within brackets.

S.No.	Circuit Paramètres	Fe-19.2Al-3.3C-0.07Ce						Fe-18.5Al-3.6C			Fe-20.0Al-2.0C		
		LT		ST		RD		1 hour	24 hours		1 hour	24 hours	
		1 hour	24 hours	1 hour	24 hours	1 hour	24 hours						
1	L_1 (Henri-cm ²)	6.141E-7 (5.456)	5.94E-7 (2.826)	6.967E-7 (2.756)	7.009E-7 (6.28)	7.924E-7 (5.129)	6.645E-7 (2.603)	8.312E-7 (8.715)	6.264E-7 (5.456)		8.317E-7 (7.154)	6.476E-7 (5.817)	
2	R_1 (ohms-cm ²)	0.4361 (6.839)	0.7056 (7.36)	1.072 (8.697)	0.8139 (15.5)	0.6818 (7.965)	0.7003 (5.305)	0.4966 (10.82)	0.4701 (8.32)		0.6753 (11.48)	0.4906 (8.888)	
3	R_s (ohms-cm ²)	0.5157 (1.335)	0.2362 (1.446)	0.5405 (0.9919)	0.395 (2.319)	0.7964 (1.171)	0.8267 (0.4856)	1.274 (0.7649)	0.9346 (0.5757)		0.6645 (1.296)	1.306 (0.4478)	
4	Q_1 (S-sec ⁿ /cm ²)	0.0002897 (8.48)	0.003686 (12.75)	0.0002667 (5.912)	0.003193 (19.25)	0.0002968 (8.043)	0.001575 (5.363)	0.008226 (10.86)	0.02069 (10.52)		0.003209 (11.51)	0.0406 (12.31)	
5	n	0.9096 (1.086)	0.8282 (1.97)	0.9115 (0.7556)	0.8171 (3.163)	0.8871 (1.082)	0.8311 (0.8533)	0.835 (2.291)	0.7872 (2.402)		0.8876 (1.997)	0.7687 (3.179)	
6	R_p (ohms-cm ²)	3.942 (1.746)	0.8752 (2.432)	2.941 (0.5388)	1.715 (4.059)	3.847 (1.183)	2.065 (0.9087)	1.571 (1.563)	0.8311 (1.731)		1.897 (1.571)	0.7442 (2.551)	
7	L_2 (Henri-cm ²)	1.338 (153.5)	68.3 (58.82)	614.9 (30.32)	213.1 (111.1)	958.1 (64.48)	220.7 (27.67)	0.00245 (51.22)	20.55 (63.9)		83.91 (53.6)	9.431 (77.16)	
8	R_3 (ohms-cm ²)	147.6 (63.54)	12.29 (31.73)	28.42 (52.13)	23.29 (72.21)	72.64 (59.39)	28.97 (16.19)	1.421 (99.29)	11.46 (29.75)		17.97 (33.47)	9.812 (33.38)	
9	Q_2 (S-sec ⁿ /cm ²)	-	0.415 (37.27)	-	0.5027 (72.73)	0.3939 (74.44)	0.4389 (19.72)	-	-		-	-	
10	N	-	0.9993 (15.55)	-	1 (36.28)	1 (30.69)	1 (9.452)	-	-		-	-	
11	R_2 (ohms-cm ²)	-	0.1788 (16.92)	-	0.2582 (39.84)	0.2295 (28.91)	0.2767 (10.16)	-	-		-	-	
	Chi-Square	4.252e-04	7.012e-04	3.013e-04	2.252e-03	5.835e-04	1.113e-04	4.176e-04	2.660e-4		1.176e-3	1.819e-04	

Table 14 Values of all the circuit parameter for Mild Steel, 304 SS and 430 SS obtained after fitting the experimental data in acidic solution with the circuit shown in Figure 74. The percentage error is shown within brackets.

S.No	Circuit Parameters	Mild steel		304 SS		430 SS		316L SS	
		1 hour	24 hours	1 hour	24 hours	1 hours	24 hours	1 hours	24 hours
1	L_1 (Henri-cm ²)	7.575E-7 (7.254)	7.922E-7 (5.72)	-	-	5.956E-7 (3.199)	6.455E-7 (10.04)	-	-
2	R_1 (ohms-cm ²)	0.9768 (19.58)	1.206 (19.45)	-	-	0.7472 (8.101)	0.6398 (20.49)	-	-
3	R_s (ohms-cm ²)	0.4808 (2.903)	0.4243 (1.781)	0.5057 (6.893)	0.4871 (24.55)	0.7334 (0.6186)	1.063 (0.9097)	0.4451 (6.832)	0.4641 (7.352)
4	Q_1 (S-sec ⁿ /cm ²)	6.664E-5 (8.537)	8.952E-4 (6.207)	1.509E-4 (5.476)	1.569E-4 (15.35)	4.492E-4 (3.175)	255.0E-4 (5.993)	1.615E-4 (5.779)	1.586E-4 (4.705)
5	N	0.9833 (1.003)	1 (0.9757)	0.8964 (1.026)	0.8428 (2.978)	0.8999 (0.459)	0.8478 (1.769)	0.9014 (1.055)	0.8859 (0.9252)
6	R_p (ohms-cm ²)	21.69 (1.314)	15.63 (1.386)	2.807E4 (12.96)	3.281E4 (36.3)	7.045 (0.4448)	3.439 (1.483)	1.253E4 (8.03)	8.223E4 (19.43)
7	L_2 (Henri-cm ²)	645.1 (24.36)	-	-	-	156.7 (12.42)	-	-	-
8	R_3 (ohms-cm ²)	80.6 (20.9)	-	-	-	48.34 (7.123)	-	-	-
	Chi-Square	2.599e-03	2.707e-03	2.764e-02	2.508e-01	1.889e-04	1.092e-03	2.715e-02	2.940e-02

Table 15 Values of all the circuit parameters for Al 6063 obtained after fitting the experimental data in acidic solution with the circuit shown in Figure 74e. (Error is shown in the brackets)

S. No.	Circuit Parameters	Al 6063	
		1 hour	24 hours
1	R_s (ohms-cm ²)	0.5511 (10.63)	0.4465 (17.52)
2	Q (S-sec ⁿ /cm ²)	1.511E-5 (5.6)	1.088E-5 (13.44)
3	n	1 (2.103)	0.9922 (1.588)
4	R_p (ohms-cm ²)	521.6 (7.009)	1654 (6.641)
5	R_l (ohms-cm ²)	3662 (150.9)	6628 (79.38)
6	L (Henri-cm ²)	4908 (191)	5638 (58.14)
7	C_l	0.06835 (84.77)	0.02636 (48.89)
8	R_c (ohms-cm ²)	359.5 (114.5)	1216 (82.75)
9	Chi-Square	4.649e-02	3.299e-02

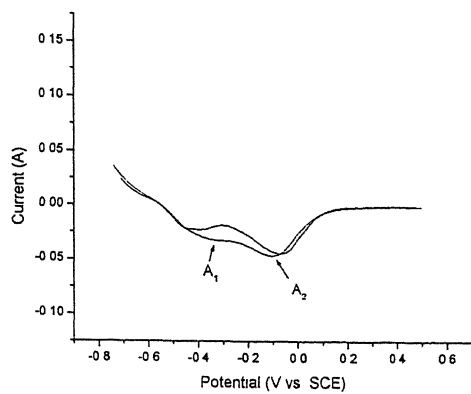
4.4 Cyclic Voltammetry

The electrochemical behavior of the as-received Fe-20.0Al-2.0C, Fe-18.5Al-3.6C and Fe-19.2Al-3.3C-0.07Ce alloys was also understood in the 0.25 mol/lit H_2SO_4 solution by means of cyclic voltammetry. The experiments were conducted in the potential range of -0.75 V to 0.5 V vs. SCE (forward scan -0.75 V to 0.5 V and reverse scan 0.5 V to -0.75 V). Moreover, the experiments were conducted just after immersion without the stabilization of free corrosion potential.

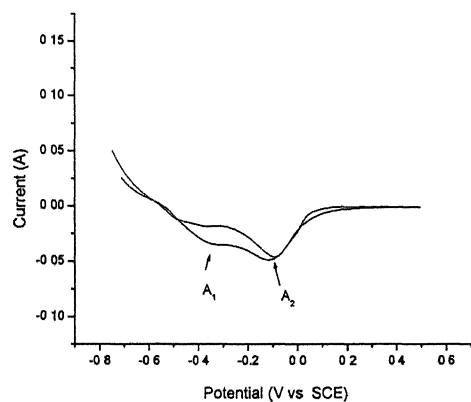
Figures 75, 76 and 77 show the cyclic voltammograms of all the three carbon-alloyed intermetallics in 0.25 mol/lit H_2SO_4 . It can be observed that two anodic peaks appear in the forward scan of voltammetry all these carbon-alloyed intermetallics. The first peak is designated as A_1 while the second peak is designated as A_2 in the voltammograms (Fig. 75, 76 and 77). Moreover, it can also be observed from the voltammetry responses of these intermetallics that peaks appeared only in the forward (anodic) scan. The peaks do not appear in the reverse (cathodic) scan (Fig. 75, 76 and 77). The reason for the absence of cathodic peaks in the inverse scan may be the irreversible nature of the electrode reactions [93].

Table 16 lists the possible redox reactions [117] expected in the system. Using Table 16 and the position of the peaks that appear in Fig. 75, 76 and 77, it can be inferred that peak A_1 may be due to the redox reaction shown in equation (3) whereas peak A_2 can be attributed to either of the redox reactions shown in equation (9) and (10). It can also be noted that only the peaks corresponding to the redox reactions of iron were obtained in the voltammograms. The peaks for the redox reactions of aluminium and cerium were absent. The reason for the absence of Al and Ce peaks may be because no redox reactions for aluminum and cerium occur in the potential range in which experiments were conducted (refer Table 16). Values of peak potentials and peak currents for the peaks obtained are presented in Table 17 for all the three alloys. From Table 17, it can be observed that generally the values of the peak currents for all the three alloys increased with the scan rate. This result is reasonable because peak current is directly proportional to the scan rate [93].

(a)



(b)



(c)

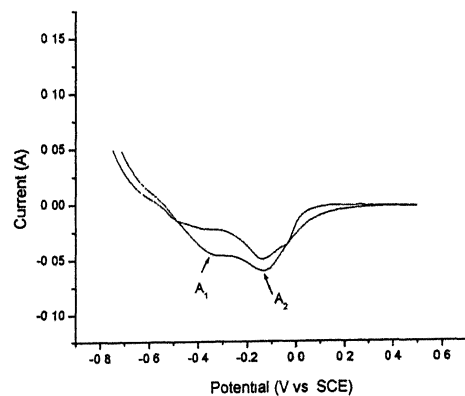
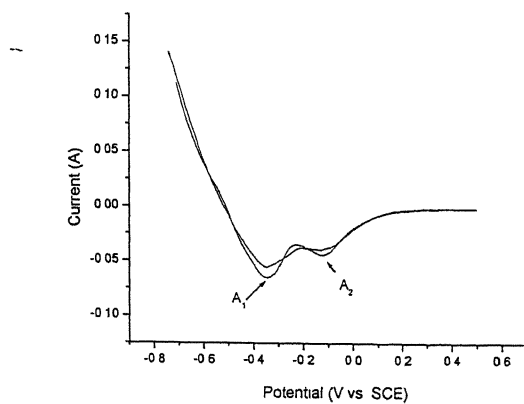
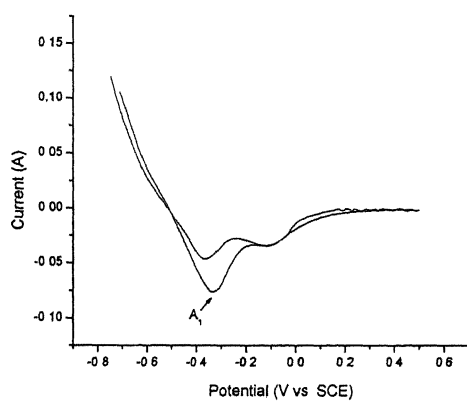


Fig. 75 Cyclic voltammograms for Fe-19.2Al-3.3C-0.07Ce in 0.25 mol/lit H_2SO_4 (a) 10 mV/sec (b) 50 mV/sec (c) 100 mV/sec

(a)



(b)



(c)

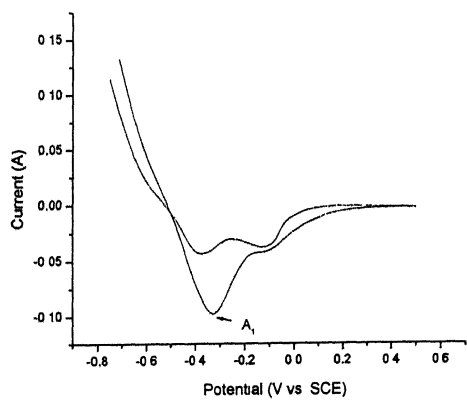
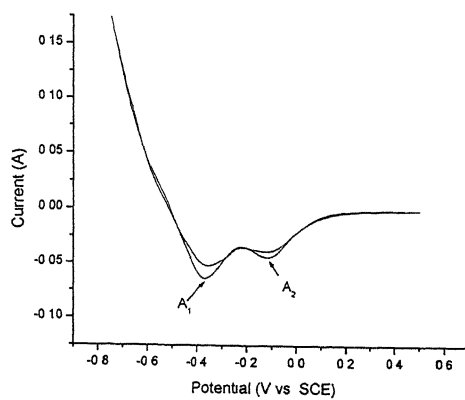
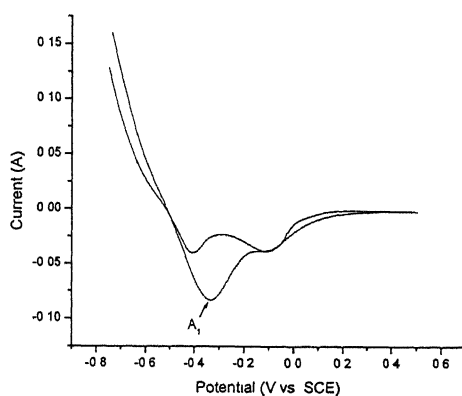


Fig.76 Cyclic voltammograms for Fe-18.5Al-3.6C in 0.25 mol/lit H_2SO_4 (a) 10 mV/sec
(b) 50 mV/sec (c) 100 mV/sec

(a)



(b)



(c)

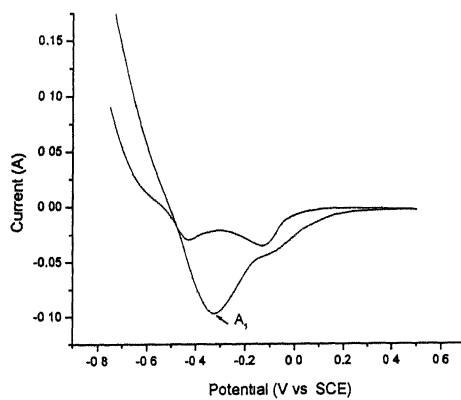


Fig. 77 Cyclic voltammograms for Fe-20.0Al-2.0C in 0.25 mol/lit H_2SO_4 (a) 10 mV/sec
(b) 50 mV/sec (c) 100 mV/sec

On comparing the cyclic voltammetry responses of Fe-20.0Al-2.0C and Fe-18.5Al-3.6C in freely aerated 0.25 mol/lit H_2SO_4 (Figures 76 and 77) it can be observed that, at low scan rate of 10 mV/sec, both A_1 and A_2 peaks were obtained for these alloys. It can also be seen that peaks for both these alloys appeared at nearly same positions with almost same values of the peak currents (refer Table 17). Moreover, it can be noted that for both of these intermetallics that A_2 peak disappeared when the cyclic voltammograms were recorded at higher scan rates of 50 and 100 mV/sec (see Fig. 76 and 77). Peaks A_1 has been attributed to be due to the redox reaction shown in Equation (3) (which results in the formation of Fe_3^+ ion) whereas peak A_2 is attributed to the redox reaction shown in Equations (9) and (10) (which result in the formation of $\text{Fe}(\text{OH})_2^+$ and FeOH^{+2} ions, respectively). Since the peak A_1 was much more prominent than the other peak, it can be concluded that in Fe-20.0Al-2.0C and Fe-18.5Al-3.6C, mainly Fe_3^+ ion forms on the oxidation of iron. From Table 17 it can also be observed that on increasing the scan rate, peak potential for both these intermetallics shifted towards positive potentials. Overall, it can be observed that both the alloys exhibited similar behavior. This is reasonable because the carbon contents are not significantly different and moreover the carbide distribution in these alloys was similar.

The effect of the addition of Ce to the intermetallics become more clear when the cyclic voltammetry responses of alloys Fe-18.5Al-3.6C and Fe-19.2Al-3.3C-0.07Ce are compared, as these two alloys contain equal aluminum and carbon contents. As already discussed, the cyclic voltammogram of Fe-18.5Al-3.6C revealed two anodic peaks (A_1 and A_2) whereas for Fe-19.2Al-3.3C-0.07Ce only the second anodic peak (A_2) was obtained. This peak A_2 can be attributed to either of the oxidation reactions shown in Equations (9) and (10) in Table 16. It can be observed from the Table 17 that peak potentials in the case of Fe-19.2Al-3.3C-0.07Ce shifted towards negative potentials on increasing the scan rate. This trend in shift of peak potential with scan rate was opposite to that observed in the case of Fe-18.5Al-3.6C and Fe-20.0Al-2.0C. As the peak due to the oxidation reaction shown in equation (3) was not present in the cyclic voltammogram of Fe-19.2Al-3.3C-0.07Ce, it can therefore be concluded that the direct dissolution of iron in the form of Fe^{+3} ions into the solution may have been retarded due to the presence of cerium in Fe-19.2Al-3.3C-0.07Ce. Moreover, in Fe-19.2Al-3.3C-0.07Ce, the peaks

due to the formation of $\text{Fe}(\text{OH})_2^+$ and FeOH^{+2} ions were observed. These ions may aid passivation by adsorbing on the surface.

Dissolution of iron seems to be prominent for non-Ce alloyed sample, whereas the formation of $\text{Fe}(\text{OH})_2^+$ and FeOH^{+2} seem to be prominent for Ce-alloyed sample. These ions adsorbing on the surface may enhance the passivity in case of Ce-alloyed iron aluminide and result in lower corrosion rate as function of time. Improved surface film properties were indicated, in the case of Ce-alloyed iron aluminide as compared to the other iron aluminides in acidic solution (refer Table 13). Therefore, by combining the results of EIS studies and cyclic voltammetry in acidic solution, it can be concluded that the improved corrosion resistance of Ce-alloyed iron aluminide may be due to the formation of ions which adsorb on the surface and enhance its passivity.

Table 16 List of anticipated redox reactions [117].

Equation. No.	Balanced half reaction	E° vs.SHE (V)	E° vs.SCE (V)
1	$\text{Al}^{3+} + 3\text{e}^- \rightleftharpoons \text{Al}$	- 1.662	-1 903
2	$\text{Al}(\text{OH})_3(\text{s}) + 3\text{e}^- \rightleftharpoons \text{Al}(\text{s}) + 3\text{OH}^-$	- 2.300	-2 541
3	$\text{Fe}(\text{s}) \rightleftharpoons \text{Fe}^{3+} + 3\text{e}^-$	- 0.040	-0.281
4	$\text{Fe}^{3+} + \text{e}^- \rightleftharpoons \text{Fe}^{2+}$	+0.771	+0 530
5	$\text{FeOH}^+ + 2\text{e}^- \rightleftharpoons \text{Fe} + \text{OH}^-$	-0.560	-0 801
6	$\text{Fe}(\text{OH})_3 + \text{e}^- \rightleftharpoons \text{Fe}(\text{OH})_2 + \text{OH}^-$	-0.560	-0 801
7	$\text{FeSO}_4 + 2\text{e}^- \rightleftharpoons \text{Fe} + \text{SO}_4^{2-}$	-0.510	-0.751
8	$\text{Fe}^{2+} + 2\text{e}^- \rightleftharpoons \text{Fe}$	- 0.440	-0 681
9	$\text{FeOH}^{+2} + 3\text{e}^- \rightleftharpoons \text{Fe} + \text{OH}^-$	0.100	-0.141
10	$\text{Fe}(\text{OH})_2^+ + 3\text{e}^- \rightleftharpoons \text{Fe} + 2\text{OH}^-$	0.120	-0.121
11	$\text{Fe}(\text{OH})_2 + 2\text{e}^- \rightleftharpoons \text{Fe} + 2\text{OH}^-$	-0.880	-1 121
12	$\text{Ce}^{3+} + 3\text{e}^- \rightleftharpoons \text{Ce}$	- 2.480	-2 721
13	$\text{Ce}(\text{OH})_3 + 3\text{e}^- \rightleftharpoons \text{Ce} + 3\text{OH}^-$	-2.870	-3 111
14	$\text{CeSO}_4^+ + 3\text{e}^- \rightleftharpoons \text{Ce} + \text{SO}_4^{2-}$	-2.520	-2.761

Table 17 Peak potential and peak current values at different scan rate for different peaks in the voltammogram of Fe-18.5Al-3.6C, Fe-20.0Al-2.0C and Fe-19.2Al-3.3C-0.07Ce

Alloy	Scan Rate (mV/sec)	Peak Potential (mV vs. SCE)		Peak Current (mA/cm ²)	
		A ₁	A ₂	A ₁	A ₂
Fe-19.2Al-3.3C-0.07Ce	10	-108	-	45	-
	50	-115	-	48	-
	100	-130	-	59	-
Fe-18.5Al-3.6C	10	-342	-123	64	43
	50	-334	-	75	-
	100	-327	-	97	-
Fe-20.0Al-2.0C	10	-367	-117	63	44
	50	-332	-	82	-
	100	-327	-	96	-

4.5 Scanning electron microscopy

In attempt to understand the effect of cerium on the formation and growth of oxide film in Fe-19.2Al-3.3C-0.07Ce and Fe-18.5Al-3.6C the specimen surfaces of these alloys were examined using scanning electron microscopy. SEM micrographs were taken after exposing both the alloys to 0.25 mol/lit H_2SO_4 solution for a period of 24 hours. Fig. 78 through Fig. 84 shows the surface morphology of both the alloys examined by SEM. It can be noted, that the SEM micrographs of both the alloys after immersion for 24 hours in 0.25 mol/lit H_2SO_4 solution revealed only the formation a corrosion product layer. The effect of cerium could not be revealed through these micrographs. Moreover, it can also be noted that the SEM micrographs of Fe-19.2Al-3.3C-0.07Ce without immersion in the acidic solution showed small carbide particles finely distributed in the matrix.

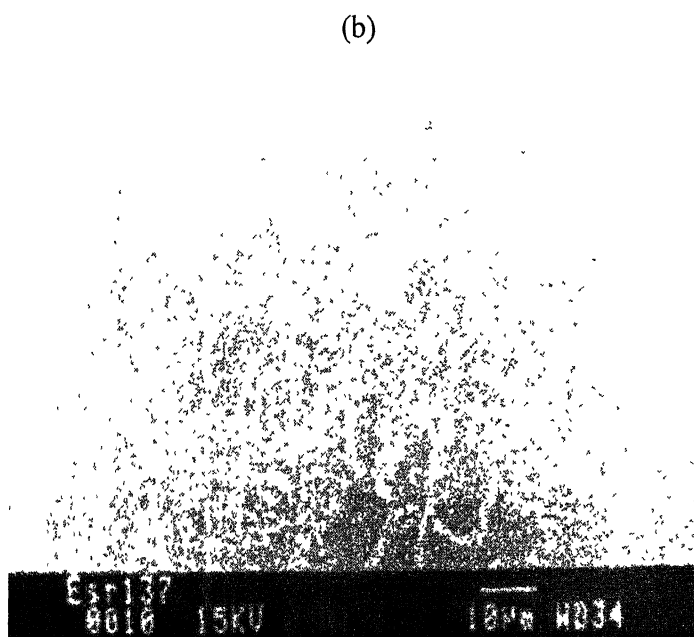
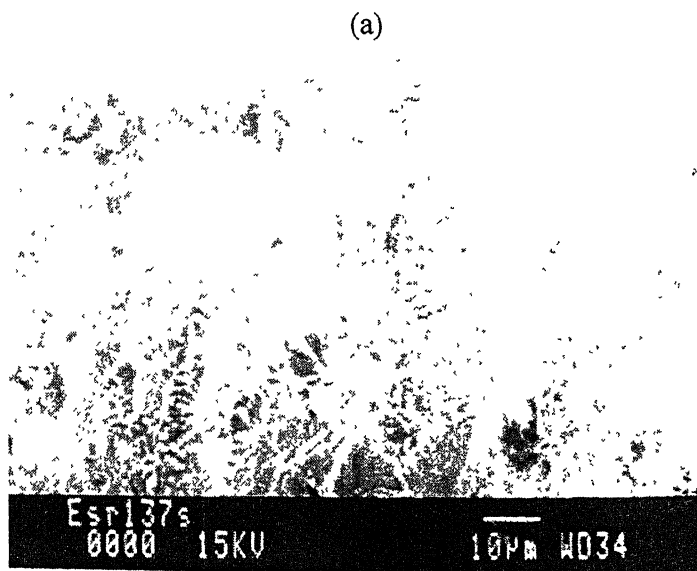


Figure 78 SEM Micrograph of Fe-19.2Al-3.3C-0.07Ce (ESR137) (a) after immersion in freely aerated 0.25 mol/lit H_2SO_4 solution for 24 hour (b) without immersion in acidic solution.

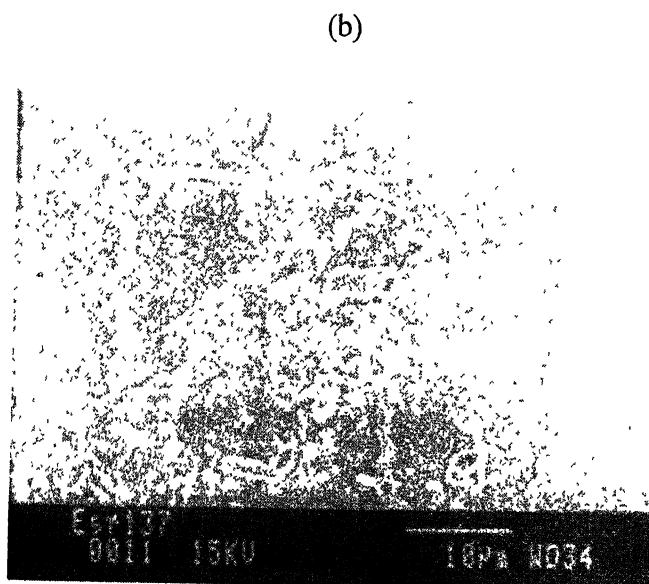
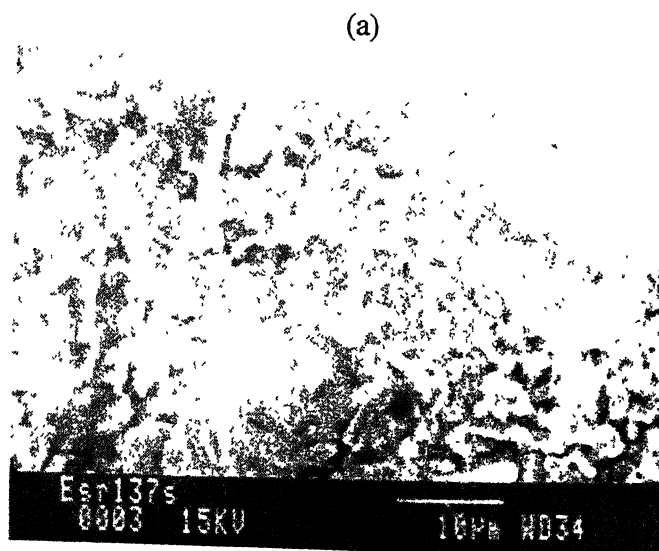
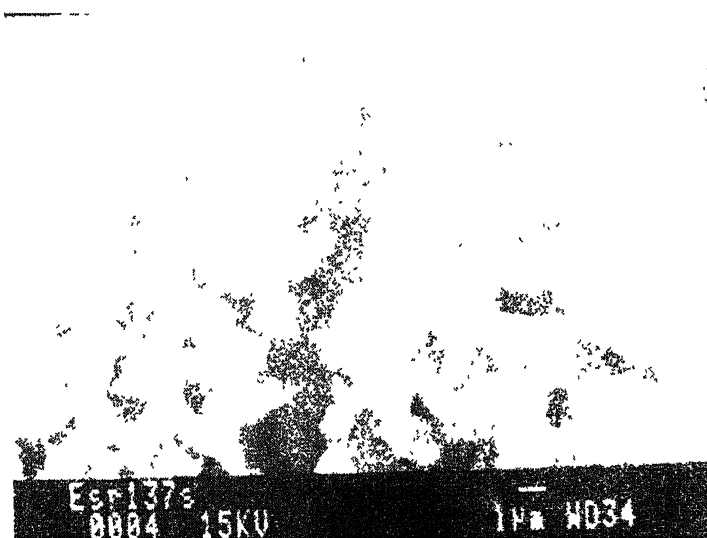


Figure 79 SEM Micrograph of Fe-19.2Al-3.3C-0.07Ce (ESR137) (a) after immersion in freely aerated 0.25 mol/lit H_2SO_4 solution for 24 hour (b) without immersion in acidic solution.

(a)



(b)

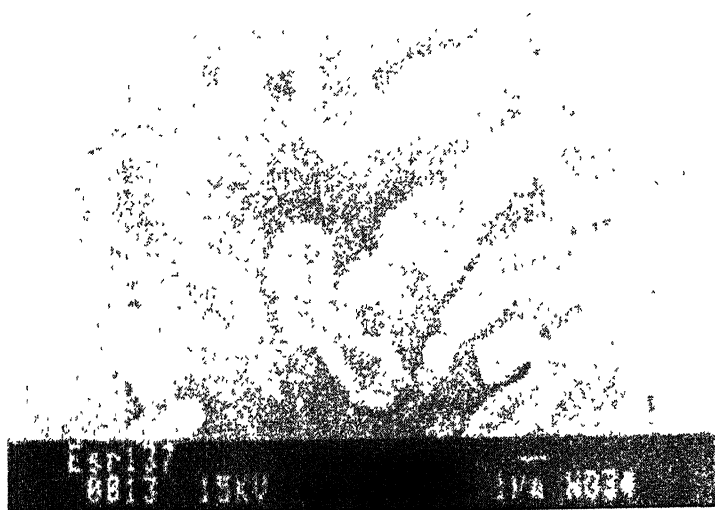


Figure 80 SEM Micrograph of Fe-19.2Al-3.3C-0.07Ce (ESR137) (a) after immersion in freely aerated 0.25 mol/lit H_2SO_4 solution for 24 hour (b) without immersion in acidic solution.

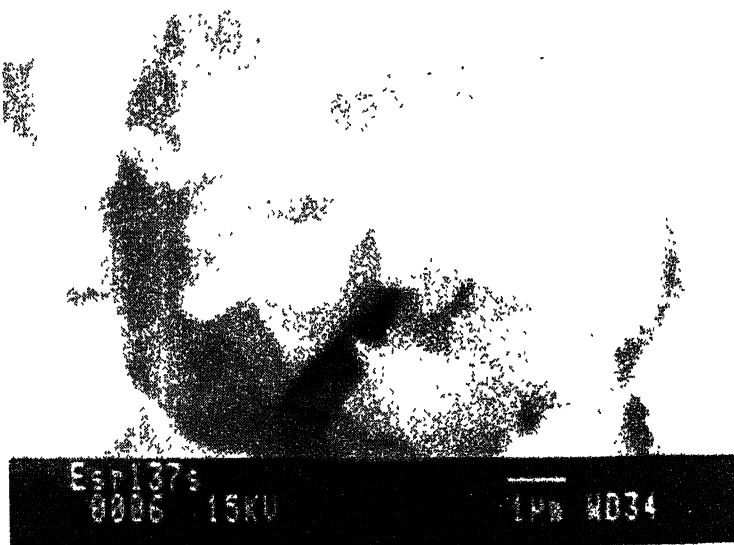


Figure 81 SEM Micrograph of Fe-19.2Al-3.3C-0.07Ce (ESR137) after immersion in freely aerated 0.25 mol/lit H_2SO_4 solution for 24 hours.

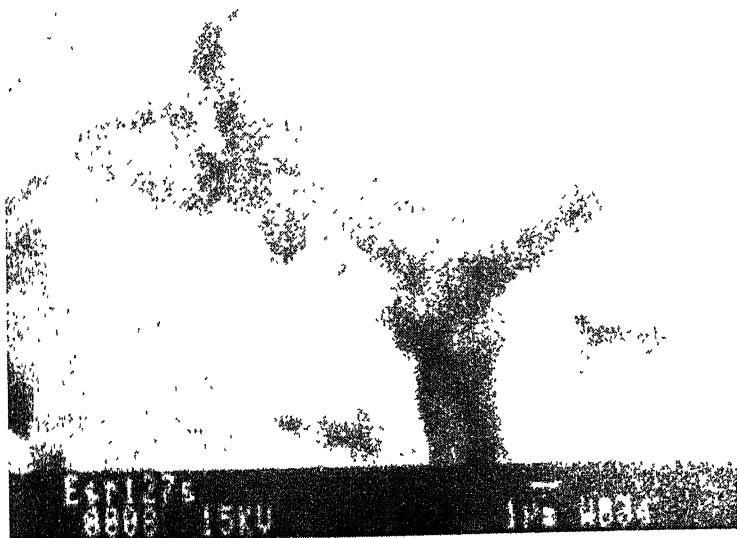


Figure 82 SEM Micrograph of Fe-18.5Al-3.6C (ESR127) after immersion in freely aerated 0.25 mol/lit H_2SO_4 solution for 24 hour.

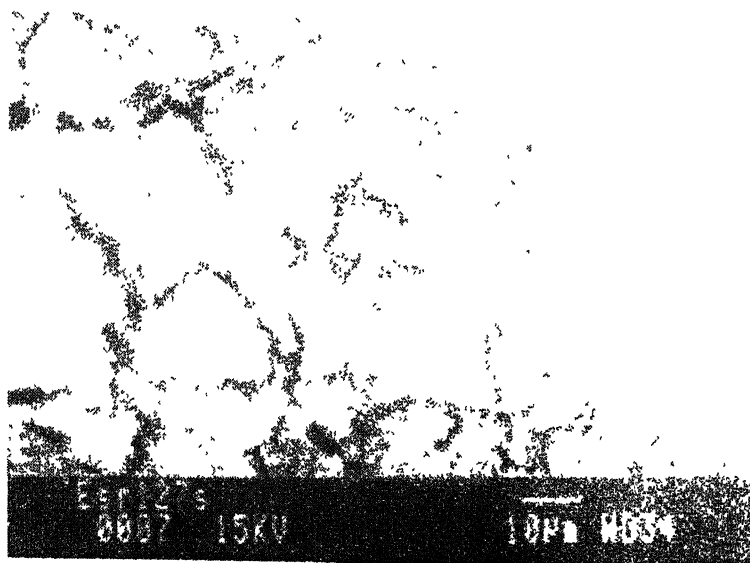


Figure 83 SEM Micrograph of Fe-18.5Al-3.6C (Es127) after immersion in freely aerated 0.25 mol/lit H_2SO_4 solution for 24 hour.

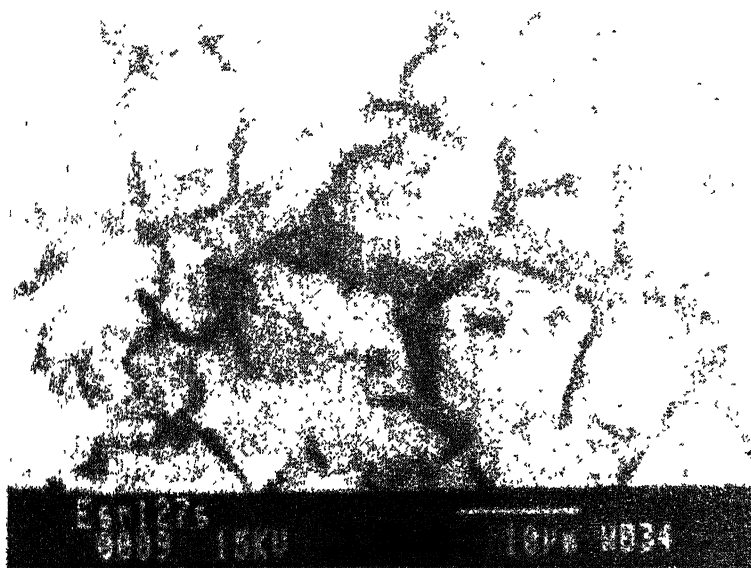


Figure 84 SEM Micrograph of Fe-18.5Al-3.6C (ESR127) after immersion in freely aerated 0.25 mol/lit H_2SO_4 solution for 24 hour.

SUMMARY

5.1 Conclusions

The electrochemical behaviour of the carbon-alloyed iron aluminides in borate buffered solution, of pH= 7.6, was studied using potentiodynamic polarization and electrochemical impedance spectroscopy (EIS) and in 0.25 mol/lit H_2SO_4 solution, of pH=0.74, by using electrochemical impedance spectroscopy and cyclic voltammetry techniques. Electrochemical impedance spectroscopy studies were conducted both in borate buffered solution as well as in 0.25 mol/lit H_2SO_4 solution at free corrosion potential (FCP), for long immersion times. The immersion time in borate buffered solution was 168 hours, whereas in 0.25 mol/lit H_2SO_4 solution the samples were immersed for a period of 24 hours. For comparison purpose, the long term immersion studies for low carbon mild steel, 316L SS, and Al6063 alloys were also conducted in both the solutions, using electrochemical impedance spectroscopy. Long term immersion studies of 304 SS and 430 SS were also carried out in addition to other alloys, in 0.25 mol/lit H_2SO_4 solution. Cyclic voltammetry of the three carbon-alloyed iron aluminides was performed in 0.25 mol/lit H_2SO_4 solution, without the stabilization of free corrosion potential at scan rates of 10, 50 and 100 mV/sec. The SEM micrographs of Fe-18.5Al-3.6C and Fe-19.2Al-3.3C-0.07Ce were taken after immersion in 0.25 mol/lit H_2SO_4 solution for 24 hours. All the results were then analyzed in detail. The following are the salient conclusions of the study:

1. The free corrosion potential (FCP) for all the alloys (carbon-alloyed iron aluminides, low carbon mild steel, 316L SS and Al6063) in borate buffered solution, moved from active to noble direction with time. This indicated thickening of surface film with time. The magnitude of shift was comparable for all other alloys except Al 6063. The shift in FCP in the case of Al 6063 was much higher than that of the other alloys. This has been attributed to the thickening of the highly protective surface film formed on the surface of Al 6063 in neutral pH conditions.

2. The free corrosion potential (FCP) in 0.25 mol/lit H_2SO_4 for all the alloys (carbon-alloyed iron aluminides, low carbon mild steel, 304 SS, 430 SS and 316L SS) except Al 6063 moved from active to noble direction on first immersion. This indicated the thickening of the surface film with time for these alloys. The FCP of Al 6063 moved from noble to active direction. This may be attributed to the active dissolution of Al in 0.25 mol/lit H_2SO_4 solution, of pH = 0.74. After 24 hours of immersion the FCP of all the alloys except 304 SS and mild steel, shifted towards the noble direction. Moreover, the sequence of the stable FCP for 316L SS, 430 SS, 304 SS, 0.05%C mild steel after 24 hours of immersion in acidic solution was exactly the same as these alloys come in the galvanic series.
3. The FCP of all the alloys in 0.25 mol/lit H_2SO_4 solution stabilized at more active potentials than in borate buffered solution. This has been attributed to the aggressively corrosive nature of 0.25 mol/lit H_2SO_4 solution compared to the mildly corrosive borate buffered solution.
4. In borate buffered solution, all the three carbon-alloyed iron aluminides and low carbon mild steel, passivated readily on immersion without showing active-passive behaviour and exhibited stable passive behaviour. The passive current densities of the carbon-alloyed iron aluminides and low carbon mild steel were similar. The breakdown potential for all the alloys was around 1000 mV vs. SCE. All the aluminides exhibited similar behaviour and the effect of Ce could not be revealed using potentiodynamic polarization in this solution.
5. EIS studies revealed that the stability of the surface film on Fe-19.2Al-3.3C-0.07Ce improved while that of Fe-18.5Al-3.6C deteriorated slightly, after seven days of immersion in borate buffered solution. The improvement in the surface film properties of Fe-19.2Al-3.3C-0.07Ce with time may be attributed to the effect of cerium addition. The nature of surface film on Fe-20.0Al-2.0C was more protective in nature compared to that on Fe-18.5Al-3.6C, both on first immersion and after seven

days of immersion in borate buffered solution. This was attributed to the lower carbon content of Fe-20.0Al-2.0C as against Fe-18.5Al-3.6C, as the carbide matrix interfaces are ideal locations for initiation of localized corrosion processes.

6. Generally, surface film properties of low carbon mild steel, Al6063 and 316L SS alloys improved after seven days of immersion in borate buffered solution. Moreover, the surface film on 316L SS, 304 SS and Al6063 alloys was much more protective, as compared to that on 430 SS and the carbon alloyed iron aluminides in 0.25 mol/lit H_2SO_4 solution. This was attributed to the presence of chromium and nickel in 304 SS and 316L SS.
7. The surface film properties (and may be the corrosion resistance) of Fe-18.5Al-3.6C and Fe-20.0Al-2.0C were comparable in 0.25 mol/lit H_2SO_4 solution. The effect of carbon could not be clearly revealed in acidic solution. The carbide distribution in these alloys was similar. The surface film formed in 0.25 mol/lit H_2SO_4 solution, was more compact and protective in the case of Fe-19.2Al-3.3C-0.07Ce than the other two carbon-alloyed iron aluminides. As the surface film on Ce-alloyed iron aluminide is more protective, it was concluded that Ce addition had modified the surface film. Moreover, the nature of surface film that forms on the long transverse (LT) and short transverse (ST) sections, in 0.25 mol/lit H_2SO_4 solution, was comparable to that of the rolling direction (RD) section of Fe-19.2Al-3.3C-0.07Ce
8. The surface film properties of all the three carbon-alloyed iron aluminides, mild steel and 430 SS deteriorated after 24 hours of immersion in 0.25 mol/lit H_2SO_4 solution. The nature of the surface film on 304 SS, 316L SS and Al 6063 improved after 24 hours of immersion in 0.25 mol/lit H_2SO_4 solution. Moreover, in the case of 316L SS, 304 SS and Al6063 alloys, the surface film was much more protective as compared to that on 430 SS and the carbon-alloyed iron aluminides in 0.25 mol/lit H_2SO_4 solution. This can be attributed to the presence of chromium and nickel in 304 SS and 316L SS

9. The surface film that forms in 0.25 mol/lit H_2SO_4 solution, in the case of mild steel was found to be more protective than that of the carbon-alloyed intermetallics. This suggests that the Al contents at this level present in the alloys (19.2 wt% in Fe-19.2Al-3.3C-0.07Ce, 18.5 wt% in Fe-18.5Al-3.6C and 20.0 wt% in Fe-20.0Al-2.0C) did not significantly affect surface sensitive properties. The formation of more protective surface film in the case of low carbon mild steel may be due the lower carbon content of mild steel as compared to that of carbon-alloyed iron aluminides. The higher dissolution rate of carbon-alloyed iron aluminide samples compared to the low-carbon mild steel has been explained to result due to the preferential attack of matrix near carbide particles.
10. The nature of the surface film (and may be the corrosion resistance) of 304 SS and 316L SS alloys were generally comparable in 0.25 mol/lit H_2SO_4 solution. The surface film formed on 316L SS and 304 SS was found to be more protective as compared to that on Al 6063 alloy. This can be attributed to the dissolution of the surface film on Al 6063 in 0.25 mol/lit H_2SO_4 solution of pH= 0.74.
11. The surface film that formed on carbon-alloyed iron aluminides, in the borate buffered solution offered a higher corrosion resistance than that formed in 0.25 mol/lit H_2SO_4 solution. This was attributed to the aggressively corrosive nature of acidic solution as against mildly corrosive nature of the borate buffered solution.
12. Cyclic voltammetry responses of the carbon-alloyed intermetallics revealed that on polarizing into the anodic region from the zero current potential, direct dissolution of iron into Fe^{+3} ions occurred in Fe-20.0Al-2.0C and Fe-18.5Al-3.6C. In the case of Fe-19.2Al-3.3C-0.07Ce, the major reactions identified were formation of $\text{Fe}(\text{OH})_2^+$ or FeOH^{+2} ions. The enhanced passivity of Ce-alloyed iron aluminide has been explained based on the adsorption
13. Scanning electron micrographs of Fe-18.5Al-3.6C and Fe-19.2Al-3.3C-0.07Ce obtained after exposing these alloys to the 0.25 mol/lit H_2SO_4 solution for a period of

24 hours revealed the formation of a corrosion product layer. The effect of cerium could not be revealed through these micrographs.

5.2 Suggestions for future work

Some additional works, which may be undertaken in order to resolve certain issues raised in this thesis, are listed below.

1. Stereological and electrochemical analysis can also be performed for the short and long transverse sections of the three alloys Fe-20.0Al-2.0C and Fe-18.5Al-3.6C.
2. The characterization of surface film on carbon-alloyed iron aluminides, after immersion in 0.25 mol/lit H_2SO_4 solution, may be performed using XPS technique. In fact, several other surface characterization methods (like SEM, ESCA etc) can also be applied to understand the nature of surface.
3. The electrochemical polarization behaviour of the alloy can also be performed using different electrolytes (like HCl, NaCl etc) other than H_2SO_4 to understand surface nature. Addition of suitable ions to the solution can help in understanding passivation process on these materials.
4. The high temperature oxidation behaviour of the Ce-alloyed intermetallic should be studied to validate its potential as candidate high temperature material.
5. The microstructure of both the Ce-alloyed and non-Ce alloyed samples can be varied using thermo-mechanical treatments, and the effect of change in microstructure on the mechanical and electrochemical behaviour can be studied.
6. High temperature hydrogen attack in the Ce-alloyed iron aluminides can be studied to understand the utility of these alloys at a high temperature in atmosphere containing hydrogen.

REFERENCES

1. N. S. Stoloff, "Ordered alloys – physical metallurgy and structural applications," *International Metal Review*, 29, 1984, pp 123-135.
2. T. Yamamoto. "The development of Sendust and other ferromagnetic alloys," Chiba: *Committee of Academic achievements*, 1980, pp 1-6.
3. C. T. Liu, J.O. Stiegler and F.H. Froes, "Ordered Intermetallics," *Metals Handbook*, 10th ed., ASM, Metals Park, USA, 2, 1990, pp. 913-942.
4. G. Sauthoff, *Z. Metallkd.*, 80, 1989, pp 337-344.
5. A. J. Bradley and A.H. Jay, *J of Iron and Steel Institute*, 125, 1932, p 339.
6. C Sykis and J. Bampfylde, *J of Iron and Steel Institute*, 130, 1934, p 389.
7. C. T. Liu and K.S. Kumar, "Ordered Intermetallic Alloys, Part 1, Nickel and Iron aluminides," *JOM*, 45, 1993, pp. 38-44.
8. C. T. Liu, C.G. McKamey and E. H. Lee, "An environmental effect as the major cause room temperature embrittlement in FeAl," *Scripta Metall.*, 23, 1996, pp. 875-880.
9. C. G. McKamey and C.T.Liu. "Chromium addition and environmental embrittlement Fe₃Al," *Scripta Metall. Mater.* 24, 1992, pp. 119-2122.
10. Zhonghua, S. Yangshan, L. Guijun, and G. Jun, "Ductility improvement of Fe₃Al based alloys with surface coating," *Scripta Mater.*, 34, 1996, pp 1071-1075.
11. R. Balasubramaniam, "On the role of chromium in minimizing room temperature hydrogen embrittlement in iron aluminides," *Scripta Mater.*, 34, 1996, pp.127-133.
12. R. Balasubramaniam, "Alloy development to minimize room temperature hydrogen embrittlement in iron aluminides," *J. Alloys and Comp.*, 1994, pp. 253-254.
13. R G. Baligidad, U. Prakash, A. Radhakrishna and V. Ramakrishna Rao, "Effect of carbides on embrittlement of Fe₃Al based intermetallic alloys," *Scripta Mater.*, 36, 1997, pp. 667-671.
14. R. G. Baligidad, U. Prakash, A. Radhakrishna and V. Ramakrishna Rao, "Effect of carbon contents on high temperature tensile properties of Fe₃Al based intermetallic alloy," *Scripta Mater.*, 36, 1997, pp.105-109.

15. S. Yangshan, Y. S. Zhengjun, Z. Zhonghua and H. Haibo, "Mechanical Properties of Fe₃Al based Alloys with Ce addition," *Acta Metall. Mater.*, 33, 1995, pp. 811 – 812.
16. M. Palm and G. Inden "Experimental determination of phase equilibria in the Fe-Al-C system," *Intermetallics*, 3, 1995, pp. 443-454.
17. V. Raghavan, Phase diagram of ternary iron alloys, Part I, Indian Institute of Metals, 1991, pp. 89-97.
18. R.G. Baligidad, U. Prakash and A. Radhakrishna, "Effect of processing on mechanical properties of an Fe–8.5 wt.% Al–1.1 wt.% C alloy," *Mater. Sci. Engg. A*, 255, 1998, pp 162-168.
19. S. Frangini, N.B. De Cristofaro, J. Lascovich and A. Mignone, *Corros. Sci.* 35, 153 (1993).
20. N. De Cristofaro, S. Frangini, and A. Mignone, *Corros. Sci.* 38, 307 (1996).
21. J.N. Defrancq, *Werkst. u. Korrosion* 28, 480 (1977).
22. 16. K. Cho, C.H. Hwang, Y.S. Ryeom, and C.S. Pak, in The Proceedings of the Fourth International Conference on Quenched Me/a/s (edited by T. Masumoto and K. Suzuki), The Japan Institute of Metals, Senday, Vol. II, 1982. 1479.
23. S. Frangini, N. B. D. Cristofaro, A. Mignone, J. Lascovich and R. Giorgi, "A combined electrochemical and XPS study on the passivity of B2 iron aluminides in the sulphuric acid solution," *Corrosion Science*, Vol. 39, No. 8, pp. 1431- 1442, 1997.
24. A. Agarwal, M. J. Akhtar and R. Balasubramaniam, "Effect of alloying on aqueous corrosion and mechanical behaviour of iron aluminide Fe₃Al," *J Mat. Sci.*, 31, 1996, pp. 5207-5213.
25. V.K. Sikka, "Processing and applications of iron aluminides," in *Processing, Properties and Applications of Iron aluminides*, eds J.H. Schneibel and M.A. Crimp, TMS, Warrendable, USA, 1994, pp 3-18.
26. A. Agarwal and R. Balasubramaniam, "Role of surface passive films on the hydrogen embrittlement of iron aluminides," *Bull. Mater.Sci.*, 19, 1996, pp. 91-102.
27. E. Underwood, Quantitative Stereology, Addison-Wesley Publishing Company, New York, USA, 1970, pp.25-103.
28. C G McKamey, J.A. Horton and C. T. Liu, "Effect of chromium on room temperature ductility and fracture mode in Fe₃Al," *Scripta Metall.*, 22, 1988, pp 1679-1681.

29. S. Mukherjee and R. Balasubramaniam, "Deciphering the potentiodynamic polarisation curves of iron aluminides Fe_3Al and $\text{Fe}_3\text{Al}+\text{Cr}$," *Bull. Mater.Sci.*, 19, 1996, pp 831-835.
30. C. G. McKamey and D.H. Pierce, "Effect of recrystallisation on room temperature tensile properties of Fe_3Al based alloy," *Scripta Metall. Mater.*, 28, 1993, pp 1173-1176.
31. D. Lin, A. Shan and D. Li, "Superplasticity in Fe_3Al -Ti alloy with large grains," *Scripta Metall. Mater.*, 31, 1994, pp 1455-1460.
32. A. Agarwal, R. Balasubramaniam and S. Bhargava, "Effect of thermomechanical treatment on the room temperature mechanical behaviour of iron aluminide," *Met.Mater.Trans.*, 27A, 1994, pp 2985-2994.
33. A. Agarwal and R. Balasubramaniam, "Fracture characteristics of alloyed iron aluminides," *Pract. Metallogr.*, 33, 1996, pp 453-466.
34. M.A. Crimp and K.M. Vedula, "Effect of boron on the tensile properties of B2 FeAl ," *Mat.Sci. Eng.*, 78, 1986, pp 1993-1999.
35. C. T. Liu and E P. George. "Environmental embrittlement in boron free and boron doped FeAl alloys," *Scripta Metall. Mater.*, 24, 1990 pp 1285-1290.
36. P. Banerjee and R. Balasubramaniam, "Mechanical behaviour of chromium and titanium alloyed iron aluminides with molybdenum addition," *Scripta Materialia*, 38, 1998, pp 1143-1147.
37. P. Banerjee, "Hydrogen behaviour in Chromium and Titanium Alloyed Iron Aluminides," M.Tech Thesis, I.I.T, Kanpur, 1997.
38. X. Yu and Y. Sun, "The oxidation improvement of Fe_3Al based alloy with Ce addition at temperature above 1000°C ," *Materials Sci and Engg.* 363, 2003, pp 30-39
39. N. Babu, "Room Temperature Aqueous Corrosion and High Temperature Oxidation Behaviour of Iron Aluminides," M.Tech thesis, I.I.T Kanpur, 1998.
40. ASM Handbook, 9th edition, Vol. 13, "Corrosion," ASM international, the materials international society.
41. ASM Handbook, 9th edition, Vol. 2, "Properties and selection: Non ferrous alloys and special-purpose materials," ASM international, the materials international society.

42. R. G. Baligidad, U. Prakash and A. Radhakrishna, *Mater. Sci. Engg. A*, 249, 1998, pp 97-102.
43. R. G. Baligidad, U. Prakash, V. R. Rao and P. K. Rao, *ISIJ International*, 36, n. 12, 1996, pp. 1453-1458.
44. R. G. Baligidad, U. Prakash and A. Radhakrishna, "Thermal stability and elevated temperature mechanical properties of electroslog remelted," Fe-16wt.%Al-(0.14-0.5) wt.%C intermetallic alloys *Mater. Sci. Engg. A*, 230, 1996, pp. 188-193.
45. M. Sen, R. Balasubramaniam and A.V. Ramesh Kumar, "Corrosion of carbon alloyed iron aluminides," *Bull. Mater. Sci.*, 23, 2000, pp. 399-403.
46. R.G. Baligidad, U. Prakash and A. Radhakrishna, "On elevated temperature stability of high carbon Fe-Al alloys," *Mater. Sci. Engg. A*, 265, 1999, pp. 301-305.
47. R.G. Baligidad, and A. Radhakrishna, *Mater. Sci. Engg. A*, 281, 1999, pp. 97-102.
48. Sriram, "Effect of cerium addition on the electrochemical behaviour of carbon alloyed Fe₃Al based intermetallics," M.Tech. Thesis, IIT Kanpur, 2004.
49. R. G. Baligidad, U. Prakash, A. Radhakrishna and V. R. Rao, 1997, *Scr. Matter.* 36, 667.
50. K R. Trethwey and J. Chamberlain, *Corrosion for Students of Science and Engineering*, John Wiley & Sons, Inc., New York, 1988.
51. D. A.Jones, *Principles and Prevention of Corrosion*, Maxwell Macmillan International Editions, NY, 1992, pp. 117-524.
52. M. G. Fontana and N.D. Greene, *Corrosion Engineering*, McGraw-Hill International Book Company, 2nd edition, 1983.
53. A.J. Bard, L.R. Faulkner, "Electrochemical Methods; Fundamentals and Applications," Wiley Interscience publications, 1980.
54. J.R. Scully, D.C. Silverman, and M.W. Kendig, "Electrochemical Impedance: Analysis and Interpretation," ASTM, 1993.
55. Cottis and Stephen Turgoose, "Electrochemical Impedance and Noise," Robert NACE International, 1440 South Creek Drive, Houston, TX 77084-4906.
56. J.R. Macdonald, "Impedance Spectroscopy; Emphasizing Solid Materials and Systems," Wiley Interscience publications, 1987.
57. A.V. Oppenheim and A.S. Willsky, "Signals and Systems," Prentice-Hall, 1983.

58. J.A.L. Dobbelaar, "The Use of Impedance Measurements in Corrosion Research; The Corrosion Behavior of Chromium and Iron Chromium Alloys," PhD thesis TU-Delft, 1990.
59. F. Geenen, "Characterization of Organic Coatings with Impedance Measurements; A Study of Coating Structure, Adhesion and Underfilm Corrosion," PhD thesis, TU-Delft, 1990.
60. C. Gabrielle, "Identification of Electrochemical Processes by Frequency Response Analysis," Solartron Instrumentation Group, 1980.
61. O.R. Brown and J.S. Whitley. *Electrochim. Acta* 32 (1987), p. 545.
62. S.E. Frers, M.M. Stefenel, C. Mayer and T. Chierchie. *J. Appl. Electrochem.* 20 (1990), p. 996.
63. C.M.A. Brett. *J. Appl. Electrochem.* 20 (1990), p. 1000.
64. C.M.A. Brett. *Corr. Sci.* 33 (1992), p. 203.
65. J.B. Bessone, D.R. Salinas, C.E. Mayer, M. Ebert and W.J. Lorenz. *Electrochim. Acta* 37 (1992), p. 2283.
66. A. Frichet, P. Gimenez and M. Keddam. *Electrochim. Acta* 38 (1957), p. 1993.
67. H.J.W. Lenderink, M.V.D. Linden and J.H.W. De Wit. *Electrochim. Acta* 38 (1989), p. 1993.
68. C. Casenave, N. Pebere and F. Dabosi. *Mater. Sci. Forum* 192–194 (1995), p. 599.
69. J.H.W. De Wit and H.J.W. Lenderink. *Electrochim. Acta* 41 (1996), p. 1111.
70. L. Garrigues, N. Pebere and F. Dabosi. *Electrochim. Acta* 41 (1996), p. 1209.
71. M. Keddam, C. Kuntz, H. Takenouti, D. Schustes and D. Zuili. *Electrochim. Acta* 42 (1997), p. 87.
72. I. Epelboin and M. Keddam. *J. Electrochem. Soc.* 117 (1970), p. 1052.
73. S. Gudic, J. Radoevic and M. Kukic. *J. Appl. Electrochem.* 26 (1996), p. 1027.
74. H.J. De Wit, C. Wijenberg and C. Crevecoeur. *J. Electrochem. Soc.* 126 (1979), p. 779.
75. L. Péter, J. Arai and H. Akahoshi. *J. Electroanal. Chem.* 482 (2000), p. 125.
76. L. Bai and B.E. Conway. *J. Electrochem. Soc.* 138 (1991), p. 2897.
77. I.V. Aoki, M.C. Bernard, S.I. Cordoba de Torresi, C. Deslouis, H.G. de Melo, S. Joiret, B. Tribollet, "AC- impedance and Raman spectroscopy study of the

- electrochemical behaviour of pure aluminium in citric acid media,” *Electrochimica Acta*, 46, 2001, 1871–1878.
78. H. B. Shao, J.M. wang. Z.Zhang, J. Q. Zhang, C.N. Cao, “Electrochemical impedance spectroscopy analysis on the electrochemical dissolution of aluminum in an alkaline solution,” *Journal of Electroanalytical Chemistry*. 549, (2003), pp. 145-150.
 79. S. S. A. E. Rehim, H. H. Hassan and M. A. Amin, “ Corrosion and corrosion inhibition of Al and some alloys in sulphate solutions containing halide ions investigated by an impedance technique,” *Applied Physics science*, 187, 2002, 279-290.
 80. F. Mansfeld, S. Lin, S. Kim, H. Shih, *Corros. Sci.* 27 (1987) 997.
 81. F. Mansfeld, S. Lin, S. Kim, H. Shih, *Werkst. u. Korros.* 39 (1988) 487.
 82. H.J.W. Lenderink, M.V.D. Linden, J.H.W. De Wit, *Electrochim. Acta* 38 (1993) 1989.
 83. W.J. Lorenz, F. Mansfeld, *Corros. Sci.* 21 (1981) 647.
 84. J.R. Macdonald, *Impedance Spectroscopy*, Wiley, New York, 1987.
 85. C.M.A. Brett, *Corros. Sci.* 33 (1992) 203.
 86. I. Epelboin, C. Gabrielli, M. Keddam, in: E. Yeager, J.O.M. Bockris, B.E. Conway, S. Sarangapani (Eds.), *Comprehensive Treatise of Electrochemistry*, Vol. 9, Wiley, New York, 1985, p. 83.
 87. R.T. Foley, T.H. Nguyen, *J. Electrochem. Soc.* 129 (1982) 464.
 88. F.M. Al-Kharafi, W.A. Badawy, *Corrosion* 54 (1998) 377.
 89. S. S. A. E. Rehim, H. H. Hassan and M. A. Amin, “Corrosion inhibition study Al and some of its alloys in 1.0 M HCl solution by impedance technique,” *Corrosion Science*, 46, 2004, pp. 5-25.
 90. D.D. Macdonald, *Electrochem. Acta* 35 (1990) 1509.
 91. F. Mansfeld, S. Lin, S. Kim, H. Shih, *Werkst. Korros.* 39 (1988) 487.
 92. S. Gudic, J. Radosevic, M. Kliskic, “Study of passivation of Al and Al-Sn alloys in borate buffer solutions using electrochemical impedance spectroscopy,” *Electrochimica Acta*, 47, 2002, pp. 3009-3016.
 93. C. M. A. Brett, A. M. O. Brett, “Electrochemical principles, methods and Application,” Oxford New York Tokyo, 1993.

94. D. K. Gosser, Jr., "Cyclic voltammetry: simulation and analysis of reaction mechanisms" New York, 1994
95. M. Keddah, O.R. Mattos, H. Takenouti, J. Electrochem. Soc. 128 (1981) 257.
96. E. Barcia, O.R. Mattos, Electrochim. Acta 35 (1990) 1601.
97. H. Schweickert, W.J. Lorenz, H. Friedberg, J. Electrochem. Soc. 127 (1980) 1693.
98. L. Bai, B.E. Conway, J. Electrochem. Soc. 137 (1990) 3737.
99. M. Itagaki, T. Suzuki and K. Watanabe, "Anodic dissolution of Fe-Mo in sulfuric acid solution as investigated by electrochemical impedance spectroscopy combined with channel flow double electrode," *Corrosion Science*, Volume 40, Issue 8, 1 August 1998, Pages 1255- 1265.
100. Houyi Ma, Guiqiu Li, Shenhao Chen, Shiyong Zhao, Xiaoliang Cheng, "Impedance investigation of the anodic iron dissolution in perchloric acid solution," *Corrosion Science*, 44, 2002, pp. 1177-1191..
101. R. G. Baligidad, U. Prakash, V. R Rao, P.K. Rao and N.B. Ballal, "Electroslag remelting of Fe-28at% Al intermetallic alloy," *Iron and Steel making*, 21, 1994, pp 324-331.
102. Metals Test Methods and Analytical Procedures, "Annual Book of ASTM Standard", ASTM, Philadelphia, USA, 03.02, Section 3, 1999, p.58.
103. N.D. Tomashov and G.P. Chernova, "Passivity and Protection of Metals Against Corrosion," Plenum Press, USA, (1967), pp.14-28.
104. N. D. Cristofaro, S. Frangini and A. Mignone, "passivity and passivity breakdown on a β -FeAl intermetallic compound in sulphate and chloride containing solutions," *Corrosion Science*, 38, pp. 307- 315, 1996.
105. L. J. Oblonsky and T. M. Devine, "A surface enhanced raman spectroscopic study of the passive films formed in borate buffer on iron, nickel, chromium and stainless steel," *Corrosion Science*, 37, No. 1, pp. 17-41, 1995.
106. M. F. Montemor, M. G. S. Ferreira, N. E. Hakiki and M. Da Cunha Belo, "Chemical composition and electronic structure of the oxide films formed on 316L stainless steel and nickel based alloys in high temperature aqueous environments," *Corrosion Science*, 42, 9, 2000, pp. 1635-1650.

- 107.M. Pourbaix, "Atlas of electrochemical equilibria in aqueous solutions," Oxford. London. Toronto. Paris. Frankfurt. Cebelcor.
- 108.M. Schumacher, "Sea water corrosion: Handbook," Noyes data corporation, Park Ridge. New Jersey, USA, 1979.
- 109.J. R. Macdonald, "Impedance Spectroscopy- emphasizing solid materials and Systems," John Wiley & Sons, New York.
- 110.J.E.G Gonzalez, J.C. Mirza-Rosca, "Study of the corrosion behavior of titanium and some of its alloys for biomedical and dental implant applications," *J of Electroanalytical chemistry*, 471 (1999) 109- 115.
- 111.R. Kirchheim, B. Heine, S. Hofmann and H. Hofmann, "Compositional changes of passive films due to different transport rates and preferential dissolution," *Corrosion Science*, 31, pp. 573, 1990.
- 112.G. Moretti, F. Guidi, G. Grion, "Tryptamine as green iron corrosion inhibitor in 0.5 M deaerated sulphuric acid," *Corrosion Science*, 46, 2004, pp. 387- 403.
- 113.E. Ahlberg and M. Friel, "An ac impedance study of the electrochemical behaviour of iron in acidic acetonitrile- water solutions," *Electrochimica Acta*, Vol. 34, No. 11, pp. 1523-1528, 1989.
- 114.H. J. E. Lenderink, M. V. D. Linden, J. H. N. De Wit, *Electrochim. Acta*, 38, 1993, 1989.
- 115.M. Metiko, S. Hukovic and S. Omanovic, "Thin indium film oxide formation and growth: Impedance Spectroscopy and Cyclic Voltammetry Investigations," *Journal of Electroanalytical Chemistry*, 455, 1998, pp. 181-189.
- 116.H. Ma, X. Cheng, S. Chen, C. Wang, J. Zhang, H. Yang, "An ac impedance study of the anodic dissolution of iron in sulphuric acid solutions hydrogen sulphide," *Journal of electroanalytical chemistry*, 451, 1998, pp. 11-17.
- 117.M. S. Antelman, F. J. Harris, Jr., "The encyclopedia of chemical electrode potentials," Plenum press, New York and London.

APPENDIX A

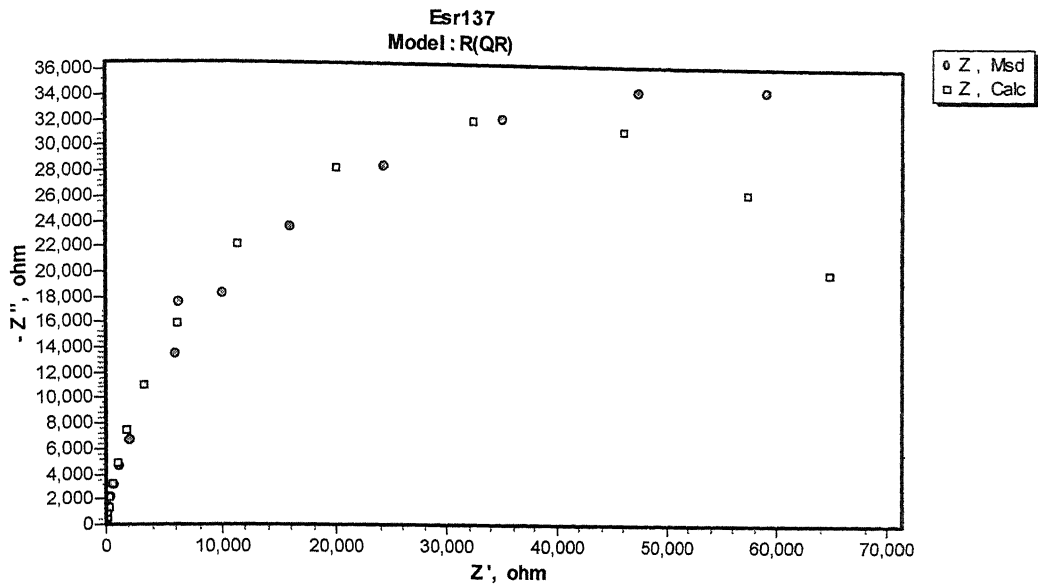


Figure A-1 Experimental (Msd.) and simulated (Calc.) Nyquist plots for Fe- 19.2Al-3.3C-0.07Ce after first immersion in borate buffered solution.

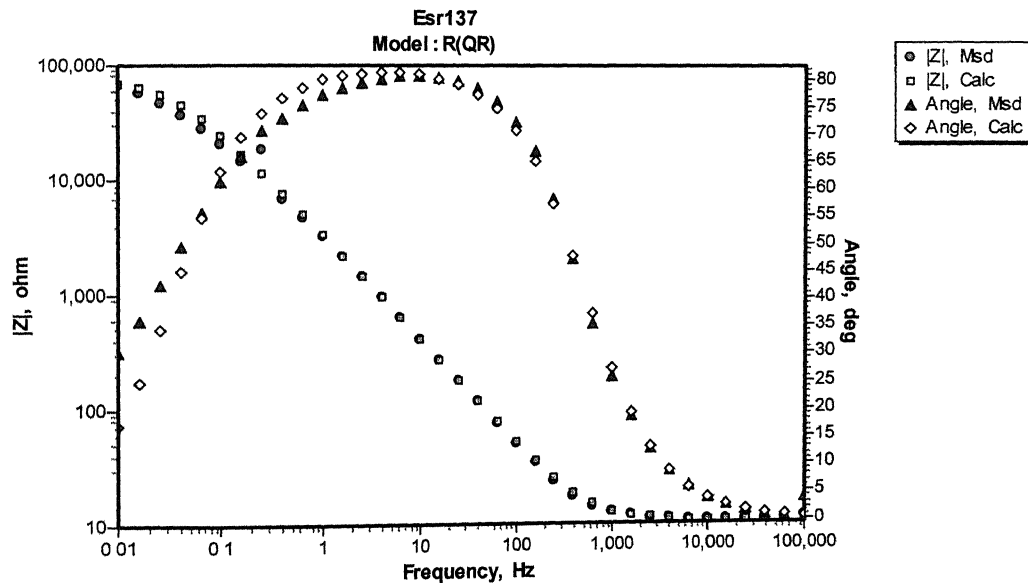


Figure A-2 Experimental (Msd.) and simulated (Calc.) Bode plots for Fe- 19.2Al-3.3C-0.07Ce after first immersion in borate buffered solution.

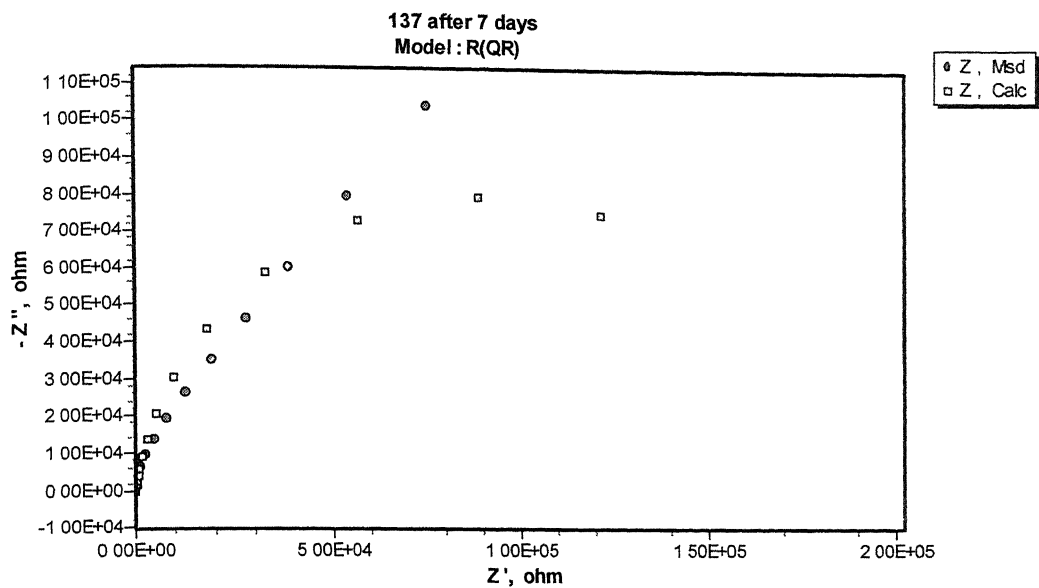


Figure A-3 Experimental (Msd.) and simulated (Calc.) Nyquist plots for Fe- 19.2Al-3.3C- 0.07Ce after 168 hours of immersion in borate buffered solution.

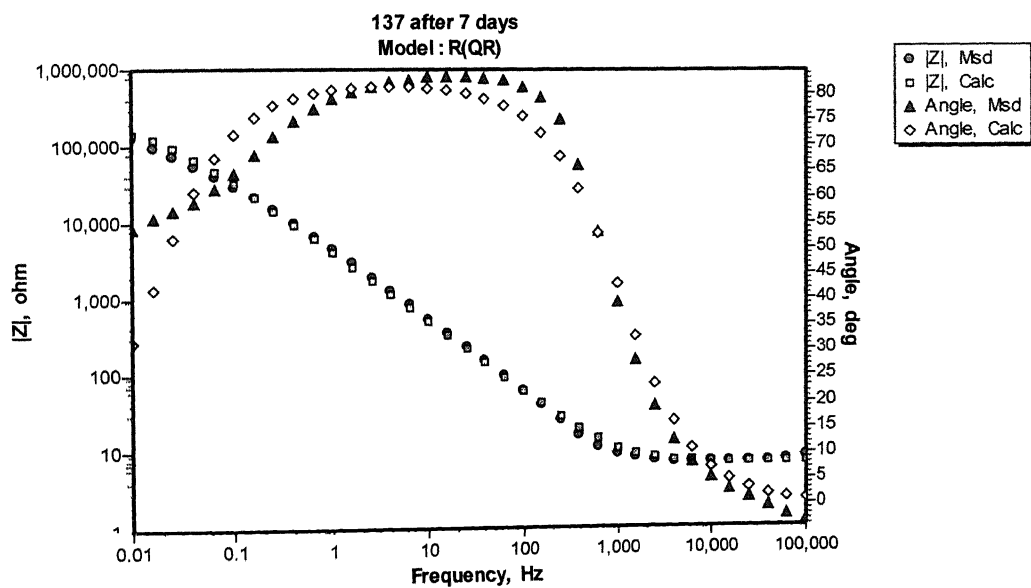


Figure A-4 Experimental (Msd.) and simulated (Calc.) Bode plots for Fe- 19.2Al-3.3C- 0.07Ce after 168 hours of immersion in borate buffered solution.

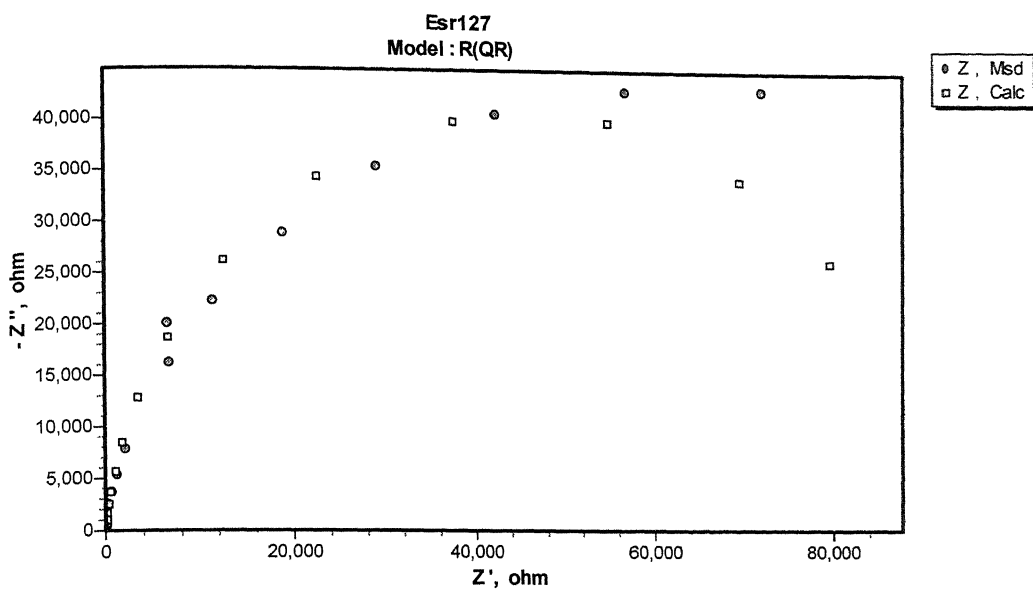


Figure A-5 Experimental (Msd.) and simulated (Calc.) Nyquist plots for Fe-18.5Al-3.6C after first immersion in borate buffered solution.

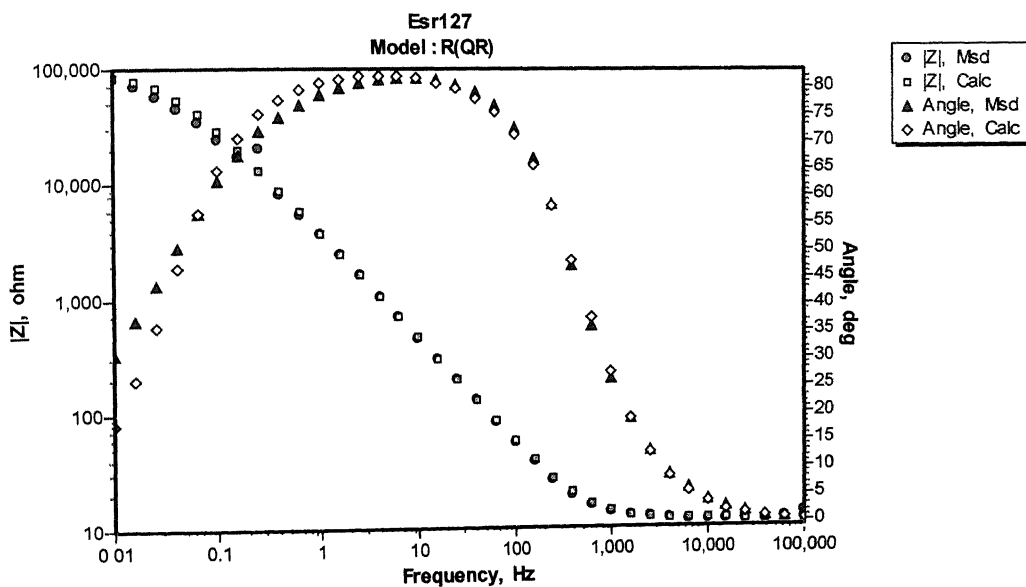


Figure A-6 Experimental (Msd.) and simulated (Calc.) Bode plots for Fe-18.5Al-3.6C after first immersion in borate buffered solution.

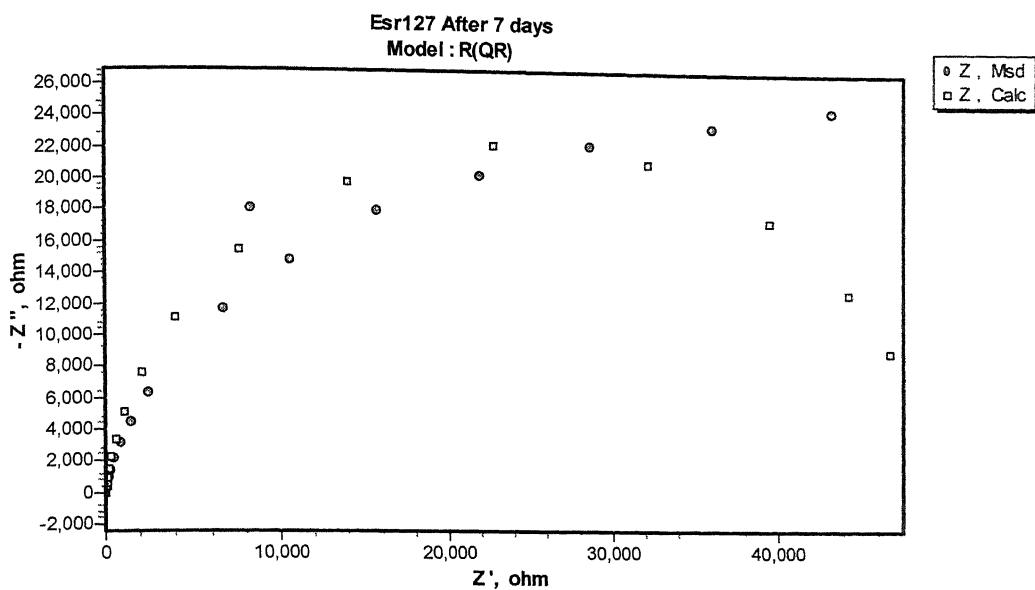


Figure A-7 Experimental (Msd.) and simulated (Calc.) Nyquist plots for Fe-18.5Al-3.6C after 168 hours of immersion in borate buffered solution.

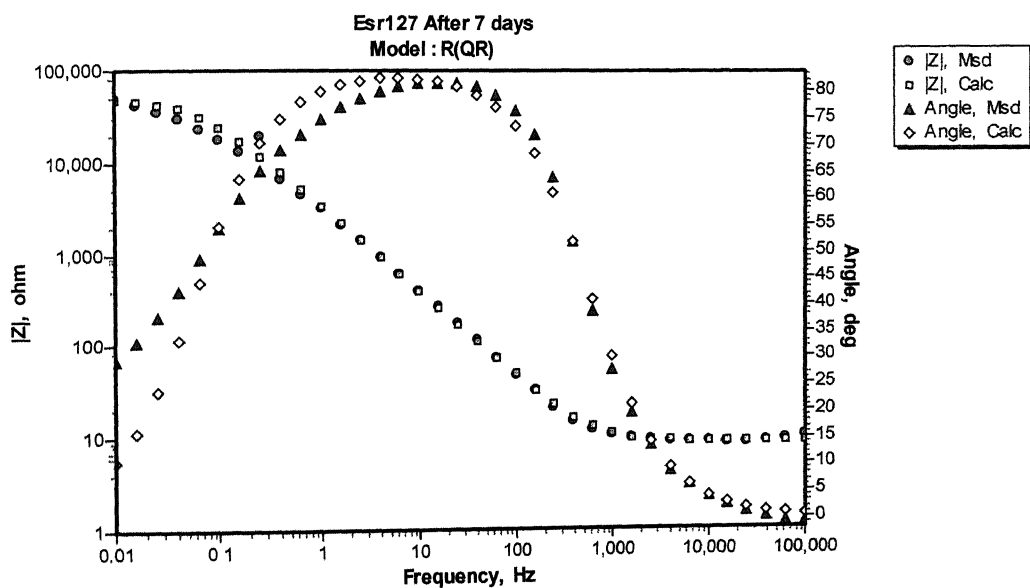


Figure A-8 Experimental (Msd.) and simulated (Calc.) Nyquist plots for Fe-18.5Al-3.6C after 168 hours of immersion in borate buffered solution.

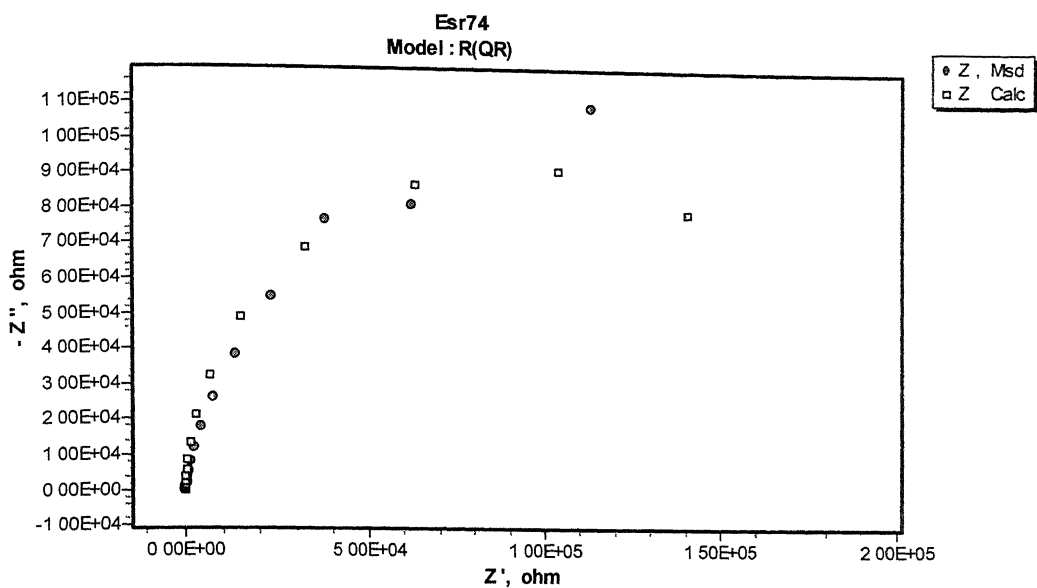


Figure A-9 Experimental (Msd.) and simulated (Calc.) Nyquist plots for Fe-20.0Al-2.0C after first immersion in borate buffered solution.

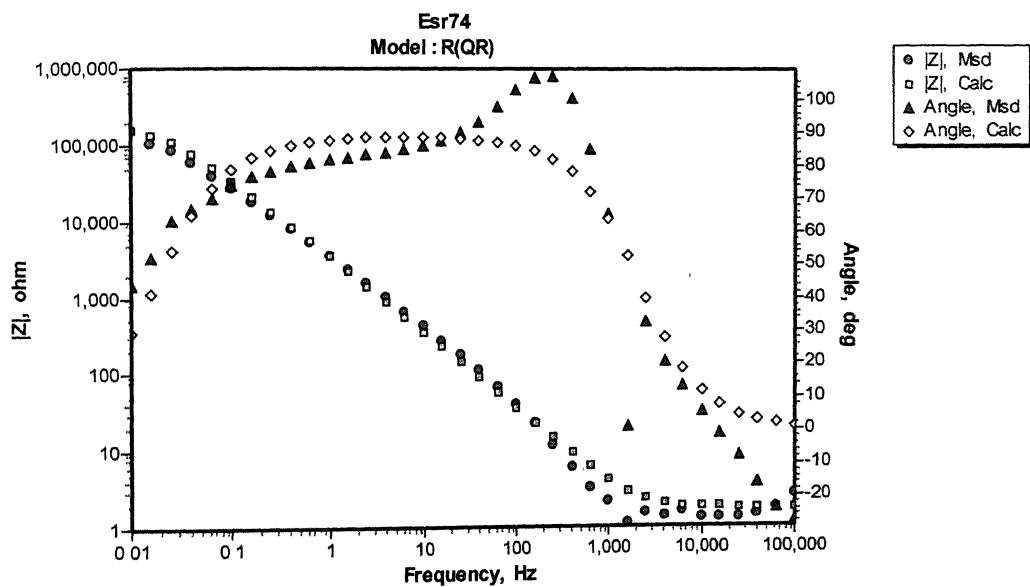


Figure A-10 Experimental (Msd.) and simulated (Calc.) Bode plots for Fe-20.0Al-2.0C after first immersion in borate buffered solution.

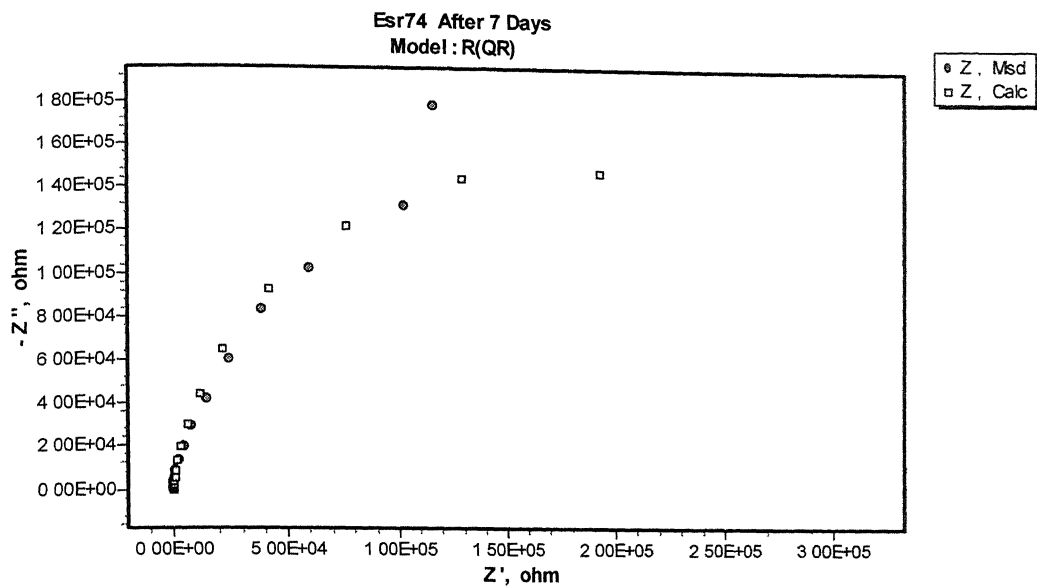


Figure A-11 Experimental (Msd.) and simulated (Calc.) Nyquist plot for Fe-20.0Al-2.0C after 168 hours of immersion in borate buffered solution.

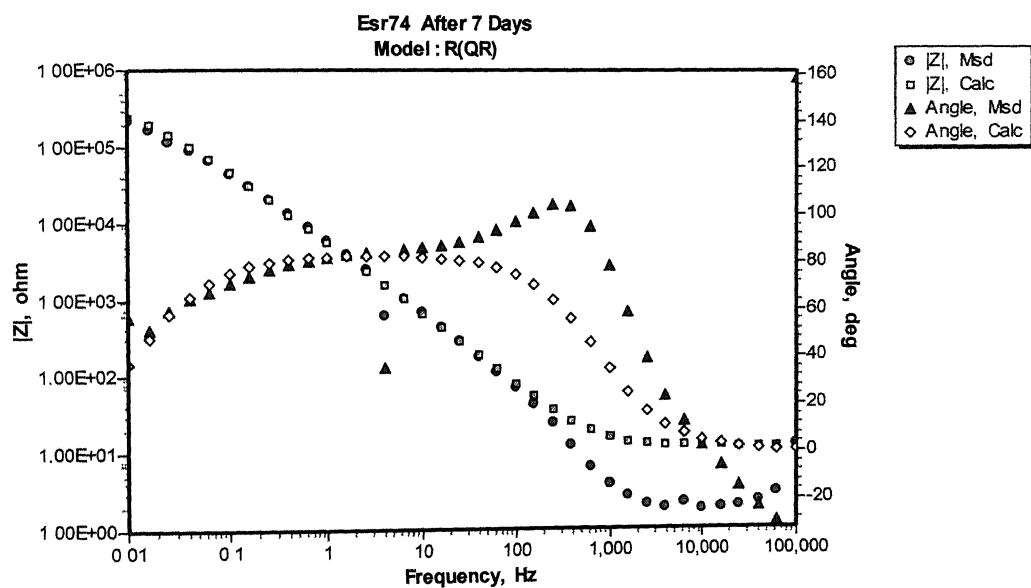


Figure A-12 Experimental (Msd.) and simulated (Calc.) Bode plots for Fe-20.0Al-2.0C after 168 hours of immersion in borate buffered solution

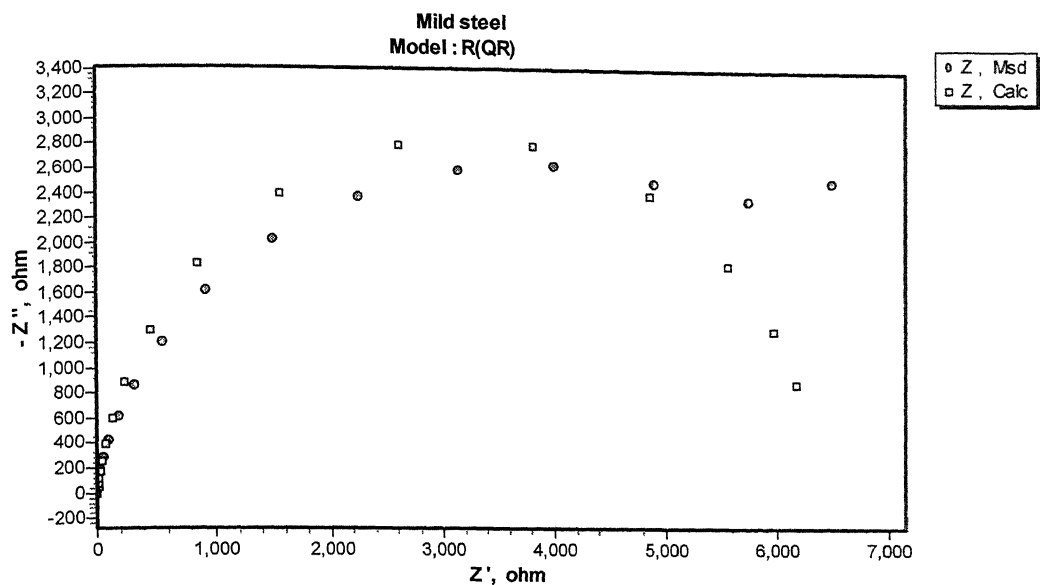


Figure A-13 Experimental (Msd.) and simulated (Calc.) Nyquist plot for 0.05 %C mild steel after first immersion in borate buffered solution.

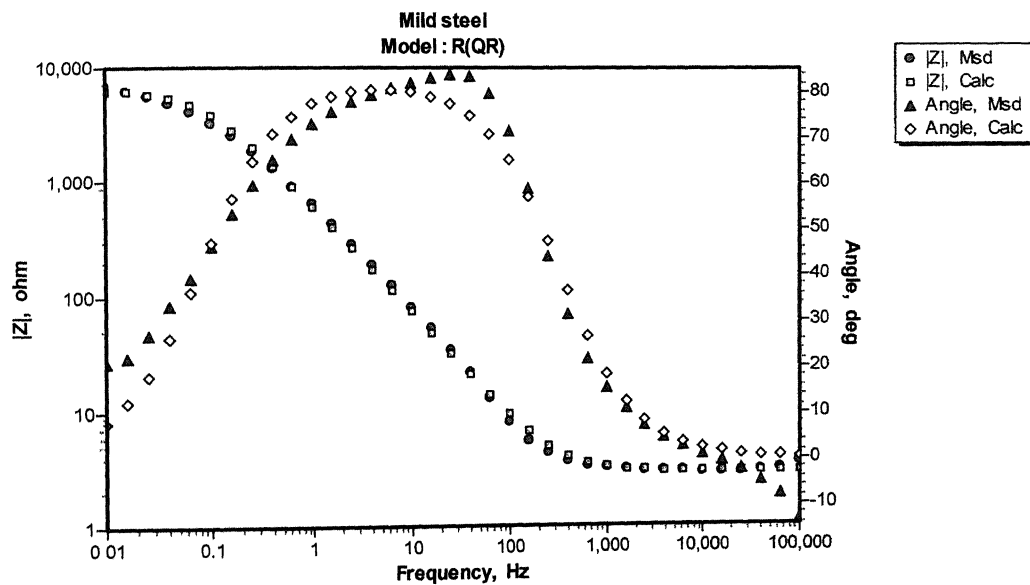


Figure A-14 Experimental (Msd.) and simulated (Calc.) Bode plot for 0.05 %C mild steel after first immersion in borate buffered solution.

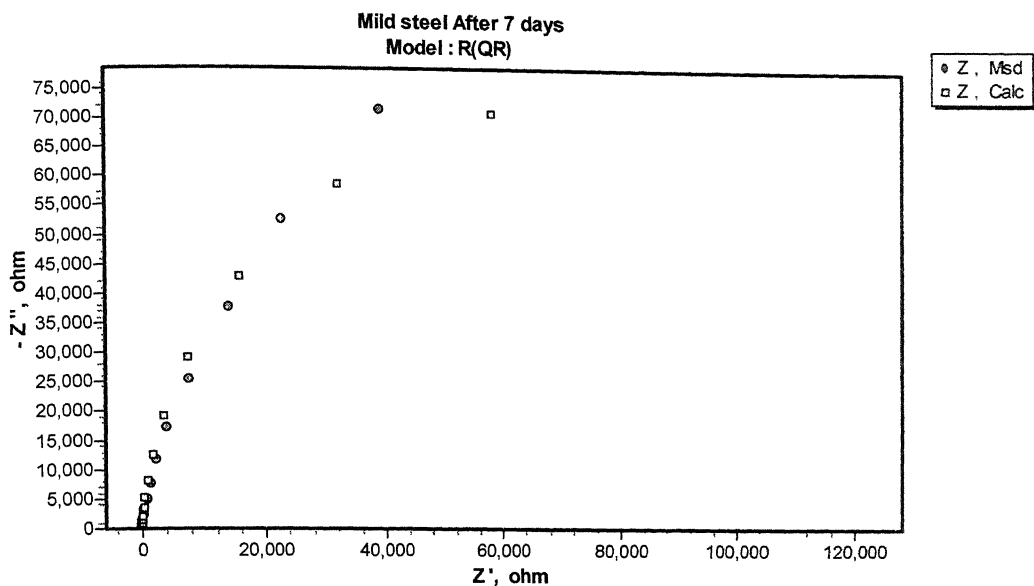


Figure A-15 Experimental (Msd.) and simulated (Calc.) Nyquist plot for 0.05 %C mild steel after 168 hours of immersion in borate buffered solution.

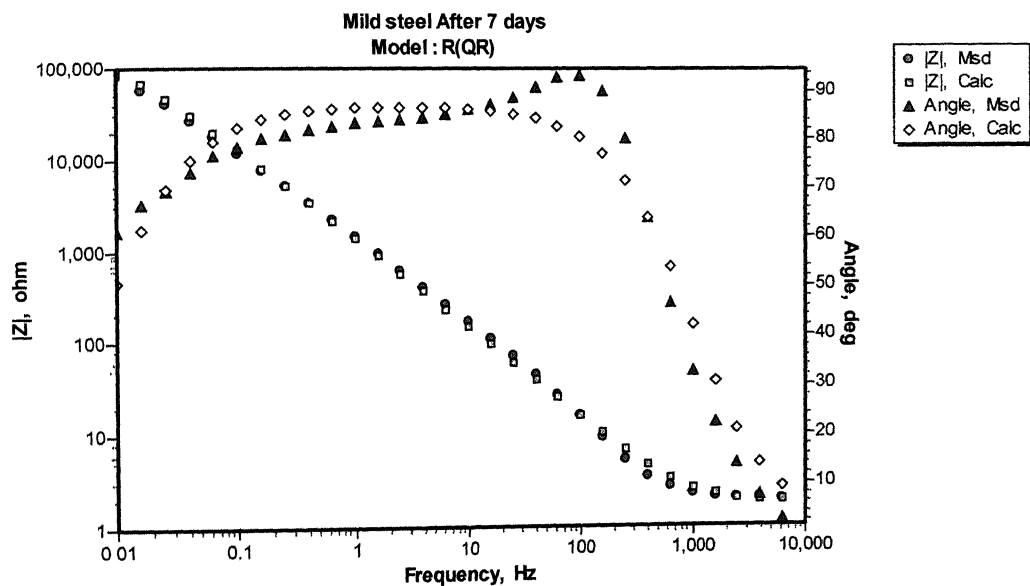


Figure A-16 Experimental (Msd.) and simulated (Calc.) Bode plot for 0.05 %C mild steel after 168 hours of immersion in borate buffered solution.

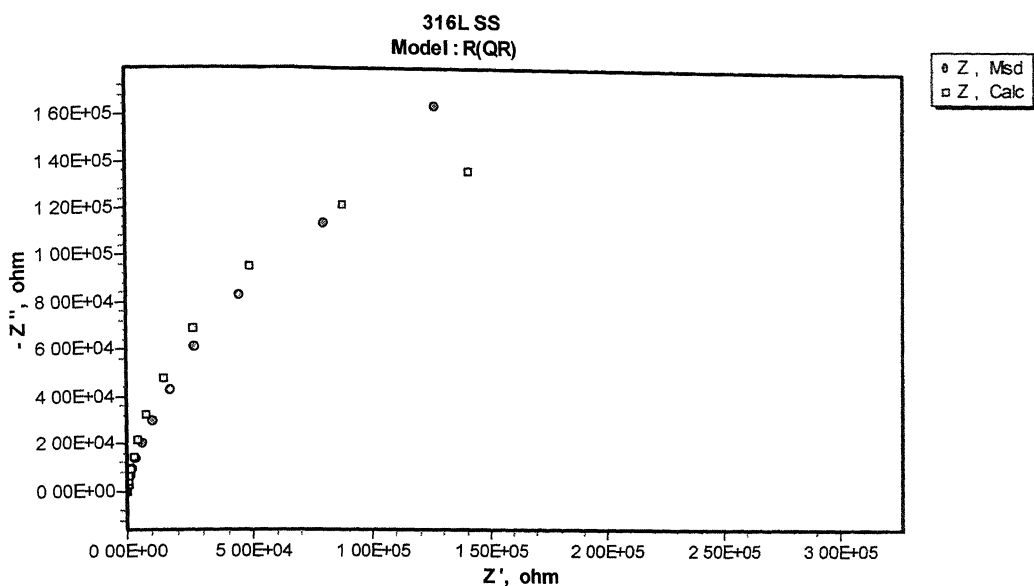


Figure A-17 Experimental (Msd.) and simulated (Calc.) Nyquist plot for 316L SS after first immersion in borate buffered solution.

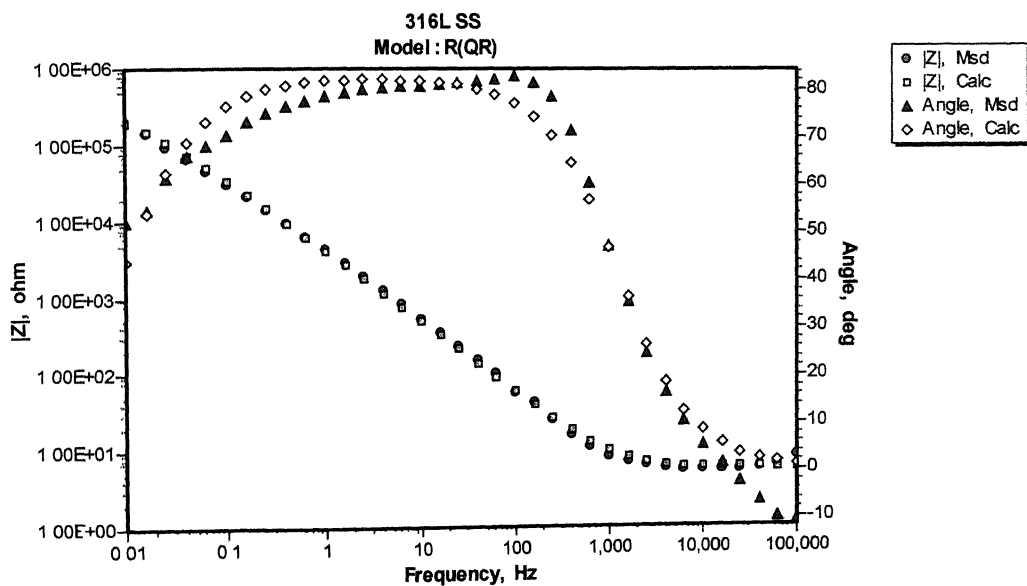


Figure A-18 Experimental (Msd.) and simulated (Calc.) Bode plot for 31L SS after first immersion in borate buffered solution.

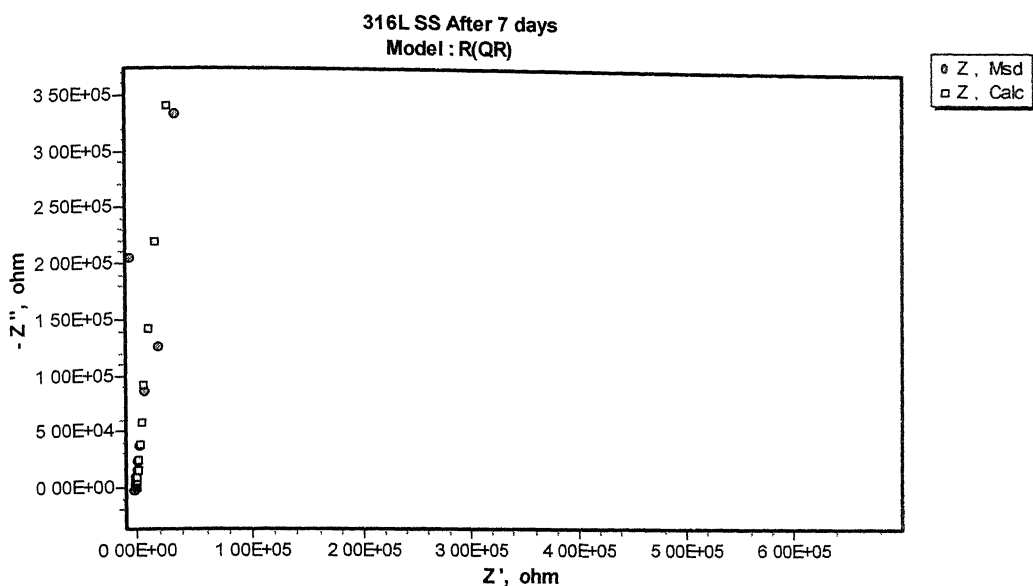


Figure A-19 Experimental (Msd.) and simulated (Calc.) Nyquist plot for 31L SS after 168 hours of immersion in borate buffered solution.

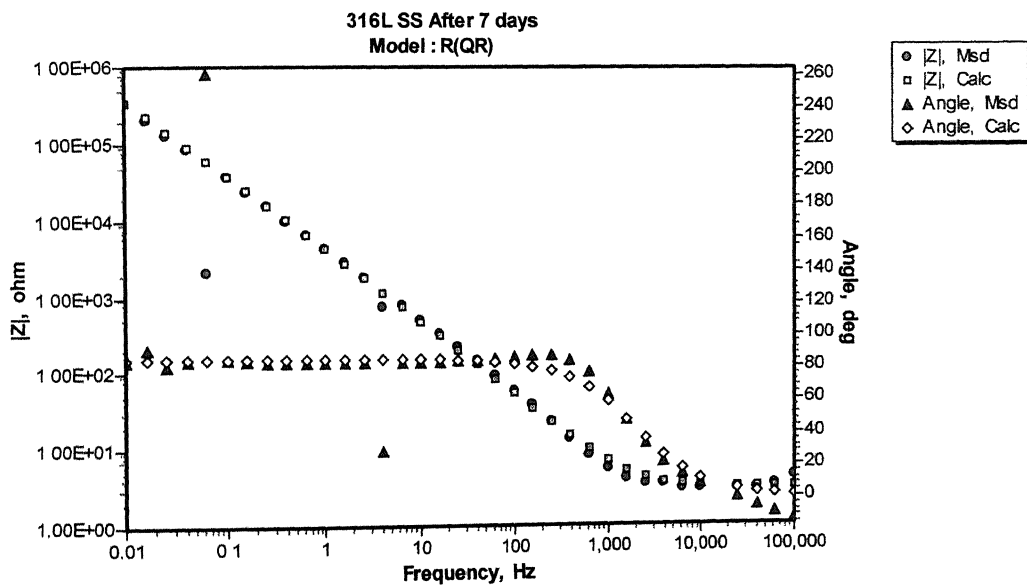


Figure A-20 Experimental (Msd.) and simulated (Calc.) Bode plot for 31L SS after 168 hours of immersion in borate buffered solution.

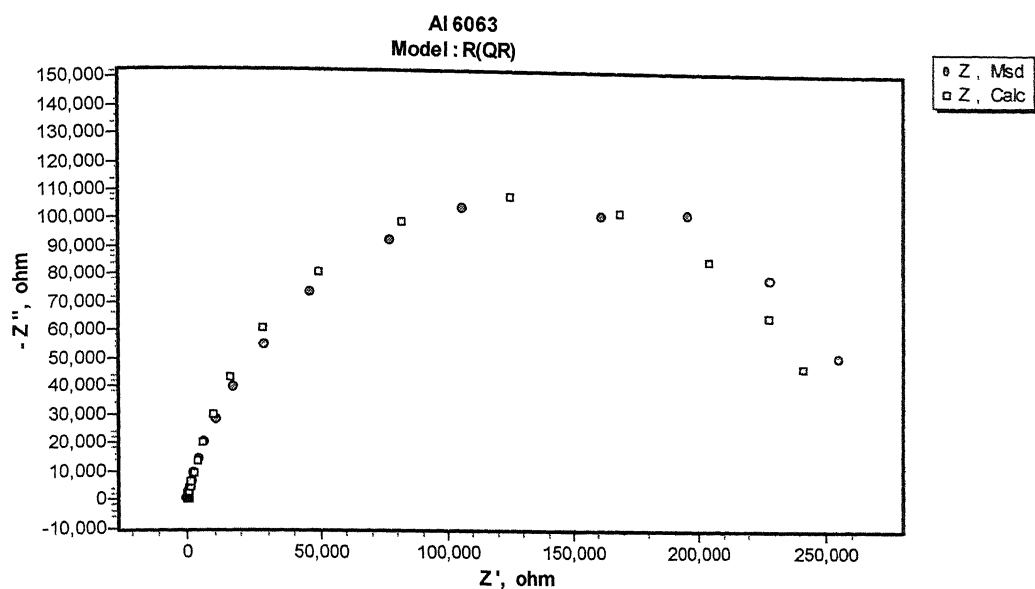


Figure A-21 Experimental (Msd.) and simulated (Calc.) Nyquist plot for Al 6063 after first immersion in borate buffered solution.

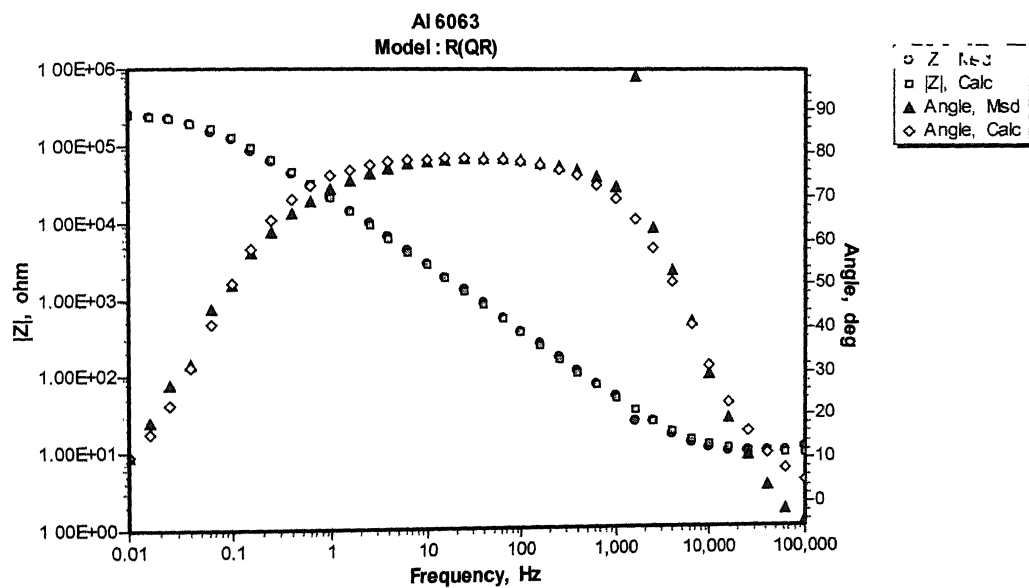


Figure A-22 Experimental (Msd.) and simulated (Calc.) Bode plots for Al 6063 after first immersion in borate buffered solution.

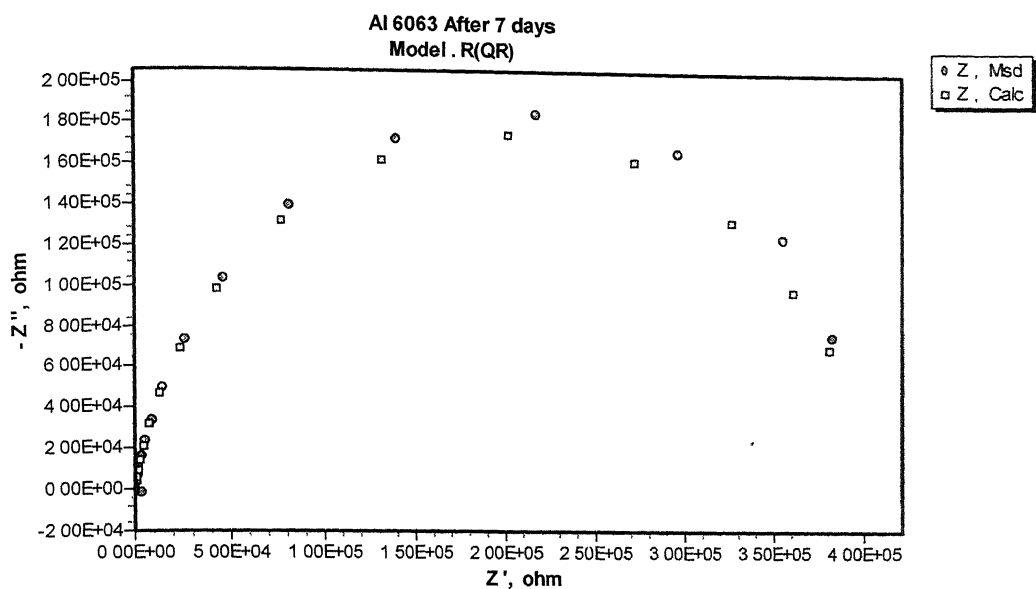


Figure A-23 Experimental (Msd.) and simulated (Calc.) Nyquist plot for Al 6063 after 168 hours of immersion in borate buffered solution.

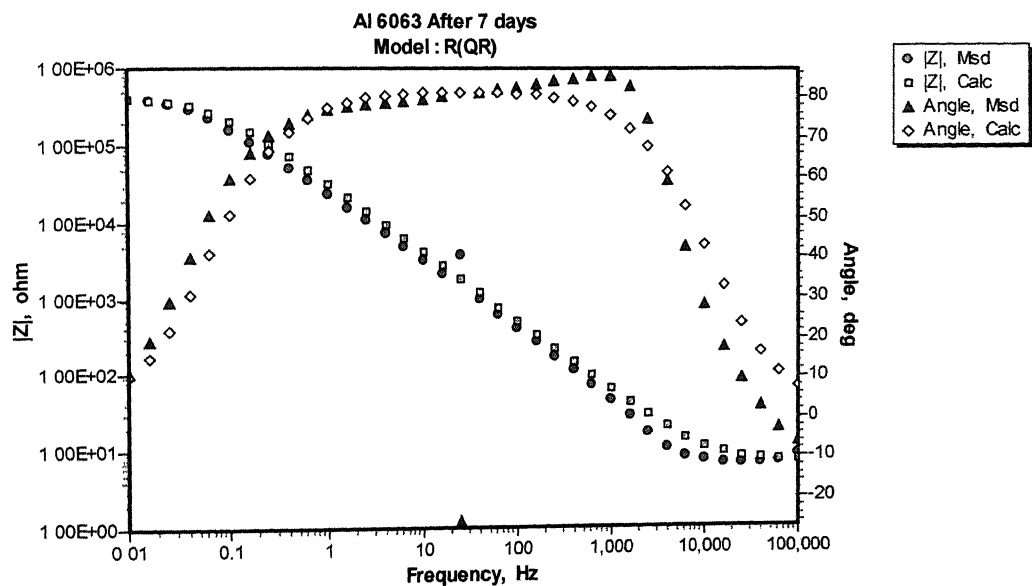


Figure A-24 Experimental (Msd.) and simulated (Calc.) Bode plot for Al 6063 after 168 hours of immersion in borate buffered solution.

APPENDIX B

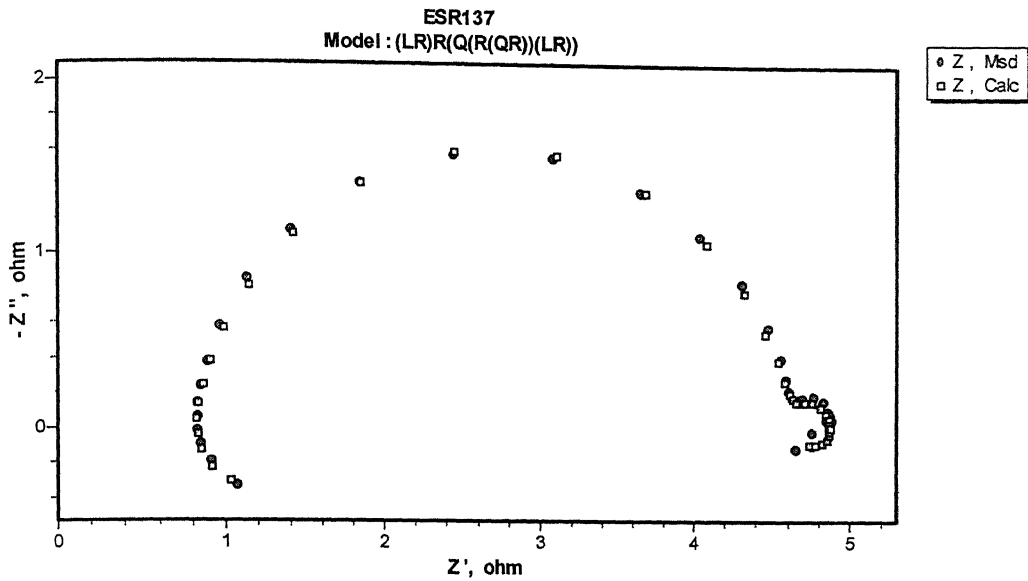


Figure B-1 Experimental (Msd.) and simulated (Calc.) Nyquist plots for Fe- 19.2Al-3.3C-0.07Ce after first immersion in 0.25 mol/lit H_2SO_4 .

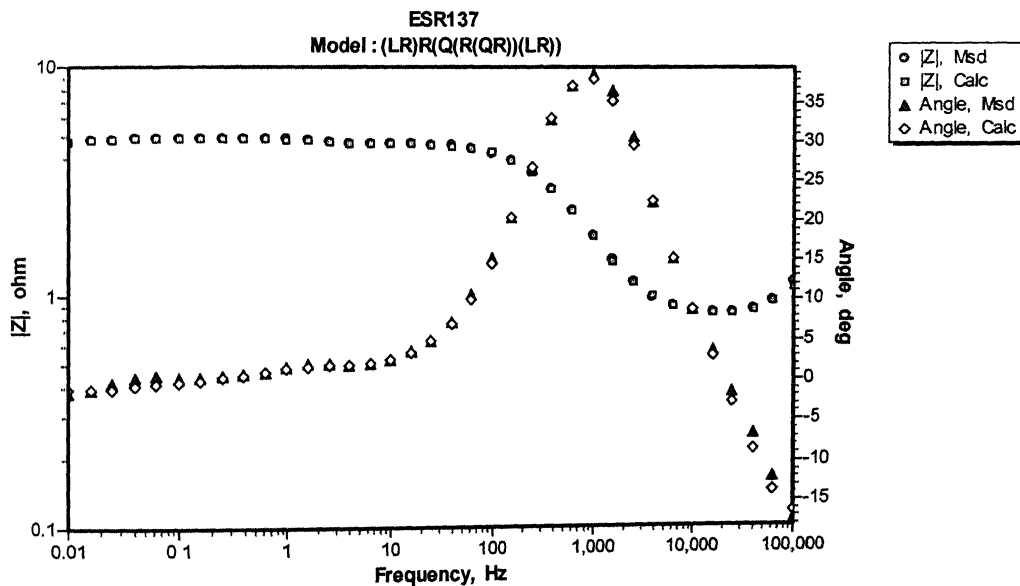


Figure B-2 Experimental (Msd.) and simulated (Calc.) Bode plots for Fe- 19.2Al-3.3C-0.07Ce after first immersion in 0.25 mol/lit H_2SO_4 .

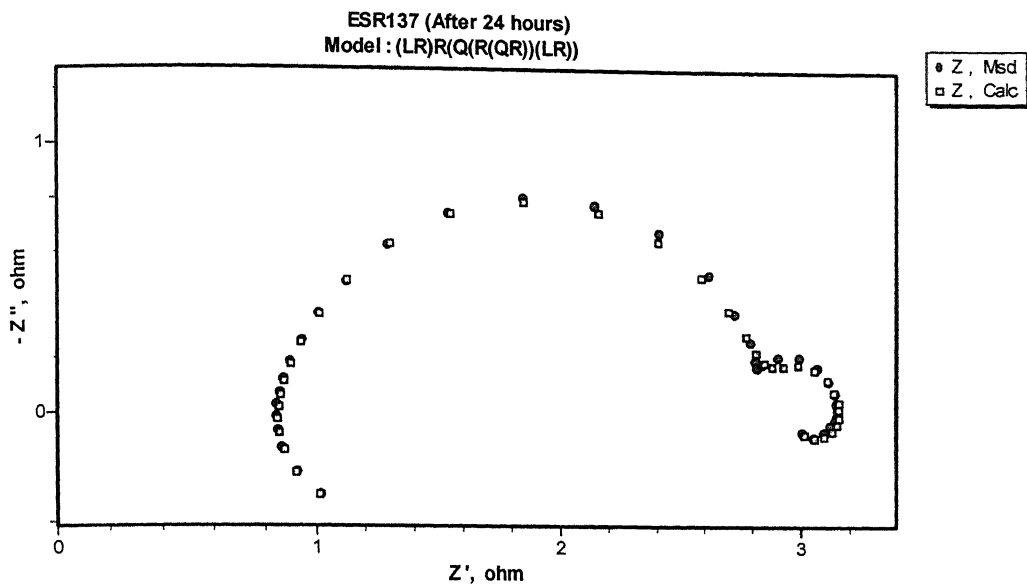


Figure B-3 Experimental (Msd.) and simulated (Calc.) Nyquist plots for Fe- 19.2Al-3.3C- 0.07Ce after 24 hours of immersion in 0.25 mol/lit H_2SO_4 .

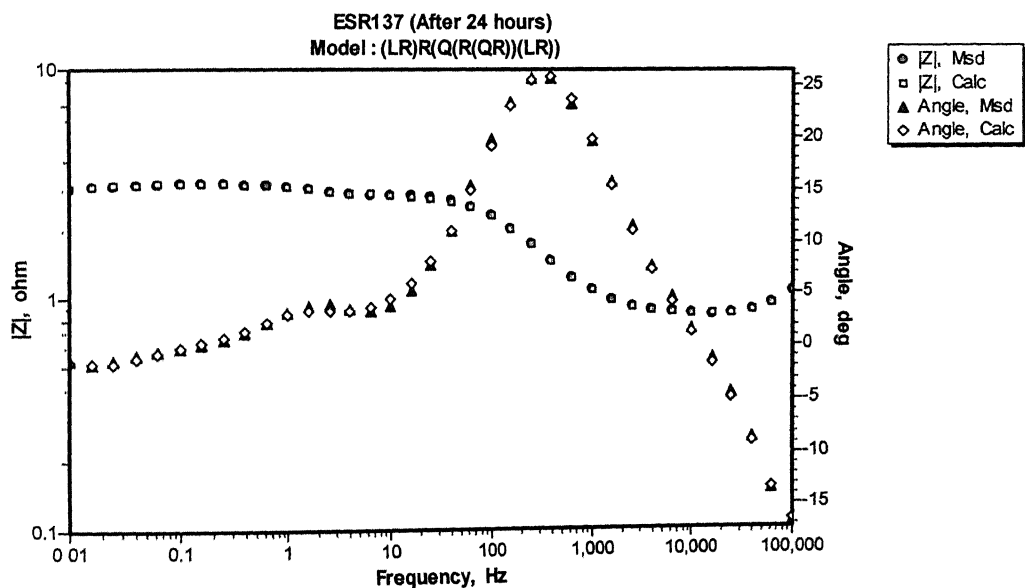


Figure B-4 Experimental (Msd.) and simulated (Calc.) Bode plots for Fe- 19.2Al-3.3C- 0.07Ce after 24 hours of immersion in 0.25 mol/lit H_2SO_4 .

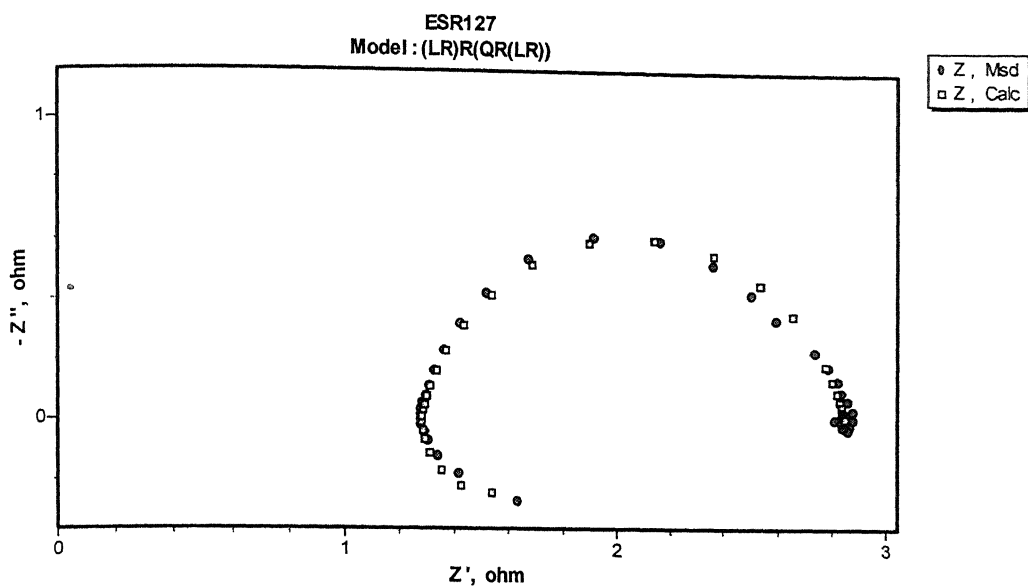


Figure B-5 Experimental (Ms.) and simulated (Calc.) Nyquist plots for Fe-18.5Al-3.6C after first immersion in 0.25 mol/lit H_2SO_4 .

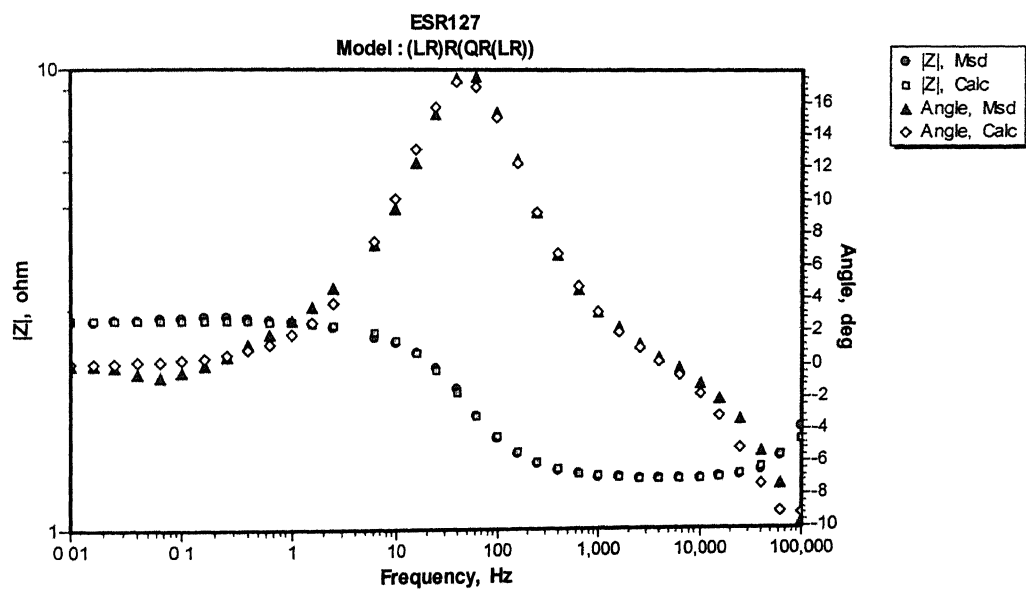


Figure B-6 Experimental (Ms.) and simulated (Calc.) Bode plots for Fe-18.5Al-3.6C after first immersion in 0.25 mol/lit H_2SO_4 .

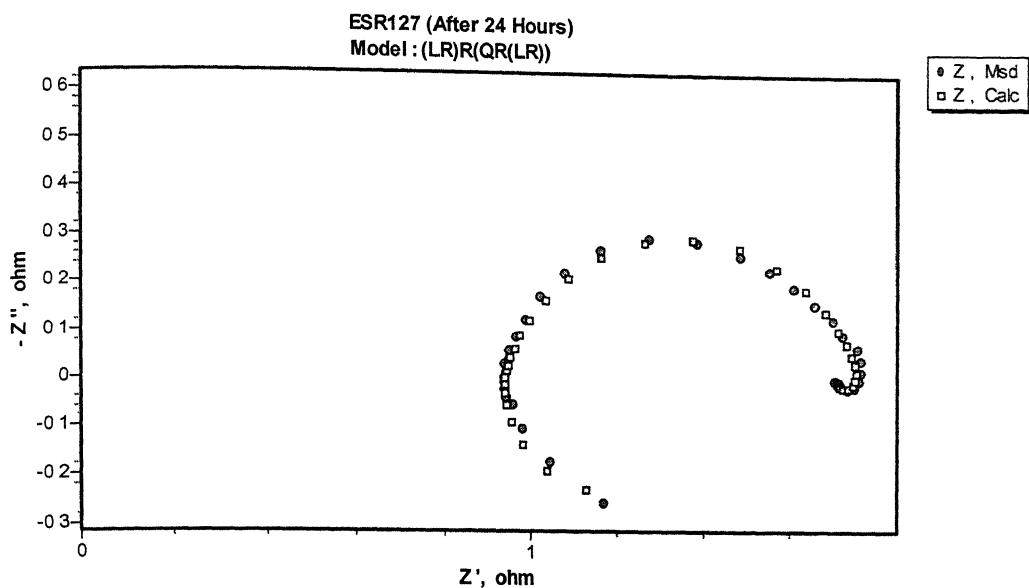


Figure B-7 Experimental (Msd.) and simulated (Calc.) Nyquist plots for Fe-18.5Al-3.6C after 24 hours of immersion in 0.25 mol/lit H_2SO_4 .

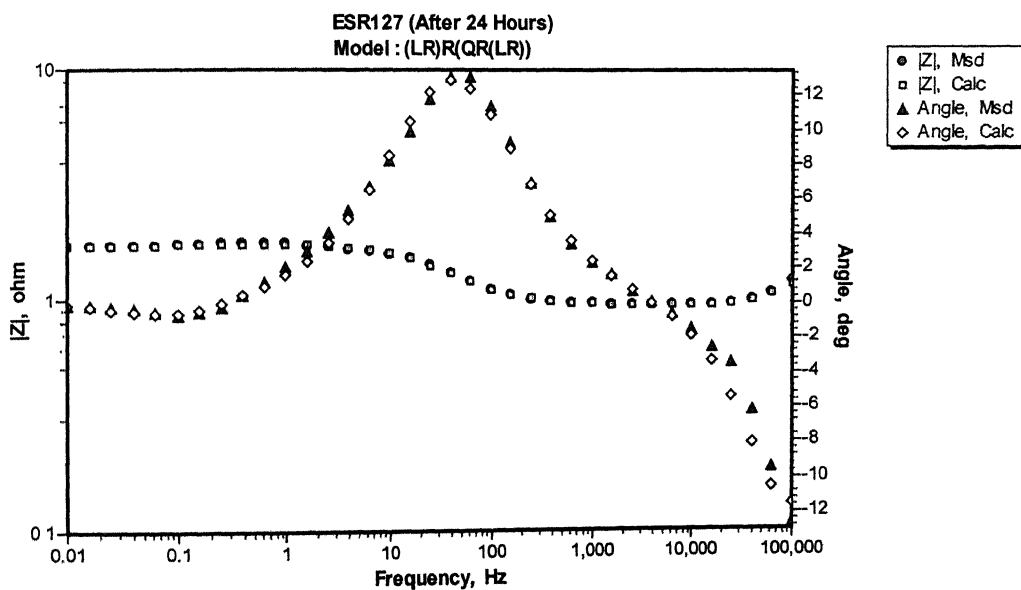


Figure B-8 Experimental (Msd.) and simulated (Calc.) Bode plots for Fe-18.5Al-3.6C after 24 hours of immersion in 0.25 mol/lit H_2SO_4 .

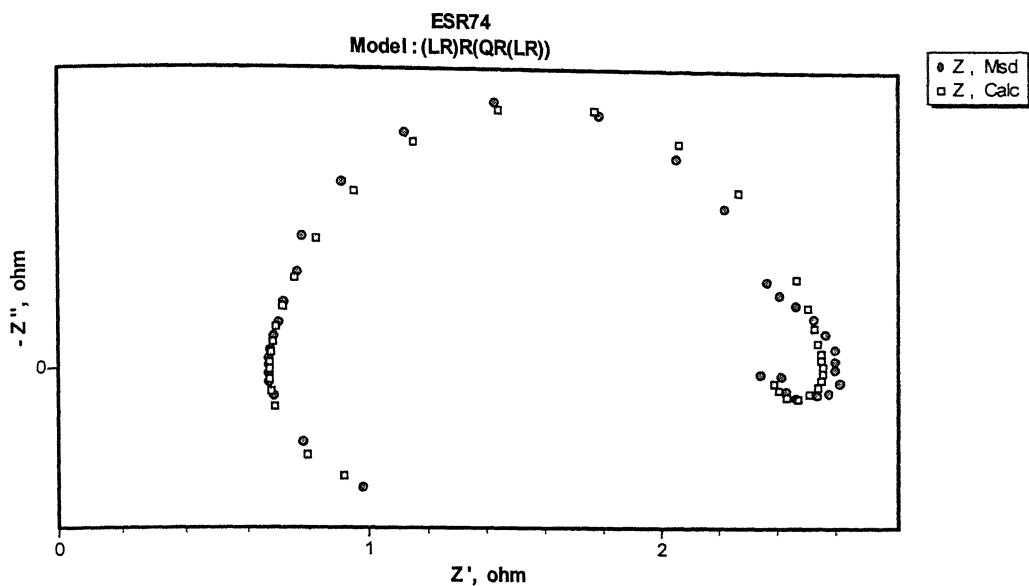


Figure B-9 Experimental (Msd.) and simulated (Calc.) Nyquist plots for Fe-20.0Al-2.0C after first immersion in 0.25 mol/lit H_2SO_4 .

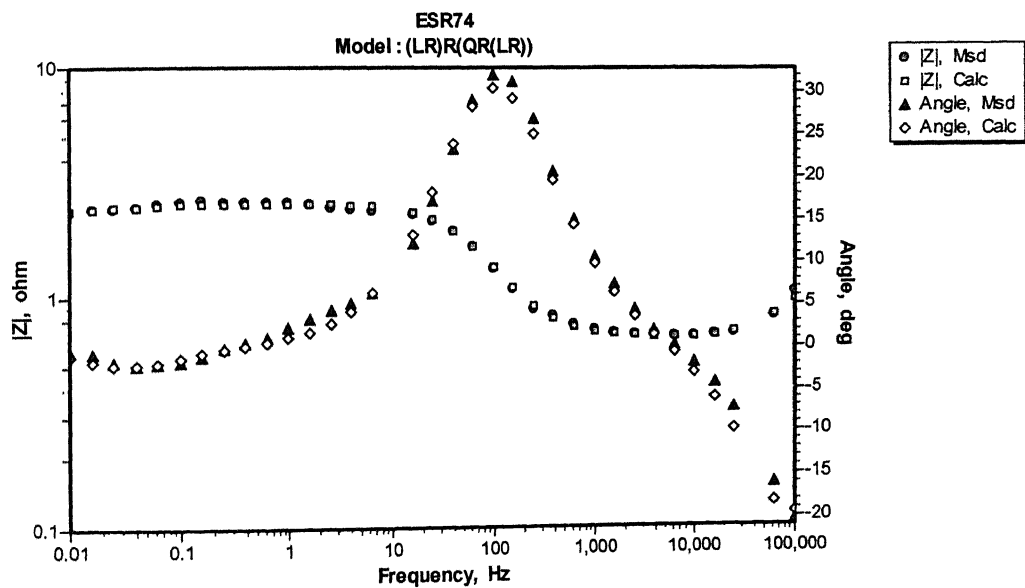


Figure B-10 Experimental (Msd.) and simulated (Calc.) Bode plots for Fe-20.0Al-2.0C after first immersion in 0.25 mol/lit H_2SO_4 .

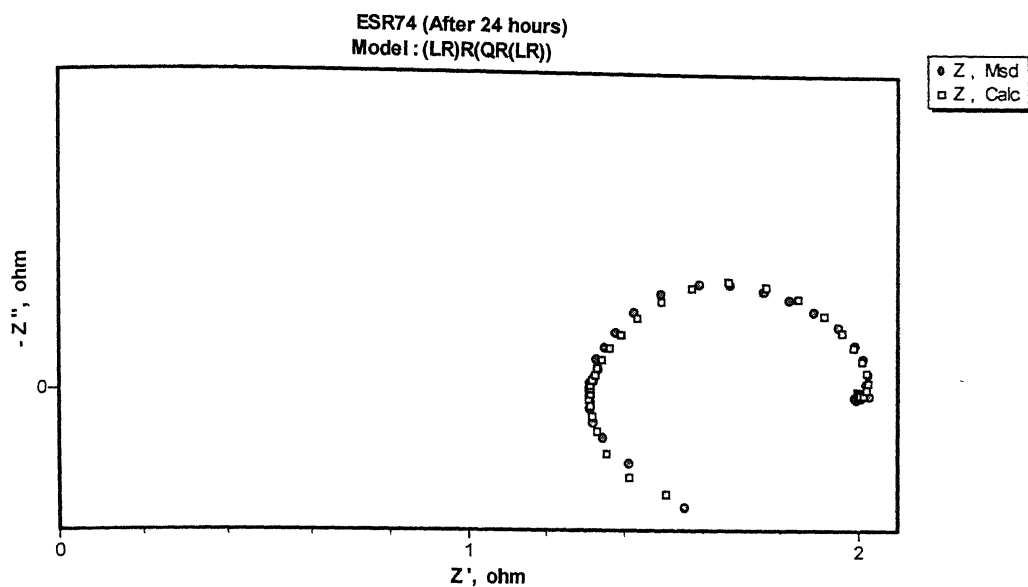


Figure B-11 Experimental (Msd.) and simulated (Calc.) Nyquist plots for Fe-20.0Al-2.0C after 24 hours of immersion in 0.25 mol/lit H_2SO_4 .

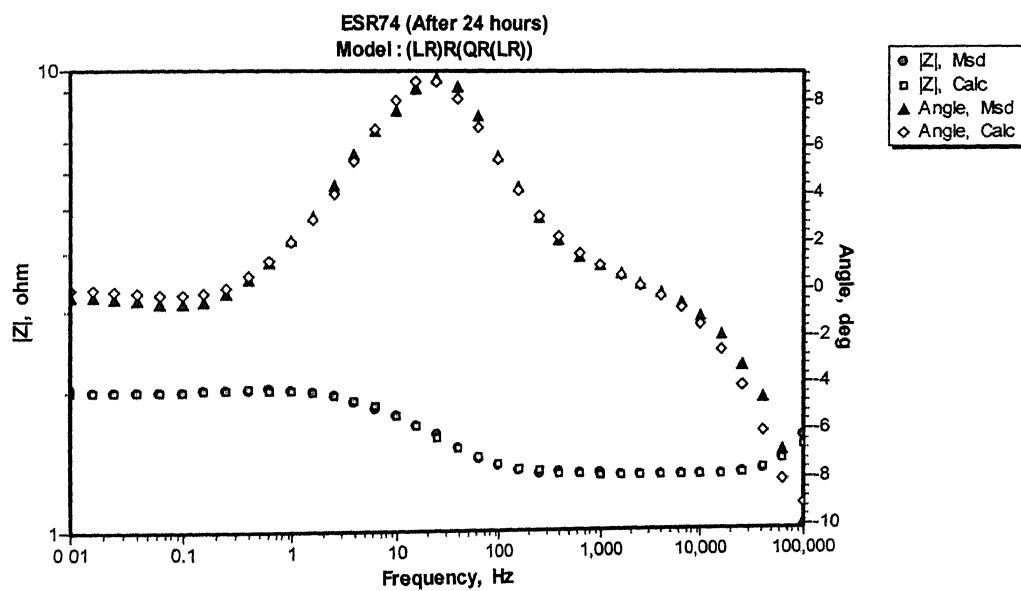


Figure B-12 Experimental (Msd.) and simulated (Calc.) Bode plots for Fe-20.0Al-2.0C after 24 hours of immersion in 0.25 mol/lit H_2SO_4

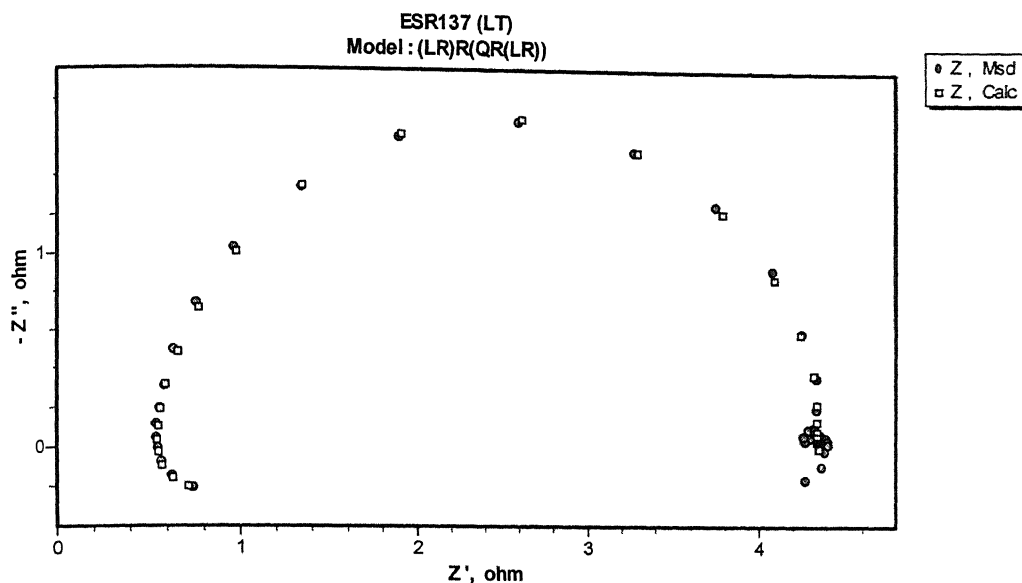


Figure B-13 Experimental (Msd.) and simulated (Calc.) Nyquist plots for long transverse section of Fe- 19.2Al-3.3C-0.07Ce after first immersion in 0.25 mol/lit H_2SO_4 .

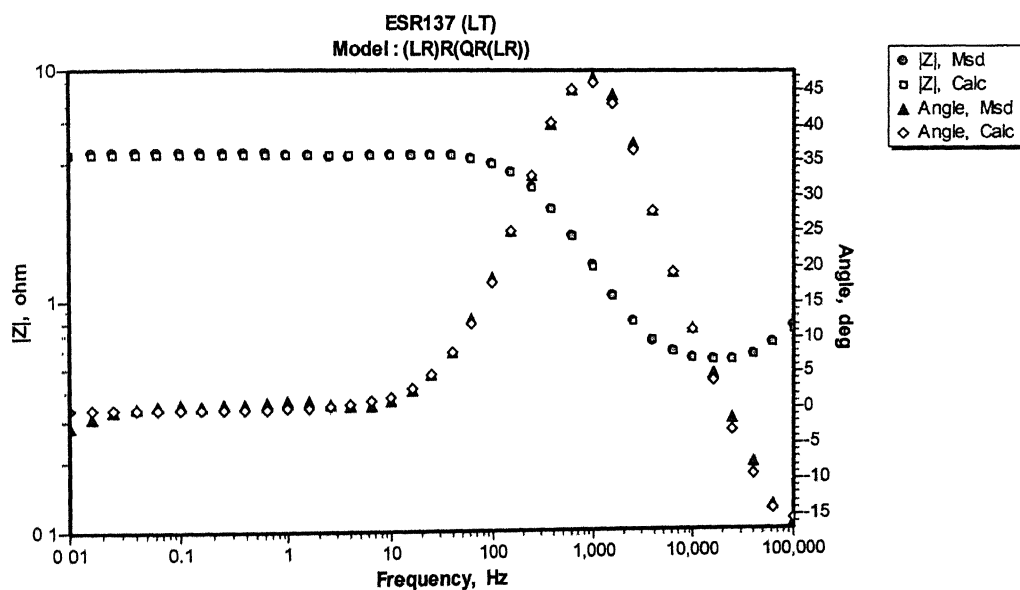


Figure B-14 Experimental (Msd.) and simulated (Calc.) Bode plots for long transverse section of Fe- 19.2Al-3.3C-0.07Ce after first immersion in 0.25 mol/lit H_2SO_4 .

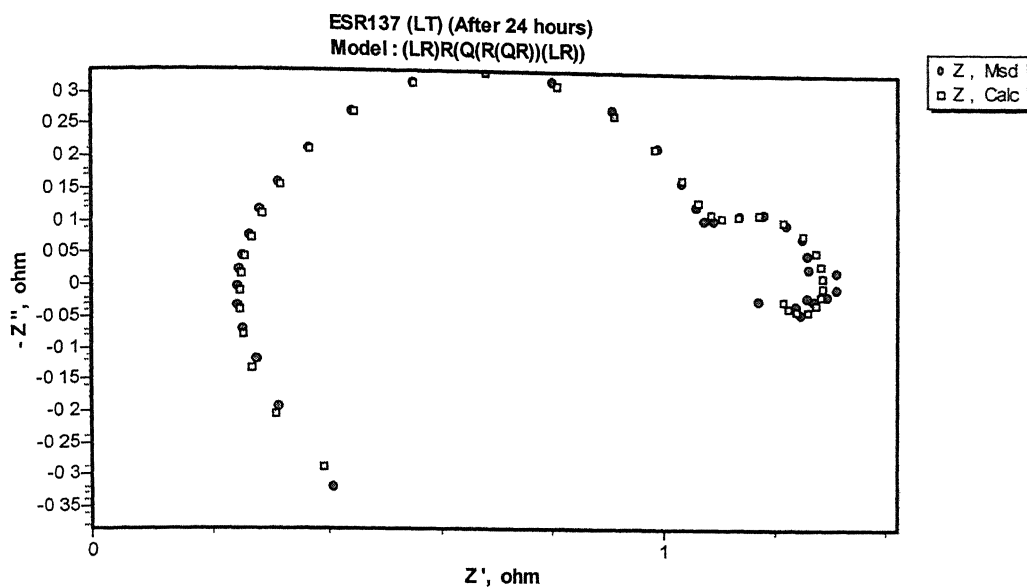


Figure B-15 Experimental (Msd.) and simulated (Calc.) Nyquist plots for long transverse section of Fe- 19.2Al-3.3C-0.07Ce after 24 hours of immersion in 0.25 mol/lit H_2SO_4 .

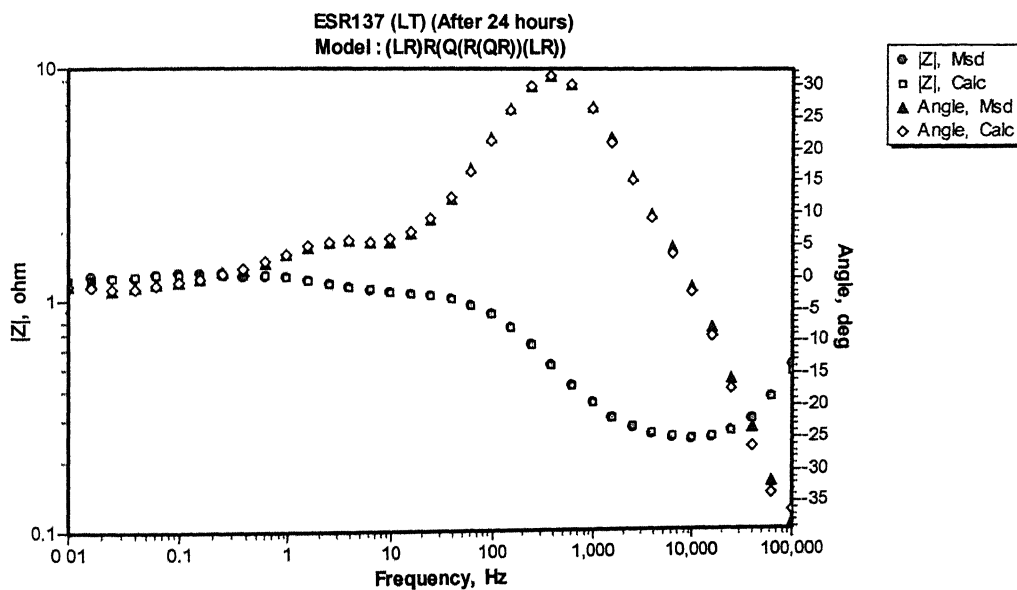


Figure B-16 Experimental (Msd.) and simulated (Calc.) Bode plots for long transverse section of Fe- 19.2Al-3.3C-0.07Ce after 24 hours of immersion in 0.25 mol/lit H_2SO_4 .

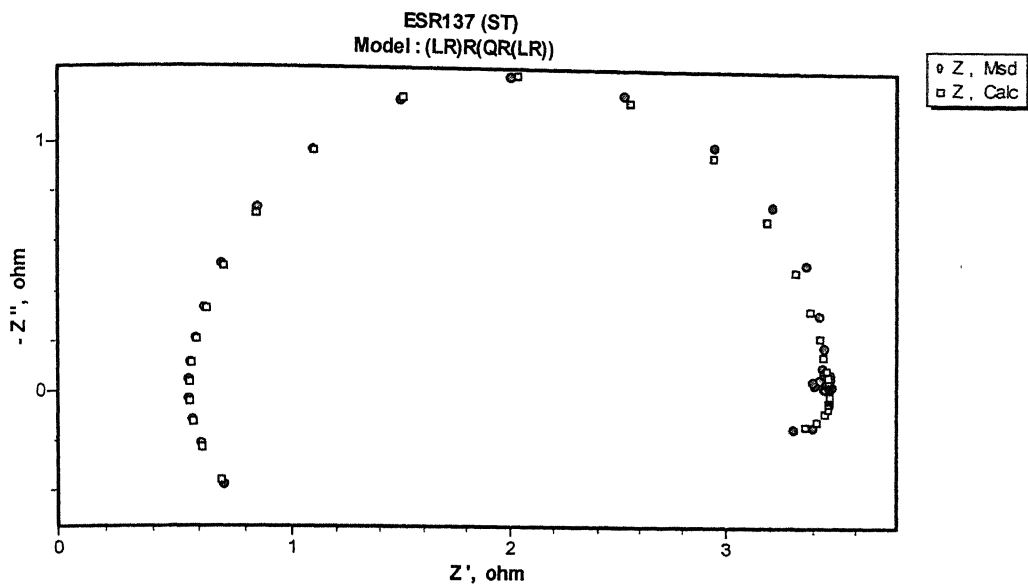


Figure B-17 Experimental (Msd.) and simulated (Calc.) Nyquist plots for short transverse section of Fe- 19.2Al-3.3C-0.07Ce after first immersion in 0.25 mol/lit H_2SO_4 .

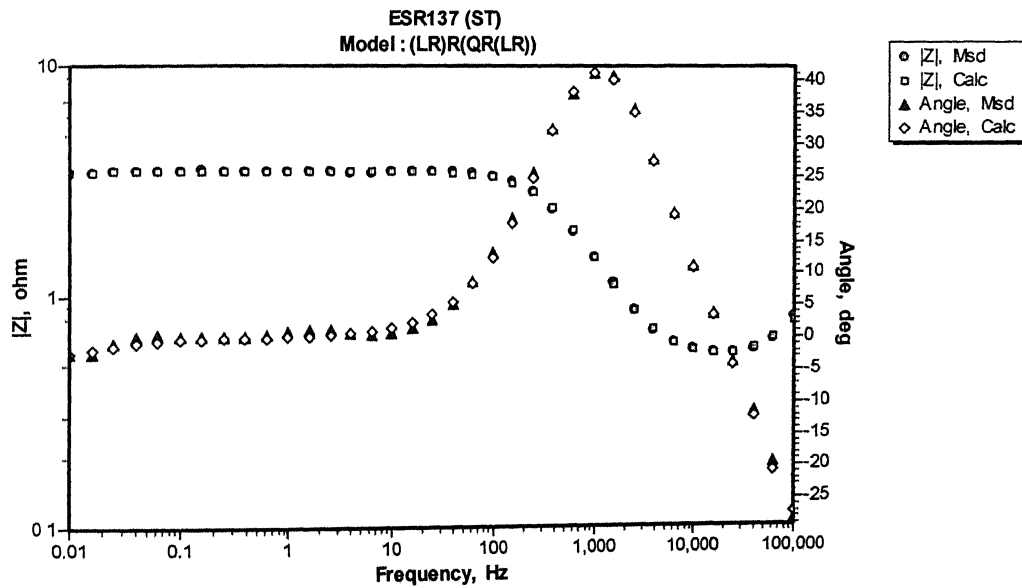


Figure B-18 Experimental (Msd.) and simulated (Calc.) Bode plots for short transverse section of Fe- 19.2Al-3.3C-0.07Ce after first immersion in 0.25 mol/lit H_2SO_4 .

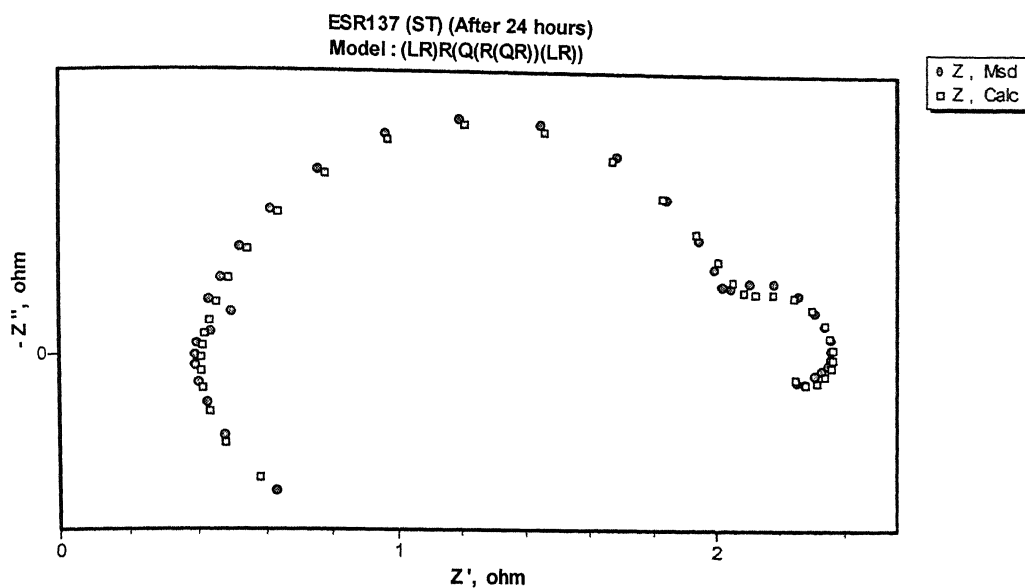


Figure B-19 Experimental (Msd.) and simulated (Calc.) Nyquist plots for short transverse section of Fe- 19.2Al-3.3C-0.07Ce after 24 hours of immersion in 0.25 mol/lit H_2SO_4 .

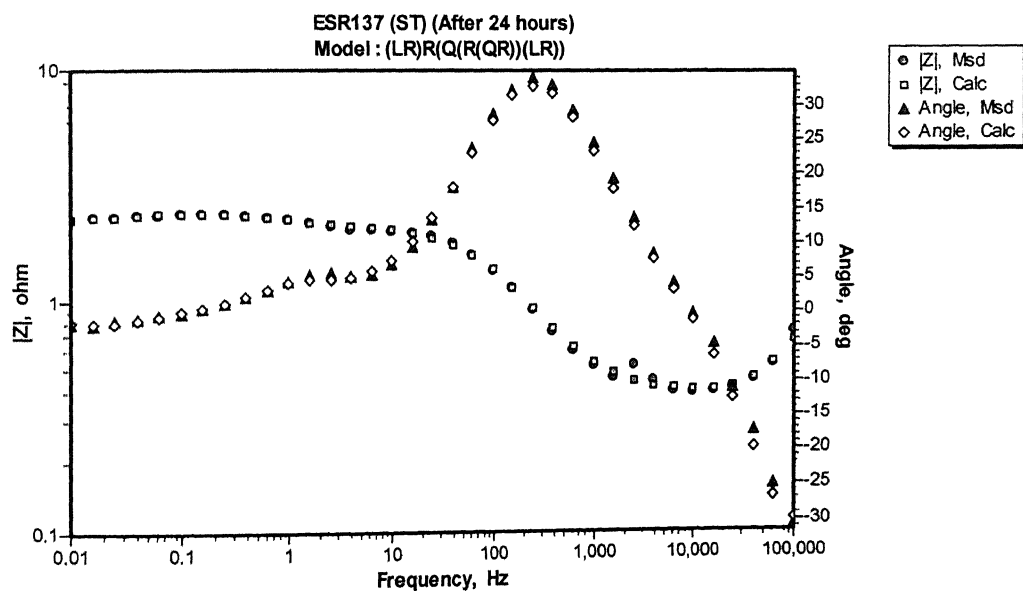


Figure B-20 Experimental (Msd.) and simulated (Calc.) Bode plots for short transverse section of Fe- 19.2Al-3.3C-0.07Ce after 24 hours of immersion in 0.25 mol/lit H_2SO_4 .

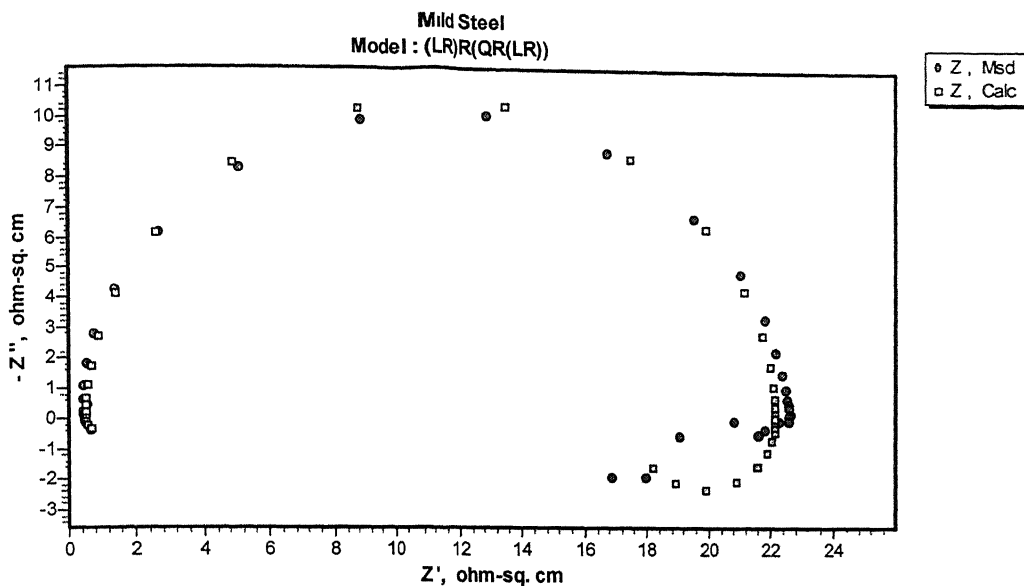


Figure B-21 Experimental (Msd.) and simulated (Calc.) Nyquist plots for 0.05 %C mild steel after first immersion in 0.25 mol/lit H_2SO_4 .

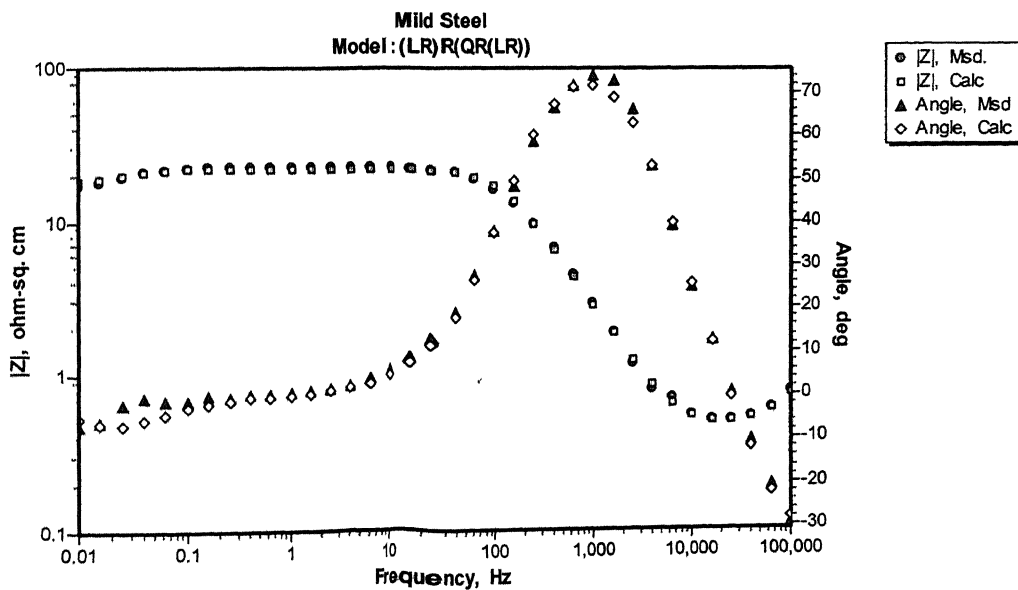


Figure B-22 Experimental (Msd.) and simulated (Calc.) Bode plots for 0.05 %C mild steel after first immersion in 0.25 mol/lit H_2SO_4 .

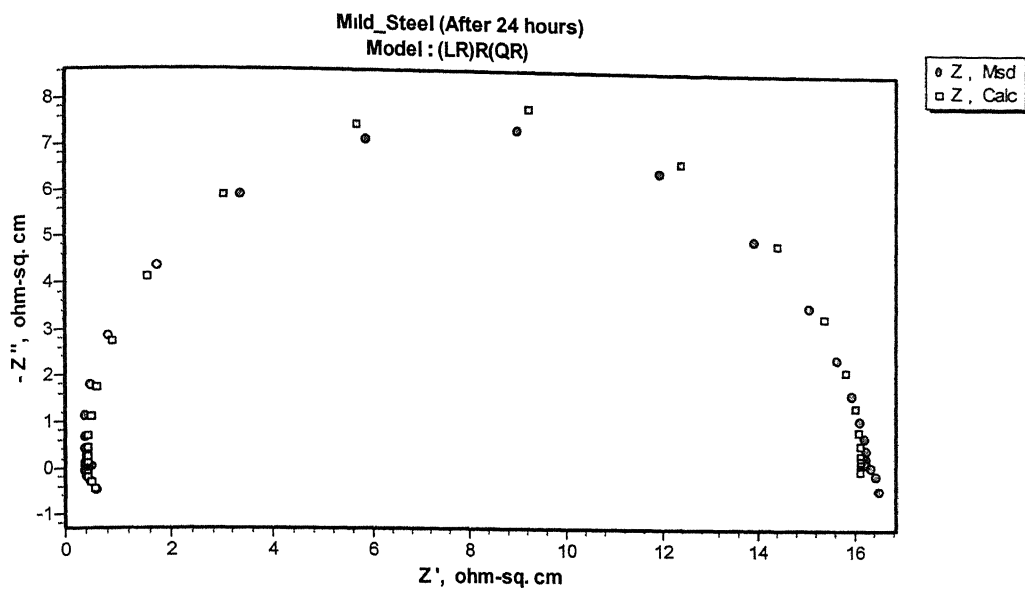


Figure B-23 Experimental (Ms.) and simulated (Calc.) Nyquist plots for 0.05 %C mild steel after 24 hours of immersion in 0.25 mol/lit H_2SO_4 .

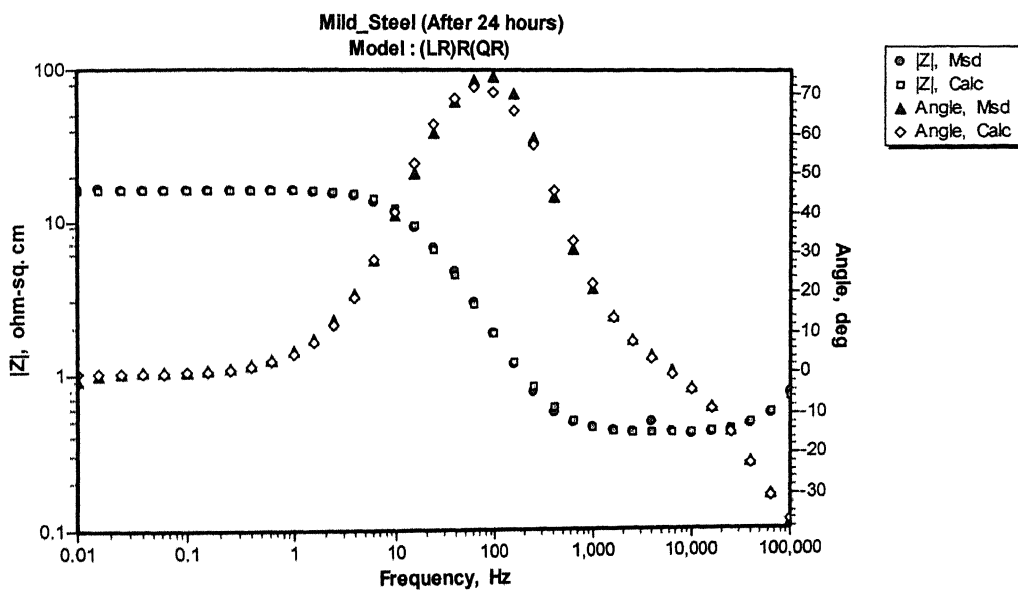


Figure B-24 Experimental (Ms.) and simulated (Calc.) Bode plots for 0.05 %C mild steel after 24 hours of immersion in 0.25 mol/lit H_2SO_4 .

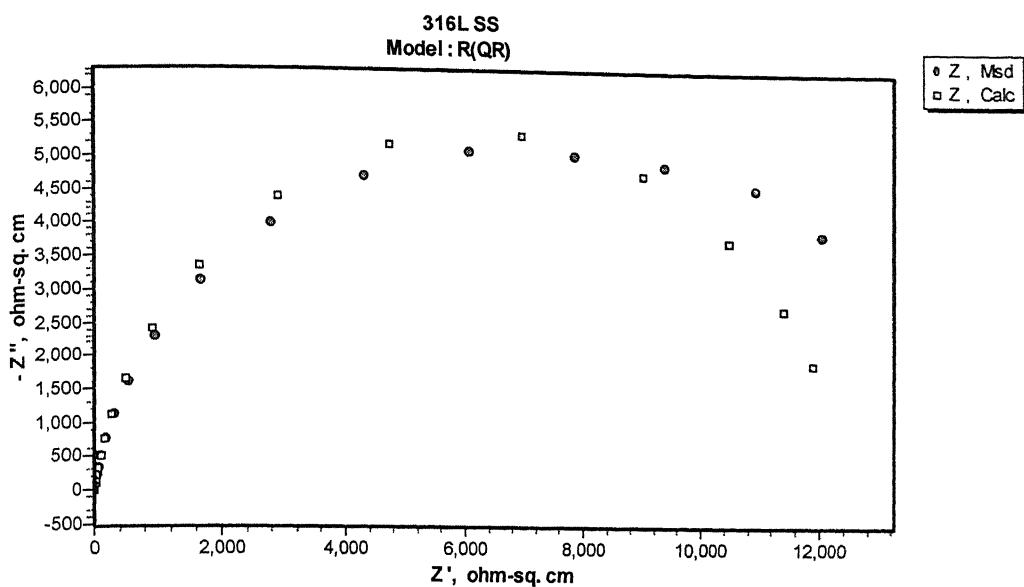


Figure B-25 Experimental (Msd.) and simulated (Calc.) Nyquist plots for 316 SS after first immersion in 0.25 mol/lit H_2SO_4 .

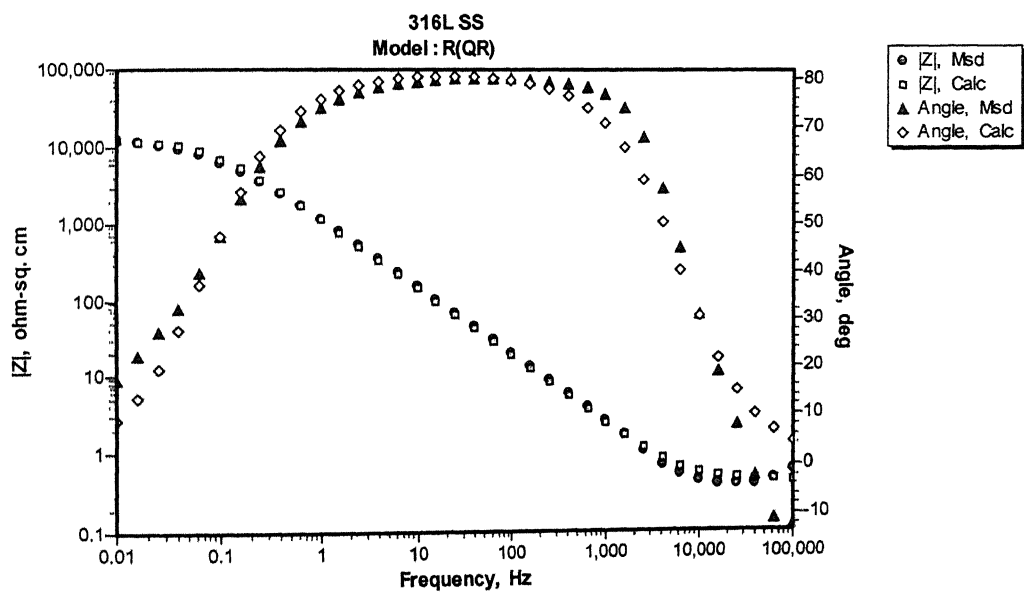


Figure B-26 Experimental (Msd.) and simulated (Calc.) Bode plots for 316 SS after first immersion in 0.25 mol/lit H_2SO_4 .

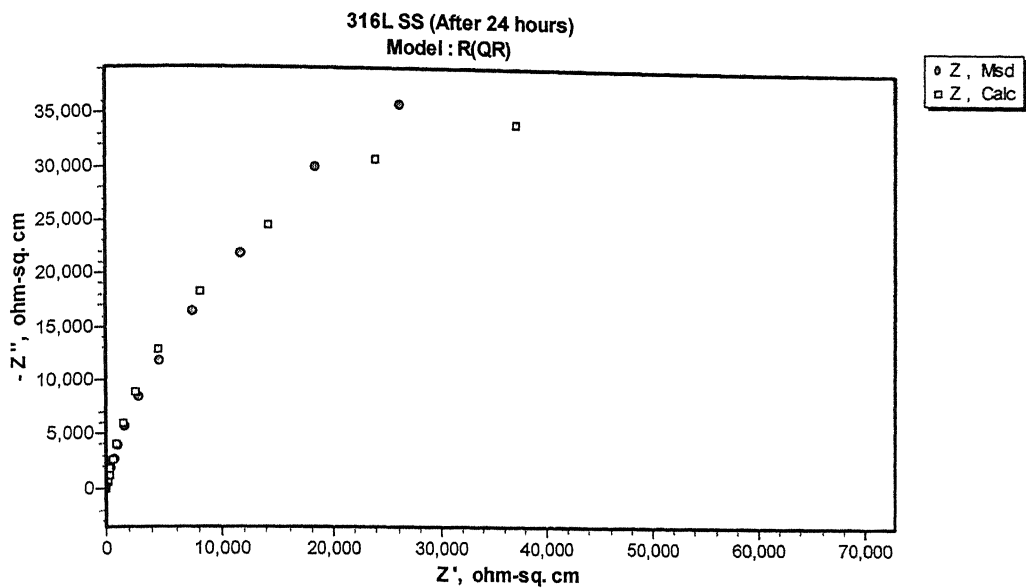


Figure B-27 Experimental (Msd.) and simulated (Calc.) Nyquist plots for 316 SS after 24 hours of immersion in 0.25 mol/lit H_2SO_4 .

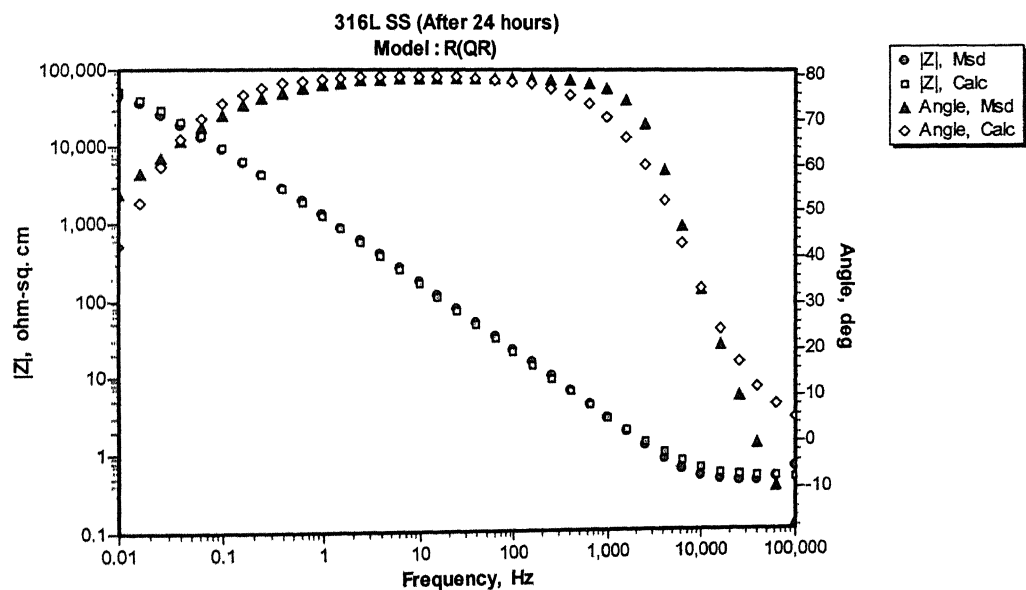


Figure B-28 Experimental (Msd.) and simulated (Calc.) Bode plots for 316 SS after 24 hours of immersion in 0.25 mol/lit H_2SO_4 .

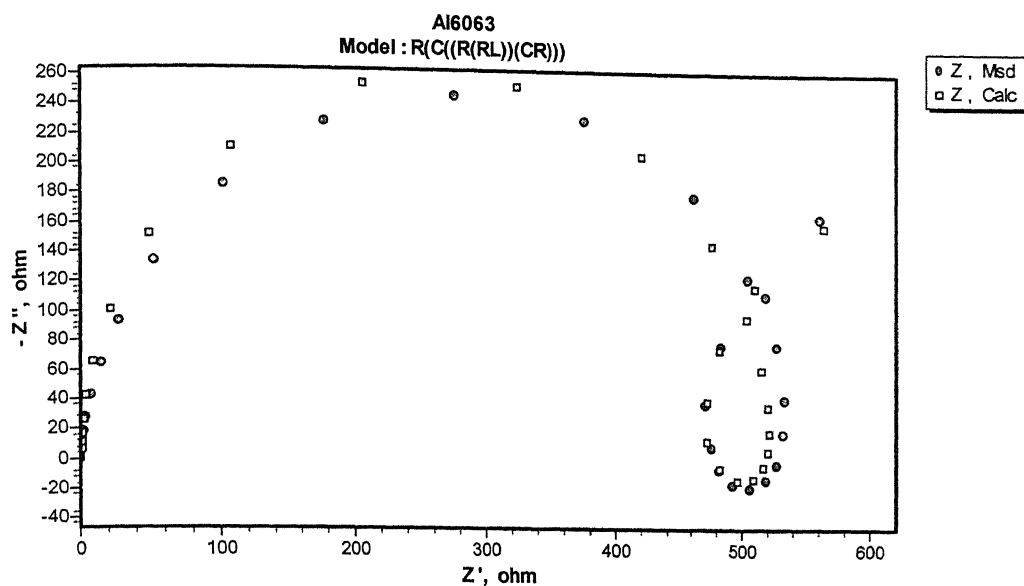


Figure B-29 Experimental (Msd.) and simulated (Calc.) Nyquist plots for Al 6063 after first immersion in 0.25 mol/lit H_2SO_4 .

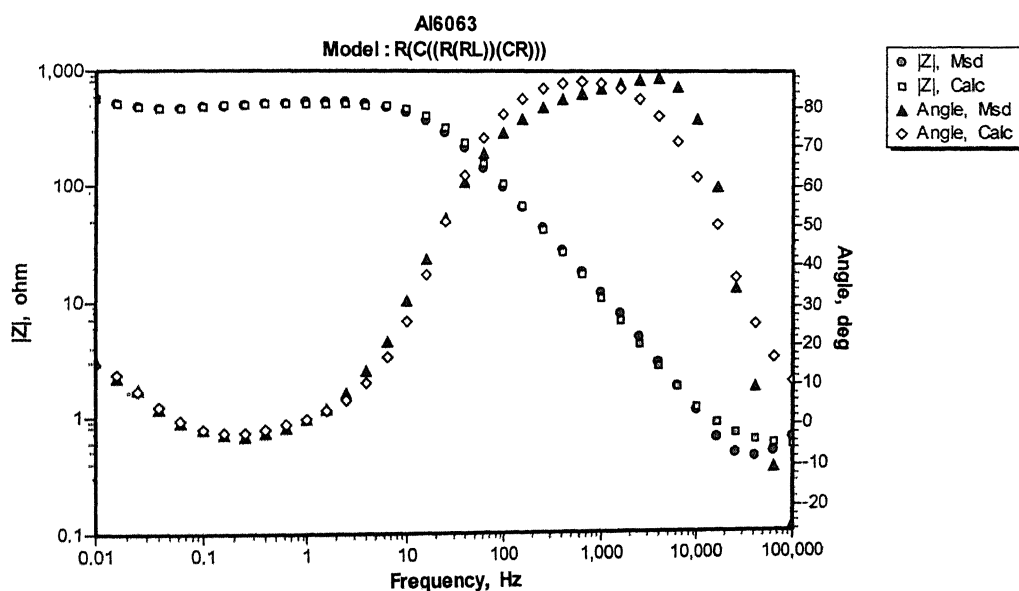


Figure B-30 Experimental (Msd.) and simulated (Calc.) Bode plots for Al 6063 after first immersion in 0.25 mol/lit H_2SO_4 .

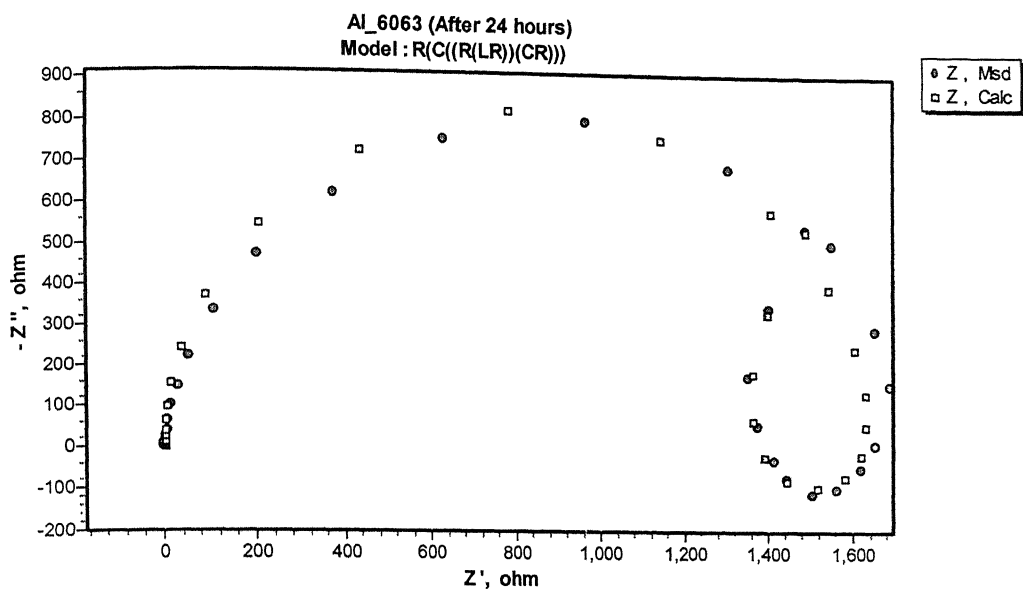


Figure B-31 Experimental (Msd.) and simulated (Calc.) Nyquist plots for Al 6063 after 24 hours of immersion in 0.25 mol/lit H_2SO_4 .

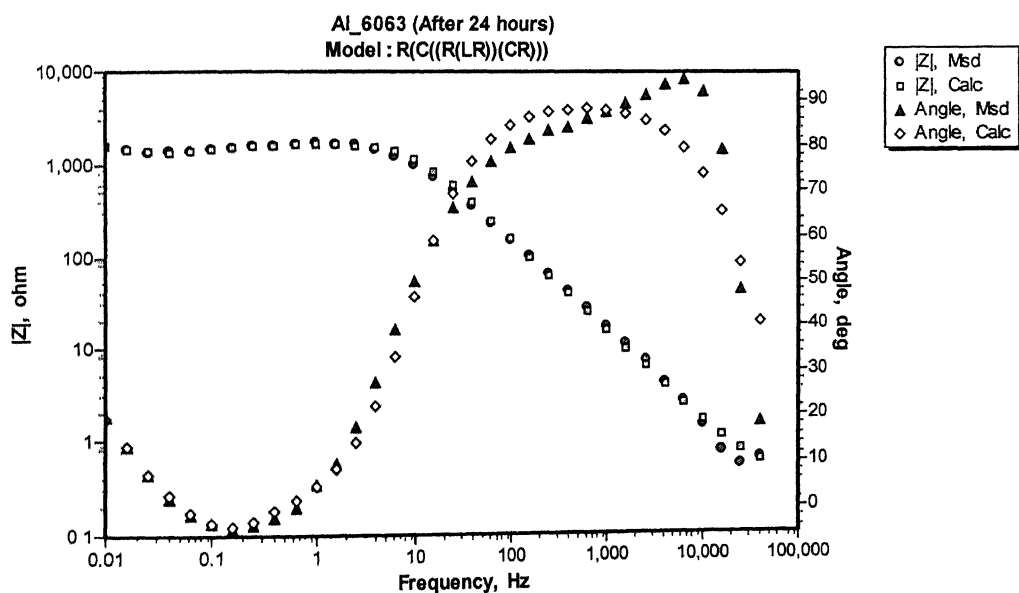


Figure B-32 Experimental (Msd.) and simulated (Calc.) Bode plots for Al 6063 after 24 hours of immersion in 0.25 mol/lit H_2SO_4 .

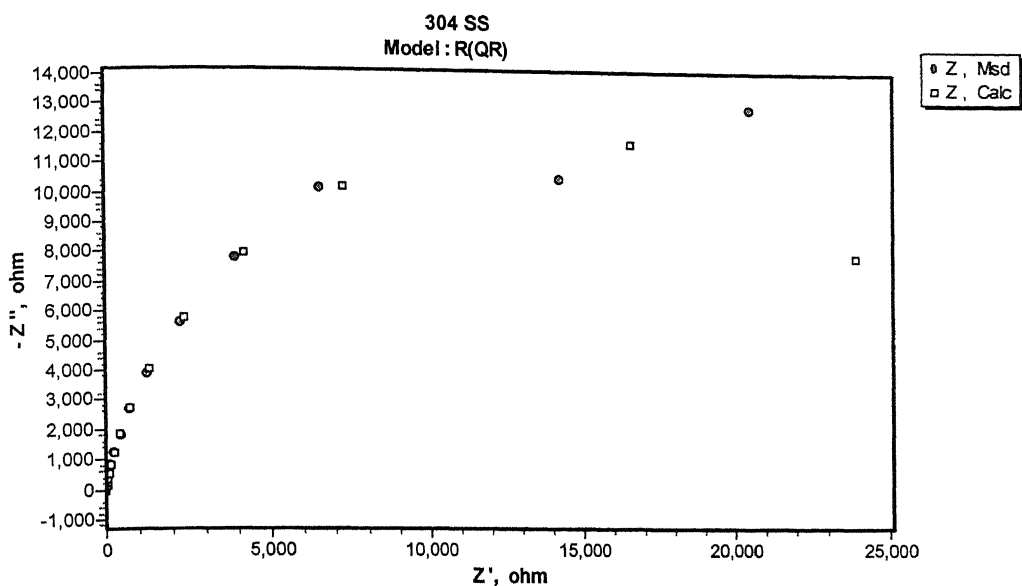


Figure B-33 Experimental (Msd.) and simulated (Calc.) Nyquist plots for 304 SS after first immersion in 0.25 mol/lit H_2SO_4 .

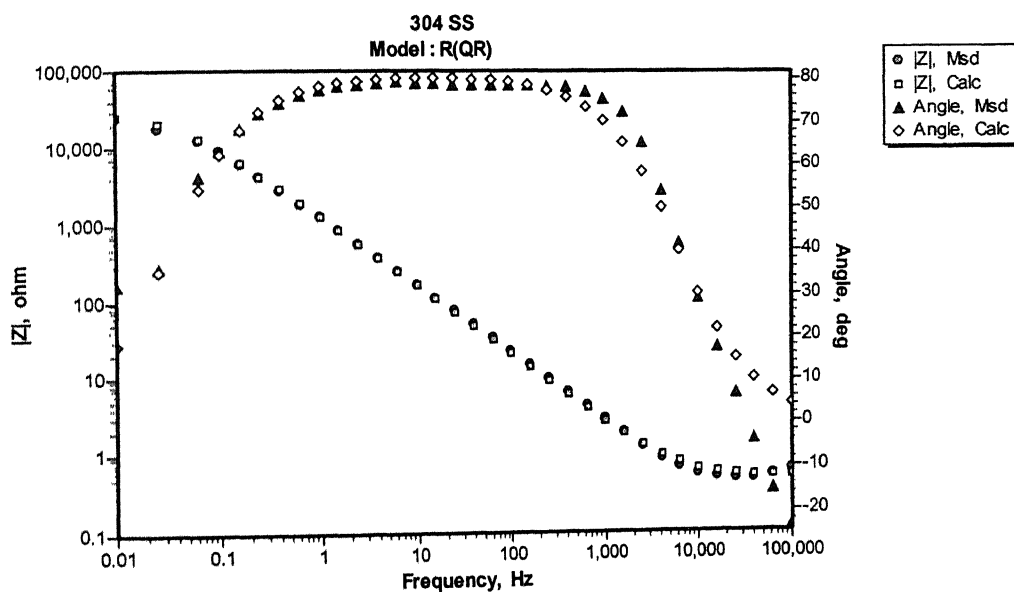


Figure B-34 Experimental (Msd.) and simulated (Calc.) Bode plots for 304 SS after first immersion in 0.25 mol/lit H_2SO_4 .

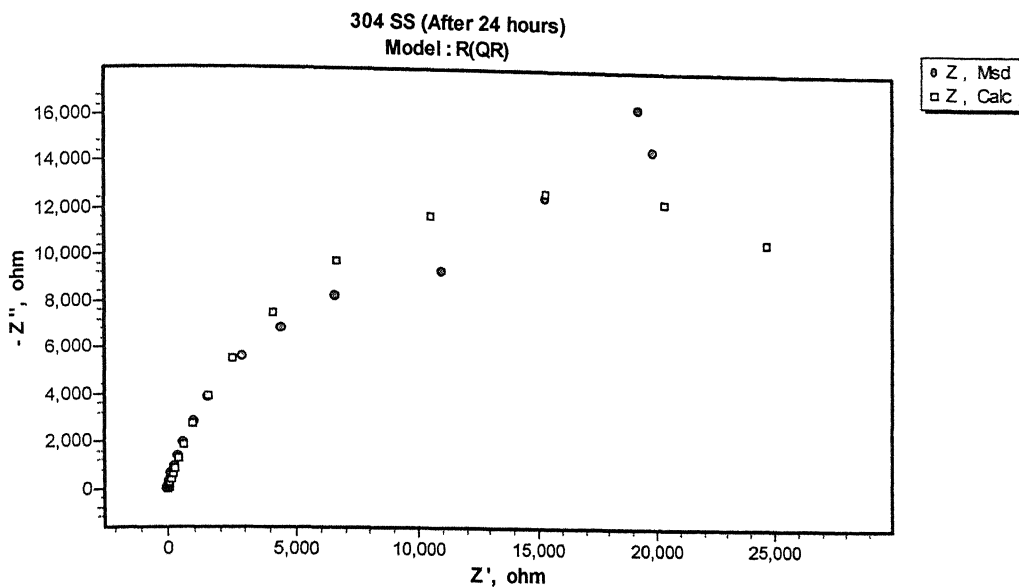


Figure B-35 Experimental (MsD.) and simulated (Calc.) Nyquist plots for 304 SS after 24 hours immersion in 0.25 mol/lit H_2SO_4 .

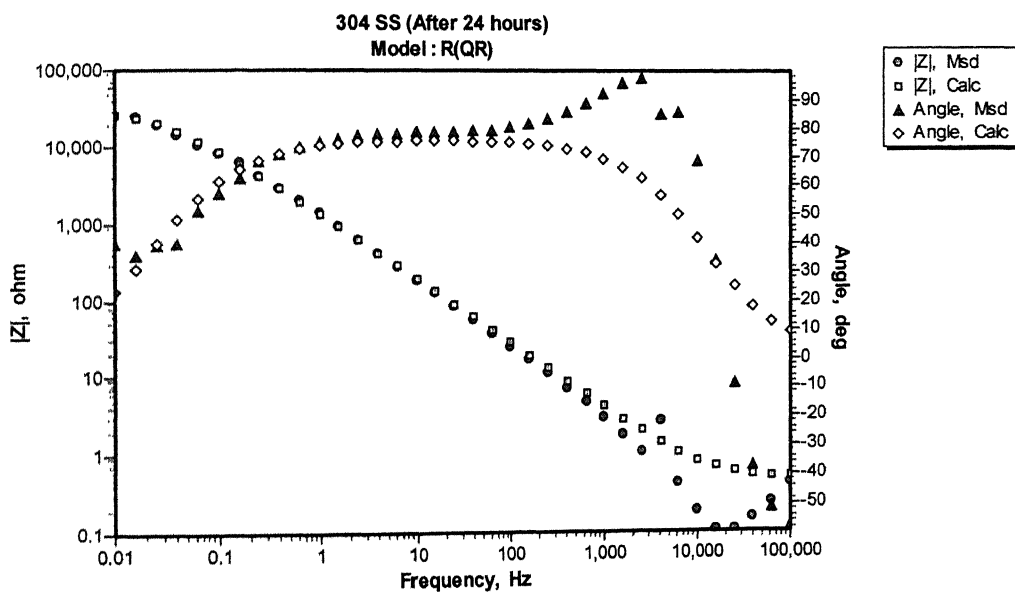


Figure B-36 Experimental (MsD.) and simulated (Calc.) Bode plots for 304 SS after 24 hours immersion in 0.25 mol/lit H_2SO_4 .

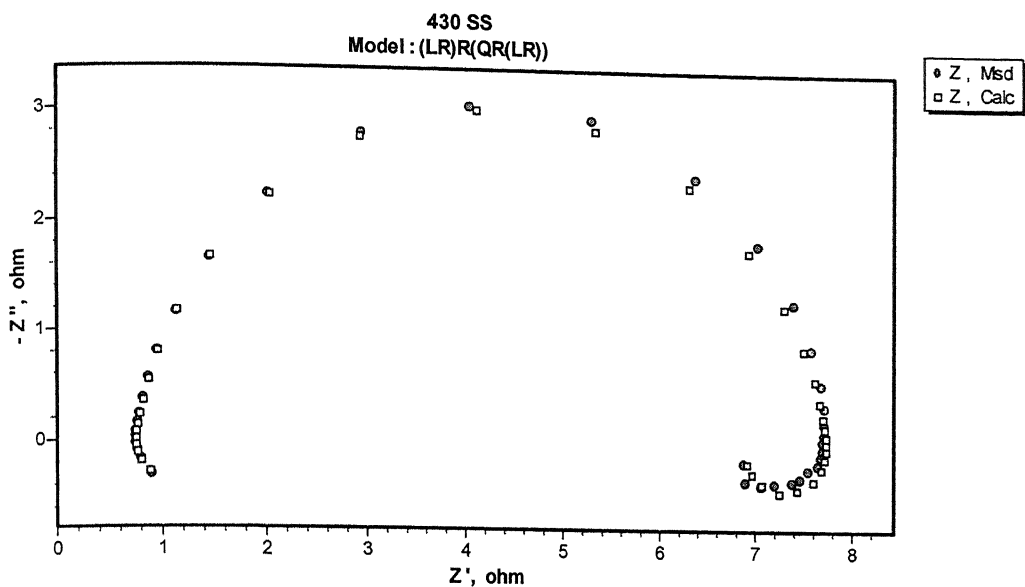


Figure B-37 Experimental (Msd.) and simulated (Calc.) Nyquist plots for 430 SS after first immersion in 0.25 mol/lit H_2SO_4 .

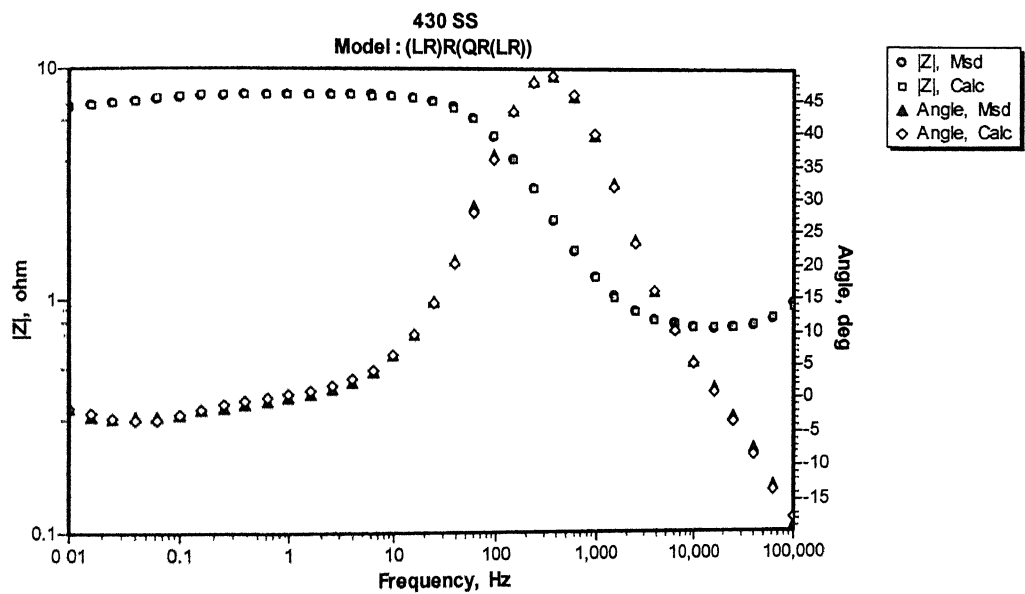


Figure B-38 Experimental (Msd.) and simulated (Calc.) Bode plots for 430 SS after first immersion in 0.25 mol/lit H_2SO_4 .

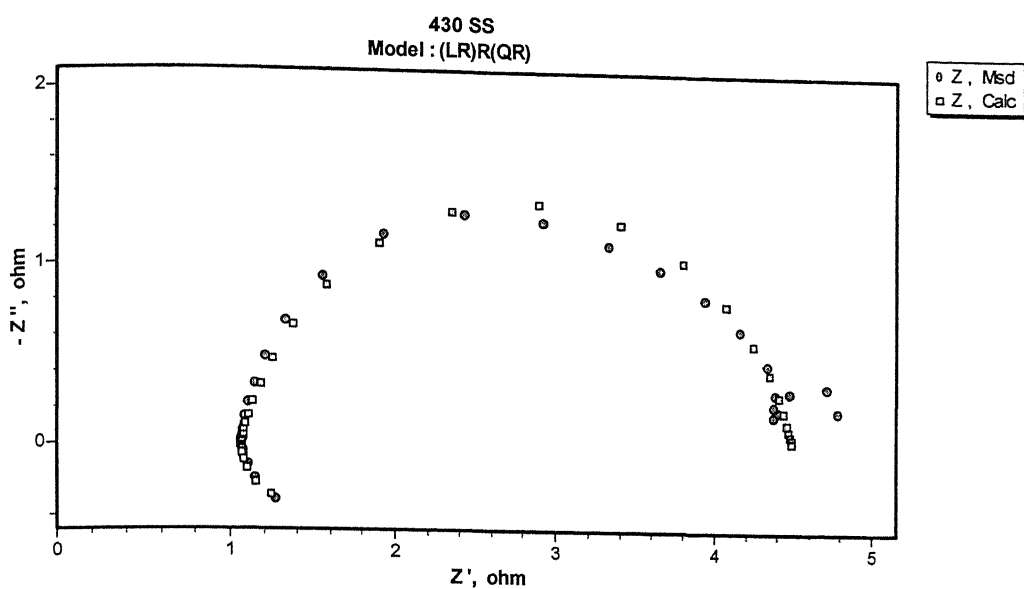


Figure B-39 Experimental (Msd.) and simulated (Calc.) Nyquist plots for 430 SS after 24 hours of immersion in 0.25 mol/lit H_2SO_4 .

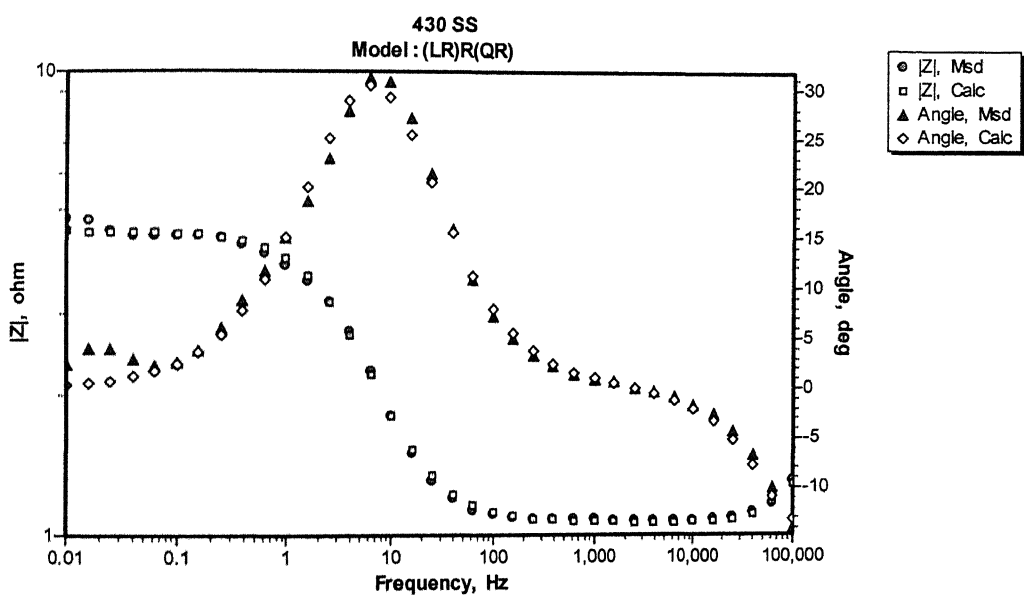


Figure B-40 Experimental (Msd.) and simulated (Calc.) Bode plots for 430 SS after 24 hours of immersion in 0.25 mol/lit H_2SO_4 .